Soil structure formation through the action of plants

Dissertation

zur Erlangung des

Doktorgrades der Naturwissenschaften (Dr. rer. nat.)

der

Naturwissenschaftlichen Fakultät III
Agrar- und Ernährungswissenschaften,
Geowissenschaften und Informatik

der Martin-Luther-Universität Halle-Wittenberg,

vorgelegt von

Herrn Lucas, Maik
Geb. am 22.05.1992 in Lingen (Ems)

Abstract

Soil structure is one of the most important properties of soil, as it influences many processes and thus soil functions, such as yield, water storage and filtration, as well as the property of being a potential habitat for an innumerable number of organisms. Natural influences and anthropogenic, such as wetting-drying cycles or soil tillage, lead to the consequence that soil structure, defined as the spatial arrangement of pores and solids, is not static but subject to constant changes. One of these influences are plant roots, that directly and indirectly affect soil structure while growing into soil. However, these changes are difficult to quantify because they occur in soil that is opaque and are often masked by other processes such as tillage. For example, there are no quantitative data sets on how fast and to what extent plants create biopores. In addition to the missing quantification of these processes, there is also an ongoing discussion about to what degree plant roots compact the rhizosphere, i.e. the soil in the direct vicinity, as they need a certain amount of space when they grow into the soil.

This thesis aims to quantify the influence of plants on soil structure. Therefore, undisturbed samples of a chronosequence were analysed using X-ray microtomography (X-ray μCT). Samples from fields of different ages (0, 1, 3, 6, 12 and 24 years after recultivation) and from two depths (0-20 cm and 40-60 cm) are the basis of the analysis. Due too the trade-off between sample-size and resolution for X-ray μCT a hierarchical sampling approach was used (sample diameters of 10 cm, 3 cm and 0.7 cm in diameter), which resulted in different voxel resolutions of 57 μm, 19 μm and 5 μm.

Parameters such as biopore length density, pore connectivity and pore size distribution were used to characterize the pore system. In order to determine these parameters, numerous demands were made on the X-ray μCT method. Thus, in addition to the application of state-of-the-art imaging analysis methods, several new protocols have been developed or improved. These protocols enabled e.g. the segmentation of biopores and the analysis of gradients around roots/biopores. In addition, the hierarchical sampling procedure made it necessary to investigate the scale dependency of connectivity measures, including the topological metric Euler number, χ, and the connection probability of two random points within the pore system, i.e. the Γ indicator: Different to χ, Γ provides highly biased information in small samples as long-distance connections are destroyed. Hence, a joint-Γ-curve was calculated for the first time to address this problem and which can be used to describe pore connectivity across scales. It has been shown that the joint evaluation of the two connectivity metrics can be used to unravel different pore types with χ and to identify the contribution of different pore types to total pore connectivity with the Γ-indicator. Moreover, a new method was developed, which uses the correlative analysis of X-ray μCT and imaging infrared spectroscopy (imVNIR) to investigate the interplay of biogeochemical properties and soil structure in undisturbed soil samples.

One of the most important results of this work is that a complex system of biopores was established over time that reached an equilibrium state already after 6 years in the topsoil and after 12 years in the subsoil. This is characterised by biopore length densities close to 20 cm^{-3} and revealed that the majority of biopores was between 0.04 and 0.25 mm in diameter. The distribution of the biopore diameters corresponded to the root diameters of the plants used in the crop rotation, which shows that they were mainly the result of growth

of plant roots. This network of biopores is able to connect pores >0.1 mm and thus build up a highly connected macropore system. This work additionally demonstrates that the mutual interaction of soil structure and plant roots must be taken into account in order to characterise the influence of plants on the soil. In other words, the influence of plants on soil structure cannot be predicted without the context of their environment: Thus, it could been shown that despite the increasing biopore density over time, no changes in pore size distribution due to the growth of plant roots could be detected. This indicates that the existing system of macropores provided sufficient "space" for plant growth and therefore they only had to rearrange the existing pore system. Furthermore, the interaction of plant roots and soil structure is also an important factor for the porosity of the rhizosphere: An experiment with corn plants (*Zea Mays*) and different soil densities in combination with the data set of the chronosequence has shown that the rhizosphere of plants is only compacted when roots grow into a soil with a small volume of unconnected macropores. On the other hand, roots in soils with a sufficient volume of macropores can colonise the existing system of macropores. The latter leads to a more porous rhizosphere compared to the mean density of the soil. This work also shows the potential of a correlative analysis of X-ray μCT and imVNIR, even if only a small number of samples could be evaluated. The correlative analysis showed that organic material accumulates at higher distances from macropores and that the amount of organic material around the biopores depends on local density gradients of the biopore walls.

In summary, this thesis provides the first comprehensive analysis of soil structure formation through the action of plants by establishing a quantitative framework for detecting changes in three-dimensional pore structure over time.

Zusammenfassung

Bodenstruktur ist eines der wichtigsten Eigenschaften von Böden, die viele Prozesse und damit Funktionen des Bodens, wie Ertrag, Wasserspeicherung und -filtration sowie die Eigenschaft, ein potentieller Lebensraum für eine Vielzahl von Organismen zu sein, beeinflusst. Bodenstruktur, d.h. die räumliche Anordnung von Poren und Festsubstanz, ist jedoch keinesfalls statisch, sondern unterläuft ständigen Änderungen durch anthropogene und natürliche Einflüsse, wie z.B. Feuchte-Trocknungs-Zyklen oder Bodenbearbeitung. Einer dieser Einflüsse sind Pflazenwurzeln, die während sie in den Boden wachsen, direkt und indirekt auf die Bodenstruktur einwirken. Diese Veränderungen sind jedoch schwer zu quantifizieren, da sie im für uns undurchsichtigen Boden geschehen und oft durch andere Prozesse wie die Bodenbearbeitung überlagert werden. Es gibt z.B. keine quantitativen Daten, wie schnell und in welchem Umfang Pflanzen Bioporen erstellen. Außerdem gibt es Kontroversen darüber, in welchen Ausmaß Pflanzenwurzeln, die in den Boden wachsen und damit einen gewissen Raum einnehmen, die Rhizosphäre, also den Boden in ihrer direkten Umgebung, verdichten müssen.

Die vorliegende Arbeit versucht den Einfluss von Pflanzen auf die Bodenstruktur zu quantifizieren. Dazu, wurden ungestörte Proben einer Chronosequenz mit Hilfe von Röntgenmikrotomographie (μCT) analysiert. Proben unterschiedlichen Alters (0, 1, 3, 6, 12 und 24 Jahren nach Rekultivierung) und aus zwei Tiefen (0-20 cm und 40-60 cm) bilden die Grundlage für die Analysen. Da es bei Analysen mit μCT einen starken Zusammenhang zwischen Probengröße und Auflösung gibt, wurde eine hierarchische Probennahme angewendet (Probengrößen von 10 cm, 3 cm und 0.7 cm), entsprechend ergaben sich Voxelauflösungen von 57 μm, 19 μm und 5 μm.

Parameter wie Bioporenlängendichte, Konnektivität des Porenraums und Porengrößenverteilung dienten als wichtige Kenngrößen um den Porenraum zu charakterisieren. Zur Ermittlung dieser Kenngrößen, wurden zahlreiche Anforderungen an die μCT-Methode gestellt. Neben der Anwendung modernster bildgebender Analyseverfahren, wurden mehrere neue Protokolle entwickelt bzw. weiter entwickelt. Diese ermöglichten z.B. die Segmentierung von Bioporen und die Analyse von Gradienten um Wurzeln/Bioporen. Durch die hierarchische Probennahme, wurde außerdem die Untersuchung der Skalenabhängigkeit von Konnektivitätsmaßen notwendig. Die topologische Metrik Eulerzahl, χ, und die Verbindungswahrscheinlichkeit von zwei zufälligen Punkten innerhalb des Porensystems, d.h. der Γ-Indikator wurden dabei untersucht: Da in kleinen Probenvolumina Verbindungen fehlen, die sich über lange Distanzen erstrecken, liefert Γ, im Gengensatz zu χ hochgradig verzerrte Informationen in Unterproben. Zur Korrektur dieses Problems, wurde zum ersten Mal eine Joint-Γ-Kurve berechnet, welche die Konnektivität des Porenraums über Skalen hinweg beschreiben kann. Es hat sich gezeigt, dass mit einer gemeinsamen Auswertung der Konnektivitätsmetriken verschiedene Porentypen mit χ entwirrt und der Beitrag verschiedener Porentypen zur Gesamtporenkonnektivität mit dem Γ-indikator identifiziert werden kann. Zu guter Letzt, konnte eine neue Methode entwickelt werden, welche die korrelative Analyse von μCT und bildgebender Infrarot-Spektroskopie (imVNIR) ermöglicht, um neue Erkenntnisse über das Zusammenspiel von Bodenstruktur und biogeochemische Prozessen zu gewinnen.

Eines der entscheidenden Ergebnisse dieser Arbeit ist, dass im Laufe der Zeit ein komplexes System von Bioporen entstand, dass mit Werten nahe 20 cm cm^{-3}, bereits nach 6 Jahren im Oberboden und nach 12 Jahren im Unterboden einen Gleichgewichtszustand erreichte. Die Mehrheit dieser Bioporen hatte Durchmesser zwischen 0,04 und 0,25 mm. Die Verteilung der Bioporendurchmesser entsprach den Wurzeldurchmessern der Kulturpflanzen in der Fruchtfolge, was zeigt, dass Bioporen auf das Wachstums von Pflanzenwurzeln zurückzuführen sind. Dieses Netz an Bioporen war im Stande Poren >0,1 mm zu verbinden und so ein hochvernetztes Makroporensystem aufzubauen. Diese Arbeit zeigt außerdem, dass die gegenseitige Wechselwirkung von Bodenstruktur und Pflanzenwurzel berücksichtigt werden muss, um den Einfluss von Pflanzen auf den Boden zu charakterisieren. Mit anderen Worten bedeutet dies, dass der Einfluss von Pflanzen auf die Bodenstruktur ohne den Kontext der Umgebung nicht vorhergesagt werden kann: So hat sich gezeigt, dass trotz der ansteigenden Bioporendichte über die Zeit, keine Veränderungen der Porengrößenverteilung auf das Wachstum von Pflanzenwurzeln nachgewiesen werden konnten. Dies zeigt, dass das bestehende System der Makroporen genügend "Raum" für das Wachstum der Pflanzen bot und sie daher nur das bestehende Porensystem neu anordnen mussten. Darüber hinaus ist die Wechselwirkung von Pflanzenwurzeln und Bodenstruktur ein wichtiger Faktor für die Physik der Rhizosphäre: Ein Versuch mit Maispflanzen (*Zea Mays*) und unterschiedlichen Bodendichten in Verbindung mit dem Datensatz der Chronosequenz, hat veranschaulicht, dass die Rhizosphäre der Pflanzen nur dann verdichtet wird, wenn Wurzeln in einem Boden mit einem kleinen Volumen an unverbundenen Makroporen wachsen. Dagegen können Wurzeln in Böden, die ein ausreichendes Volumen an Makroporen bieten, das bestehende System an Makroporen besiedeln. Aus letzterem ergeben sich Wurzeln mit Rhizosphären hoher Porosität im Vergleich zum restlichen Boden. Diese Arbeit veranschaulicht außerdem das Potenzial der korrelativen Analyse von Röntgen-μCT und imVNIR, auch wenn nur eine geringe Anzahl von Proben ausgewertet werden konnte. Die korrelative Analyse ergab, dass sich organisches Material in höheren Distanzen von Makroporen anreichert und dass die Konzentration an organischem Material um Bioporen von lokalen Dichtegradienten der Bioporenwände abhängt.

Zusammenfassend lässt sich sagen, dass diese Arbeit die erste umfassende Analyse der Bodenstrukturbildung durch die Wirkung von Pflanzen bietet. Dies wurde durch die Schaffung eines quantitativen Rahmens für die Erkennung von Veränderungen in der dreidimensionalen Porenstruktur im Laufe der Zeit erreicht.

Contents

List of Figures

List of Tables

List of Abbreviations

AMS	**A**ccelerator **M**ass **S**pectrometry
C_{mic}	**Mic**robial biomass **C**arbon
CT	**C**omputer **T**omograhpy
DNA	**D**esoxyribo**N**ucleic **A**cid
DOC	**D**issolved **C**arbon
DON	**D**issolved **N**itrogen
EM	**E**quivalent **M**ass
EPS	**E**xtracellular **P**oly**S**accharides
EDT	**E**uclidean **D**istance **T**ransform
FeOX	**Fe O**xide
fig.	**F**igure
ICP-OES	**I**nductively **C**oupled **P**lasma **O**ptical **E**mission **S**pectrometry
imVNIR	**Im**aging **V**is-**NIR**
ITS	**I**nternal **T**ranscribed **S**pacer
LSU	**L**inear **S**pectral **U**nmixing
N_{mic}	**Mic**robial biomass **N**itrogen
nanoSIMS	**Nano**scale **S**econdary **I**on **M**ass **S**pectrometry
OM	**O**rganic **M**atter
PCR	**P**olymerase **C**hain **R**eaction
PSD	**P**ore **S**ize **D**istribution
REV	**R**epresentative **E**lementary **V**olume
ROI	**R**egion **O**f **I**nterest
rRNA	**R**ibosomal **R**ibo**N**ucleic **A**cid
SOC	**S**oil **O**rganic **C**arbon
SOM	**S**oil **O**rganic **M**atter
TC	**T**otal **C**arbon
TN	**T**otal **N**itrogen
Vis-NIR	**Vis**ible light **N**ear **I**nfra**R**ed spectroscopy
Vol-%	**Vol**ume percent
WRB	**W**orld **R**eference **B**ase for Soil Resources
Γ	Connection probability
Φ-vis	**Vis**ible porosity
χ	Euler number

Chapter 1

Introduction

1.1   Scope of the thesis

Soils are unique three-dimensional heterogeneous structures constructed out of mineral and organic components. The spatial organisation of these components, i.e. the arrangement of solids and voids, is called soil structure (Rabot et al., 2018). Important soil properties and processes such as hydraulic conductivity, gas exchange and water retention as well as soil organic matter and nutrient dynamics are controlled by soil structure (Bronick et al., 2005; Rabot et al., 2018). Therefore, soil structure is of fundamental importance for soil functions such as crop yield, water storage and to provide the habitats of various organisms (Vogel et al., 2019).

From the definition it follows that soil structure can be described from the perspective of solids, e.g. aggregate sizes and stability, as well as from the perspective pores, e.g. pore sizes and pore connectivity (Rabot et al., 2018). However, since a part of the spatial information is always lost through the investigation of aggregates, some important processes based on connectivity, tortuosity and heterogeneity of the pore space cannot be sufficiently investigated by investigating the solid space (Baveye et al., 2018; Young et al., 2001). Examples of these processes are water flow and gas diffusion, which can be directly attributed to changes in the architecture of the pores (Koestel et al., 2018; Naveed et al., 2013).

Furthermore, soil structure is not static, but is subject to constant changes due to anthropogenic and natural influences, such as soil tillage or wetting-drying cycles. These changes in soil structure are located over several spatial and temporal scales and have potential impact on physical and biological processes (Rabot et al., 2018).

1.1.1   Plants - one out of many actors changing soil structure

One of the main actors changing the complex soil environments are plant roots, while growing into the soil. Once they die and decay, they leave behind pores or channels known as biopores (Yunusa et al., 2003). In addition to roots, various burrowing organisms, such as earthworms, but also the hyphae of fungi form biopores. Thus, their size varies from a few micrometres to millimetres in diameter (Yunusa et al., 2003). Already in 1983, Tippkötter could link an connected network of biopores between 0.1 and 1 mm, with a maximum between 0.15 and 0.25 mm to the morphology of cereal roots (Tippkötter, 1983) . For the analysis of biopores, however, there are a number of methodological approaches, which are often limited by the spatial resolution (Athmann et al., 2013; Han et al., 2015; Kautz et al., 2013; Stirzaker et al., 1996; White et al., 2010; Wuest, 2001). Measurements along a profile wall for example allow a high spatial resolution, but are only two-dimensional, while endoscopy only allows the investigation of relatively large pores in the mm range. Thus, research in recent decades has mainly focused on biopores >1 mm, and quantification of the temporal dynamics of biopore networks as a result of root growth is missing (Kautz, 2015). Biopores are cylindrical in shape and can extend over the entire soil profile, showing low tortuosity

and high vertical continuity (Kautz, 2015). Consequently, they significantly influence infiltration and preferential flow phenomena (Jarvis, 2007; Koestel et al., 2014; Naveed et al., 2013; Rasse et al., 2000; Wuest, 2001). Particularly in dense subsoils, root growth seems to benefit from such an existing pore network (Gao et al., 2016). This shows that there is a close relationship between old biopores, new root growth and their water extraction (Stirzaker et al., 1996).

If roots rearrange existing soil particles and thus form biopores, it is assumed that they induce a compaction of the soil in their immediate vicinity (Aravena et al., 2011; Bruand et al., 1996; Dexter, 1987). For plants these changes are particularly relevant for the transport of water and nutrients. Aravena et al. (2011, 2014) have shown that increased compaction (reduced porosity) around roots had a positive effect on the uptake of root water. Root induced compaction of the soil surrounding the roots seems reasonable, since root diameters are usually larger than the existing pores. However, recently some studies have shown contradictory results, i.e. an increased porosity in the vicinity of roots (Feeney et al., 2006; Helliwell et al., 2017; Helliwell et al., 2019; Whalley et al., 2005).

Soil structure is also indirectly influenced by roots through water uptake, wherein water extraction fronts are a function of time and root architecture (Pierret et al., 2011). The uptake of root water can locally lead to changes in swelling and shrinking dynamics (Carminati et al., 2013; Helliwell et al., 2019). Roots not only rearrange particles in their immediate vicinity, but also create a diversified microbiological and chemical environment known as the rhizosphere (Hinsinger et al., 2009). Root growth leads to carbon input in different soil depths, including deep soil layers. For fine roots alone, Jackson et al. (1997) estimated that they account for 33% of the world's annual net primary production. The release of organic compounds leads to stabilization of macropore structures (Pierret et al., 2011). In addition, biopores created or reused by earthworms are often coated with body-surface secreted mucus, urine and casts (Görres et al., 2001).

Contrary to roots and earthworms, which are able to directly alter the pore system and provide carbon sources, microbes are mainly responsible for turnover processes and were therefore called "soil architects" (Ramirez et al., 2014). On the microscale, microbes form habitat patches by altering the pore wall surface through the secretion of extracellular polymeric substances (EPS) (Colica et al., 2014). Together with plant polysaccharides, EPS forms the " glue" for the stabilisation of mineral particles and thus the soil structure (Totsche et al., 2018; Watteau et al., 2006).

In addition to biota, agricultural management, soil cultivation, in particular tillage, may have a strong impact on soil structure. In conventionally cultivated soils, for example, an increased volume of macropores is observed (Ambert-Sanchez et al., 2016; Kay et al., 2002; Kravchenko et al., 2011; Pires et al., 2017; Rasmussen, 1999), while soils cultivated without tillage are characterised by lower macroporosity, lower air capacity and higher bulk densities. However, biotic factors dominate in the latter, i.e. higher amounts of earthworms occur in soils which are not tilled (Jarvis et al., 2017; Rasmussen, 1999; Schlüter et al., 2018b).

1.1.2   Observing soil structure over time

All the different biota listed in section 1.1.1 interact with weathered mineral material. Thus, on different spatial scales (e.g. aggregates, pore network, horizons and profiles), unique structural features emerge depending on site-specific climatic conditions and parental material. Therefore, structures of soils provide a time-related "memory" of the past (Lin, 2010). In naturally grown soils, however, it is difficult to disentangle these structures and, above all, to assign them in chronological order to the processes from which they emerged. Therefore, in this thesis investigations were carried out on a chronosequence, which was established during reclamation of open-cast lignite mining sites in Rhineland, Germany. Through this

uniquely large field experiment, the influence of plants on the development of soil structure from freshly deposited and homogeneous loess material can be observed over 24 years. Details about the reclamation procedure and management of these soils can be found in the next chapter. An interesting side-note is that reclaimed soil (Dump Regosol), which is represented in six areas of Germany, covering a total area of 150,000 ha, is the Soil of the Year 2019 (Milbert et al., 2019)[1]. These dump regosols are at the beginning of soil formation, which starts bare, largely uninhabited and poor in humus (Milbert et al., 2019).

Different to typical approaches which describe the changes in the mineral phase, we here describe the changes in the pore structure of reclaimed soils via X-ray computer microtomography (X-ray µCT). Nowadays, various non-invasive imaging methods allow the investigation of changes in the soil structure induced by plant roots through direct visualisation of the intact pore space. X-ray µCT is one of these imaging techniques, which has been increasingly used and further developed in recent years to describe pore systems and their dynamics with parameters such as connectivity, macroporosity and pore size distribution (Kravchenko et al., 2011; Kuka et al., 2013; Naveed et al., 2013; Pires et al., 2017; Schlüter et al., 2018b, 2011a).

1.2 Objectives and Outline

The overaching goal of this thesis is to quantify the influence of plants on soil structure.

We hypothesise that a secondary pore network will be created within years mainly through plant roots. This pore network is assumed to show high connectivity, which would affect aeration and water conductivity. We further assume that this process is interrupted by soil cultivation.

An important aspect of this thesis will be also to characterise the walls of the biopores, i.e. the former rhizosphere. We're assuming that root induced compaction depends on soil pore characteristics and decreases with the amount of connected macropores, since roots which grow into existing macropores do not necessarily have to align soil particles.

To reveal changes in the soil structure on the field scale undisturbed samples from the chronosequence will be analysed with regard to their pore structure. For this, X-ray μCT is one of the main tools used in this thesis.

The hypotheses come along with a row of demands made on the evaluation of μCT images. Therefore, the following methodological questions arise:

1. Is X-ray µCT suitable to investigate the main changes in soil structure over time (e.g. the formation of biopores), i.e. which parameters are sensible and can the important scales be covered?

2. How can connectivity measures be used to unravel different pore types to characterise the entire pore system with regard to its formation?

3. Can we combine information from the pore system (derived from X-ray µCT) with chemical information (derived from image spectroscopy) to investigate undisturbed soil samples in a holistic way?

Chapters 2-6 are the main chapters of this work. Although they can be read independently, together they try to answer the overarching questions about soil structure formation through the action of plants. These chapters have already been published (Chapter 2-4) or submitted (Chapter 5 and 6). In order to improve the legibility of the thesis, formatting was

---

[1]The action "Soil of the year" is a joint initiative of the German Soil Science Society, the Federal Soil Association of Germany and the Austrian soil science society

adapted. Besides language changes (UK English instead of USA English) a common bibliography is provided. The final synthesis and discussion can be found in Chapter 7. The references of the main chapters as well the objective and the central findings can be found below:

Chapter 2 Pihlap, E., M. Vuko, M. Lucas, M. Steffens, M. Schloter, D. Vetterlein, M. Endenich, and I. Kögel-Knabner (2019). "Initial soil formation in an agriculturally reclaimed open-cast mining area - the role of management and loess parent material". In: Soil and Tillage Research 191, pp. 224–237. DOI: 10.1016/j.still.2019.03.023.

Chapter 3 Lucas, M., S. Schlüter, H.-J. Vogel, and D. Vetterlein (2019). "Soil structure formation along an agricultural chronosequence". In: Geoderma 350, pp. 61–72. DOI: 10.1016/j.geoderma.2019.04.041.

Chapter 4 Lucas, M., S. Schlüter, H.-J. Vogel and D. Vetterlein (2019). "Roots compact the surrounding soil depending on the structures they encounter". In: Scientific reports, 9, 16236. DOI: 10.1038/s41598-019-52665-w.

Chapter 5 Lucas, M., D. Vetterlein, H.-J. Vogel and S. Schlüter (submitted). "Pore connectivity across scales and resolutions".

Chapter 6 Lucas, M., E. Pihlap, M. Steffens, D. Vetterlein, and I. Kögel-Knabner (submitted). "Combination of Imaging Infrared Spectroscopy and X-ray Computed Microtomography for the Investigation of Bio- and Physicochemical processes in Structured Soils".

Chapter 3
Soil structure formation along an agricultural chronosequence

1. Objective

Quantify the influence of plants on soil structure (e.g. the temporal development of biopores towards an equilibrium biopore density) and characterize how this process is interrupted by soil cultivation.

2. Methods

X-ray µCT was used to characterize the pore system with parameters such as pore size distribution and connectivity. To overcome the trade-off between sample sizes and resolution tree different sample sizes were evaluated. A new protocol was developed to detect biopores by their tubular shape.
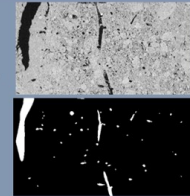
3. Results

- The biopore length densities increased throughout year zero to year 6 in the topsoil and reached an equilibrium. Similar densities were observed 12 years after the reclamation in the subsoil.
- Ploughed layers showed higher macroporosity but surprisingly also high biopore densities.

Reclaimed soil   24 year old soil

Main message

Plant roots create a stable and connected biopore system, which is disrupted by soil tillage.

Chapter 4
Roots compact the surrounding soil depending on the structures they encounter

1. Objective

The rhizosphere is the bottleneck water and nutrients have to pass before entering the root. However, contradictory evidence exists regarding whether and to which extend roots change soil structure in their vicinity. We here investigate the influence of the existing structure on root-induced compaction.

2. Methods

Porosity gradients extending from the root/biopore surface into the bulk soil were investigated with X-ray µCT for 3 cm samples from the chronosequence as well as for a laboratory experiment with *Zea mays* growing into three different bulk densities.

Bulk density [g cm^{-3}]
1.30   1.45   1.60
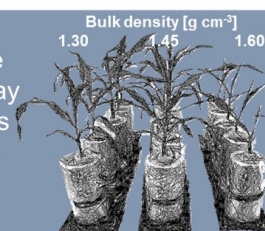
3. Results

- In the laboratory experiment only roots in the intermediate bulk density showed a clear compaction of the rhizosphere
- A compaction around roots/biopores in the field was only observed in combination with high root/biopore length densities

Change in porosity
—— 1.30 g cm^{-3}
······· 1.45 g cm^{-3}
Distance to root
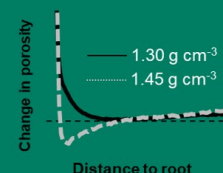
Main message

Roots compact the rhizosphere only if the initial soil structure does not offer a sufficient volume of well-connected macropores.

Chapter 5
Pore connectivity across scales and resolutions

1. Objective

This chapter investigates the changes in pore connectivity with changing samples size. With this we wanted to address whether pore types formed by different processes in agricultural soil leave characteristic traces in certain connectivity metrics.

2. Methods

The connection probability, Γ, and the Euler number, χ, were calculated as a function of pore sizes based on the maximum inscribed sphere method

Resolution

57 µm   19 µm   5 µm
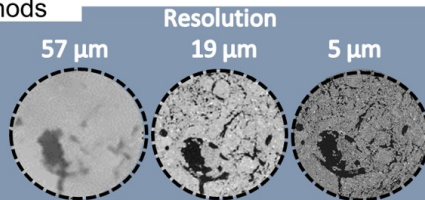
3. Results

- Γ gives highly biased information in small samples when connected pore clusters tend to become fragmented. Therefore, we developed a new method for a joint- Γ connectivity function
- χ does not require such a scale fusion
- Biopores mainly connect the pore system of diameters between 0.1 and 0.5 mm.

Joint-Γ-indicator

Biopore length density

Main message

A joint evaluation of both connectivity metrics can be used to disentangle different pore types with χ and to identify the contribution of different pore types to the overall pore connectivity with Γ.

Chapter 6
Combination of imaging infrared spectroscopy and X-ray computed microtomography for the investigation of bio- and physicochemical processes in structured soils

1. Objective

To understand the relationship between soil structure, carbon dynamics and biogeochemical processes, it is crucial to characterize undisturbed soil samples. However, this relationship is often investigated by techniques based on soil disturbance. We here show a new method of the correlative analysis of 2D imaging visible light near-infrared spectroscopy and 3D X-ray computed microtomography

2. Methods

Samples from the same substrate but different soil management and depth were compared in order to evaluate this method in a diversely structured soil. Images were registered using the software elastix and thus organic matter such as iron-oxide distribution around (bio-) pores could be analysed
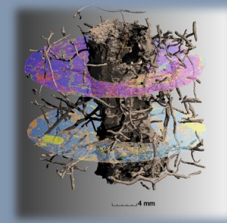
3. Results

- OM can be found mainly at greater distances from macropores and close to biopores
- alterations were observed because of disturbances by tillage

Main message

The correlative application of the two techniques provide new insights into the biochemical processes affected by soil structural changes.

Chapter 2

Initial soil formation in an agriculturally reclaimed open-cast mining area - the role of management and loess parent material
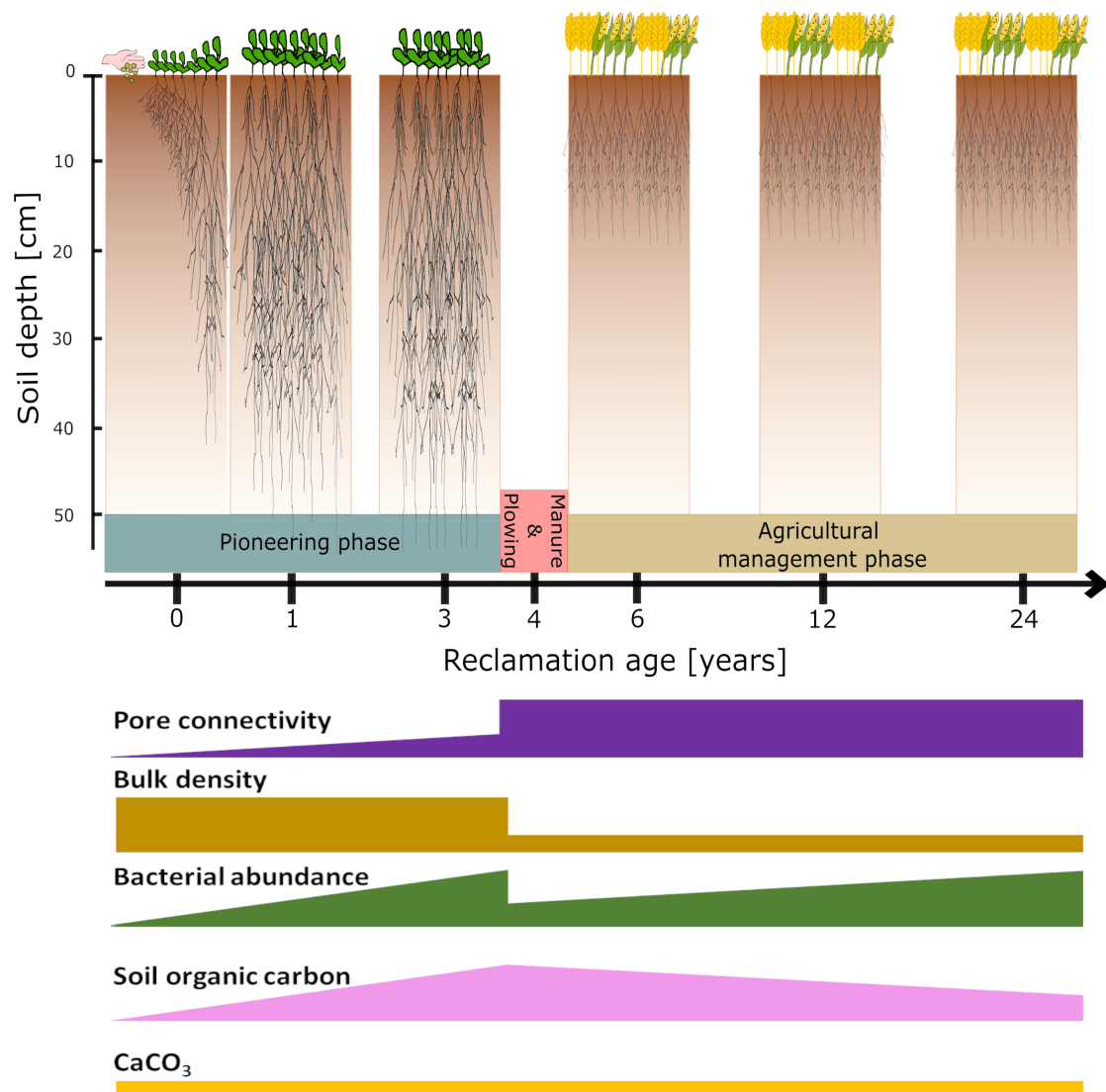
After reclamation of open-cast mining pits, soil formation starts from the deposited calcareous loess characterised by its basic physical and chemical properties whereas soil biology and structure need to develop to achieve a fully functional soil. In this study we used a chronosequence approach to elucidate soil formation on agriculturally reclaimed loess soils in an open-cast lignite mining area in Garzweiler (Germany). We selected six fields aged 0, 1, 3, 6, 12, and 24 years after the first seeding in order to observe the initial stage of development of soil properties and assess the role of management with conventional crop rotation in soil structure formation and soil organic carbon (SOC) accumulation. Loess parent material had a strong impact on aggregation, as CaCO$_3$ acted as a strong cementing agent. Alfalfa cultivation in the pioneering phase was of high importance in the development of microbial biomass, as it protects microbes from N limitation. Soil macroporosity and pore connectivity increased only after compost application and ploughing during agricultural crop rotation. Soil organic matter (SOM) build-up was strongly dependent on the addition of compost, as crop residues from conventional crop rotation are not sufficient to maintain high SOC contents.

2.1 Introduction

Reclaimed soils can be described by low nutrient concentrations, deficits in soil structure formation and low microbial diversity (Shrestha et al., 2011), which is a great concern not only in terms of agricultural productivity, but also for other important soil functions including safeguarding of drinking water or protection from erosion. Several studies have been conducted to elucidate changes that appear after restoring open-cast mining areas (Bradshaw, 1997; Harris et al., 1989; Liu et al., 2017; Zhou et al., 2017), which all indicated that it takes decades before reaching full recovery (Insam et al., 1988; Liu et al., 2017). Most of these studies used the regeneration of nutrient transformation as an indicator. To accelerate the restoration of soil functionality, plant selection and growth coupled with careful agricultural practice is of high importance (Helingerová et al., 2010; Zhao et al., 2013). However, after restoring the land surface, soil formation is a complex development of intertwined biogeochemical processes. Successful reclamation is achieved not only by increasing soil organic matter and nutrient content, but also by soil structural development and its ability to sustain functionality for a longer period.

We consider the spatial arrangement of solids and voids across various spatial scales as soil structure. Deficits in soil structure formation could counteract further soil development and affect soil functions (Kaufmann et al., 2009; Weisskopf et al., 2010). For instance, less favourable aggregate building conditions can lead to aggregate breakdown followed by soil compaction with negative effects on soil aeration and water permeability (Czyż, 2004; Greenland, 1977; Sheoran et al., 2010). Thus, soil structural development as deduced from aggregate formation is a key indicator for soil reclamation success.

There are no universal methods to define and characterise soil structural development (Diaz-Zorita, 2002; Rabot et al., 2018). Bulk density has been often considered as one of the main parameters to describe soil structure and compaction. However, bulk density alone is not sufficient to describe the complex three-dimensional structures like habitats and niches in soil and other soil parameters such as pore size distribution, soil texture, and soil organic matter (SOM) concentration should be taken into account to understand abiotic and biotic processes in soil (Rabot et al., 2018). Macroporosity and its connectivity are important determinants of soil structure. A highly connected macropore system can promote root growth and therefore soil exploration by plants (Lipiec et al., 2003; Rabot et al., 2018). This feeds back to solid phase arrangements, microbial abundance and decomposition of organic matter in soil (Kravchenko et al., 2017; Rabot et al., 2018; Ruamps et al., 2013). It has been found that organic matter content in soil is a crucial factor in reclamation areas for structural development and aggregate formation as well as increasing biological activity (Delschen, 1999; Pagliai et al., 2004; Qiang et al., 2007; Six et al., 2004). However, the formation of stable organic matter pools in soils is a long-lasting process, and therefore it is difficult to achieve the same level as before mining activities took place. Vegetation increases organic matter accumulation, accelerates biological processes in soil (Kołodziej et al., 2016; Moreno-de las Heras, 2009) and thus triggers aggregate formation and stabilisation. Microorganisms, mostly bacteria, influence aggregation via the production of extracellular polysaccharides (EPS) (Chenu, 1995), which makes the microbial biomass an important parameter in soil structural development. In addition, fungi have long been recognised as an important aggregation factor due to their hyphal structure which entangles soil microaggregates and cements them together (Six et al., 2004). Conventional tillage practices increases macroporosity with small changes in micro- and mesoporosity (Kravchenko et al., 2011; Rasmussen, 1999), and thus strongly harm the development of hyphal networks (Boddington et al., 2000; Jansa et al., 2002). In addition microaggregates and fine particles are produced from the breakdown of unstable aggregates (Zhang et al., 2008). This underlines the necessity to understand the close interplay between the soil's chemical, physical, and biological

processes for the development of a stable soil structure in the initial soil reclamation stages.

In our study, we elucidate the development of soil structure as well as the soil's physical, chemical and biological parameters during the initial development of soils in the reclaimed open-cast lignite mining area in Garzweiler, Germany, starting from the initial loess material. We used a chronosequence with six time stages covering the first 24 years after reclamation. For each time point we selected three replicate plots and characterised physio-chemical and biological parameters. In the study we hypothesised: (H1) soil organic carbon concentration will continuously increase throughout the reclamation process and will reach the highest concentrations after 24 years of land use; (H2) the formation of soil aggregate structures in a reclaimed loess will be influenced by the SOM input and accumulation; (H3) the soil's physical properties such as macroporosity will increase and bulk density will decrease over time, and as a function of tillage and development of soil structure. At the initial stage of soil formation, the macroporosity in loess will be low, resulting in soil compaction; and, (H4) as a result of increased soil formation and SOC concentration, microbial biomass will increase during the reclamation process in the first three years and will be negatively affected by soil management in the subsequent time points despite the input of fertilisers.

2.2   Materials and methods

2.2.1   Study area

The study area is situated in the lignite mining area of Rhineland in western Germany between the cities of Cologne, Mönchengladbach and Aachen. Our study sites are located in the Garzweiler (51° 5′ N, 6° 28′ E) post-mining fields, 5 km west of Grevenbroich. Mean annual rainfall and mean annual temperature in the region are 720 mm and 9.5°C, respectively. The natural parent material in the region is loess, which was deposited during the Weichselian glaciation period, approximately 12,000-100,000 years ago, with a thickness of more than 20 metres. Loess is an aeolian sediment with a light yellow colour, high content of silt and calcaric material (concentration can vary between 10-200 mg g^{-1} with cementing properties (Lehmkuhl et al., 2016; Pécsi, 1990). Loess deposition in Garzweiler belongs to Lower Rhine Embayment, where its distribution and sequence are described by Kels et al. (2010), Lehmann et al. (2015) and Schirmer (2016). The typical soil type developed from the loess in the region is Haplic Luvisol (Aric, Hypereutric, Ochric, Siltic) according to the World Reference Base for Soil Resources (WRB) (IUSS Working Group WRB, 2015).

2.2.2   Reclamation procedure

Open-cast lignite mining has two simultaneous processes: lignite mining on one side, and land reclamation on the other, already exploited side of the mining pit. To this day in Rhineland, about 33,000 ha of land have been removed and about 23,000 ha have been reclaimed either as agricultural land (12,000 ha) or forest (9,000 ha). The current reclamation technique was developed in the 1990s (Dumbeck, 1992; Dumbeck, 2014). During the mining process, an approximately 20-metre-thick layer of loess including about 2.2 m of developed Luvisol is excavated, mixed together (Luvisol/loess ratio about 1:10) and deposited on the side with spreaders to a thickness of at least two metres. After three months of settling time in stockpiles, the mixture is levelled with special loess caterpillars and seeded with alfalfa (*Medicago sativa*). The first phase of reclamation is a pioneering phase, where alfalfa is cultivated for its deep rooting system and nitrogen enrichment, which is supposed to lead to biological activation of the fresh loess deposits during the first three years. The second phase of the reclamation process always starts in year 4 and is based on a crop rotation including *Triticum aestivum* L. (wheat) and *Hordeum vulgare* L. (barley) until year 6, and a variation of

Triticum aestivum L. (winter wheat and summer wheat), *Hordeum vulgare* L (winter barley), *Brassica napus* L. (rapeseed) and *Zea mays* L. (maize) in the years after. About 30 t/ha of organic fertiliser (compost or manure) is added in the 4th and 7th year of land management. During the first seven years reclaimed areas are managed by the mining company (RWE power AG). After seven years the land is returned to the farmers.

2.2.3   Sampling scheme

We used a chronosequence approach with sites from six different time stages during the reclamation process: 0, 1, 3, 6, 12 and 24 years after the first seeding of alfalfa (Fig A.1). Our chronosequence is defined as fields that originate from a similar loess parent material and go through the same pioneering phase, followed by the same agricultural soil management periods, but differ in the years of soil development. The youngest chronosequence stages (0, 1 and 3 years) are fields representing the first reclamation management period of the pioneering phase, with the cultivation of alfalfa. Older chronosequence stages (years 6, 12 and 24) are managed in agricultural rotation. In order to characterise typical soil properties of mature soils in the region before the mining starts, we selected a reference field situated next to the mining pit, but not yet affected by the mining process. In each field (areas between 2 and 35 ha), we identified three replicated plots each of approximately 200 m^2. In these 18 plots we conducted four sampling campaigns in total using two different soil sampling strategies.

2.2.4   Sampling for physico-chemical and biological analyses

Sampling for physico-chemical and biological analyses was done in a joint sampling campaign in October 2016. Samples were taken from four independent sampling points in each of the three replicate plots. Undisturbed bulk samples were taken with 100 cm^{3}steel cylinders in triplicate (total bulk sample volume 300 cm^3) at three different sampling depths. Topsoil was sampled at 1-5 cm and 16-20 cm at each of the sampling points, while subsoil (41-45 cm) was only sampled once per field replicate plot. For soil physico-chemical analysis all samples were oven-dried at 40°C in order to standardise their weight and moisture content. For biological analyses, samples from the four independent sampling points were pooled and homogenised. After homogenisation, samples were immediately cooled in the field and stored at 4°C and 80°C until further analyses.

2.2.5   Sampling for structural analyses

To analyse structural changes with μCT, a custom-made drill for undisturbed sampling of cylindrical soil cores (UGT GmbH, Germany) was used. To avoid long storage time and changes in pore structure, samples were taken during four sampling campaigns between October 2016 and March 2018. To cover both the management affected and unaffected layers, samples were taken in topsoil at a depth of 1-21 cm and in subsoil at a depth of 40-60 cm. The second depth of a 0-year-old area was not sampled, as a small gradient over the depth was expected due to the mechanised reclamation. A total of 99 soil cores with a diameter of 10 cm and a height of 20 cm were drilled out (3 individual cores per field replicate). All samples were stored at 4°C to prevent soil drying and reduce biological activity.

2.2.6   Analysis of soil physical parameters

For bulk soil measurements, sub-samples were taken from undisturbed steel cylinders. Bulk density of the soil was calculated with the oven-dry (105°C) sample mass divided by total sample volume of 300 cm^3 as described by Poeplau et al. (2017).

Soil texture was analysed from subsoil samples for characterising parent material. Inorganic carbon was removed with 1 M HCl solution and due to very low SOC concentration in subsoils (2.7 $\pm$0.8 mg g^{-1}), organic matter removal was not conducted. After the pre-treatment, samples were suspended in 0.025 M Na$_4$P$_2$O$_7$ solution, dispersed by ultrasonication at 450 J ml^{-1}and wet sieved for sand fractions extraction (Emerson, 1971; Schmidt et al., 1999). Silt and clay size fractions (<63 μm) were freeze dried and their distribution was measured with X-ray sedimentation using Sedigraph III Plus (Micrometrics GmbH, Germany).

For soil aggregate measurements we used a jaw crusher set to 20 mm to break samples into aggregates after drying at 40°C. Broken samples were dry sieved into four different macro aggregate size classes: 6.3-20 mm, 2-6.3 mm and <2 mm. Aggregate size classes of 20-6.3 mm, 6.3-2 mm and <2 mm from each field replicate plot at two sampling points and from each sampling depth (1-5 cm, 16-20 cm and 41-45 cm) were measured for TC and CaCO^3 (see below).

2.2.7   Analysis of soil chemical parameters

pH was measured from each field replicate plot at a depth of 16-20 cm. For the measurement, soil samples were suspended in 0.01 M CaCl$_2$ solution with a ratio of 1:5. Total carbon (TC), total nitrogen (TN) and carbonate concentration were measured by dry combustion with an EuroEA Elementar analyser (HEKAtech GmbH, Wegberg, Germany). CaCO$_3$ concentration was measured using a Scheibler Calcimeter (Eijkelkamp, Giesbeek, The Netherlands). Soil inorganic carbon (SIC) concentration was calculated by dividing measured CaCO$_3$ [mg g^{-1}] concentration with the constant of 8.33. Soil organic carbon (SOC) concentration was calculated as the difference between total and inorganic carbon concentration. In the samples of the mature soil from reference field, no CaCO$_3$ was observed, therefore the measured total carbon concentration was considered as the total soil organic carbon concentration present in soil. The C/N ratio was calculated using SOC and TN values.

Bulk density values and SOC concentrations were used to calculate soil organic carbon stocks of three depth increments (0-10 cm, 10-30 cm and 30-50 cm). Normally, SOC stocks are calculated with bulk density at a fixed depth. However, this method leads to wrong stock assessment, when different treatments with contrasting bulk densities are being compared to each other (Wendt et al., 2013). In order to take into account changes of bulk density and soil volume at different time points, the equivalent mass approach was applied (Ellert et al., 1995). To consider changes in soil volume over the time period, we grouped study fields with the same treatment and the transformation of soil management. Therefore, four different SOC stocks calculations were conducted: a) year 0 soil mass was used as an equivalent mass for calculating stocks at the years 1 and 3; b) year 3 field soil mass was used to correct soil volume and stock calculations after changing soil management at year 6; c) year 6 fields' former soil mass was an equivalent mass for calculating SOC stocks in years 12 and 24; and, d) year 24 fields' soil mass was used as equivalent mass for calculating stocks in the reference field. For SOC stock calculations with equivalent mass approach, the equation was applied according to Ellert et al. (1995):

$$SOC_{stock} = EM * SOC * 10^{-3} \qquad (2.1)$$

where SOC$_{stock}$is the soil organic carbon stock [kg SOC m^{-2}], EM is the equivalent mass [kg m^{-2}], and SOC is the soil organic carbon concentration [mg g^{-1}]. Radiocarbon ^{14}C activity was measured for each age at the centre of one plot at a depth of 1-5 cm and 41-45 cm.

The measurements were carried out at the CologneAMS Centre by accelerator mass spectrometry (AMS) (Rethemeyer et al., 2013). All samples were pre-treated for 72 hours with 1 hour of heating at 60°C and with the addition of 1% HCl solution to remove carbonates.

In soils SOM consists of a fresh SOC originating from input by plants and organic fertilisers, and old carbon named "dead" carbon, which has been in soils for a longer period. In order to assess recent SOM input, the proportion of "dead" carbon was calculated from radiocarbon ^{14}C activity according to the equation (Rumpel et al., 2000):

$$\textit{"Dead" carbon}[\%] = (1 - \frac{^{14}C_{activity}}{115}) * 100 \tag{2.2}$$

where ^{14}C activity represent measured radiocarbon activity.

2.2.8 Biological analysis

Microbial biomass carbon and nitrogen (C_{mic} and N_{mic}) were determined based on the chloroform fumigation extraction method (Joergensen, 1996; Vance et al., 1987). C_{mic} and N_{mic} were calculated as the difference between total dissolved carbon (DOC) and nitrogen (DON) in fumigated and non-fumigated samples, with a k_{ec} value of 0.45 (Vance et al., 1987) for carbon, and k_{en} value of 0.54 (Brookes et al., 1985) for nitrogen. DON and DOC values were obtained from the non-fumigated control samples.

DNA was extracted from approximately 300 mg of each sample using the NucleoSpin Soil extraction kit (Macherey-Nagel, Germany). Sample material was suspended in lysis buffer SL1, with a supplement of 150 μl of Enhancer SX. A blank DNA extraction without any sample template was performed in each extraction run as the negative control. DNA quality was assessed by A260nm/A280nm and A260nm/A230nm measurements on the NanoDrop 1000 Spectrophotometer (PeqLab, Erlangen, Germany). DNA concentrations were quantified with the Quant-iT PicoGreen dsDNA Assay Kit (Life Technologies, USA). Extracted DNA was stored at -20°C until further processing.

The quantification of bacterial and archaeal 16S rRNA genes, and the fungal ITS region was performed on a 7300 Real-Time PCR System (Applied Biosystems, Germany) using SYBR Green (Applied Biosystems, Germany) for detection. PCR conditions, standards and primers used are given in the Table A.1. The volume of each PCR reaction was 25 μl.

Based on pre-tests, DNA samples were diluted 1:20 in order to minimise the effect of PCR inhibitors (data not shown). Serial plasmid dilutions ranging from 101 to 107 gene copies per microlitre were used as standards. All standards were analysed in triplicates, and negative controls were included in each PCR run. Amplification efficiencies were calculated with the equation

$$Eff = [10^{\frac{-1}{slope}} - 1] \tag{2.3}$$

and resulted with 92% for 16S bacteria, 84% for 16S archaea, and 83% for ITS genes. The melting curve analysis confirmed the specificity of amplicons after each PCR run and indicated no primer dimer formation.

2.2.9 Structural analysis with μCT

Cylindrical soil cores were scanned with an X-ray microtomograph (X-TEk XCT 225, Nikon Metrology) with an Elmer-Perkin 1620 detector panel (1750 x 2000 pixels). Separate scans for the upper and lower part of the cores had to be conducted to capture the complete soil core at optimal resolution. The following X-ray μCT settings were chosen: 165 keV, 570 μA, 2500 projections per scan and an exposure time of 1 s (one frame per projection). The reconstruction of three-dimensional images via filtered back projection was performed using the

CT Pro 3-D software package (version XT 4.35, Nikon Metrology NV) at a spatial resolution of 57 μm and an 8-bit grayscale resolution for density differences.

As a first step after reconstruction, a non-local means filter implemented in Fiji (version 1.4.6) (Buades et al., 2011; Darbon et al., 2008) with a noise level parameter of σ= 25 was used to reduce noise. This was done to improve the robustness of automatic, histogram-based threshold detection methods. Small fractures in the sample wall were removed using a cylindrical region of interest (ROI). In samples with deep cracks, an adaptive rectangle in VGStudio was used to mask these pores, which are a result of sampling. Compared to a change of the cylindrical ROI at various spots, this is a fast way to reduce errors in pore space volume induced by cracks starting at the margin. At the same time, less volume is lost for the final analysis. Threshold detection was done with 5 different segmentation methods (Maximum Variance, Minimum Error, Maximum Entropy, Fuzzy C-means and Shape) in Quantim as described in Schlüter et al. (2014). The average of 5 mean and lower percentile values of this method were used for hysteresis thresholding in Fiji (Ollion et al., 2013, 3D Segmentation plugin, Version V3.83). Compared to simple thresholding, it reduces segmentation noise while simultaneously maintaining the intact pore network. In an inverted X-ray μCT image this causes roots (which are normally brighter than empty pores) to be labelled as pores. The resulting binary images were used to calculate total visible porosity and visible porosity as a function of depth. The latter was used to calculate the macroporosity at depths of 1-5 cm, 16-20 cm and 41-45 cm in order to compare them with bulk density. Macroporosity was defined by the effective resolution of 114 μm (2 pixels). Pore connectivity is evaluated from the second moment of the cluster size distribution, known as connection probability or Γ-indicator (Renard et al., 2013; Schlüter et al., 2014). The range of Γ extends from 0 (many equally large, isolated pores) to 1, which represents a perfectly connected pore network. The parameter is highly correlated with the normalised square volume of the largest pore network. The cluster size distribution was calculated using the MorphoLibJ plugin (Legland et al., 2016) in Fiji.

2.2.10   Statistical analysis

To identify significant differences throughout the reclamation chronosequence, the Kruskal-Wallis test followed by Dunn's multiple comparisons test was used for physico-chemical and biological analyses (Dunn, 1964; Kruskal et al., 1952). Statistical comparison was performed within a sampling depth and between every time point in order to assess the effect of soil development on a depth scale. Statistical significance analyses were carried out using the software R Studio (R version 3.4.2) and differences were considered significant when the probability was 0.05 or less.

We used a two-Step Cluster Analysis in SPSS Statistics 25.0 software (SPSS Inc., Chicago, USA) to cluster soil formation phases throughout the chronosequence according to measured physical, chemical and biological parameters. In order to identify the variables that contribute to clustering the most, a Discriminant Analysis was performed. To understand the reclamation time and soil management role on soil development, a general linear model was applied with reclamation age and management as influencing factors. As soil productivity starts to increase with OM input and influence of agricultural management, the contribution of SOC concentration, macroporosity and bulk density in predicting soil chemical and biological parameters was measured. The independent variable (influencing factor) predicted a significant relationship with dependent variable (observed parameter) when the p-value of the model was equal to or less than 0.05. When residuals from the model were not normally distributed according to the Shapiro-Wilk normality test, a log transformation

was performed. Additionally, Pearson's correlation test was performed to understand correlations and dependence of variables between the pioneering and agricultural management phases.

2.3 Results

2.3.1 Soil description

Reclaimed soils in the area were classified as Calcaric Regosol (Aric, Ochric, Siltic, Pantotransportic) according to the World Reference Base for Soil Resources (WRB) (IUSS Working Group WRB, 2015). The soil texture was silty clay loam (Sand 3.5 $\pm$2.0%, Silt 65.1 $\pm$2.6%, Clay 31.4 $\pm$1.8%) and did not differ between the sites along the chronosequence. All samples were slightly alkaline with pH values ranging from 7.4-7.6 and contained carbonate in all stages of the chronosequence. Measured $CaCO_3$ concentrations in the reclamation area were between 33.1 $\pm$1.5 mg g^{-1} and 124.5 $\pm$54.9 mg g^{-1}, and no significant differences were observed between ages and soil depths (Table 2.1). Even for the oldest site, no depth gradient in $CaCO_3$ could be depicted, while the reference site was free of carbonate throughout the profile.

In year 0 the development of alfalfa started from the seed, and in years 1 and 3 the rooting depth was beyond the observed depth of 1 metre. In year 3 organic matter accumulation via plant litter was visible as a dark, organic matter rich layer at a depth of 1-5 cm. In year 3, one field replicate plot was excluded due to high difference in measured physico-chemical parameters. After the soil management changed from the pioneering phase to agricultural management, an initial Ap horizon started to develop and was clearly visible after 6 years in a depth of approximately 30-35 cm, which corresponds to the ploughing depth in years 6, 12 and 24.

2.3.2 Bulk density and macroporosity

Initially (year 0), the average bulk density at a depth of 1-5 cm was 1.46 $\pm$0.01 g cm^{-3} and increased at a depth of 16-20 cm to 1.63 $\pm$0.01 g cm^{-3} (Fig. 2.1). Mean values of macroporosity and bulk density throughout the chronosequence are represented in the Table A.2. In year 1 and 3 bulk density remained stable and high in the whole topsoil. Changes to bulk density were found in year 6, 12 and 24, where loess was less dense in the first two sampling depths compared to younger fields. For the sampling depth of 41-45 cm bulk density was around 1.5-1.6 g cm^{-3} and did not change significantly with age. Likewise, macroporosity (>0.1 mm, Fig. 2.1) in the topsoil increased from 2.3 Vol-% to 8.8 Vol-% 24 years after reclamation. The largest increase in macroporosity was observed between years 3 (2.5 Vol-%) and 6 (6.8 Vol-%). No changes in macroporosity were observed at the 41-45 cm depth.

The scatterplot of visible porosity and pore connectivity reveals different trends (Fig. 2.2). The younger fields at the first 0–20 cm depth are characterised by low macroporosities and thus low connection probabilities, i.e. the lowest Γ-values close to 0 are found in the year 0. On the other hand, high connection probabilities (Γ>0.7) are only found in the first 20 cm of the years 6, 12 and 24, which are also characterised by high macroporosity. The general non-linear correlation between visible porosity and pore connectivity is similar to earlier studies (Schlüter et al., 2016a; Schlüter et al., 2018b). At the second depth (40-60 cm) the Γ-indicator does not reach values higher than 0.7 due to the generally low macroporosity. Different to the first depth, this increase does not go along with high increases in macroporosity. However, at the same macroporosity, connection probabilities of the older fields tend to be higher.

TABLE 2.1: *Mean values of chemical and biological parameters and ^{14}C activity, estimated ^{14}C age, and composition of "dead" carbon and recent carbon calculated according to Rumpel et al. (2000). Standard deviations are calculated from field replicates (n=3, except at 3 years where n=2) and ^{14}C activity and radiocarbon ^{14}C age represents standard error from the measurement.*

Reclamation age [years]	Depth [cm]	CaCO$_3$ [mg g^{-1}]	TC [mg g^{-1}]	SOC [mg g^{-1}]	TN [mg g^{-1}]	C/N ratio	^{14}C activity [FM]	^{14}C [yr BP]	Ancient carbon [%]
0	0-5	33.1 ±1.5	5.5 ±0.4	1.5 ±0.3	0.25 ±0.01	6	0.228 ±0.002	11,874 ±72	88.8
3		57.9 ±20.7	10.2 ±2.4	3.3 ±0.2	0.36 ±0.03	9	0.473 ±0.002	6,013 ±42	60.6
6		64.5 ±10.8	12.2 ±0.1	4.5 ±1.1	0.47 ±0.12	9.4	0.532 ±0.003	5,073 ±39	53.8
12		73.7 ±4.1	15.0 ±0.4	6.1 ±0.7	0.57 ±0.05	10.7	0.843 ±0.004	1,369 ±34	18
24		79.1 ±8.8	15.1 ±0.9	5.6 ±0.2	0.51 ±0.02	11.2	0.753 ±0.003	2,280 ±36	28.4
Mature		72.8 ±14.7	14.7 ±1.8	5.9 ±0.1	0.55 ±0.02	10.8	0.680 ±0.003	3,100 ±36	36.8
0	16-20	48.7 ±9.0	7.7 ±0.7	1.8 ±0.6	0.26 ±0.07	6.9	-	-	-
3		65.0 ±12.7	10.1 ±0.6	2.4 ±0.5	0.21 ±0.01	10.7	-	-	-
6		71.9 ±7.9	10.2 ±1.6	1.8 ±0.3	0.21 ±0.01	9	-	-	-
12		72.2 ±3.2	10.4 ±1.2	2.9 ±0.8	0.30 ±0.02	8.5	-	-	-
24		78.0 ±9.3	10.1 ±2.3	2.6 ±0.5	0.25 ±0.02	10.7	-	-	-
Mature		72.8 ±15.7	16.3 ±0.7	1.9 ±0.1	0.19 ±0.01	11.7	-	-	-
0	41-45	73.7 ±19.4	14.4 ±1.9	2.9 ±0.7	0.25 ±0.02	10.6	0.416 ±0.002	7,055 ±43	67.2
3		73.2 ±7.2	11.8 ±2.1	2.6 ±0.5	0.22 ±0.01	10.4	0.369 ±0.002	8,015 ±52	72.6
6		95.6 ±30.4	11.4 ±1.0	1.9 ±0.1	0.19 ±0.01	10	0.172 ±0.002	14,149 ±87	95.2
12		78.4 ±13.5	13.3 ±3.7	1.9 ±0.5	0.22 ±0.03	10.9	0.331 ±0.002	8,883 ±52	76.9
24		83.4 ±25.7	13.6 ±2.8	3.6 ±0.7	0.25 ±0.06	14.2	0.433 ±0.003	6,725 ±47	65.2
Mature		124.5 ±54.9	18.0 ±7.2	3.1 ±0.7	0.53 ±0.04	16.7	0.218 ±0.002	12,248 ±64	90

Reclamation age [years]	Depth [cm]	Recent carbon [%]	DOC [µg g^{-1}]	DON [µg g^{-1}]	DOC/DON ratio	C$_{mic}$ [µg g^{-1}]	N$_{mic}$ [µg g^{-1}]	C$_{mic}$/N$_{mic}$ ratio	DNA [ng µl^{-1}]
0	0-5	11.2	11.38 ±1.6	1.8 ±0.8	6.3	434.9 ±52.7	3.3 ±1.1	138.3	2.2
3		39.4	19.19 ±10.8	4.1 ±1.3	4.7	415.4 ±59.7	8.7 ±1.1	48.6	12.2
6		46.2	10.25 ±3.3	7.38 ±1.2	1.4	476.9 ±18.1	15.1 ±1.8	31.7	20.1
12		82	8.12 ±2.6	2.2 ±1.6	3.7	445.2 ±33.6	10.7 ±2.1	42.1	20.1
24		71.6	13.05 ±6.2	6.88 ±2.1	1.9	502.6 ±6.7	12.1 ±1.1	42.5	21.9
Mature		63.2	11.36 ±1.9	5.68 ±2.8	2	489.8 ±49	10.9 ±1.1	45.6	29.4
0	16-20	-	25.86 ±8.2	2.12 ±0.9	12.2	324.9 ±63.2	3.3 ±0.4	97.4	3.6
3		-	11.96 ±2.3	0.7 ±0.8	17.1	268.1 ±38.1	5.2 ±3.6	58.6	5.3
6		-	12.52 ±2.9	31.16 ±11.1	0.4	255.6 ±173.9	2.5 ±0.8	108.2	3.2
12		-	14.41 ±4	5.09 ±1.1	2.8	420.7 ±34.2	11.4 ±2.2	37.5	24.3
24		-	16.98 ±7	14.26 ±2	1.2	420.0 ±34.6	12.1 ±2.8	36.1	21
Mature		-	10.43 ±3	1.91 ±0.9	5.5	441.4 ±18.8	9.7 ±1	45.8	21.9
0	41-45	32.8	9.22 ±0.6	0.52 ±0.1	17.7	356.8 ±36.6	6.6 ±2	59.9	5.2
3		27.4	29.56 ±27.7	0.4 ±0.1	73.9	236.7 ±55.3	4.5 ±0.9	52.1	4.5
6		4.8	6.77 ±2.2	5.79 ±3.4	1.2	155.0 ±78.1	3.2 ±0.7	45.6	1.1
12		23.1	9.39 ±0.4	1.13 ±0.7	8.3	165.2 ±47.1	3.4 ±0.7	37.7	1.7
24		34.8	11.28 ±1.6	8.61 ±2.1	1.3	319.3 ±8.5	5.2 ±3	34.9	12.6
Mature		10	-	-	-	328.8 ±15.4	2.6 ±1	143.8	3.8

FIGURE 2.1: *Scatterplot of macroporosity [Vol-%] and bulk density [g cm^{-3}] across the chronosequence at three sampling depths (1-5 cm, 16-20 cm and 41-45 cm)*
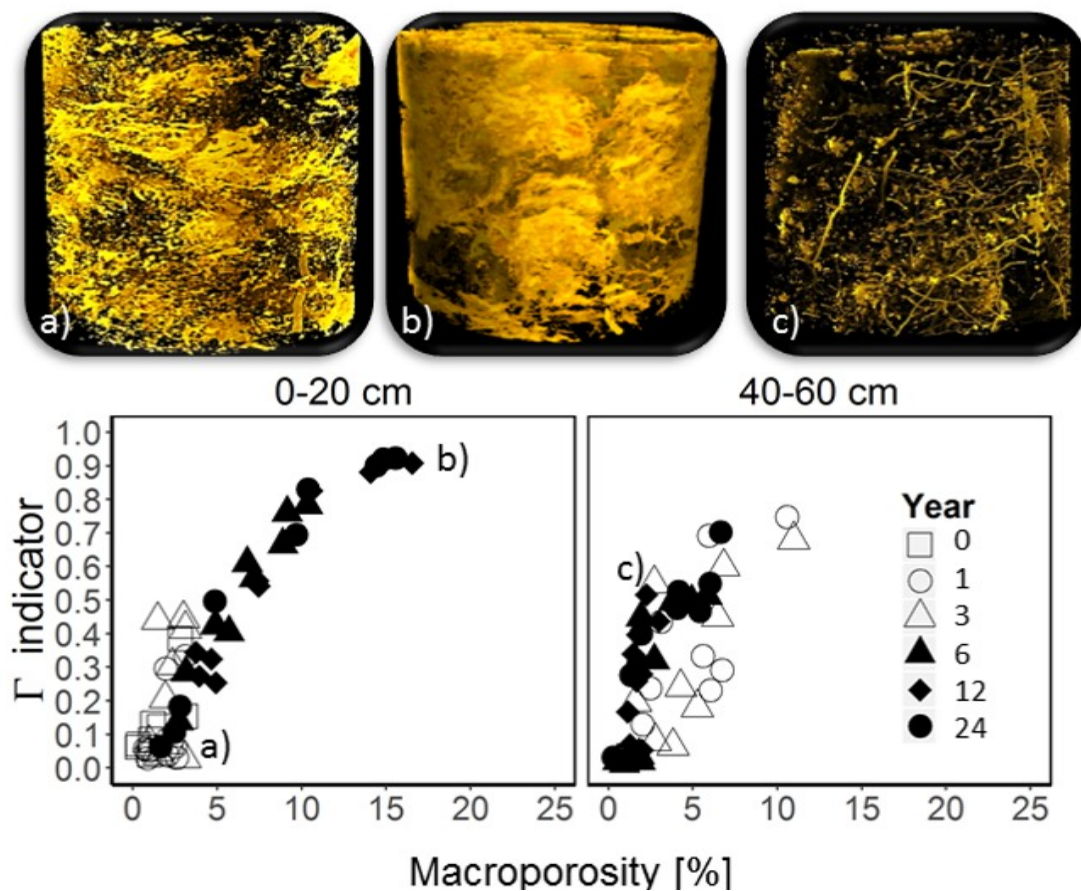
FIGURE 2.2: *Scatterplot of the Γ-indicator [-] and macroporosity [Vol-%] across the chronosequence at two sampling depths (0-20 cm and 40-60 cm). Letters indicate 3D visualisation of the pore system at a) 0 year and 0-20 cm depth, b) 24 years and 0-20 cm depth and, c) 24 years and 40-60 cm depth.*

2.3.3 Carbon and nitrogen fractions

Total carbon (TC) concentration increased throughout the chronosequence (Table 2.1). Increases in topsoil were statistically significant; in year 24 TC concentration was three times as high at the sampling depth of 1-5 cm and twice as high at 16-20 cm than in year 0. High CaCO$_3$ and low TC concentrations in the pioneering phase of reclamation indicated that CaCO$_3$ accounted for a substantial part of soil's total carbon concentration.

The duration of reclamation and management had an effect on soil organic carbon (SOC) concentrations (Table 2.1). In year 0, SOC concentrations were low in all sampling depths

and increased significantly during the pioneering phase at a depth of 1-5 cm. For deeper depths, no increase with time was observed during the first 3 years. After agricultural management started, SOC concentration increased significantly ($p < 0.05$) at a depth of 16-20 cm from 1.75 $\pm$0.27 mg g^{-1} in year 3 to 9.35 $\pm$2.68 mg g^{-1} in year 6. In the agricultural management phase, SOC concentrations decreased in years 12 and 24. SOC stocks showed a similar trend to SOC concentrations. Increase of SOC stocks was observed with the implementation of agricultural management (Figure 2.3). The most significant increase was observed at a depth of 10-30 cm in year 6 with 3.04 $\pm$0.87 kg SOC m^2. Thereafter (year 12 and 24) SOC stocks decreased in the whole topsoil (0-30 cm) and remained lower than the SOC stocks found in the mature soil. At the sampling depth of 41-45 cm SOC concentrations and stocks were low in all age classes.
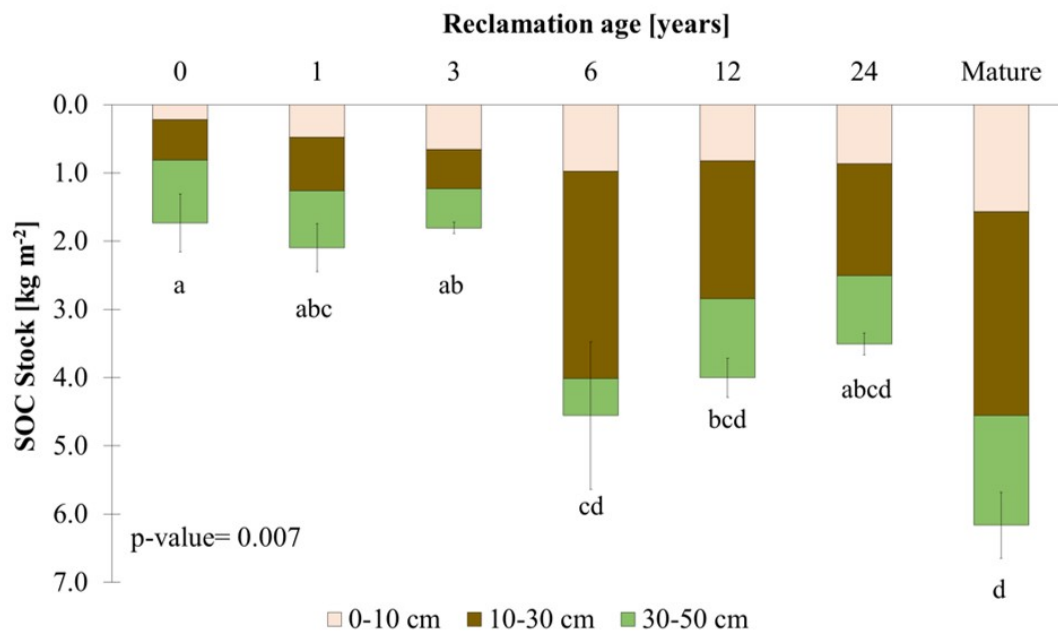
FIGURE 2.3: *Mean SOC stocks [kg m^{-2}] calculated with equivalent masses at three depths (0-10 cm, 10-30 cm and 30-50 cm) along the chronosequence and in the mature soil. Standard deviation is calculated through total SOC stocks at a depth of 50 cm from three field replicates, except at 3 years n=2. P-value characterises significant differences across the chronosequence and letters group ages that are not significantly different.*

Radiocarbon ^{14}C activity (FM) (Table 2.1) increased from 0 to 6 years of soil management. At the first sampling depth of 1-5 cm radiocarbon activity was 0.228 $\pm$0.002 in year 0, whereas in year 6 it increased to 0.843 $\pm$0.004, which might be due to fresh plant organic carbon input. Radiocarbon activity decreased again in years 12 and 24, where organic carbon contribution from old carbon increased. No trend in radiocarbon activity was observed at the sampling depth of 41-45 cm and most of the OC present (between 65-95%) was dead carbon inherited from the loess.

Comparable to SOC concentrations, total nitrogen (TN) concentrations (Table 2.1) depended on soil management. Constant increase was visible in the first depth of 1-5 cm throughout the chronosequence, whereas after application of agricultural management, the highest concentration was detected at a depth of 16-20 cm in year 6. In the starting point of reclamation, the C/N ratio was around 6, and thereafter it increased with values between 9 and 11. The highest ratio was detected at the 41-45 cm depth in years 12 and 24, where it reached 14.2 and 16.7, respectively. As the C/N ratio in whole topsoil (1-5 cm and 16-20 cm) remained below 12, there was no indication for the deposition of lignite dust; thus carbon

concentration correction was not necessary (Insam et al., 1988).

The reclamation age did not significantly influence the DOC concentrations in any of the sampled depths (Table 2.1). DOC concentrations varied between 6.77 μg g^{-1} and 29.2 μg g^{-1}, and obviously depended more on the actual management than the age of reclamation. Surprisingly, no stratification in the different sampling depths over time could be observed in the DOC values. In contrast, DON values increased over time at all soil depths. However, a clear stratification could not be observed for DON values either, and the highest value was measured at the second sampling depth in year 6. The ratio between DOC and DON decreased with time of reclamation and was mostly observed in the topsoil. In the deepest soil depth, the ratio increased during the pioneering phase and decreased afterwards. At the 16-20 cm soil depth a clear trend was not visible due to the high variability most likely introduced by the management.

2.3.4 Macro aggregate size distribution and SOC concentration in aggregate size classes

Macro aggregate size distribution by mass proportions after dry sieving was similar throughout the chronosequence (Figure 2.4). Aggregates measuring 6.3-20 mm had the highest abundance, followed by the aggregate sizes of 2-6.3 mm and <2 mm. No trend in aggregate size distribution was observed between reclamation ages, or sampling depths. This is in contrast to the mature soils from the reference field, which no longer contains $CaCO_3$, and have a larger proportion of aggregates less than 2 mm (Figure 2.4).

SOC concentrations within the aggregates (Fig. A.2) at depths of 1-5 cm and 16-20 cm were significantly different throughout the chronosequence. The largest change was found between years 3 and 6, and the highest SOC concentrations were found in the smallest aggregates (<2 mm). The most significant increase was observed in year 6 at the sampling depth of 16-20 cm with the SOC concentration of 9.7 $\pm$2.2 mg g^{-1}. In the plough layer (1-5 cm and 16-20 cm) of the mature soil, SOC concentration was higher in all aggregate size classes (Fig. A.2) and the contribution of aggregate sizes to the total SOC concentration was equally distributed between aggregate size classes (Fig. 2.5). In reclaimed fields the highest proportion of SOC was stored in larger aggregates of 6.3-20 mm throughout the chronosequence (Fig. 2.5). No significant differences between SOC concentrations within the aggregates were observed at the last sampling depth (41-45 cm).
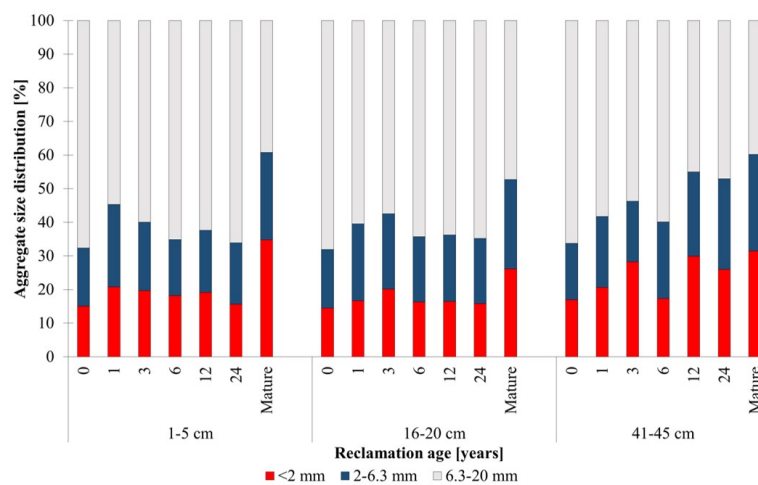
FIGURE 2.4: *Mean macro aggregate size distribution [%] from aggregate sizes of <2 mm, 2-6.3 mm and 6.3-20 mm at three sampling depths (1-5 cm, 16-20 cm and 41-45 cm) along the chronosequence and in the mature soil.*
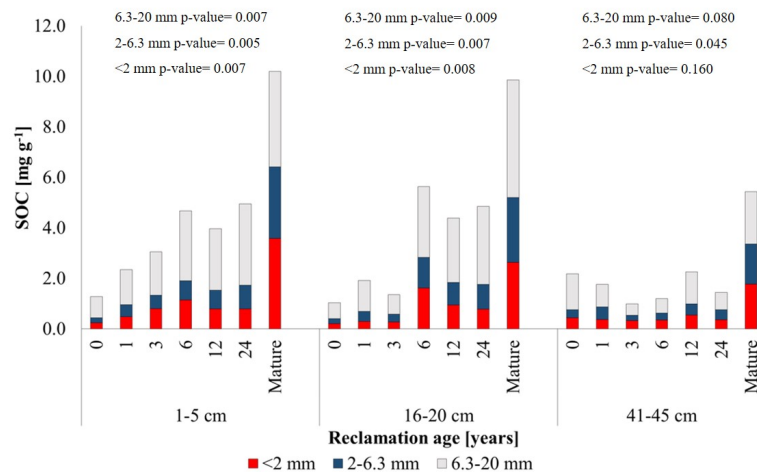
FIGURE 2.5: *Contribution of different aggregate sizes to the total amount of SOC at three sampling depths (1-5 cm, 16-20 cm and 41-45 cm) along the chronosequence and in the mature soil. P-value characterises significant difference within the sampling depth.*

2.3.5   Soil microbiota

C_{mic} in the topsoil increased only marginally over time (434.9 $\pm$52.7 μg g^{-1} directly after reclamation started, to 489.8 $\pm$49 μg g^{-1} 24 years later; Table 2.1). In contrast, a clear increase in microbial biomass over time was visible at the second sampling depth (16 – 20 cm), which was mostly based on a significant increase of C_{mic} between 3 and 6 years after reclamation. At the deepest sampling depth C_{mic} values were fluctuating and no clear trend in response to reclamation time was visible. At the pioneering phase, a stratification was observed between the first and the second sampling depths, whereas at later stages this stratification was less pronounced, most likely as a result of agricultural management, with the differences mostly observed between the second and the third sampling depths. A clear increase of N_{mic} in the top soil depth during the initial phase of reclamation was observed, whereas at later timepoints no additional increase was observed. Interestingly, a clear increase in N_{mic} was also observed at the second sampling depth, but it occurred later than in the topsoil; between years 3 and 6 after reclamation started. For the deepest soil depth analysed no effect of the reclamation was found. Similar to C_{mic}, a clear stratification between the two top soil depths in N_{mic} values became less clear over the reclamation time and the main differences occurred between the second (16-20 cm) and the third (41-45 cm) sampling depths. C/N ratios of the microbial biomass decreased both in whole topsoil (1-5 cm and 16-20 cm). However, most pronounced differences in the topsoil depth were found between the initial loess material and the first year of reclamation, whereas for the second soil depth these effects occurred later, between 3 and 6 years of reclamation.

The time of reclamation had a significant effect on the abundance of microbes at the first sampling depth (Fig. 2.6). At the deepest soil depth (41-45 cm), as expected from the C_{mic} and N_{mic} data, no clear trend over time of reclamation was observed. At the uppermost soil depth during the pioneering phase (year 1–3) both bacteria and fungi increased in abundance. As a result of the introduction of agricultural management after three years of pioneering phase, fungal biomass decreased, and only bacterial biomass strongly increased up to 1.5 x 10^{10} 16S rRNA gene copies 24 years after reclamation. At the second soil depth the effect on bacterial and fungal biomass was low in the first three years of alfalfa cultivation, and bacterial biomass increased mainly between years 3 and 6. Interestingly, at later stages of soil reclamation, bacterial biomass slightly decreased at the second sampling depth compared to the values found after 6 years. A clear stratification for bacteria was observed

between the first and the second soil depths in the pioneering phase, which changed to significant differences between the second and the third soil depths at later stages. For fungi on the other hand, a stratification was only observed in the pioneering phase (years 1–3).
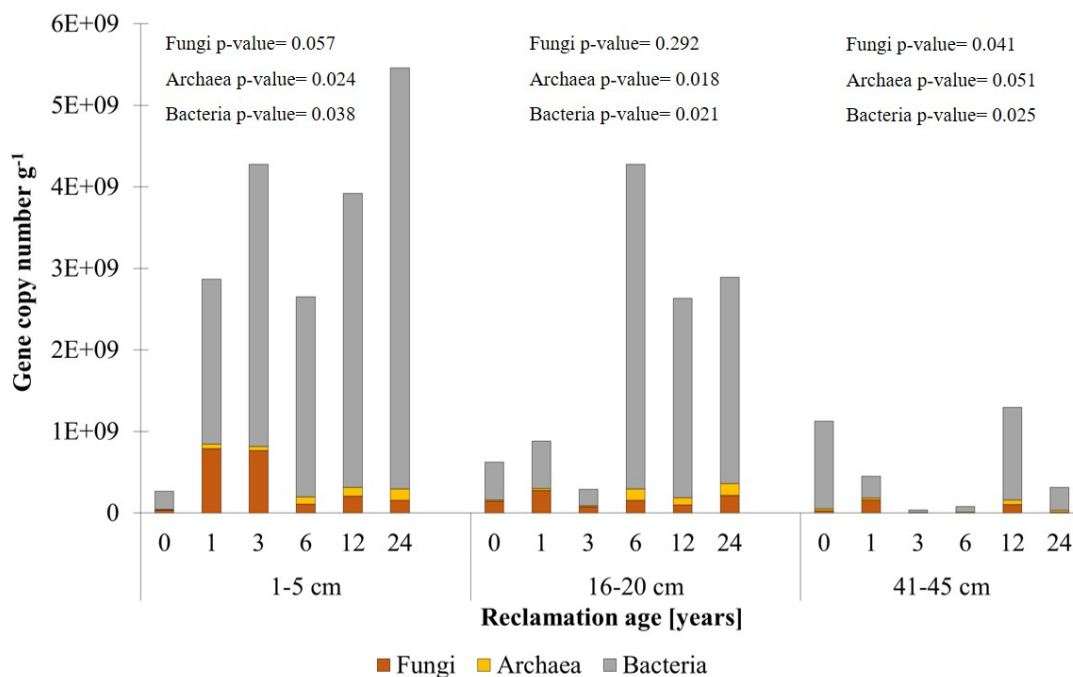
FIGURE 2.6: *Bacterial, archaeal and fungal gene abundances, calculated as gene copy numbers per gram of dry soil. P-value characterises significant difference within the sampling depth.*

2.3.6 Multivariate analysis

Discriminant Analysis showed that at sampling depths of 1-5 cm SOC (24%) and TN (21%) strongly contributed to the clustering of two phases, followed by macroporosity (21%) and extracted DNA concentrations (12%) (Fig. 2.7).

At the second depth of 16-20 cm, the contribution of these parameters was equally distributed 11-16%. According to linear models there is a clear differentiation between sampling depths (Figures 2.8 and 2.9, tables A.3 and A.4). Although reclamation time had the highest influence on soil parameters in the whole topsoil, the influence of soil management became more evident at a depth of 16-20 cm (Fig. 2.8b) and the influence of SOC and bulk density on other soil parameters also increased (Fig. 2.9b). TN concentration and C/N ratio were overall significantly predicted by the input of SOM. At the same time, SOC and physical parameters did not show high contribution

FIGURE 2.7: *Contribution of parameters in defining identification between Cluster 1 and Cluster 2 according to Discriminant Analysis at the sampling depths of 1-5 cm and 16-20 cm. Sampling depth 41-45 cm clustered together in one group throughout the chronosequence, therefore no Analysis was conducted.*

in defining microbial parameters staying predominantly below 50%. The differentiation

between the sampling depths of 1-5 cm and 16-20 cm were also evident with Pearson's correlation analysis (Tables A.5-A.7), where during the pioneering phase reclamation age, SOC, DON, N_{mic}, TN, extracted DNA concentrations, and C_{mic}/N_{mic} ratio were significantly correlated to each other only at the first soil depth (1-5 cm). After the conversion to the agricultural management phase in year 6 (Table A.6), a significant correlation between age, macroporosity, bulk density, DON, N_{mic}, TN and SOC was observed at the second sampling depth (16-20 cm).
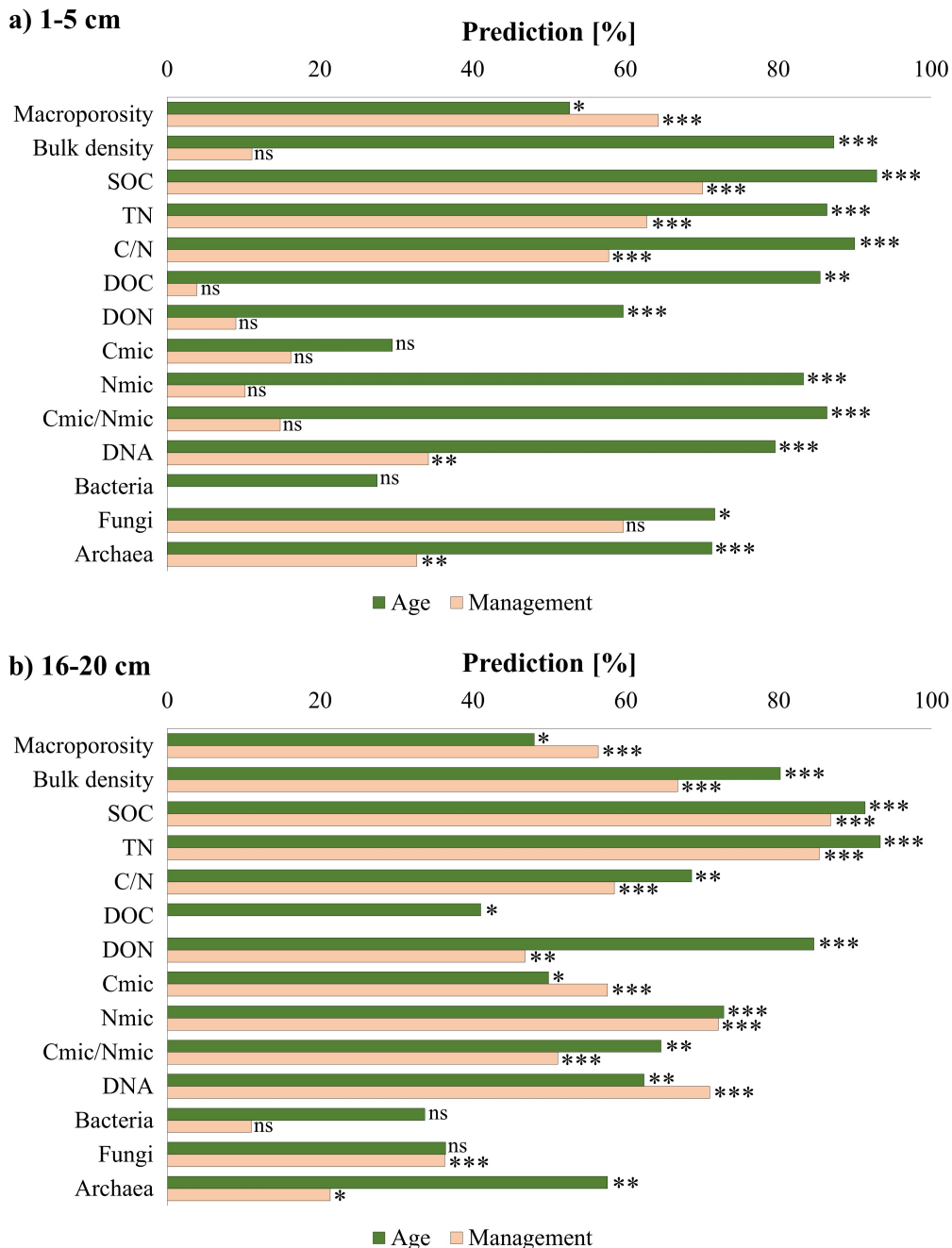
FIGURE 2.8: *Reclamation age and management influence on predicting soil parameters at depths of 1-5 cm (a) and 16-20 cm (b). Significance levels: *p $\preceq$0.05, **p $\preceq$0.01, ***p $\preceq$0.001 and ns-no significance.*

a) 1-5 cm
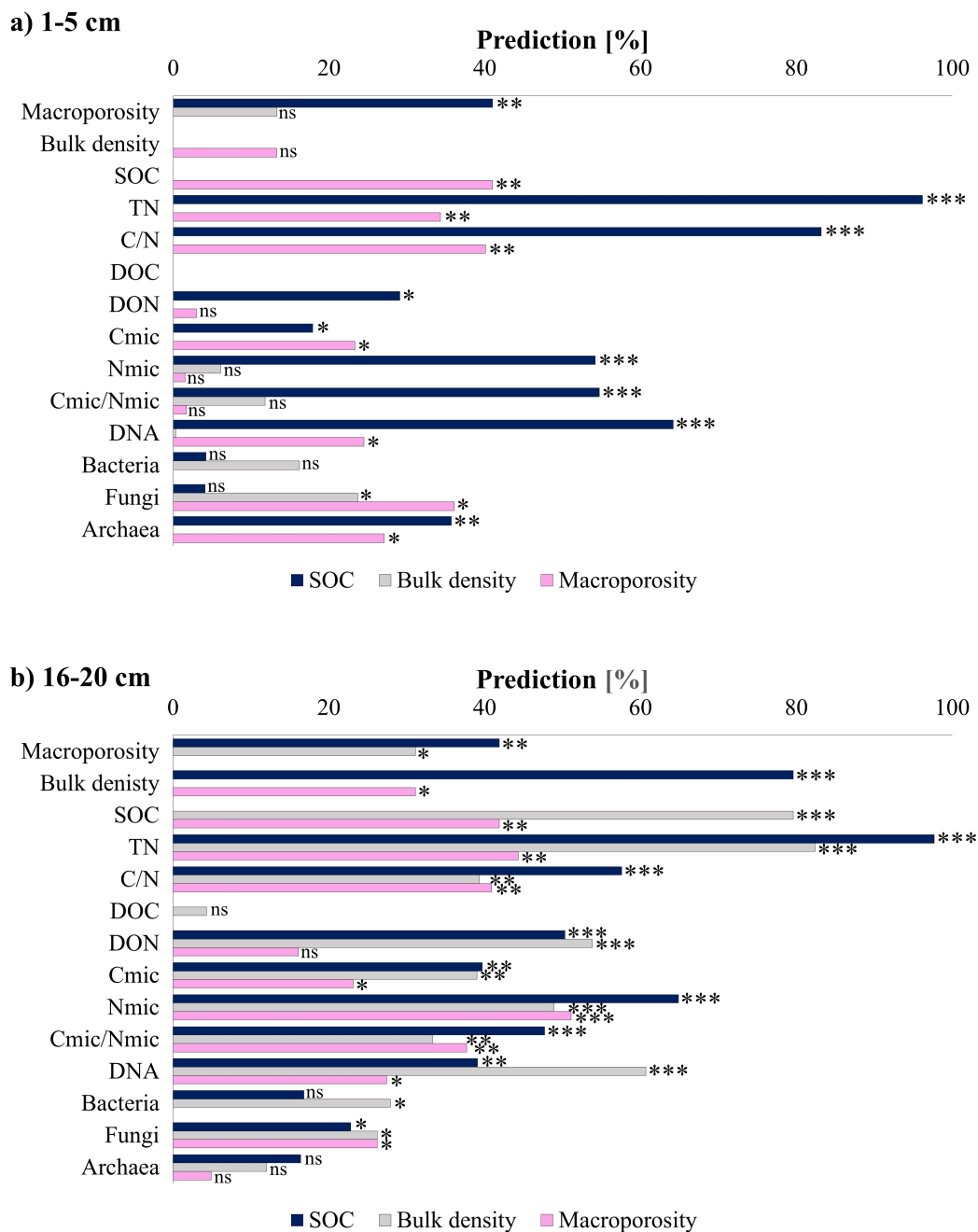
b) 16-20 cm

FIGURE 2.9: *The influence of SOC concentration, bulk density and macroporosity on defining soil properties at depths of 1-5 cm (a) and 16-20 cm (b). Significance levels: *p $\leq$0.05, **p $\leq$0.01, ***p $\leq$0.001 and ns-no significance.*

2.4 Discussion

The similarity in soil texture and $CaCO_3$ concentrations throughout the chronosequence indicated that the chosen sites meet an important requirement for the "false" chronosequence approach selected in this study; the parent material used for reclamation is the same for all time points. The Two-Step Cluster analysis indicated that soil development along the chronosequence can be divided into two groups: 1) the pioneering phase and, 2) the agricultural management phase. The sampling depth of 41-45 cm of both phases did not differ

and was assigned to the pioneering phase. This indicates that the impact of agricultural management on soil properties is only effective in the plough layer. Likewise, the alfalfa deep rooting system does not affect subsoil properties in the pioneering phase – at least not for the properties investigated in this study.

2.4.1   Soil initial development in the pioneering phase

The pioneering phase of soil reclamation is characterised by low macroporosity and high bulk density (Fig. 2.1), comparable with studies from other post-mining areas (King, 1988; Krümmelbein et al., 2012; Mukhopadhyay et al., 2016; Shrestha et al., 2011; Zhao et al., 2013). Such conditions can affect the development of root systems in deeper soil layers (Nosalewicz et al., 2014), soil aggregate structure and physical stability. However, according to our observations of long alfalfa rooting systems in the soil profiles, bulk densities were not high enough to have an impact on root development. The pioneering phase soils show low concentrations of SOC, TN, DOC, DON and N_{mic} (Table 2.1), as well as a low abundance of bacteria, fungi and archaea (Fig. 2.6). In the beginning of the reclamation process, "dead" carbon is a substantial part of soil's organic carbon content. Reserves of ancient carbon are an important carbon source for microbes in the initial phases of ecosystem development (Rumpel et al., 2004), but activity is mostly limited by low nutrient concentrations. Thus, neither bacteria nor fungi are able to benefit from the carbon stocks present. However, during the first three years of the reclamation process soil organic carbon stocks (Fig. 2.3) and the proportion of recent carbon increased at the first sampling depth (1-5 cm). With an increasing N pool introduced by the alfalfa cultivation and the related fixation of nitrogen by symbiotic rhizobia, fungal abundance increases as carbon stocks can be utilised under these conditions. This corroborates the concept of an increasing fungal to bacterial ratio during ecosystem development (Bardgett et al., 2005). Increasing fungal abundances in year 1 and year 3 fields are following plant development and input of fresh organic matter in the topsoil. A build-up of organic matter during this time is evident by the increasing concentrations of organic carbon, dissolved organic carbon and nitrogen (Table 2.1). Total nitrogen and microbial biomass nitrogen concentrations (Table 2.1) reached a peak value at the end of the pioneering phase (year 3) as a result of the input of alfalfa residues. All C, N and biological parameters showed a stronger development at a depth of 1-5 cm compared to deeper layers. The development of microbial biomass in nutrient poor subsoil strongly depends on the provision of fresh organic carbon from plant roots (Grayston et al., 2004; Paterson et al., 2007). Our data indicates that the plant litter of alfalfa is a better C and N source for microbes compared to the input by rhizodeposition and dead roots in deeper soil. The cultivation of alfalfa leads to a strong development of the litter degradation – SOM formation cycle is visible in the first 1-5 cm of our reclamation system. Despite the deep and intensive root system of alfalfa, the SOM input decreases rapidly with depth. At the same time, the soil's physical parameters indicate that soil structural development has not yet been initialised. Alternatively, physical parameters investigated here may not have been sensitive enough to capture the initiation of soil structure formation.

2.4.2   Enhanced soil development during the agricultural management phase

The effect of changing to the agricultural management phase leads to a clear stratification between plough layer and subsoil. It is most evident in a general increase of the soil's organic parameters and shifts in microbial abundance and community composition within the plough layer (Table 2.1, Fig. 2.6). We were surprised that no change in the aggregation was detected with age or depth. The transition from the pioneering phase to the agricultural management phase with annual ploughing or grubbing is characterised by a decrease in

bulk density and an increase in macroporosity. However, despite this generally consistent trend we found no correlation between bulk density and macroporosity both in the plough layer and below (Fig. 2.1). This may indicate a shift in the pore size distribution or an underestimation of macropores in the analysis of bulk density. The former is in line with studies that compared fields with no tillage to fields under conventional tillage practices (Kravchenko et al., 2011; Pires et al., 2017; Rasmussen, 1999).

SOC stocks, DOC and DON concentrations all showed highest values in year 6 of the reclamation (Table 2.1, Fig. 2.3), most probably owing to organic fertiliser amendment. The Discriminant Analysis (Fig. 2.7) confirmed that SOC and TN concentrations are the most contributing parameters in the clustering of the two phases. The SOC losses in the agricultural management phase may be due to low OC inputs, as the last application of manure is in the 7th year of the reclamation process, after which only mineral fertilisers are used. The losses of organic carbon observed in years 12 and 24 may also be due to higher mineralisation rates over time in reclaimed soils (Böhme et al., 2005; Delschen, 1999; Rochette et al., 1998). But such increased mineralisation rates are not supported by the low C_{mic} values (Table 2.1). This loss of SOC in the later development stages is not compensated by OC input from crop residues, dead roots or rhizodeposition. This loss of recent SOC is corroborated by the radiocarbon ^{14}C activity (Table 2.1) which showed the highest input of fresh organic matter in year 6, and with continuous tillage an increase in the proportion of "dead" organic carbon in year 12. This indicates that soil formation in our study sites is controlled more by the agricultural management and SOM amendments rather than soil-plant interaction. In addition, high pore connectivity ($\Gamma > 0.9$) is only found at depths of 0-20 cm of the older fields affected by soil management (Fig. 2.2). However, the tendency of higher pore connectivity probability of the older fields at low macroporosity at depths of 40-60 cm indicates that plant roots do not lead to an increase in macroporosity at greater depths, but to a restructuring of the pore system characterised by higher connectivity.

C_{mic} (Table 2.1) did not vary significantly in the first sampling depth of 1-5 cm; overall concentrations were comparable to studies in a similar post-mining chronosequence, where a fast recovery of C_{mic} concentration to levels characteristic of undisturbed soils (570 μg g^{-1}) was reported after 15-20 years of reclamation (Clayton et al., 2009; Insam et al., 1988). The decrease of bacterial and fungal abundances (Fig. 2.6) in year 6 of the reclamation process can be explained by the start of ploughing practices. Following a three-year pioneering phase without disturbances, ploughing could have been a stressor for the microbial community. Roy et al. (2017), reported the same trend in a study focusing on the succession of arbuscular mycorrhizal (AM) fungi; a rapid recovery in the first three years of the reclamation process, but also a rapid decline after a few years of conventional agriculture. These fluctuations of SOC concentrations and microbial abundance in reclaimed soils indicate the sensitivity of SOM which most probably has large proportions in labile forms. In order to achieve high SOC contents similar to the mature soils in this region, the reclaimed soils need higher and repeated C input over longer periods.

High DOC/DON and C_{mic}/N_{mic} ratios, low DNA amounts and microbial abundance found in year 0 were coupled with strong positive correlations between microbial biomass nitrogen, extracted DNA amounts and microbial abundance (Table 2.1). These results suggest that nitrogen, rather than carbon, is the major limiting factor for microbial community development in the pioneering phase of the reclamation process in this loess-dominated soil material. This corroborates the general assumption that available nitrogen is low during the initial development of ecosystems characterised by low plant diversity and abundance (Brankatschk et al., 2011). As N limitation is likely to worsen in the absence of symbiotic N fixation (Menge et al., 2012), the pioneering phase with N-fixing legume plants such as alfalfa is essential for the development of a fully functional reclaimed soil.

2.4.3   Calcium carbonate and SOC accumulation in aggregates

Carbonate concentration of the loess parent material is between 30 and 120 mg g^{-1} (Table 2.1), which is in the range generally found for loess deposits varying from 10-200 mg g^{-1} (Laszlo et al., 1995; Smalley et al., 2011). Under dry conditions loess forms soft rock-like structures which diminish when in contact with water or with an increase of moisture content (Li, 2018; Yates et al., 2018). These soft rock-like structures were dominant in all sampled reclamation stages and depths, thus dry sieving showed no trend in dry aggregate size distribution (Fig. 2.4). SOC concentration in aggregates was low and CaCO$_3$ concentration was high during the pioneering phase (Table 2.1, A.2). CaCO$_3$ as a cementing agent dominated the aggregation process in all soils of the chronosequence, leading to a predominance of aggregates larger than 6.3 mm. Even though the SOC concentration in the agricultural management phase increased, the CaCO$_3$ concentration remained high and still dominated as the cementing agent. In contrast, the higher content of SOC (A.2) in combination with the loss of CaCO$_3$ and regular ploughing in the mature soil leads to an aggregate distribution dominated by aggregates smaller than 6.3 in the plough layer (Fig. 2.4). Figure 2.5 shows that the SOC contribution is equally distributed over all aggregate size classes in the mature soil, whereas we find a much smaller contribution of the finer aggregates to SOC storage even after 24 years of soil reclamation. These data indicate that longer and regular input of organic residues is necessary to build up the SOM stocks in the finer aggregates. In addition, the CaCO$_3$ cementing of fine soil particles may prevent SOM binding via interactions with the mineral surfaces.

2.5   Conclusion

Our study demonstrates that in reclaimed soils the inherent properties of the loess parent material controlled the formation of aggregates. Despite the improvements in soil porosity and an increase of SOC stocks throughout the chronosequence, the parent soil was still characterised by soft-rock aggregate formation. Although macroporosity increased over time, with the parameters chosen, we did not observe any further structural development nor changes in aggregate size distribution. Our findings underscore the influential role of CaCO$_3$ as a cementing agent in early soil development on carbonaceous loess. The soil management practice during the reclamation has a clear effect on soil development. In the pioneering phase, where no agricultural management is applied, SOM accumulation is observed in the topsoil, showing that litter incorporation in topsoil rapidly improves soil quality. The following agricultural management distributes SOC and microbial biomass throughout the 30 cm plough layer and increases SOC content via compost application. As the development of microbial biomass is limited by nitrogen, alfalfa's nitrogen fixation potential is essential for the formation of a fully functional soil. The crop residues as sole input of OM in the conventional crop rotation are not sufficient to build up a stable SOM content in the plough layer in the long term.

Chapter 3

Soil structure formation along an agricultural chronosequence
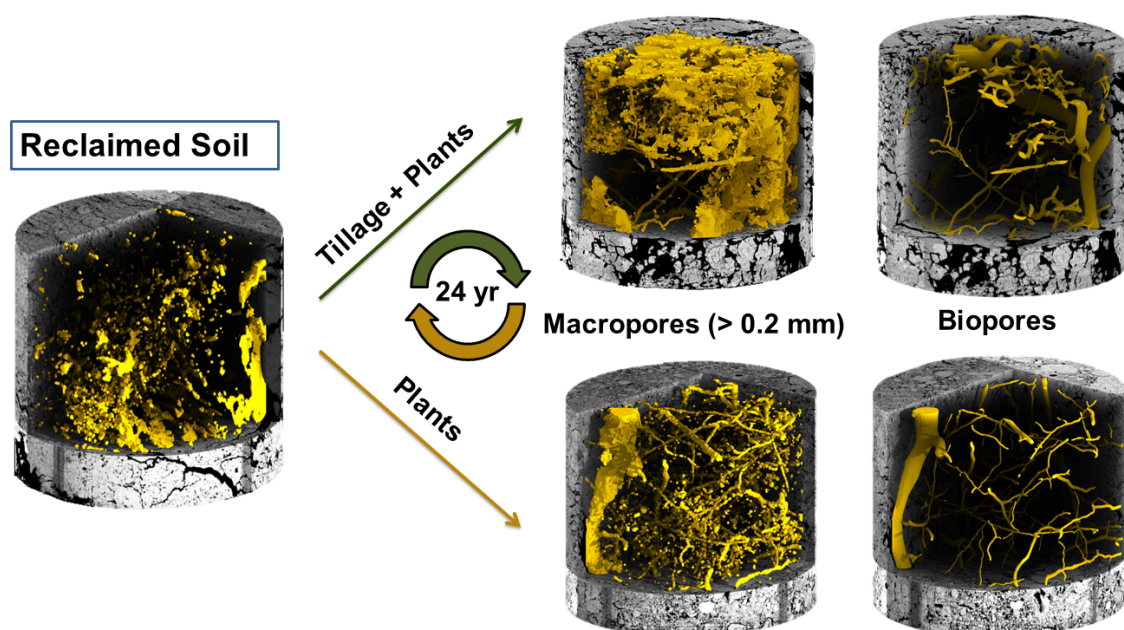
During soil formation, the interaction of different biota (plants, soil fauna, microbes) with weathered mineral material shapes unique structures depending on the parental material and the site specific climatic conditions. While many of these interactions are known, the relative importance of the different biota is difficult to unravel and therefore difficult to quantify. Biological soil structure formation is often superimposed by soil management and swell-shrink dynamics, making it even more difficult to derive mechanistic understanding.

We here explore soil structure formation within a "space-for-time" chronosequence in the Rhenish lignite mining area. Loess material from a depth of 4-10 m has been used for reclamation in a standardised procedure for 24 years. Changes in soil pore system are characterised by properties such as connectivity (Euler number) and pore size distribution using undisturbed soil columns with a diameter of 10 cm. They were taken from two different depths (0-20 cm and 40-60 cm) at different sites ranging in age from 0 to 24 years. X-ray μCT is used for scanning the original columns as well as undisturbed subsamples of 3 and 0.7 cm diameter. This hierarchical sampling scheme was developed to overcome the trade-off between sample size and resolution.

For the first time also information on the development of biopores could be measured by separating them from other structural pores based on their unique shape. The data were complemented by destructive sampling and determination of root length with

WinRHIZO to give an estimate of how many biopores are filled with roots. Furthermore HYPROP measurements of water retention curves were conducted and showed a general agreement with the image-derived pore size distribution merged across three scales. An increase in biopore density throughout year zero to year 12, in particular in 40-60 cm soil depth, was observed. The biopore length densities of approximately 17 cm / cm^3 obtained in year 12 was similar to the one measured in year 24, suggesting that equilibrium was reached. Only about 10% of these biopores were filled with roots. In the topsoil (0-20 cm) the equilibrium value in biopore density is already reached after six years due to a higher root length density. Ploughing lead to higher mean pore size and to lower connectivity compared to the well-connected, very stable pore network in 40 – 60 cm depth. This study shows how fast plant roots create a stable and connected biopore system and how this is disrupted by soil tillage, which produces completely contrasting pore characteristics.

3.1 Introduction

Soil structure is a prerequisite for the functioning of soil and thus its ability to support life of plants and animals. It controls various important soil properties and processes such as soil water conductivity and retention, gaseous exchanges and erosion. In addition, soil organic matter and nutrient dynamics, root penetration and crop yield are also strongly influenced by soil structure (Bronick et al., 2005; Rabot et al., 2018). Soil structure changes constantly during soil formation, i.e. it is shaped by the interaction of different biota (plants, soil fauna, microbes) with weathered mineral material, and is depending on the parental material and the site specific climatic conditions. The relative contribution of the different biota to soil structure formation is difficult to disentangle, in particular in managed systems. Growing roots or burrowing earthworms reorganise the spatial arrangements of soil particles as they align individual minerals of various types and sizes and organic substances and may compact the soil along the biopores they form (Bruand et al., 1996; Kautz, 2015). Biopores can extend along the whole soil profile, are cylindrical in shape, show a low tortuosity and high vertical continuity. Thus, they significantly affect infiltration and preferential flow phenomena (Koestel et al., 2014; Naveed et al., 2013; Rasse et al., 2000; Wuest, 2001). It has been suggested, that in dense soils and with increasing depth, root growth depends more on an existing pore network (Gao et al., 2016), which results in an intimate relation between old biopores, new root growth and water extraction (Stirzaker et al., 1996).

While vegetation and earthworms have the ability to directly change the pore system and deliver carbon sources for soil organisms, microbes are responsible for the vast majority of turnover processes and, therefore, have been described as "soil architects" (Ramirez et al., 2014). By secretion of extracellular polymeric substances (EPS), microbes modulate the pore wall surface, which leads to the formation of habitat patches at the micro scale (Colica et al., 2014). Together with plant polysaccharides, EPS forms the "glue" for the stabilisation of mineral particles in soil and therefore stabilises soil structure (Totsche et al., 2018; Watteau et al., 2006). In addition to biota, agricultural management, more specifically soil cultivation, may have a strong impact on soil structure. Increasing macroporosity with little change in micro- and mesoporosity has been reported for conventionally managed soils (Ambert-Sanchez et al., 2016; Kay et al., 2002; Kravchenko et al., 2011; Pires et al., 2017; Rasmussen, 1999). Soils cultivated without tillage show lower air capacity and higher bulk densities due to lower macroporosity. However, in no-till systems biotic factors dominate, e.g. higher amounts of earthworms occur (Jarvis et al., 2017; Rasmussen, 1999; Schlüter et al., 2018b).

Soil structure is typically considered as the spatial arrangement of solids and voids across various scales. Therefore, soil structure can be described both from the solid phase perspective and from the pore space perspective, as these are complementary aspects (Rabot et al., 2018). From the solid phase perspective bulk density or aggregate stability and aggregate size distribution are often used as an indicator for soil structure. However, describing aggregates does not seem to be the most suitable way to link soil structure with soil functions and processes (Rabot et al., 2018). For example water flow and gas diffusion are both directly affected by the architecture of pores (Koestel et al., 2018; Naveed et al., 2013). Nowadays different imaging techniques allow for visualising and describing the soil pore space of undisturbed samples directly. X-ray computed microtomography (X-ray μCT) as a non-invasive imaging method, has been increasingly used in recent years to describe pore systems and their dynamics using parameters such as connectivity, macroporosity and pore size distribution (Kravchenko et al., 2011; Kuka et al., 2013; Naveed et al., 2013; Pires et al., 2017; Schlüter et al., 2018b, 2011a). In X-ray μCT-analysis the image resolution is limited by the sample size, with a fixed factor of 1000–2000 between the size of a voxel and the size of the sample depending on the X-ray detector hardware (Rabot et al., 2018). Therefore, small samples in the size range of a few centimetres must be used to describe changes in

mesopore structure (here defined as pores $< 50\ \mu$m) (Kravchenko et al., 2011; Schlüter et al., 2016b). However, such small samples may not include the structure of soil in a representative way. To overcome this trade-off, we have extended the nested strategy from (Schlüter et al., 2018b) to three different sample diameters, which allowed us to representatively describe changes in soil structure down to pore sizes of $5\ \mu$m.

In order to describe soil structure from the very beginning, we have chosen a "space-for-time" chronosequence approach. We extracted undisturbed samples from reclamation sites of ages up to 24 years within an open-cast lignite mining area. Samples were taken both in 0-20 cm (directly affected by tillage) and 40-60 cm (no direct tillage effect) depth in order to separate the influence of soil management that periodically disrupts the biopores formed during a year, from the uninterrupted, biopore formation accumulated over decades beneath it. Our objectives are 1) to characterise the influence of plants on soil structure (e.g. the temporal development of biopores towards an equilibrium biopore density) and 2) to characterise how this process is interrupted by soil cultivation.

3.2   Materials and methods

3.2.1   Chronosequence / Study area

In order to investigate soil structure dynamics over time, samples were taken from a reclamation area in the Garzweiler open-cast mine (Germany). Following a reclamation technique standardised since 1990, these sites were created from a homogeneous initial substrate, which consists of Luvisol and unweathered loess (ratio is about 1:10) from the Weichselian glaciation period. This soil substrate (at least 2 m thick) is therefore characterised by a silty clay loam soil texture with about 65% silt and 31% clay. Low initial SOC contents can be found ($\sim$2 mg^{-1}). The whole chronosequence is characterised by slightly alkaline pH values (7.4-.7.6), high CaCO$_3$ concentrations (30-120 mg^{-1}) and high bulk densities of around 1.6 g cm^{-3} (in layers not affected by tillage) (Pihlap et al., 2019, Table A.2). In the pioneering phase, lucerne (*Medicago sativa*) is cultivated for developing deep rooting system and facilitating nitrogen enrichment, which stimulates biological activation of the young loess deposits. No tillage practice is used within this phase. After three years the lucerne fields are ploughed and a crop rotation of wheat and barley is used to support and stabilise the yield and functionality of the sites (Fig. 3.1). After seven years of cultivation by the mining company (RWE power AG), the land is handed over to local farmers who add typical regional crops such as corn, rapeseed and carrots to the crop rotation. Further details for the reclamation procedure and associated soil management over time can be found in Fig. 3.1 and in Pihlap et al. (2019, Chapter 2.2).
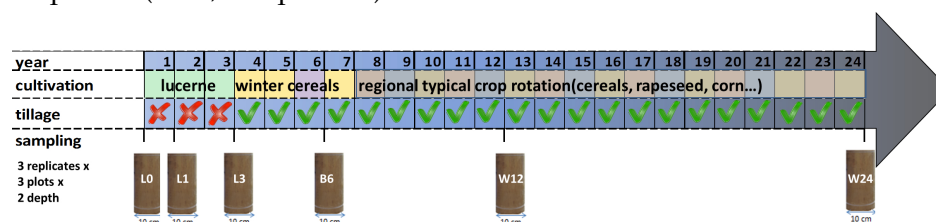
FIGURE 3.1: *Chronosequence at the reclamation area of Garzweiler (open cast lignite mining area, Germany). Reclamation procedure standardised since >24 years with loess material. Crop rotation is the same for all fields within the first 7 years (3 years lucerne, 2 years winter wheat, 1 year winter barley, 1 year winter wheat). Sampling of: L0, L1, L3 (lucerne sites; 0, 1, 3 years after recultivation); B6 (barley field, 6 years after recultivation; W12 and W24 (wheat fields; 12 and 24 years after recultivation).*

3.2.2 Sampling

Soil samples were taken from the chronosequence of 0, 1, 3 years after the first sowing, representing the pioneering phase and 6, 12 and 24 years after the first sowing, representing the phase of conventional agriculture management. A custom-made drill for undisturbed sampling of cylindrical soil cores (UGT GmbH, Germany) was used to take undisturbed samples (encased in a stiff 5 mm PE sleeve) from 3 different plots per site representing the years after the first sowing (3 individual cores per plot).

Sample size: 10 cm
Resolution: 57 µm

1.5 mm
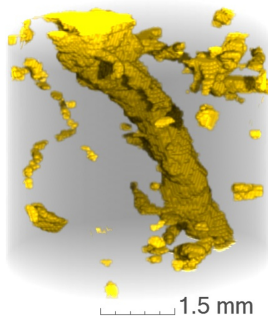
Sample size: 3 cm
Resolution: 19 µm

1.5 mm

Sample size: 0.7 cm
Resolution: 5 µm

1.5 mm

FIGURE 3.2: *Pore system on the same 7 mm wide subvolume of a 10 cm Ø sample and the corresponding 3 cm Ø and 0.7 cm Ø subsamples at the identical position reveal the relationship between sample size and resolution.*

To cover both the plough layer and the layer not directly affected by cultivation, samples were taken at depths of 0-20 cm and 40-60 cm. The 0-year old site was not sampled within the second depth, because initially only a small gradient over the depth was expected from the highly mechanised reclamation. A total of 99 soil cores with 10 cm Ø and 20 cm height were extracted. Furthermore, one additional undisturbed soil sample from each plot and depth (33 in total) was used for the independent determination of water retention curves (10 cm Ø x 10 cm height). Samples were taken during four sampling campaigns between October 2016 and March 2018 to avoid long storage periods. In addition, the samples were stored at 4°C in plastic bags to reduce changes in pore structure through drying and biological activity. As there is a trade-off between sample size and resolution, 10 cm Ø cores were scanned to ensure a representative sample volume for larger components of soil structures (large biopores, cracks). Subsequently smaller subsamples were extracted to increase the resolution. 6 subsamples with 3 cm Ø and 3 cm height (stiff PVC sleeves with a wall thickness of 2 mm) were taken from each cylinder (594 in total) with a subsampling device (UGT GmbH, Germany). 3 of these cylinders (297 in total) were used to estimate root length destructively. The remaining cylinders were scanned with X-ray µCT. In order to derive information for mesopores, also subsamples with 0.7 cm Ø , which were made out of aluminium with a wall thickness of less than 1 mm, were extracted from the 3 cm Ø cores and scanned with X-ray µCT . Soil cores (10 cm Ø) were scanned with a X-ray microtomograph (X-TEk XCT 225, Nikon Metrology) with an Elmer-Perkin 1620 detector panel (1750 x 2000 pixels). Smaller cylindrical subsamples of 3 cm Ø and 0.7 cm Ø were scanned with 130 kev / 150 µA and 95 kev / 90 µA, respectively.

The 2500 projections per scan were reconstructed by a filtered back projection algorithm with the 3D software package CT Pro (version XT 4.35, Nikon Metrology NV). In order to image the entire cylinder with optimal resolution, scans were performed for the upper and lower 10 cm separately with 165 keV, 570 µA. at a spatial resolution of 57 µm for 10 cm Ø, 19 µm for 3 cm Ø and 5 µm for 0.7 cm Ø samples with 8 bit greyscale resolution (Fig.

3.2). The gain in spatial resolution within subsamples therefore reveals information about mesopores and small roots.

From each plot and depth 3 X-ray μCT images of 10 cm Ø cores, 9 X-ray μCT images of 3 cm Ø cylinders and 9 X-ray μCT images of the smallest sample size were scanned. To reduce the effect of disturbances made by subsampling of the smallest samples, only the 99 best sub-samples of 0.7 cm Ø (3 per plot and depth) were selected and evaluated. Since one plot on the three-year site contained no carbonate (detectable by HCl-solution) and HYPROP measurements also showed clear differences to all other samples, only two plots were evaluated from the three-year old site. It was suspected that the plot behaving differently consisted of weathered former topsoil material instead of unweathered, calcareous loess parent material. In total, 792 X-ray μCT-images were taken and for this study 594 X-ray μCT-images were analysed.

3.2.3   Image processing and analysis

Noise removal for images from cylinders with 10 cm Ø was conducted with a 2D non-local-means filter (σ = 25) in Fiji (Buades et al., 2011; Darbon et al., 2008) Small fractures in the sample wall were not taken into account by reducing the cylindrical region of interest (ROI). To mask especially deep cracks caused by sampling, for some ROI's an adaptive rectangle was used in the VGStudio Max 2.1 software that adapts its boundaries to the surface of cracks extending into soil. Compared to changing the cylindrical ROI at different locations, this is a fast way to reduce pore volume errors caused by sampling without losing a large fraction of undisturbed volume for final analysis. The images of 3 cm Ø and 0.7 mm Ø cylinders were processed with almost the same workflow, but instead of a 2D non-local means filter a 3D non-local means filter (UnbiasedNonLocalMeans in ITK, Revision 1.21, Tristán-Vega et al., 2012) was used. A σ of 40 was used for the 3 cm Ø cylinders and a σ of 15 for the 0.7 Ø cm cylinders, adjusted to the respective noise level in order to improve the robustness of automatic, histogram-based threshold detection methods. Due to the non-linear transformation of the grey values by this filter in dark areas, the X-ray μCT images of 3 cm Ø and 0.7 mm Ø cylinders were previously converted to 16-bit and the value 1000 was added. After filtering, the images were reduced to 8-bit and the enhanced contrast filter in Fiji (Schindelin et al., 2012) was applied that under- and oversaturates 1% of all voxels followed by linear stretching of all remaining grey values to the full 8-bit range. Then an unsharp mask filter Schlüter et al. (2014) was applied for edge enhancement in order to ensure a good automatic threshold detection. This threshold detection was carried out for all images in Quantim (www.quantim.ufz.de) with 5 different segmentation methods as described inSchlüter et al. (2014). The averages of the mean and lower percentile values were used for hysteresis thresholding within the 3D Segmentation plugin (Version V3.83) in Fiji (Ollion et al., 2013).

Pore size distribution (PSD) and connectivity were calculated on the binary images. To compute PSD the local thickness method was used in Fiji (version 1.4.6), which uses the maximum inscribed sphere method. A joint pore size distribution was created by combining the representative pore sizes of all three sample sizes (Vogel et al., 2010). As connectivity indicator the Euler number was calculated using the MorphoLibJ plugin in Fijii (Version 1.3.3, Legland et al., 2016) and normalised by the total volume. The Euler number is the sum of the total number of objects minus the number of redundant loops plus the number of enclosed cavities, which are typically negligible. Therefore, strongly negative values indicate a high number of connections between pores. The Euler number is strongly influenced by noise or incorrect classifications (Armstrong et al., 2019). To reduce this error, a pore-size opening was performed before calculating the Euler number in Fiji to remove pores smaller

than or equal to four pixels. Scripts for image processing with Fiji and for data processing and evaluation in R are provided as supplements.

3.2.4 Biopores segmentation

In order to describe the dynamics and structure of biopores, all tubular pores from the entire pore network were also segmented. A protocol was developed to detect biopores by their tubular shape, which distinguishes them from the remaining irregularly shaped pore network (Fig. 3.3) To do so, the Tubeness plugin in Fiji was used for shape detection of biopores. In short, the eigenvalues of the Hesse matrix, i.e. the tensor of second derivatives of the local grey value, can be scored to distinguish tubular features from planar or blob-like features.

This is a method that has been originally developed for blood vessel detection (Frangi et al., 1998). This feature detection is typically combined with a scale-space approach. That is, the entire binary image was convolved with a Gaussian blur with eight different standard deviations σ to optimally detect all biopores within a wide range of diameters. With increasing σ-values biopores with increasing diameters could be optimally detected, whereas smaller roots are filtered out. However, also computational time increases with increasing σ-values. Therefore the binary images were scaled down to 40% in all three image directions and the σ-values were reduced accordingly to reduce the calculation time and still capture biopores with large diameters that would otherwise have been detected as hollow objects or not detected at all. The biopore segmentation through shape detection leads to tubular channels that are slightly smaller than the root channel itself, because the roughness of the biopore walls is excluded. 3D dilation steps were included as a postprocessing step to better capture the actual width of the biopores. Smaller misidentified pores were filtered out using a combination of Connected Components Labeling and Label Size Opening using the MorphoLibJ plugin in Fiji (Version 1.3.3, (Legland et al., 2016)). In some cases due to the large σ-values, very porous areas were detected as a biopore, which were then manually removed.

The resulting binary image was used to calculate the volume of biopores per cm^3 of soil. Similar to the PSD, local Thickness was used in Fiji to obtain information on biopore diameter. Due to the cylindrical shape of the biopores, the total length of each pore diameter class can be derived from their volume fraction and the total root length can be determined by summing over the contributions from all diameter classes.

The distance of all soil voxels to the next biopore was calculated by creating a distance map with Euclidean Distance Transform in Fiji. In this way the spatial exploration of soil through biopores can be monitored throughout the chronosequence.
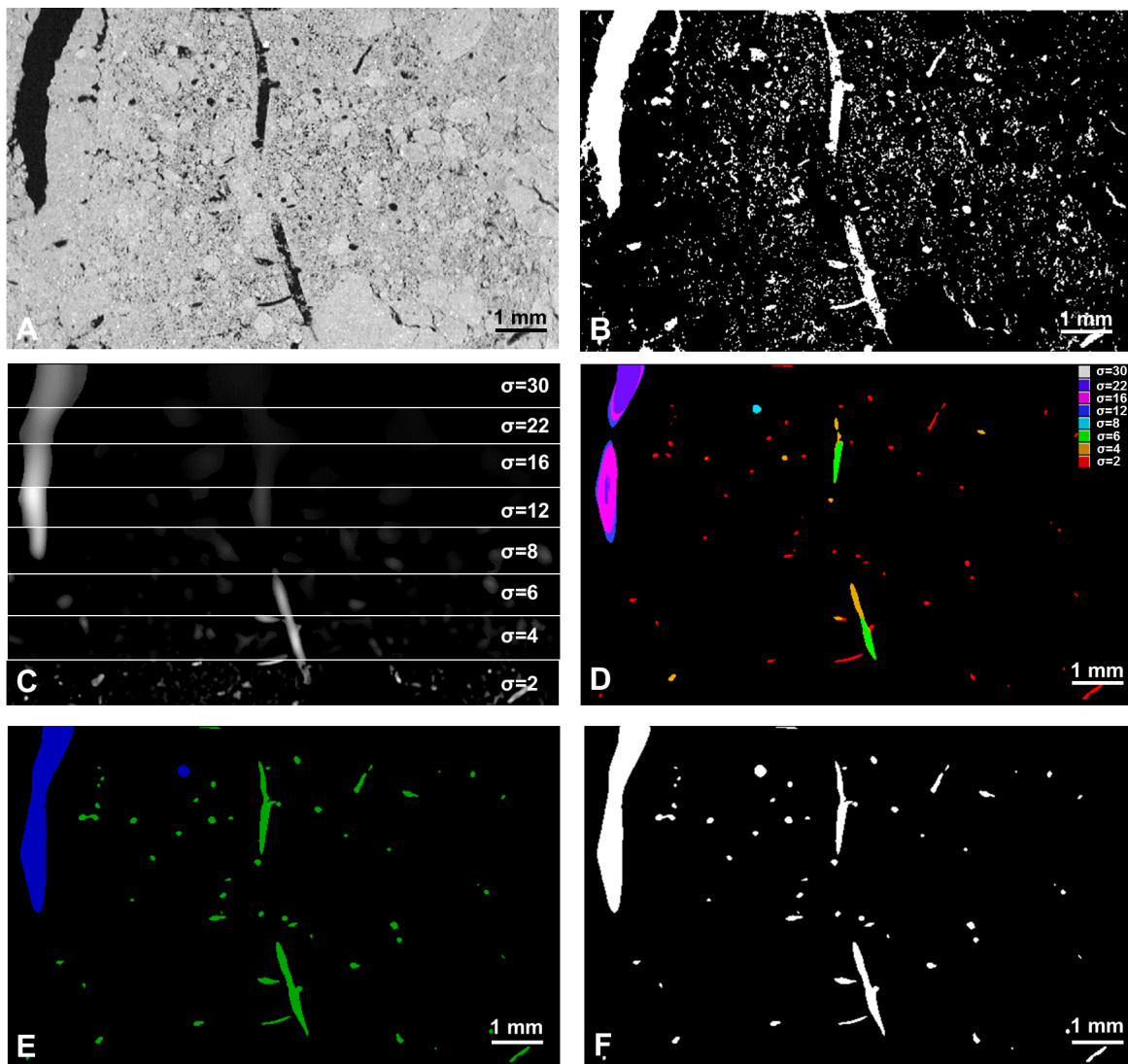
FIGURE 3.3: *Protocol of biopore segmentation. A: grey image after 3D non-local means filter. B: binary image after hysteresis thresholding, scaled down to 40%. C: image slices as examples for all 8 tubeness filters used. The σ-values correspond to the standard deviations used to convolve the image with a Gaussian blur, thus with increasing σ-values biopores with increasing diameter can be detected. D: result of the different σ-values after hysteresis thresholding of the images in C. E: combination of the smallest biopores (σ=2,4) in green and bigger biopores in blue (σ=6,8,10,12,16,22,30). For the smaller biopores one 3D dilation step was used and pores smaller 1000 voxels were removed. For bigger biopores two 3D dilation steps were used and pores smaller 10,000 voxels were removed. F: combination of all biopores and final result of biopore segmentation. (For interpretation of the references to colour in this figure legend, the reader is referred to the web version of this article.)*

3.2.5 Root length and root diameter classes

Root length and diameter classes were also measured destructively. The comparison between root length and biopore length provides an estimate for the percentage of root-filled biopores. For each 10 cm Ø column, the roots were washed out of three 3 cm Ø subsamples and scanned on a flatbed scanner with 600 dpi and 8 bit. Root length and diameter classes were measured with WinRHIZO (2009, Regent Instruments Canada Inc.). Between subsampling and analysis, roots were stored in Rotisol (Roth GmbH, Karlsruhe, Germany).

3.2.6 Measuring water retention

Samples (10 cm Ø x 10 cm height, 1 cylinder per plot and depth) were fully saturated with water before using HYPROP evaporation method (Hydraulic Property Analyser; METER former UGT, Germany). The measured data points were analysed without fitting some parametric model. In order to compare water retention data with image-derived pore size distributions, air-filled porosity was calculated by subtracting the water content at a given matric potential from the water content at saturation.

3.2.7 Statistical analysis

Standard deviation and mean values are provided in all figures for the mean of 3 plots for each year and depth in which each plot is represented by an average of the corresponding number of technical replicates (e.g. X-ray μCT scans). Differences in the data were revealed with a one-factorial ANOVA in conjunction with Tukey's HSD. The porosity data was log-transformed prior to statistical analyses. Due to the high non-linearity of the Euler number a Kruskal-Wallis test followed by Dunn's multiple comparisons test was used to reveal differences between sites of different age. Samples from 20-40 cm of the tilled fields (6, 12 and 24 years after reclamation) were compared with the samples from 40-60 cm using a two sample Students T-test and for the Euler number a Wilcoxon ranks-sum test, respectively. For all statistical analysis the software R 3.40 in combination with the package agricolae (Mendiburu, 2017) was used.

3.3 Results

3.3.1 Visible porosity and pore size distribution

The mean values of the total visible porosity, i.e. pores >10 μm (two voxels at the highest resolution) ranged from 23.7% (L0, 0-20 cm depth) to 35.6% (L3, 40-60 cm depth). No significant differences could be observed between the different years and depths due to the low sample number (n=3, i.e. average values for three plots) (Table B.1). In contrast, cumulative pore size distribution after scale fusion of all core sizes (Fig. 3.4) showed a marked difference at larger pore diameters between the pioneering phase (L0, L1, L3) and the phase of crop rotation (B6, W12, W24) for 0-20 cm depth, i.e. the depth directly affected by soil tillage. This difference is mainly related to a significant increase in macroporosity (>0.2 mm) in the tilled layer. In 40 – 60 cm all sites have very similar pore size distribution for pore larger than 0.05 mm except for L1, which exhibits a slightly higher volume fraction of pores >0.2 mm. Overall the largest increase of pore volume was detected in the range of pores smaller 0.05 mm (mesopores). Within this pore size class, no significant difference could be found between sites.
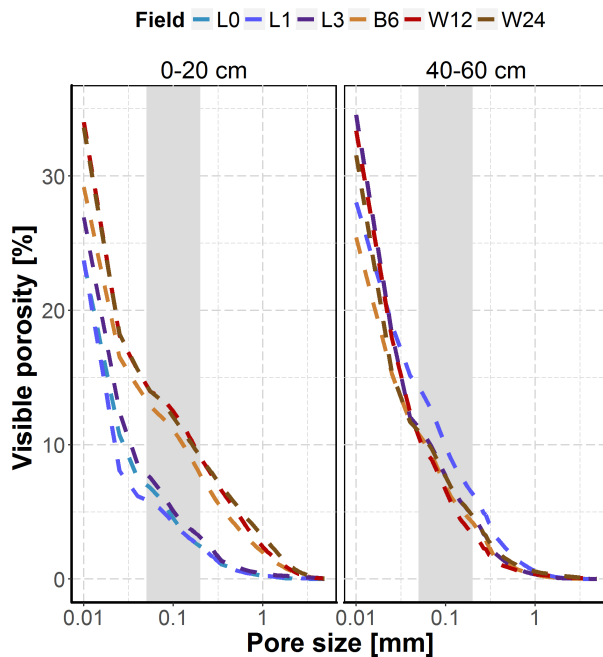
FIGURE 3.4: *Joint cumulative pore size distribution created using a scale fusion on the derivative of volume density. Each curve is the result of the average of n=3 plots, which in turn are determined by the result of 45 CT scans (L3: n=2). Grey area represents the pore sizes derived from 3 cm cylinders. L0, L1, L3 were lucerne sites (0, 1, 3 years after reclamation). B6 was a barley field (6 years after reclamation) and W12 and W24 wheat fields (12 and 24 years after reclamation).*

No stratification of macroporosity with depth (Fig. B.1) could be observed within soil columns (10 cm Ø), neither for those sampled from the top (0-20 cm), nor for whose sampled from the lower layer (40-60 cm).

Fig. 3.4 indicates that while the tilled layers (0-20 cm in B6, W12, W24) differ from all other layers, they are very similar to each other. Therefore, mean values of different pore size classes lumped across these sites were calculated for the two sampled depths and compared (Fig. 3.5). The total visible porosity, i.e. pores >10 μm, was only slightly higher in the tilled layers (Fig. 3.5). However there was a significant increase in the volume fraction of large macropores (>0.2 mm) in the tilled layers (9%) compared to the second depth (4%). The volume fraction of small macropores (0.05 and 0.2 mm) was significantly lower in the tilled layers (4.7%) compared to 40 – 60 cm depth (5.8%). The difference in the volume of pores smaller 0.05 mm was not significant.

In summary, the visible porosity does not change significant over time, but the PSDs of the tilled layers differ from those of the pioneereing phase and the subsoil.
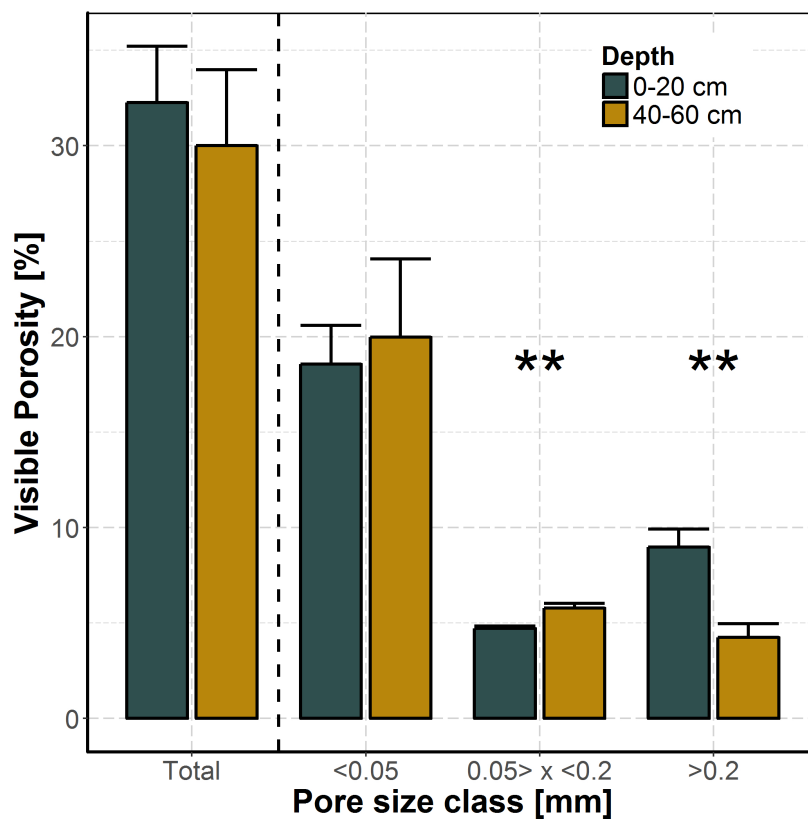
FIGURE 3.5: *Mean values of total visible porosity and individual pore size classes from the tilled layer (0–20 cm) and the lower layer (40–60 cm) of the 6, 12 and 24 year old fields. Error bars represent the standard deviation.*

3.3.2 Comparison of retention curve and pore size distribution

Water-retention curves, measured with HYPROP (without curve fitting) and corresponding visible porosity, i.e. pores >10 μm, derived from X-ray μCT images were compared for all sites and depths. For ease of comparison HYPROP result were plotted as air filled porosity, i.e. saturated pore volume minus water filled pore volume. As an example, data for both depths of 24 year old site are plotted in Fig. 3.6. Both kind of measurements show the high macroporosity in the tilled layer compared to untilled layers in 40 – 60 cm depth. The shape of the water retention curve is clearly reflected in the image-derived pore size distribution. There is an analogous variability among the plots, e.g. plot b in 40-60 cm has low macroporosity, which is reflected by lower saturated water content and a less steep drainage curve. A more detailed comparison shows that the mentioned increase of pores between Ø 0.05 mm and Ø 0.2 mm in the untilled layers (Fig. 3.5) is shifted towards pores < 0.05 mm in the water-retention curve. For pores smaller than the X-ray μCT resolution, the shape of the water retention curves are very similar for all measured samples (data not shown), indicating that pores < 0.01 mm mainly depend on initial soil texture and less on structure formation.

3.3.3 Connectivity

In general, Euler numbers decreased linearly with increasing visible porosity at each individual resolution, i.e. a gradual increase in visible porosity leads to a gradual increase in connectivity, or number of connections. In addition, the Euler numbers decreased by several orders of magnitude across different sample size even though the increase in visible
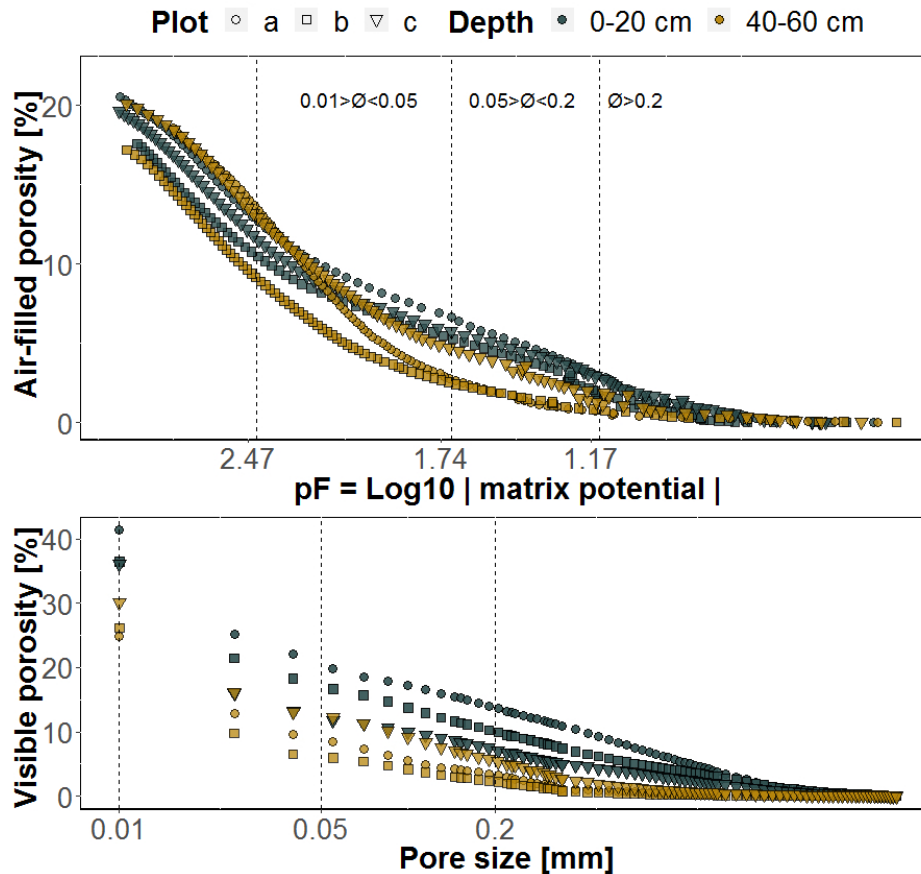
FIGURE 3.6: *Comparison of measurements of air filled porosity derived from HYPROP measurements and visible porosity derived from CT images. Each point curve represents a plot of the 2 depths of the 24 year old field.*

porosity is moderate (Ø 10 cm: Fig. B.2, Ø 3 cm: Fig. 3.7, Ø 0.7 cm: Fig. B.3). This is because, the gain in resolution reveals far more new pore connections between pore objects than objects itself (Fig. 3.2). On top of this general behaviour there is a striking difference between tilled layers and untilled soil. The tilled soil structure exhibits a less rapid decrease in Euler numbers with increasing visible porosity than the untilled soil layers (Fig. 3.7). Accordingly, the mean Euler numbers of these tilled layers within samples of 3 cm Ø were significantly higher compared to 40 – 60 cm depth (3.1), indicating reduced connectivity.

Contrasting to this, the Euler number in 10 cm Ø samples showed on average lower values in the tilled layers (-0.073 mm^{-1}) compared to 40 – 60 cm depth (-0.031 mm^{-1}). However, this is due to the increased volume of pores > 0.2 mm (Table B.1). The general pattern of lower connectivity at the same macroporosity in tilled soils is still evident at the coarser scale (Fig. B.3). In summary, as with the visible porosity, connectivity does not change significant over time, but the connectivity of the tilled layers differs from that of the pioneereing phase and the subsoil.
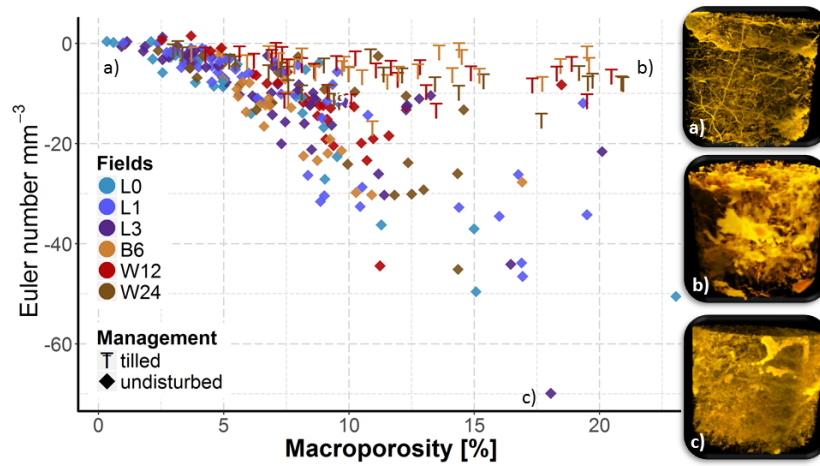
FIGURE 3.7: *Relationship between connectivity (Euler Number) and macroporosity for 3 cm Ø subsamples. Data are provided for different time points of the chronosequence for 0–20 cm (tilled layer) and 40–60 cm (undisturbed) soil depth. Low values of the Euler Number reveal a high amount of connections/ redundant loops in a pore system. 3D visualisation of the pore network of extreme values (a–c). Respective samples in the data pool are marked with the same letter. L0, L1, L3 were lucerne sites (0, 1, 3 years after reclamation). B6 was a barley field (6 years after reclamation) and W12 and W24 wheat fields (12 and 24 years after reclamation).*

TABLE 3.1: *Mean values and standard deviation of the Euler number derived from different sample sizes for samples from a chronosequence from two different depths. n = 3 plots, which in turn each are determined by the result of 3, 9 and 3 CT scans for the 10 cm, 3 cm and 0.7 cm columns (L3: n= 2). Asterisks shows significant differences at p<0.05 between the two layers of the 6, 12 and 24 year old fields revealed by Students T-test. Different letters indicate significant differences in the two depths at p<0.05 between all fields revealed by Dunn's multiple comparisons test. L0, L1, L3 were lucerne sites (0, 1, 3 years after reclamation). B6 was a barley field (6 years after reclamation) and W12 and W24 wheat fields (12 and 24 years after reclamation).*

Resolution:		0.23 mm		0.076 mm		0.02 mm	
Depth	Field	Euler number mm^{-3}		Euler number mm^{-3}		Euler number mm^{-3}	
0 – 20 cm	**L0**	-0.018	$\pm$ 0.011	-8.8^{bcd}	$\pm$ 1.9	-2859.9^{bcd}	$\pm$ 986.9
	L1	-0.017	$\pm$ 0.011	-3.3^{a}	$\pm$ 0.4	-572.1^{a}	$\pm$ 1102.2
	L3	-0.020	$\pm$ 0.006	-7.8^{abcd}	$\pm$ 2.5	-2902.9^{abcd}	$\pm$ 1483.0
	B6	-0.066	$\pm$ 0.012	-5.1^{ab}	$\pm$ 1.3	-967.6^{ab}	$\pm$ 1104.9
	W12	-0.078	$\pm$ 0.041	-5.9^{ab}	$\pm$ 3.2	-718.1^{a}	$\pm$ 645.6
	W24	-0.073	$\pm$ 0.065	-6.8^{abcd}	$\pm$ 1.2	-892.3^{a}	$\pm$ 730.8
	Mean B6-W24	-0.072*	$\pm$ 0.006	-5.9*	$\pm$ 0.8	-859.3*	$\pm$ 128.0
40 – 60 cm	**L1**	-0.026	$\pm$ 0.029	-18.9^{d}	$\pm$ 10.8	-1784.8^{abcd}	$\pm$ 1149.3
	L3	-0.086	$\pm$ 0.072	-14.4^{bcd}	$\pm$ 7.1	-5058.9^{d}	$\pm$ 2846.5
	B6	-0.011	$\pm$ 0.001	-13.3^{cd}	$\pm$ 0.6	-2132.1^{abcd}	$\pm$ 1024.6
	W12	-0.048	$\pm$ 0.049	-12.4^{bcd}	$\pm$ 3.0	-4411.1^{cd}	$\pm$ 1883.1
	W24	-0.057	$\pm$ 0.042	-12.5^{bcd}	$\pm$ 7.1	-2217.6^{abcd}	$\pm$ 1469.3
	Mean B6-W24	-0.031*	$\pm$ 0.023	-12.8*	$\pm$ 0.5	-2920.2*	$\pm$ 1291.8

3.3.4 Development of biopores

An illustration of biopore development over time derived from X-ray μCT is shown in Fig. 3.8. The derived biopores are generally cylindrical in shape, connected and reminiscent of a branched root system. Though there is no benchmark to test the completeness of biopore recovery with our new method a validation through a visual examination of original X-ray μCT images showed that most of the visible biopores were captured (Fig 3.3).
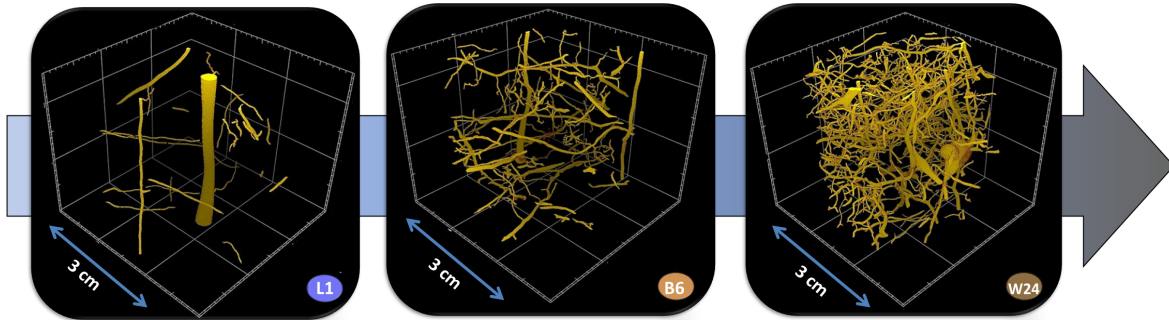
FIGURE 3.8: *Biopores in 3 cm Ø subsamples from a depth of 50 cm after 1 year (L1), 6 years (B6) and 24 years (W24) after reclamation. Different tubeness filters have been used to filter cylindrical shaped biopores out of the entire pore system.*

In 0 – 20 cm depth, the volume of biopores (Fig. B.4, Table 3.2) increased significantly within the first 6 years to 0.98 Vol-% and stayed constant afterwards. In 40-60 cm depth the increase was slower and reached the maximum value after 12 years and also stayed constant thereafter. There was only a small difference between the first (1.1 Vol-%) and the second depth (0.9 Vol-%) in the 24 year old soil. Despite the low absolute volume of biopores, their length density is considerable (Fig. 3.9). Directly after the reclamation the length density was 1.83 cm cm^{-3} which increased significantly up to 18.79 cm cm^{-3} after 6 years and stayed almost constant afterwards. In the second depth no increase could be observed between year 1 and 3, but then the length density increased to values similar to the upper layer. Almost all pores >0.5 mm in the second depth of the 12 and 24 year old sites were biopores (data not shown).

The root length density also increased significantly at a depth of 0-20 cm in the first 3 years, but then followed a decreasing trend. At a depth of 40-60 cm, the root length densities were generally lower. They increased within the first 6 years and decreased thereafter. The frequency distribution of the Euclidean distances from all soil voxels to the nearest biopore showed no marked maximum for the younger sites (Fig. 3.10). With increasing age a clear maximum is observed and shifts towards lower distances. The frequency distribution pattern of the 12 and 24 year old sites are therefore characterized by a high maximum at a distance of only 1 mm and a high right-skewed distribution at both depths. In summary, there is an increase of biopore density towards a maximum over time and already after 12 years differences between tilled layers and subsoil are low.

TABLE 3.2: *Mean values and standard deviation of biopore volume, biopore length density and root length density derived from CT-scans of 3 cm Ø samples from a chronosequence from two different depths and WhinRhizo scans respectively. n = 3 plots, which in turn each are determined by the result of 9 CT scans (L3: n= 2). Different letters indicate significant differences in the two depths at p<0.05 between all fields revealed by a Tukey's HSD test. L0, L1, L3 were lucerne sites (0, 1, 3 years after reclamation). B6 was a barley field (6 years after reclamation) and W12 and W24 wheat fields (12 and 24 years after reclamation).*

Depth	Field	Biopores [Vol-%]		Root length [cm cm^{-3}]		Biopore length [cm cm^{-3}]	
0 – 20 cm	L0	0.18^a	± 0.11	0.42^a	± 0.28	1.83^a	± 0.80
	L1	0.23^a	± 0.08	3.33^{bcd}	± 0.92	7.29^{abc}	± 0.34
	L3	0.51^{abc}	± 0.14	4.16^d	± 1.46	10.00^{abcd}	± 0.76
	B6	0.98^{cd}	± 0.13	3.54^{cd}	± 1.20	18.79^d	± 4.79
	W12	1.02^{cd}	± 0.16	1.65^{abcd}	± 0.16	18.97^d	± 4.03
	W24	1.09^d	± 0.22	1.56^{abcd}	± 0.18	17.85^d	± 3.99
40 – 60 cm	L1	0.27^a	± 0.07	0.78^{abcd}	± 0.44	3.29^a	± 0.35
	L3	0.26^a	± 0.05	0.88^{abcd}	± 0.13	3.32^{ab}	± 0.76
	B6	0.46^{ab}	± 0.11	2.50^{abcd}	± 1.40	6.91^{ab}	± 0.45
	W12	0.87^{bcd}	± 0.22	1.91^{abcd}	± 0.64	17.33^{cd}	± 4.35
	W24	0.89^{bcd}	± 0.03	0.55^{ab}	± 0.31	13.64^{bcd}	± 6.72
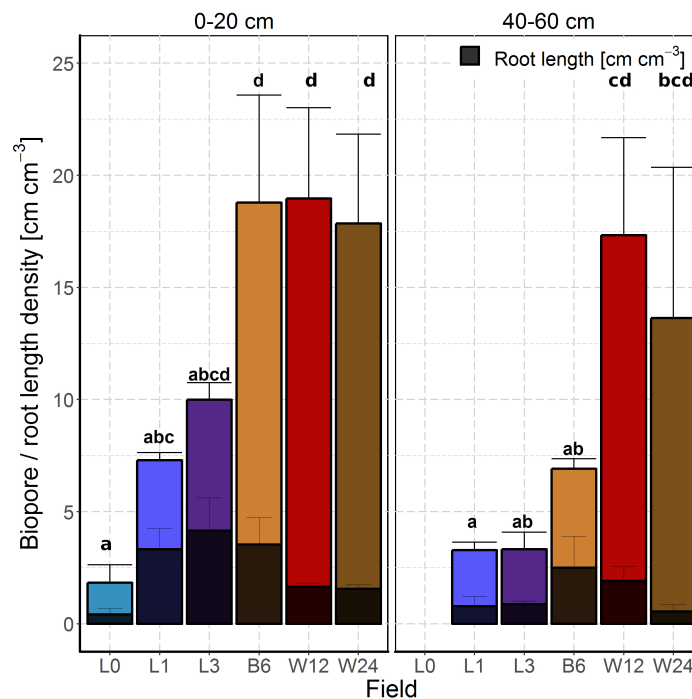
FIGURE 3.9: *Mean length density of biopores in 3 cm Ø samples from a chronosequence from two different depths and mean root length density (dark bars). Error bars show standard deviation (n= 3 Plots, each represented by 9 soil columns, L3: n= 2). Different letters indicate significant differences of biopore length density at p<0.05 between all fields revealed by a Tukey's HSD test. L0, L1, L3 were lucerne sites (0, 1, 3 years after reclamation). B6 was a barley field (6 years after reclamation) and W12 and W24 wheat fields (12 and 24 years after reclamation).*
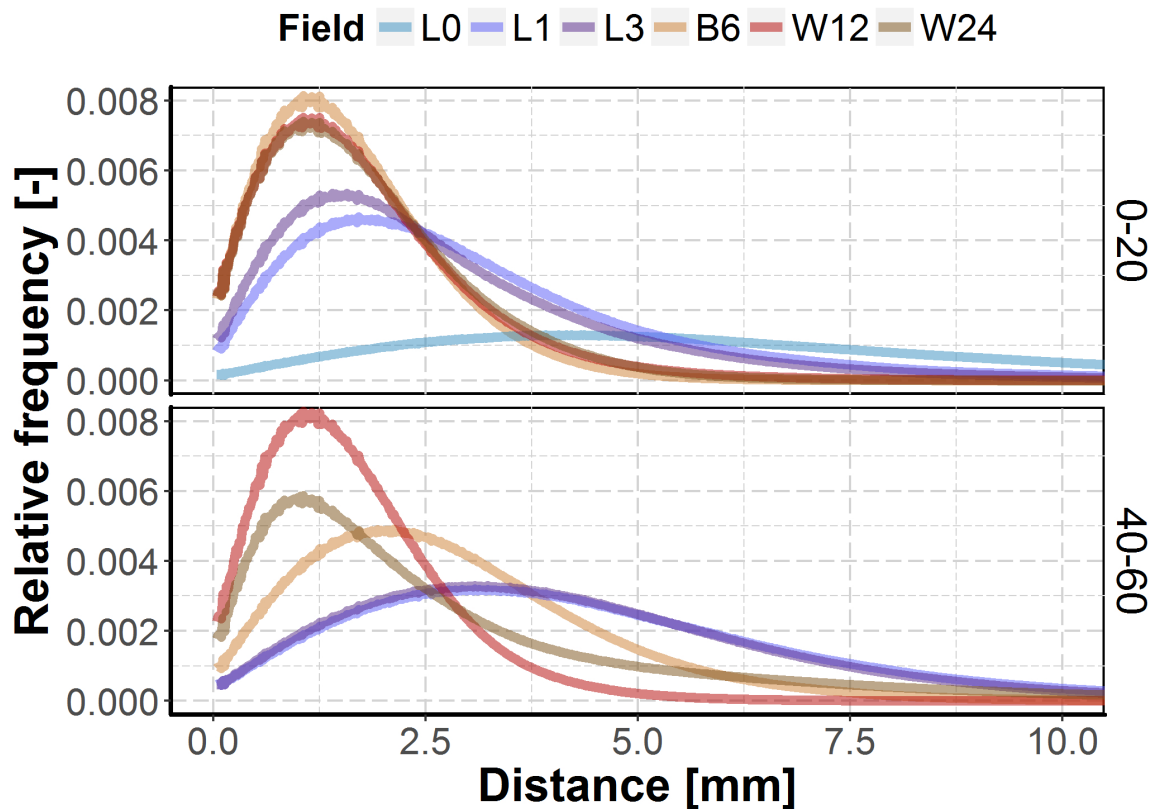
FIGURE 3.10: *Frequency histogram of distances, derived from 3 cm Ø samples from a chronosequence from two different depths, shows the euclidean distance from soil voxels to the next biopore. Each curve is the result of the average of n = 3 plots, which in turn are determined by the result of 15 CT scans (L3: n= 2). L0, L1, L3 were lucerne sites (0, 1, 3 years after reclamation). B6 was a barley field (6 years after reclamation) and W12 and W24 wheat fields (12 and 24 years after reclamation).*

3.4   Discussion

3.4.1   Changes in macropore characteristics and soil physical functions

Soil cultivation and biological activity, such as the penetration of roots, both produce macropores and thus have an influence on soil functions such as the transport of water, gas and nutrients and the storage of organic matter (Peng et al., 2015). We here introduced a hierarchical sampling method for X-ray μCT imaging at various scales to overcome typical limitations of X-ray μCT regarding sample size and resolution. The conformity of the PSDs and the water retention curves confirm that this approach was suitable to describe the changes of pore structure for the chronosequence over time. As differences between sites occur primarily in the pF value range < 2.47 (i.e. pores > 10 μm) we cover the relevant range with our hierarchical approach.

Despite the fact, that several structure forming processes are changing with soil depth (biological activity, root length density, organic matter input, temperature changes, moisture fluctuation), there is a number of factors supporting the association of the observed changes primarily with the tillage operation (0-20cm) and the lack thereof (40-60cm):

1. There are no or only small changes in the structural characteristics within the first 3 years (initial phase without ploughing activity) in both depths.

2. After 6 years, i.e. after the conversion from permanent lucerne cultivation without ploughing to cereals with ploughing, changes were marked in 0-20 cm depth but small in 40 – 60 cm depth

Furthermore, Fig. B.1 shows no clear stratification within 0-20 cm depth (except for the tendency within the first 2.5 cm), neither for L0, L1, L3 (i.e. without tillage) nor for B6, W12, W24 (with tillage), although a depth gradient in swelling/shrinking, organic matter and nutrient input and microbial composition can be expected, i.e. after the conversion from permanent lucerne cultivation without ploughing to cereals with ploughing. Finally, many macropores in these layers differ clearly in their shape from biopores and cracks, and resemble the packing pores left after ploughing (Fig. 3.7a-c).

Therefore there is some evidence that the changes in pore size distribution can mostly be attributed to tillage practices, although on this chronosequence no direct comparisons of tilled and no-tilled sites could be made over the whole period for 0-20 cm layer. Fig. 3.11 summarises the changes in pore size distribution during soil structure formation over time under the influence of plants with and without soil tillage (Fig. 3.11b) and shows how the shape of macropores changes due to tillage (Fig. 3.11a).

The effect of tillage was primarily reflected in the increase in macropores >0.2 mm. In addition, a decrease in pores ranging in size between 0.05 and 0.2 mm was observed, while the smallest pores were not affected. This is in line with several studies on conventional vs. no-tillage (Kravchenko et al., 2011; Pires et al., 2019; Rasmussen, 1999). The reduced volume of macropores in the layers which were not tilled (Fig. 3.5) lead to a smaller amount of drainable pores, i.e. air-filled pores at field capacity. An increased volume of small macropores was detected under no-tillage. This fraction of pores (0.05 mm and 0.2 mm) alters water retention curve only at higher pF values, i.e. smaller equivalence diameters. The reason for this could be the bottle neck effect of smaller pores connecting this pore class and thus a higher amount of plant-available water could be observed under no-tillage as stated in the literature (Rasmussen, 1999). The bottle neck effect can also be the reason for the increased amount of macro- and mesopores visible in the CT compared to the water retention curve, since the morphological pore size is systematically underestimated when interpreting water retention curves towards pore size distribution. A second reason for the discrepancy between water retention data and image-derived pore size distribution may also be a methodological overestimation of the pores in the CT images. Due to the improved resolution in the sub-samples, particles in macropores also become visible, which split a large pore at the coarse resolution into several smaller pores at the higher resolution, so that under certain circumstances pores in the joint cumulative pore size distribution could be counted twice.

Due to increased macroporosity (> 0.2 mm) in the 0-20 cm of the tilled layers, we observed a decrease in Euler number (Table 3.1), compared to the depth of 40 – 60 cm. That is, at the coarse scale the macropore network was better connected due to higher macroporosity in the loosened topsoil. With higher resolution vastly more pore connections emerge (Fig. 3.2) changing the Euler numbers by orders of magnitude (Table 3.1). This increase of connectivity generated by relatively small pores support the bottle neck theory. Moreover, with higher resolution the difference in visible porosity between layers disappeared and the inherently better connectivity of intact biopores led to more negative Euler numbers in the soil layers that is not disrupted by ploughing (Fig. 3.7). Similar to this, Peth et al. (2008) found significantly smaller throat surface areas and shorter flow paths in conventionally tilled aggregates compared to grassland aggregates. They concluded that this would result in limiting gas and water transport in conventional tillage sites Peth et al. (2008).
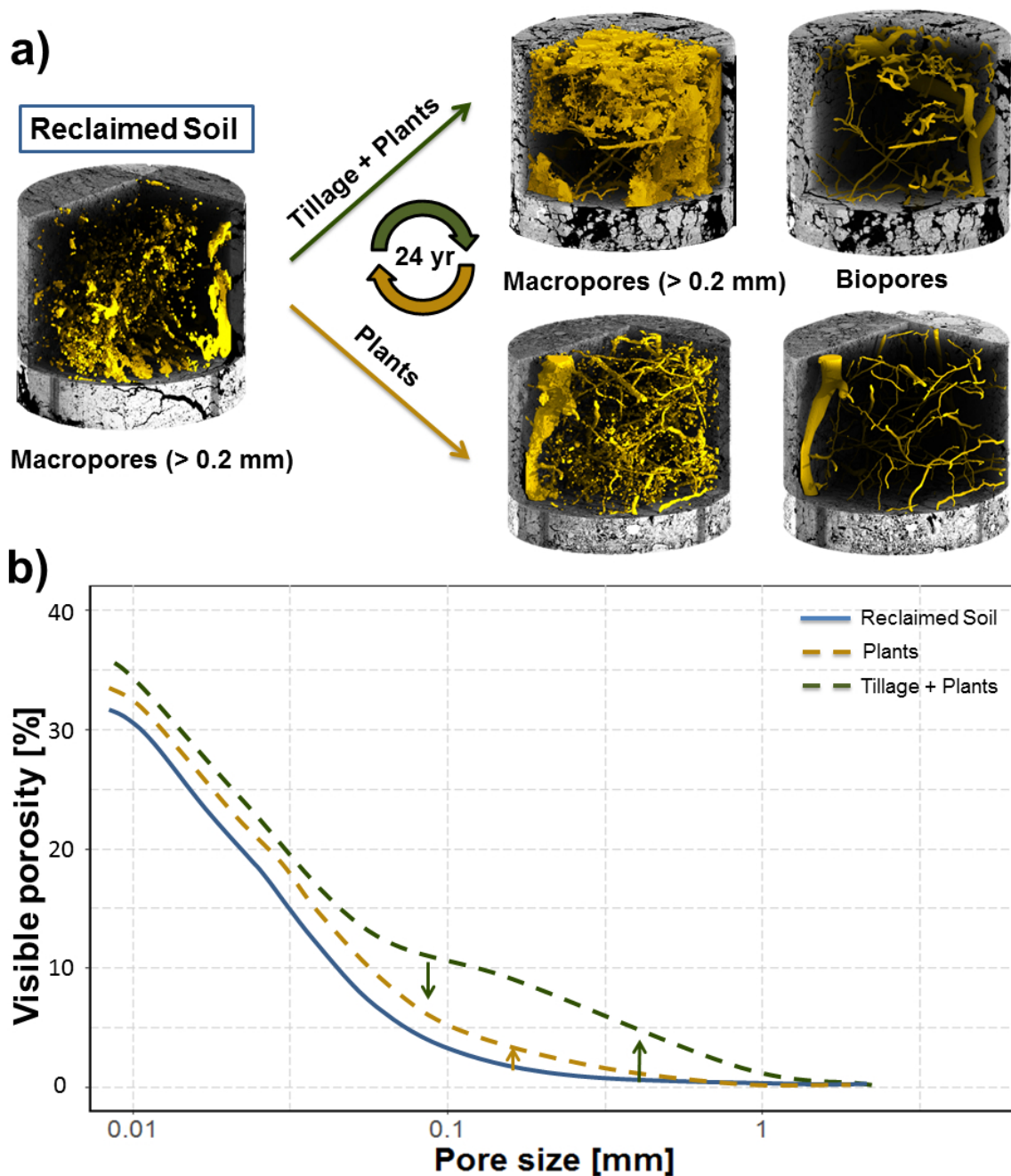
FIGURE 3.11: *Visualisation of the ongoing changes in the 3D pore system after reclamation (a) and sketch of changes in the pore size distribution (b) during soil structure formation over time under the influence of plants and soil tillage in 0-20 cm soil depth.*

3.4.2 Development of Biopores

There are a number of studies for the investigation of biopores using a range of methodological approaches, which were, however, strongly limited by the spatial resolution (Athmann et al., 2013; Han et al., 2015; Kautz, 2015; Stirzaker et al., 1996; White et al., 2010; Wuest, 2001). Endoscopy for example allows examining only relatively large pores in the mm range, while measurements along a profile wall enable higher spatial resolution but only a two-dimensional quantification. With our new methodological approach, we were

able to study the development of biopores in 3D down to a diameter of 0.038 mm (2 pixels) in 3 cm Ø subsamples, resulting in completely different biopore densities compared to traditional methods. After reclamation, roots and soil fauna developed a widely-branched network that already in the relatively short observation period occupied more than 1 Vol-% of the soil, equivalent to 18 cm biopore length per cm^{-3} (Table 3.2, 3.9). Recently, Zhang et al., 2018 investigated the response of land use and fertilisation on macropores (biopores and non-biopores) of undisturbed samples of upland and paddy subsoils. In their study, all segments in the pore network derived from X-ray μCT with a length larger than 20 times the radius where considered as biopores. On sites which are fertilised by mineral and organic fertiliser, i.e. similar to our chronosequence, the volume of biopores ranged from 0.52 to 1.55 Vol-% which is comparable to the amount of biopores in the subsoil of the 12 (0.87 Vol-%) and 24 (0.89 Vol-%) year old sites. The corresponding length densities ranged from 10 to 12 cm cm^{-3}, which is slightly lower compared to our sites. Although they investigated biopores in a total different climate and under different land use the comparable high values highlight the fast recovery of biopores in the "space-for-time" chronosequence.

The root length data must be interpreted with caution. Not all samples could be taken during the same period due to the time required for X-ray μCT analyses. Therefore, the method used does involve potential measurement error since the amount of roots could be underestimated due to degradation processes despite storage at 4°C. A visible assessment of all X-ray μCT samples showed that even columns that were scanned directly after sampling ($\sim$24h) only had a small proportion of biopores filled with roots. The standard deviation was small (3.9), hence it can be assumed that storage (cooling) of the samples prevented substantial root degradation. Empty biopores promote aeration and water infiltration (Pires et al., 2017). In addition, they can also increase the SOC content in the subsoil and therefore serve as microbial hotspots for C, N and P transformations (Banfield et al., 2017; Bauke et al., 2017; Han et al., 2017).

The biopores on site L0, are partly a result of germinating lucerne and partly derived from weed plants which established between deposition and reclamation. The substrate for reclamation consisted of Luvisol and unweathered loess (ratio is about 1:10) and thus structures conserved in old Luvisol clods could be another source of biopores.

In the topsoil of the 1-year-old lucerne sites about 50% of the biopores were already empty and not filled with roots (Table 3, 3.9), which is in line with the findings of Rasse et al. (2000). These authors observed root turnover rates of lucerne in the upper 9.5 cm of an Ap horizon. Decomposition of fine roots exceeded 75 and 50% during two different vegetation periods (Rasse et al., 2000). Our approach to estimate the proportion of filled biopores from two independent measurements, i.e. image-derived biopore length vs. root length from destructive sampling, might give a slightly biased result as some roots might grow in pores that are not detected as biopores or several small roots might grow in a big biopore. However, a direct detection of filled and empty biopores in X-ray μCT images is not possible at the moment.

The increase of biopores over time is characterised by a quasi-steady state after 6 years in 0-20 cm soil depth and interestingly in 40–60 cm depth comparable values were reached after 12 years. Since tillage destroys and changes macropores (Kay et al., 2002; Shipitalo et al., 2000; Zhang et al., 2016), the high amount of biopores in the tilled layers are surprising. However, a visual comparison of the two sampled layers (Fig. 3.11a) shows that the biopore network of the tilled layers consists on the one hand of new roots of the current culture and on the other hand of many fragments of old biopores and thus clearly differs from the intact, highly branched network of biopores at 40-60 cm depth. The frequency distribution patterns of the Euclidean distances from all soil voxels to the nearest biopore exhibit a clear transition towards a right skewed distribution with pronounced maximum around a distance of 1 mm. The very short distances show how efficiently the soil volume of

biopores is explored, which also increases the amount of potential microbial hotspots along these pores. Schlüter et al. (2018a) calculated the distance distribution for plants growing in a pot experiment for the early root development of faba bean (Blaser et al., 2018). The resulting histograms followed a similar trend over time (Schlüter et al., 2018a), indicating that in a pot experiment similar distribution patterns develop much faster (weeks) than in the field (years). This might be due to the fact that a pot experiment is spatially limited. The frequency distribution of biopore distances on the 3-year and 1-year lucerne sites is almost the same in 40-60 cm and the biopore length density is also identical. From this it can be hypothesised that the exploration of soil by root growth reached some stable maximum after one year with a biopore pattern that is characteristic for the lucerne. The high jump towards lower distances afterwards in both depths indicates, that the fibrous root systems of the cereals drastically increase the efficiency in soil exploration. However, even in 40-60 cm on the 24 year old field, biopores with the diameter and characteristics of the lucerne taproot can be found (Fig. 3.11a), indicating the importance of the initial phase (1-3 years) for the creation of large macropores that are conserved and reused, when periodical destruction by ploughing is absent. The long-term stability of old structural features is likely supported by the high carbonate content and the high bulk density, which reduces any alteration of the pore structure except through the biological activity and tillage. Biopores from a depth of 40-60 cm therefore show characteristics of all root systems over the total reclamation time.

Although there is a marked development of a system of biopores over time, we could not find any differences in PSD over time in the depth of 40 – 60 cm, i.e. no increase in macroporosity was visible. Therefore the volume fraction of biopores must have grown on the expense of other macropores, e.g. by radial compaction or by growing into loos areas that would have otherwise been detected as irregularly shaped macropores. This would be in line with various studies which stated, that plant roots use natural or artificial macropores as pathways to reach deeper soil layers and thus benefit from enhanced uptake of water and nutrients (Athmann et al., 2013; Colombi et al., 2017; Han et al., 2015; Stirzaker et al., 1996; White et al., 2010). Especially in layers with a high bulk density or in larger soil depths, often associated with higher penetrometer resistance, roots grow predominantly in existing macropores (Gao et al., 2016; Kautz et al., 2013; White et al., 2010). White et al. (2010) counted the amount of roots and macropores in undisturbed soil cores of a comparable dense clay soil and found that more than 50% of the roots of the current crop (wheat) grow into existing pores at depths of 30 to 60 cm. They concluded that due to the low proportion of total filled macropores (approximately 20% of the macropores in the top layer (<0.6 m)) combined with the high root clumping (50% of the root-bearing pores had at least 4 roots)), much of this additional pore space might be less accessible to the roots or has a low connectivity (White et al., 2010). If we transfer this assumption to the development of the biopores on our chronosequence, it can be deduced that (i.) due to the low amount and randomised distribution of macropores directly after reclamation there is a fast increase in biopore density triggered by roots, particularly in the first few years and (ii.) after a network of biopores has been established and the taproot of lucerne created big biopores, which are afterwards used by cereals to explore the subsoil, few changes occur, since new roots can grow into the well-connected network of biopores.

3.5   Conclusion

The hierarchical sampling method for X-ray imaging was suitable to describe all major changes in the pore system of the "space-for-time" chronosequence. This enabled us to describe the major changes in pore structure. These changes however, manifested themselves in different parameters for the two sampled depths. Within the upper 20 cm high biological

activity and tillage led to an increase in macroporosity (>0.2 mm), but also to a reduction in pores in the range of 0.05 mm to 0.2 mm due to the periodic disruption of biopore-networks. This reduction had a remarkably high influence on the number of pore connections (Euler number) and thus also on the hydraulic properties of the soil. Beneath the tilled layer (40-60 cm) small temporal influences on pore size distribution and connectivity could be observed. However, the use of lucerne in the pioneer phase created a macropore system which could be used by following crops to explore the subsoil. This made the establishment of a dense biopore network in 40-60 cm depth possible. As a result, both the transport of gas or water is improved and yields are stabilised through improved rootability. Tillage is a singular event followed by gradual settling, whereas root growth and associated biological bioturbation is a steady process that develops towards some dynamic equilibrium with constant biopore density. In our study a maximum was already reached after 6 years at 0-20 cm depth and 12 years at 40-60 cm depth with mean values around 18 cm cm^{-3}. Biological activity and tillage therefore do not only entail different spatial characteristics of pores, but also have different temporal characteristics.

Chapter 4

Roots compact the surrounding soil depending on the structures they encounter
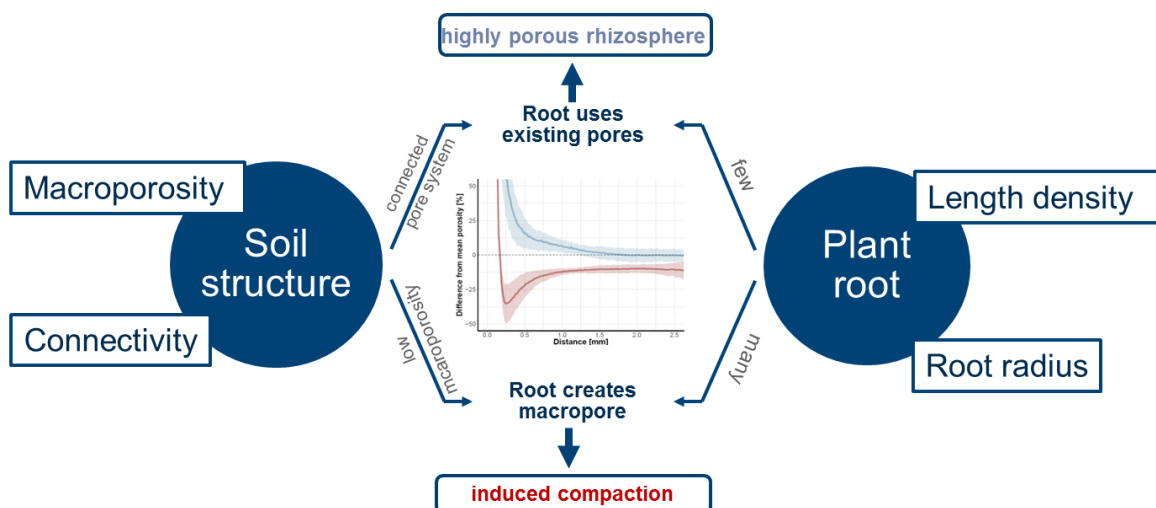
highly porous rhizosphere

Root uses
existing pores

Macroporosity

Soil
structure

Connectivity

connected pore system

low macroporosity

Root creates
macropore

induced compaction

few

many

Plant
root

Length density

Root radius

Difference from mean porosity [%]

Distance [mm]

Contradictory evidence exists regarding whether and to which extend roots change soil structure in their vicinity. Here we attempt to reconcile disparate views allowing for the two-way interaction between soil structure and root traits, i.e. changes in soil structure due to plants and changes in root growth due to soil structure.

Porosity gradients extending from the root/biopore surface into the bulk soil were investigated with X-ray μCT for undisturbed soil samples from a field chronosequence as well as for a laboratory experiment with Zea mays growing into three different bulk densities. An image analysis protocol was developed, which enabled a fast analysis of the large sample pool (n >300) at a resolution of 19 μm.

Lab experiment showed that growing roots only compact the surrounding soil if macroporosity is low and dominated by isolated pores. When roots can grow into a highly connected macropore system showing high connectivity the rhizosphere is more porous compared to the bulk soil. A compaction around roots/biopores in the field chronosequence was only observed in combination with high root/biopore length densities.

We conclude that roots compact the rhizosphere only if the initial soil structure does not offer a sufficient volume of well-connected macropores.

4.1   Introduction

Growing roots have to overcome soil mechanical resistance imposed by soil structure (Jin et al., 2013), so that compacted soils may limit root growth and plant yield (Lipiec et al., 2003; Passioura, 1991; Stirzaker et al., 1996). The availability of macropores and their connectivity are therefore often stated to be a limiting factor in plant growth, since roots preferentially grow into existing macropores and by this can bypass zones of high mechanical resistance (Colombi et al., 2017; Stirzaker et al., 1996). This influence of soil structure on root growth is often in the focus of research.

However, the interactions of plant roots and soil structure are two-way, i.e. there is also an effect of plant roots on soil structure. During soil exploration, roots push through the soil and alter physical, chemical and biological properties in their vicinity, the rhizosphere (Hinsinger et al., 2009). These alterations may persist after roots are degraded, leaving behind a dense system of connected biopores (Lucas et al., 2019, Fig. 3.9). These biopores, now an integral part of soil structure, in turn feedback on root growth providing pathways of low mechanical resistivity with wall properties reflecting former root activity and in part activity of soil fauna.

At the system scale root derived biopores enhance soil structural properties like air permeability, rootability and saturated water flow (Kautz, 2015). At the local scale of the rhizosphere, root induced structural changes are not only relevant for microbial habitat quality, but in particular for transport of water and nutrients. The rhizosphere is the bottleneck water and nutrients have to pass before entering the root. Likewise, substances released by the plant will diffuse through this zone. Aravena et al. (2011, 2014) have illustrated that it is crucial to define and describe changes in rhizosphere porosity in order to model rhizosphere processes, as an enhanced rhizosphere compaction (decreased porosity) had a positive effect on root water uptake.

Since root diameters are often larger than existing pores, growing roots are believed to compact the rhizosphere (Aravena et al., 2011; Bruand et al., 1996; Dexter, 1987). Dexter first modelled this compaction. His model describes the exponential decrease of porosity toward the roots, defined by a constant multiple of the root diameter.

More recently, different imaging techniques enabled direct in situ visualisation of the root-soil interface and the soil structure gradient extending into the bulk soil (Feeney et al., 2006; Helliwell et al., 2017; Koebernick et al., 2017; Whalley et al., 2005). Vollsnes et al. (2010) confirmed for very young *Zea mays* that the compaction around primary roots in sand is exponential and depends on the root radius. However, some of these studies revealed contradictory results, i.e. increase of porosity in the rhizosphere (Feeney et al., 2006; Helliwell et al., 2017; Helliwell et al., 2019; Whalley et al., 2005). Feeney et al. (2006) analysed not a gradient but aggregates from the rhizosphere in comparison to aggregates from an area accessible only by hyphae and a control without plants using X-ray μCT with a resolution of 4.4 μm. Their results showed a significant increase in the porosity of the rhizosphere compared to bulk soil. Helliwell et al. (2019) referred the increase in porosity they observed to processes like shrinking and swelling, which are enhanced in the rhizosphere. In a subsequent work (Helliwell et al., 2019) they showed that the porosity (density) gradients depend on plant species, texture and distance to the root surface. The latter was also observed by Koebernick et al. (2019), describing high porosity directly at the vicinity of the epidermis of roots which grew in packings of 2 mm aggregates. They assigned this to a 'surface/wall effect', i.e. the loose packing of particles against large surfaces described by Suzuki et al. (2008). Therefore, Koebernick et al. (2019) added this 'surface/wall effect', i.e. the packing geometry of spherical soil particles, to the model of Dexter (1987). In addition to the formation of new root channels, roots can also penetrate the soil by using existing pores or cracks Jin et al. (2013). In this manuscript, we reconcile the disparate views on porosity changes

in the rhizosphere by: (1) considering the gradient extending from the root surface into the soil with high spatial resolution, i.e. allowing for a differentiation between the zone immediately at the root-soil interface (0-100 μm) and the zone at slightly larger distance (up to 1 mm) and by (2) addressing the interplay between porosity and pore size distribution on the one hand, and root length distribution across different root diameter classes on the other hand and by (3) relating porosity changes in the rhizosphere to the antecedent soil structure prevailing before roots penetrated the soil.

We hypothesise that root induced compaction described by Dexter (1987) depends on soil pore characteristics and decreases with the amount of connected macropores, since roots which grow into existing macropores do not necessarily have to align soil particles as they move through the soil. We conducted an experiment in the climate chamber with *Zea mays* and three different bulk densities to observe the impact of macropore characteristics on root induced compaction and transferred this to existing field information on biopores in undisturbed field samples from Lucas et al. (2019, Chapter 3). Lucas et al. (2019) described the formation of biopores using more than 250 samples for X-ray μCT from a space-for-time chronosequence, including six time points of soil development in two different depths.

4.2 Materials and methods

4.2.1 Laboratory experiment on soil compaction

Soil for laboratory experiment on soil compaction was taken from a reclamation area at the Garzweiler open pit mine (Germany) described in Pihlap et al. (2019, Section 2.2). The soil was homogenised, passed through a 2 mm sieve and air-dried ($\sim$2% gravimetric water content). A basal fertiliser application consisting of 50 mg N kg^{-1}, 50 mg K kg^{-1}, 40 mg P kg^{-1} and 25 mg Mg kg^{-1} was applied in the form of NH_4NO_3, K_2SO_4, $MgCl_2$ x $6H_2O$ and $CaHPO_4$, respectively.

Five replicates were packed for three different bulk densities (1.30 g cm^{-3}, 1.45 g cm^{-3}, 1.60 g cm^{-3}). The columns (7 cm $\varnothing$ and 25 cm height) were filled up to 23 cm and a small cylinder (2.5 cm $\varnothing$ 4 cm height) was placed in the center of the surface area. These cylinders were packed with soil of 1.3 g cm^{-3} and the maize seeds (*Zea mays* var. B73; one seed per column) were placed within this cylinder to ensure a good germination in all treatments and to force the seminal roots to grow at a steeper angle; i.e. avoiding growth against the cylinder wall early on. The seeds were previously surface sterilised in 10% H_2O_2 for 10 minutes, washed with deionised water and then placed 2 hours in a solution of 2 mM $CaSO_4$. The entire soil surface was covered with a 2 cm thick layer of quartz gravel to reduce evaporation. The columns were watered from the top and bottom to a water content of 30 Vol-% and a 30-μm nylon mesh enabled re-watering from the bottom twice a week. The plants grew for 20 days in a climate chamber under following conditions: Relative humidity of 65%, 12 h day at 22°C with 350 μmol m^{-2} s^{-1} PAR and a night temperature of 18 °C. During harvest, shoot fresh and dry weight (24 h in an oven at 65°C) was determined. The plant samples were ground and C, N were analysed using a coupled system of elementar analyser and quadrupole mass spectrometer (Vario EL cube, Elementar Hanau, Germany; Quadropole MS ESD 100, ICI Bremen, Germany). After acid digestion ICP-OES analyses were conducted for selected plant nutrients P, K, Ca, Mg, Mn, Fe. Undisturbed subsamples (3 cm $\varnothing$; 3 cm height) were taken in three different depths (7 – 10 cm, 12-15 cm, 17-20 cm) with a subsampling device (UGT GmbH, Germany).

4.2.2   Chronosequence

An existing X-ray μCT-dataset from Lucas et al. (2019, Chapter 3) was used to investigate root induced compaction in the field. The chronosequence and sampling approach is described in detail in Lucas et al. (2019, Section 3.2) and Pihlap et al. (2019, Section 2.2). Briefly, the plots of the space-for-time chronosequence were formed by a standardised reclamation technique after lignite mining, i.e. they were all formed on the same homogenised initial substrate (unweathered loess, weak alkaline pH, high $CaCO_3$ concentration). Samples were taken on three plots and two depths (0-20 cm and 40 – 60 cm) from sites in six different age groups 0, 1, 3 years (Lucerne sites, no tillage) and 6, 12 and 24 years (cereal sites, tilled) after first sowing. Three undisturbed samples (20 cm height, 10 cm Ø) were taken per plot with a tailor-made drill for undisturbed sampling of cylindrical soil cores (UGT GmbH, Germany) and later three subsamples (3 cm height, 3 cm Ø) per sample were taken. The biopores in these samples were mainly formed by roots (Lucas et al., 2019, Subsection 3.3.4), which enables a comparison to the pot experiment.

4.2.3   X-ray microtomography

Differences in root-induced compaction between the three different treatments of the pot experiment were evaluated by scanning the 45 cylindrical subsamples of 3 cm Ø (5 replicates, 3 depths). Differences in visible porosity (limited by the resolution of 19 μm) and grey scale gradients extending from biopore walls in field samples were described based on 279 subsamples with a diameter of 3 cm Ø (6 fields, 2 depths, 3 plots, 9 replicates). The 0-year old field at the second depth and one plot of the 3-year old field were not evaluated (Lucas et al., 2019, Subsection 3.2). All samples were scanned with a X-ray microtomograph (X-TEk XCT 225, Nikon 162 Metrology) with an Elmer-Perkin 1620 detector panel (1750 x 2000 pixels) using 130 kev / 150 μA and reconstructed with an spatial resolution of 19 μm as explained in more detail in Lucas et al. (2019, 3.2) .

   3D non-local means filter (UnbiasedNonLocalMeans in ITK, Revision 1.21, Tristán-Vega et al., 2012) was used for noise removal. The images were previously converted to 16-bit and the value 1000 was added, to reduce the effect of the non-linear transformation of grey values by this filter in dark areas. The images of the Lab experiment were previously inverted to maintain a high contrast between roots and pores. After filtering, the images were reduced to 8-bit and an unsharp mask (radius 2 and mask weight 0.2) was applied using Fiji.

   For the threshold detection of pores (including roots) 5 different segmentation methods were applied as described in Schlüter et al. (2014), then Hysteresis-Thresholding of the 3D segmentation plugin (version V3.83) was applied in Fiji (Ollion et al., 2013). The latter enabled us to segment all pores, regardless of whether they were filled with air, water or roots. The pore size distribution (PSD) was calculated by local thickness method in Fiji (version 1.4.6), which uses the maximum inscribed ball method. In addition, the volumetric Euler number was also calculated with the MorphoLibJ plugin in Fiji (Version 1.3.3, Legland et al., 2016) to characterise pore topology. High negative values indicate a high number of connections between pores. Incorrect classifications and noise strongly influence the Euler number (Armstrong et al., 2019), therefore a pore opening was performed before the calculation and pores smaller than or equal to four pixels (76 μm) were removed. The Rootine Protocol (Gao et al., 2019) was used and adapted to segment all tubular biopores and roots. This protocol uses the Tubeness plugin on Fiji to separate tubular objects from the remaining irregularly shaped pore network. It is combined with a scale-space approach, i.e. convolution with a Gaussian blur of different standard deviations σ are used to detect tubes of different diameters. The number of different σ's in the scale space was different between pots (four)

and field soil (eight) with a wider range of biopore diameters. A combination of Connected Components Labeling and Label Size Opening implemented in the MorphoLibJ plugin in Fiji (Version 1.3.3, Legland et al., 2016) filtered smaller misidentified pores out. Due to the tubular shape of the segmented roots and biopores, the local thickness method in Fiji could be used to obtain information about the biopore diameter classes and corresponding length. More details on images processing and analysis of 3 cm Ø cylinders can be found in Lucas et al. Lucas et al. (2019, Section 3.2).

4.2.4 Evaluation of gradients around biopores and roots

A new protocol was developed to analyse root induced compaction by combining the images of filtered grey values, visible porosity, and euclidean distances into the different channels of a RGB-image (Fig. 4.1). The distances were was calculated using euclidean distance transform (EDT) in Fiji, which describes the Euclidean distances from all soil voxels to the nearest biopore/root. The resulting RGB image was analysed by calculating the average porosity and average grey value as a function of distance. Every fifth voxel within a loop through all slices was read out to reduce computational time.
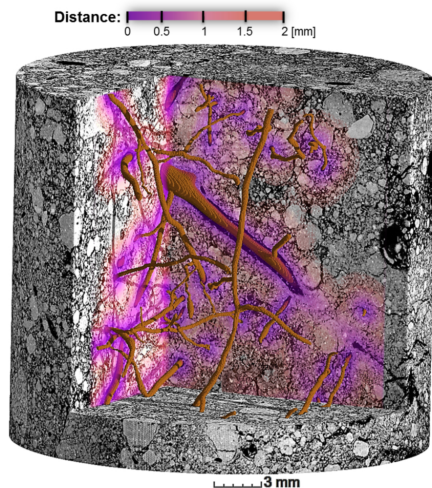
FIGURE 4.1: *3D visualisation of a RGB image created to analyse density gradients with distance to the biopore. The three channels of the RGB image contain 8-bit information on grey values, pores and the distance map (gradient color), which shows the distance from every pixel to the next biopore (brown).*

The changes in visible porosity of one biopore show a clear compaction extending up to 0.6 mm into the rhizosphere, whereas this compaction is absent around a fracture (Fig. 4.2a). In contrast, the direct vicinity of this segmented biopore shows low porosity. The main reason for this is the roughness of the pore wall since the Tubeness filter describes the biggest tube "fitting" into the pore, which excludes the porosity along the rough pore walls (Fig. 4.2b, Lucas et al., 2019). Therefore, high roughness of the pore wall increases the distance at which a possible compaction could be detected (Koebernick et al., 2019). Changes in grey values are inverse to porosity and show almost the same trend. This agreement between grey values and visible porosity indicates that image processing did not affect the changes of grey values with distance. These changes are closely related to changes in bulk density. In contrast, visible porosity is limited by image resolution and shows therefore higher local variability. Therefore, only the grey value results will be shown in the remainder of this manuscript and corresponding changes in visible porosity can be found in the supplement. In order to describe changes around roots of different size classes a Local thickness analysis was conducted on the segmented root/biopore images and the outcome was thresholded at a diameter value of 13 pixels. By this, Euclidean distances could computed separately for roots/biopores >250 μm and <250 μm. To reduce the effect of the other root class, corresponding root images were subtracted from the Euclidean distance images, e.g. the porosity and grey value of the roots >250 μm were not taken into account for the analyses of the compaction around roots < 250 μm. The roots > 250 μm were extended with five 3D dilatation

steps before they were subtracted from the EDT map of the roots < 250 μm and vice versa to exclude the potential gradients associated with the other root diameter class.
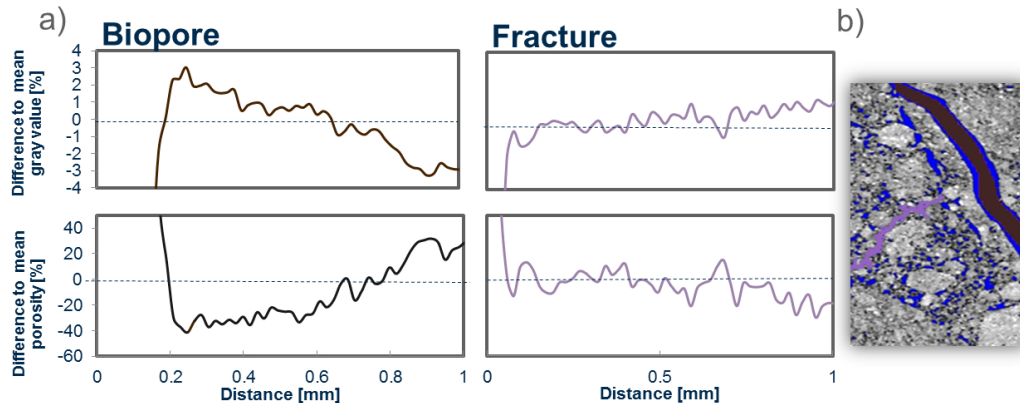
FIGURE 4.2: *(a) Average of grey values and porosity (blue) as a function of distance to the biopore (brown) and the fracture (purple) of the image left in the 2D section (b).*

4.2.5   Statistical analysis

For the pot experiment conducted in the climate chamber, standard errors and mean values of five replicates are provided. The chronosequence is described by the standard deviation and mean values of 3 plots for each year and depth in which each plot is represented by an average of the 9 technical replicates (i.e. X-ray μCT scans). A one-factorial ANOVA in conjunction with Tukey's HSD test revealed significant differences in the data. A log-transformation was used for porosity data prior to statistical analyses. A Kruskal-Wallis test followed by Dunn's multiple comparisons test was used to reveal differences within the highly non-linear Euler number. For all statistical analysis the software R 3.53 and the package agricolae (Mendiburu, 2017) was used.

4.3   Results

4.3.1   Pot experiment

Visible porosity decreased significantly with increasing bulk density (Fig. 4.3). The effect of compaction was especially high for macropores, i.e. pores >250 μm were almost completely absent in samples with bulk densities of 1.45 and 1.60 g cm^{-3}. Shoot growth decreased significantly with increasing bulk density (Table C.1). Likewise root growth (Fig.4.3 and Fig. 4.4), decreased significantly with increasing bulk density, on top of an expected decrease with depth. The Euler number, a measure for the connectivity of the pore system, revealed low connectivity (positive values) in relation to isolated macropores for almost all treatments and depth (Fig. 4.3). With increasing root length density the Euler number decreased (negative values in the first two depths within the treatment of 1.30 g cm^{-3}), i.e. numbers of pore connections are higher than the number of non-connected pores.
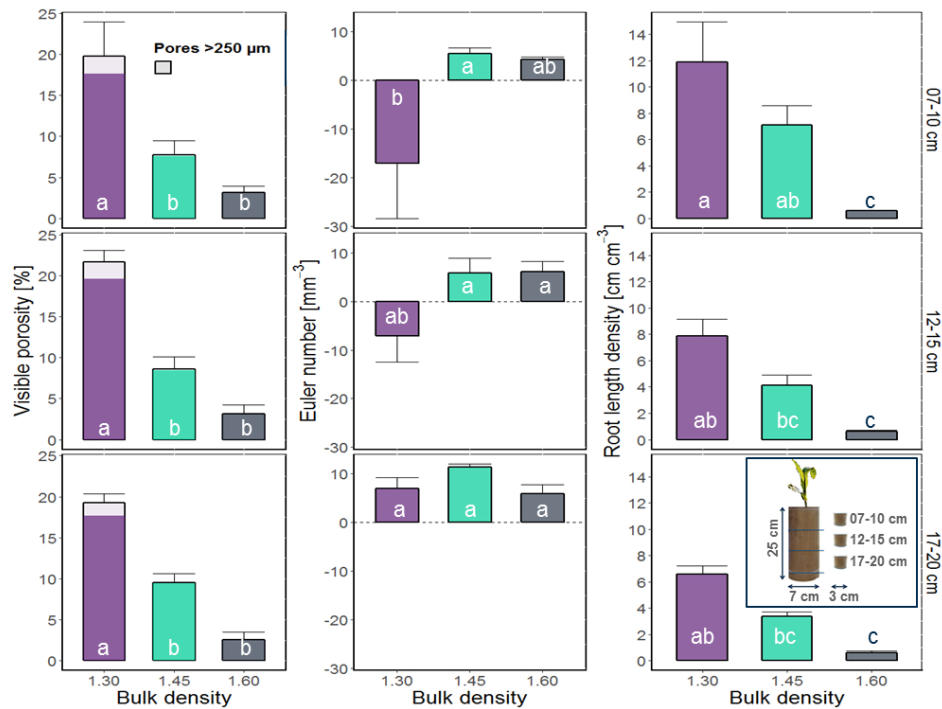
FIGURE 4.3: *Mean values and standard errors (whiskers) of visible porosity, Euler number and root length density for each of the three different treatments (bulk density of 1.30, 1.45, and 1.60 g cm^{-3}) and depth within column (7 − 10 cm, 12-15 cm, 17-20 cm) derived from μCT-scans of 3 cm Ø samples. Visible porosity shows pores > 38 μm (two voxels), the Euler number shows the connectivity of pores >76 μm. Different letters indicate significant differences (n = 5). Inset shows the subsampling scheme.*
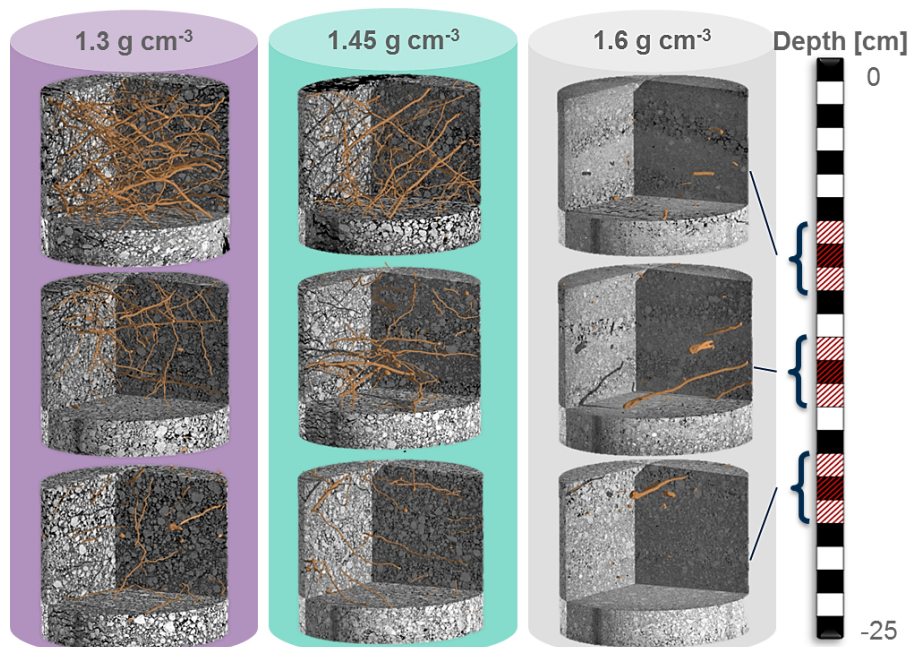
FIGURE 4.4: *3D visualisation of roots in representative 3 cm Ø subsamples for each of the three different treatments (bulk density of 1.30, 1.45, and 1.60 g cm^{-3}) and depth within column (7 − 10 cm, 12-15 cm, 17-20 cm).*

The frequency distribution of the Euclidean distances from soil voxels to the next root (Fig. C.1) showed a clear shift towards smaller distances with increasing porosity (decreasing bulk density) for all sampled depths of the columns. As expected, the grey values in the bulk soil, i.e. the distance from the root > 1.5 mm, reflected the bulk densities of randomly chosen samples of the three treatments (Fig. 4.5). The mean transects of grey values with increasing distance from the root surface differ between treatments. By normalising the data, these differences can be seen more clearly. This was achieved

FIGURE 4.5: *Change of grey values with distance to the roots for three random subsamples for each of the three treatments (bulk density of 1.30, 1.45, and 1.60 g cm^{-3}) and corresponding µCT slices showing roots within the different compacted soils.*

by dividing the data by the mean grey value of the respective sample (Fig. 4.6). Up to a distance to the roots of about 0.1 mm (5 pixels), the grey values are strongly reduced in all samples. Beyond this distance, grey values for the treatment with the intermediate bulk density (1.45 g cm^{-3}) increase above the reference value for the bulk soil and flatten out as distance to the root surface increases further. For the treatment with bulk density of 1.30 g cm^{-3}, the overshoot in normalised grey value, i.e. positive difference indicating compaction, is not as pronounced but still present. For the bulk density of 1.60 g cm^{-3} no such peak is visible.

In summary, the highest root induced compaction was detected in the samples of intermediate bulk density (Fig. 4.6). This effect reached up to 1.5 mm into soil, but there was a decreasing trend with increased depth. For the treatment with lowest bulk density, a zone with even lower bulk density in the direct vicinity to the root surface is followed by a slightly compacted zone at distances larger than about 250 µm. It should be noted that this reflects the mean transect within a sample calculated for a number of roots and that individual transects can have very different characteristics.

Fig. C.2 reveals that the mean change in visible porosity with the distance to the root surface has the same trend as the changes of grey values but standard error is generally larger. The visible porosity of the highly compacted rhizospheres in the intermediate bulk densities decreased by up to 30%. For the first depth of the treatment with a bulk density of 1.45 g cm^{-3} the model of Dexter and the extension of (Koebernick et al., 2019) are in line with the data. The fitted model of (Koebernick et al., 2019) resulted in a particle diameter of 1.974 mm, which corresponds to the 2 mm sieving. Therefore this curve can be seen as what one would have expected. However, all other curves show trends like those of the grey values.

Analysing the results separately for roots > 250 µm and those < 250 µm clearly showed that compaction at a distance > 100 µm is more likely to occur for larger root diameters at an intermediate bulk density (Fig. 4.7). The compaction in a distance >250 µm of the samples in the first depth with a bulk density of 1.30 g cm^{-3} is here the exception to the rule. Again, results expressed for visible porosity instead of grey values followed the same trend (Fig. C.3). The comparison of pore size distribution and root diameter classes based on volume (Fig. 4.8) illustrates the fraction of pores occupied by roots. Since roots are treated as pores during segmentation, the root classes must be a subset of the pore classes. The difference between the diameter classes can thus be regarded as empty macropore space, i.e. pores not filled with roots. For the lowest bulk density (1.30 g cm^{-3}) there is still a large share of empty macropores, while in the other treatments only pores smaller than 250 µm were
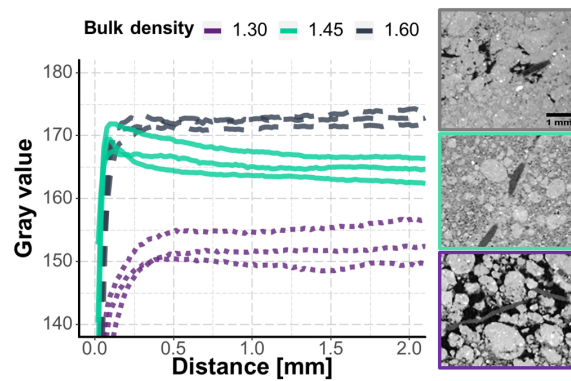
empty. Increasing bulk density led to significant increase in mean root diameters.
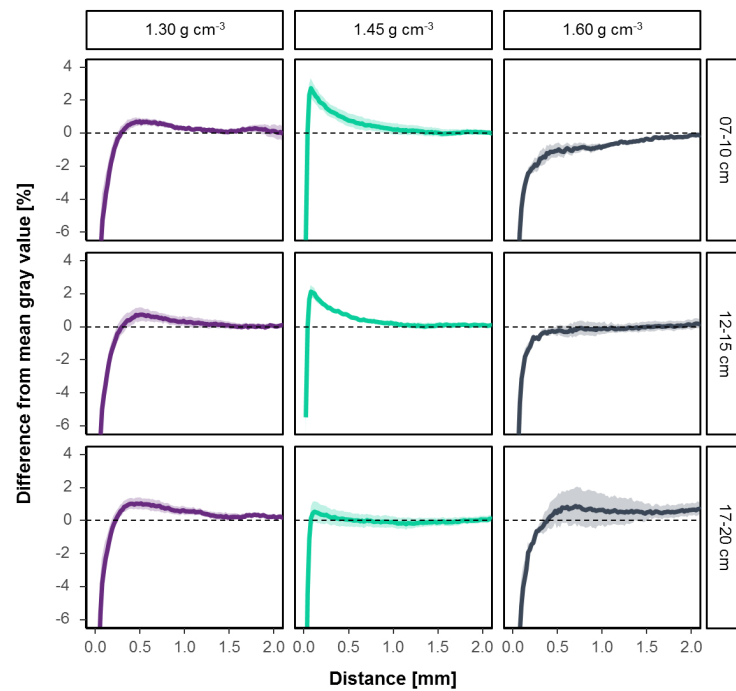
FIGURE 4.6: *Mean change in grey value with the distance to the root surface relative to the mean grey value of a sample. Shadows indicate the standard errors (n = 5).*

FIGURE 4.7: *Mean change in grey value with the distance to fine and coarse roots relative to the mean grey value of a sample. Dotted lines represent the mean changes around roots smaller 250 µm and solid lines these for roots with diameters greater than 250 µm. Shadows indicate the standard errors (n = 5).*
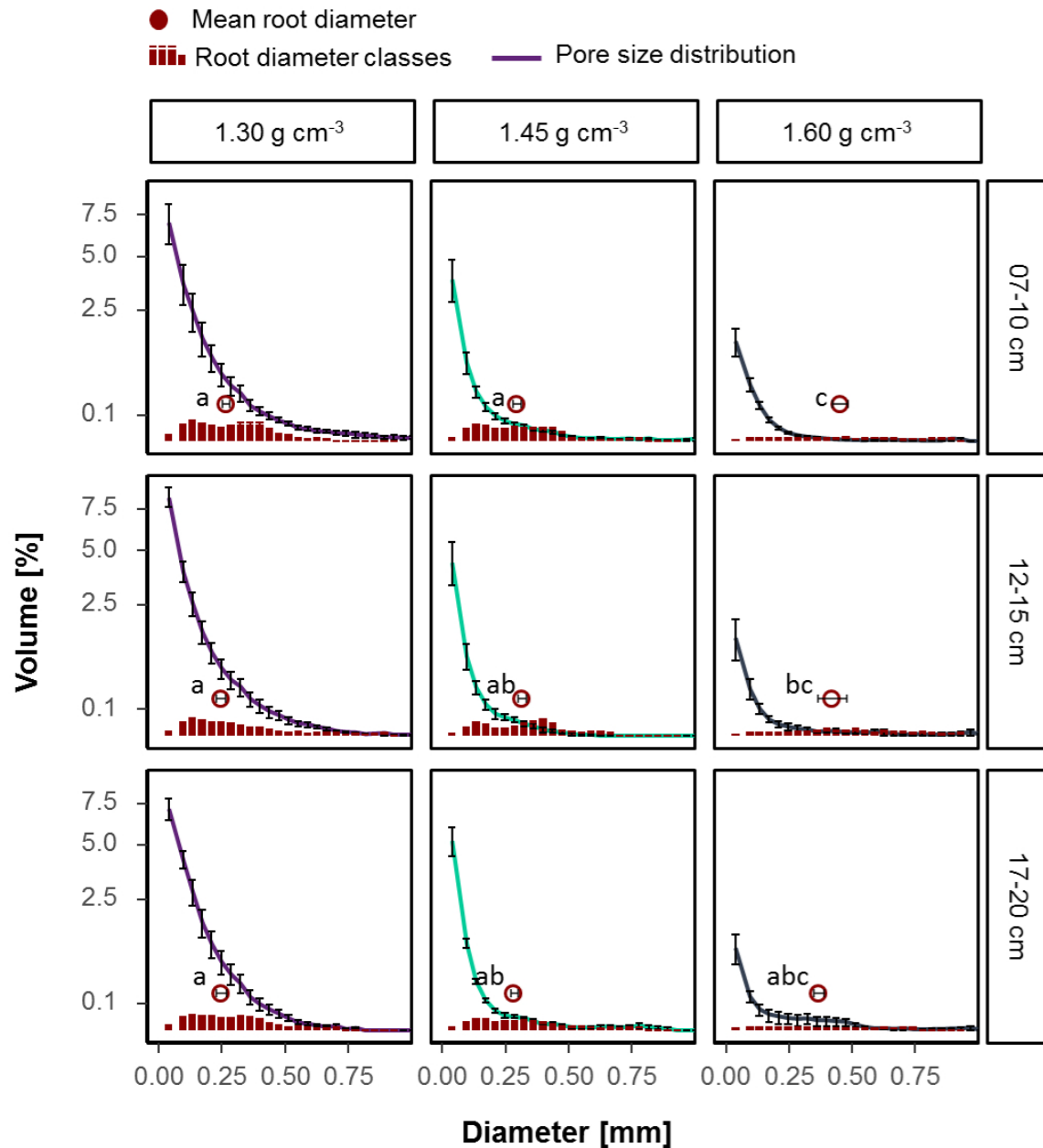
FIGURE 4.8: *Mean volume of root and pore diameter classes for each of the three different treatments (bulk density of 1.30, 1.45 and 1.60 g cm^{-3}) and depth within column (7-10 cm, 12-15 cm, 17-20 cm). Different letters indicate significant differences between mean root diameters (red circles). Whiskers show the standard error (n = 5).*

4.3.2 Chronosequence

The bulk densities in the field (same substrate as pot experiment) were in the range of 1.40-1.61 g cm^{-3} (Tables 4.1, A.2, Pihlap et al., 2019). Visible porosity was at no time less than 5%, in contrast to samples repacked to 1.60 g cm^{-3} in the lab experiment. The Euler number was negative on all fields and especially low in the depth of 40 – 60 cm (Lucas et al., 2019, Fig. 3.7).

While the biopore densities on the chronosequence increased over time, there were only minor changes in the pore size distribution (Lucas et al., 2019, 3.4). This led to a decrease in the fraction of macropores, which are not biopores. Thus, macropores are transformed to

biopores with time (Fig. C.4). There was a trend towards induced compaction of the rhizosphere/biopore wall over time too, especially in the second depth (40 – 60 cm), which was not affected by soil tillage (Fig.C.5). However, the vicinity of the biopores on the 24-year-old field in 40 – 60 cm depth was less compacted compared to samples from the 12-year-old field. Samples of tilled layers (6, 12, and 24 years after reclamation) were characterised by high standard deviations, i.e. some biopores of the samples show a high rate of compaction, while the vicinity of others is highly porous (Fig. C.5).

Thus, samples from 40-60 cm depth of the 1-year and 12-year old field (Fig. 4.9) can be regarded as "endmembers". The 1-year old field, characterised by a high amount of macropores, in relation to biopores, and highly porous biopore walls in contrast to the 12-year old field, containing macropores which are mostly biopores and which show a high compaction rate in their vicinity. For diameter classes >1 mm the biopore volume occasionally exceeded the volume of pores, although the biopores should be a subset of all visible pores. That is because the Tubeness filter also detects biopores filled by smaller particles, while the pore size distribution does not (Fig 4.9, inset).

TABLE 4.1: *Mean values and standard error of bulk density, Euler number (connectivity) and visible porosity of the chronosequence. n = 3 plots. Bulk density data from Pihlap et al. (2019, Table A.2) (mean values per plot for 1-5 and 15-20 cm depth and 41-45 cm), Euler number from Lucas et al. (2019, Fig. 3.7).*

Depth	Field	Bulk density [g cm^{-3}]		Euler number [mm^{-3}]		Visible porosity [Vol-%]	
0 – 20 cm	L0	1.54	$\pm$ 0.00	-8.0	$\pm$ 1.9	6.81	$\pm$ 1.46
	L1	1.61	$\pm$ 0.01	-3.3	$\pm$ 0.4	5.39	$\pm$ 0.55
	L3	1.61	$\pm$ 0.00	-7.8	$\pm$ 2.5	7.59	$\pm$ 0.67
	B6	1.46	$\pm$ 0.02	-5.1	$\pm$ 1.3	11.83	$\pm$ 1.53
	W12	1.5	$\pm$ 0.01	-5.9	$\pm$ 3.2	11.55	$\pm$ 3.73
	W24	1.55	$\pm$ 0.02	-6.8	$\pm$ 1.2	1 2.17	$\pm$ 3.45
40 – 60 cm	L1	1.66	$\pm$ 0.02	-18.9	$\pm$ 10.8	13.26	$\pm$ 3.04
	L3	1.4	$\pm$ 0.02	-14.4	$\pm$ 7.1	9.61	$\pm$ 2.18
	B6	1.63	$\pm$ 0.03	-13.3	$\pm$ 0.6	10.43	$\pm$ 1.85
	W12	1.5	$\pm$ 0.04	-12.4	$\pm$ 3.0	10.44	$\pm$ 2.17
	W24	1.52	$\pm$ 0.02	-12.5	$\pm$ 7.1	10.48	$\pm$ 3.37
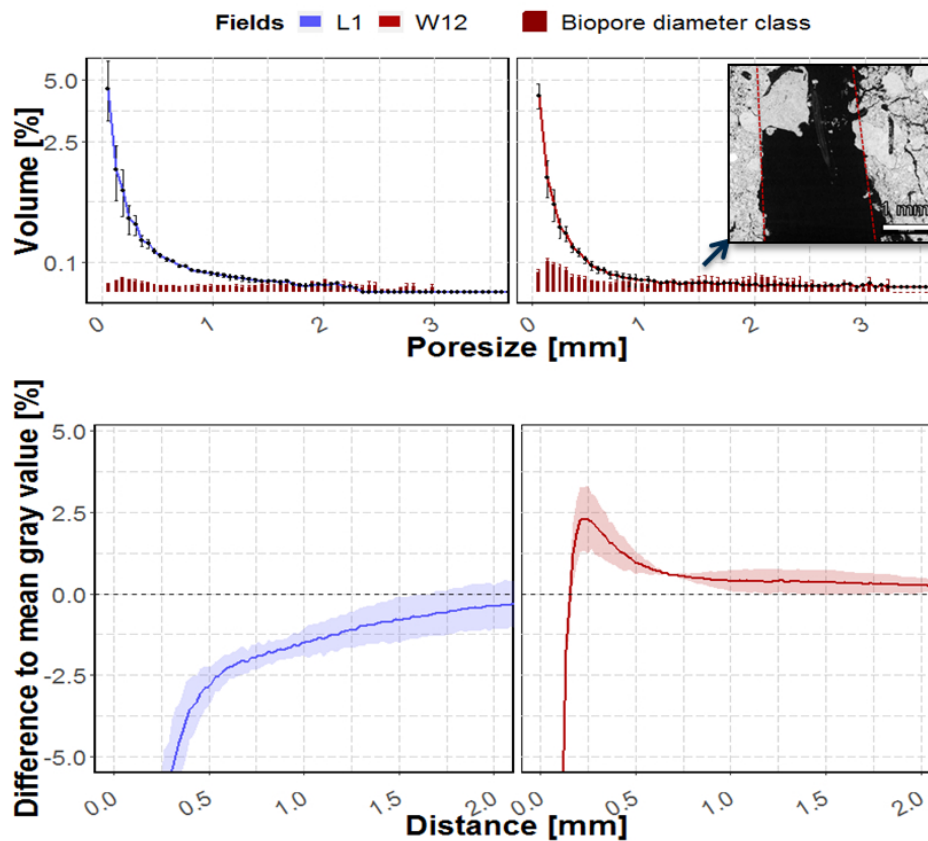
FIGURE 4.9: *Mean volume of biopore and pore diameter classes (upper graphs) and change in grey value with the distance to the biopore surface relative to the mean grey value of a sample (lower part). Samples are taken on a 1 year old field (blue) and a 12 year old field in 40–60 cm depth on the chronosequence. Inset shows a filled biopore and how the tubeness filter would assign the borders of this biopore (red line). Shadows and whiskers indicate the standard deviation (n = 3 plots, which in turn each are determined by the result of 9 μCT scans).*

4.4 Discussion

4.4.1 The effect of soil compaction on plant roots

In line with previous work (Tracy et al., 2011) increasing bulk density decreased root length densities and plant growth above ground and led to an increase in mean root diameter (Fig. 4.8). The increase in bulk density to 1.60 g cm^{-3} at the given water content lead to mechanical impedance that was too high for the maize roots to elongate. The elongation of individual roots is mostly limited by the mechanical impedance of the soil (Bengough et al., 2011; Eavis, 1972; Jin et al., 2013; Valentine et al., 2012). The decrease in root length density increased the Euclidean distances between roots (Fig. C.1). Therefore, plants of this treatment were not able to cover their nutrient demand, illustrated for phosphorus in the supplement (Table C.1).

However, bulk density alone is not adequate to describe changes in soil structure (Pihlap et al., 2019; Rabot et al., 2018). Air-filled porosity was calculated to be more than 10% for the pot experiment, which is regarded as a critical value for plant growth. However, an increase in compaction can result in much smaller equivalent pore diameters. This affects air permeability, which is correlated with pore continuity and pore sizes (Lipiec et al., 2003). The fact that high bulk densities (>1.60 g cm^{-3}) did not limit root growth in the field (Lucas
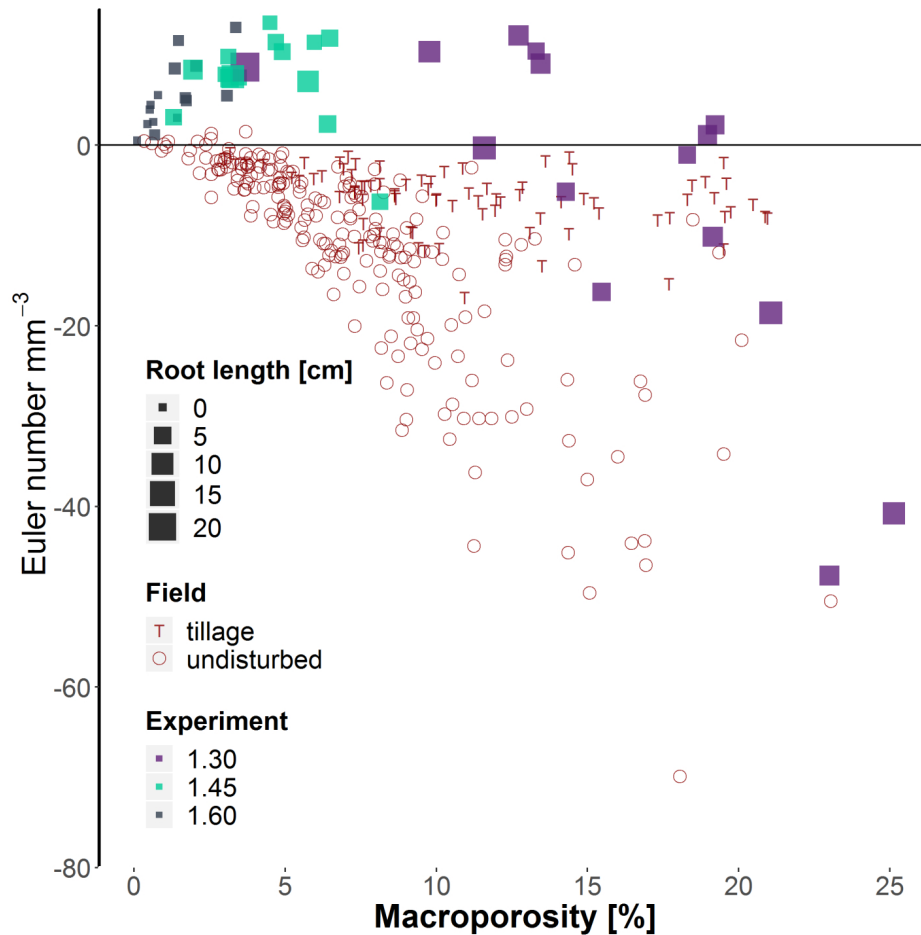
FIGURE 4.10: *Relationship between connectivity (Euler Number) and visible porosity for 3 cm Ø field samples (red) and the different treatments of the Lab experiment. Low values of the Euler Number reveal a high amount of connections/redundant loops in the pore system (>76 µm). The root length densities of the lab experiment are represented by the size of the squares.*

et al., 2019, Table 3.2), but in the repacked soil, may be explained by a completely different pore structure created during packing of the soil columns. A highly connected pore system (especially macropores > root diameter) enables roots to bypass zones of high mechanical impedance in the field (Bengough et al., 2006; Colombi et al., 2017; Passioura, 1991; Stirzaker et al., 1996; White et al., 2010), but did not exist in the pots. The only roots that could grow in the dense samples in the pot experiment were therefore found in areas with macropores that were not compacted during packing (Fig. 4.4).

Under wet conditions, penetration resistance of the soil decreases, but oxygen supply in these dense soil can become limiting (Colombi et al., 2019). The connectivity (Euler number) of the macropores is therefore a key parameter defining plant growth. Fig. 4.10 reveals strong differences in the connectivity of field samples and the lab experiment. All field samples, especially those, which are not directly affected by tillage, are characterised by a high number of connected macropores (negative values). In contrast, repacked soil samples show much higher Euler numbers at the same visible porosity. Soil aeration and the probability of growing roots to find existing macropores was therefore especially low for the dense repacked soil samples in the pot experiment, characterised by a low number of unconnected macropores. Our findings highlight therefore the importance of connected macropores for plant growth by enabling easier access to deeper soil layers and thus reducing the impact of soil compaction.

4.4.2   Root induced compaction

Our work reconciles contradictory results from previous studies where on the one hand an increase in porosity in the rhizosphere was described (Feeney et al., 2006; Helliwell et al., 2017; Koebernick et al., 2017; Whalley et al., 2005) or root induced compaction was measured (Aravena et al., 2011; Bruand et al., 1996; Koebernick et al., 2019). These contrasting results can be integrated by merging (a) the mechanistic physical effect of root growing into the soil pushing particles to the side and inducing compaction by creation of new pores, and (b) plant interaction with existing soil pore structure, i.e. root growing in existing macropores with larger diameters than the root itself (Fig. 4.11). This general interaction between growing roots and soil structure should not be seen as the only process that influences root-induced compaction. However, our results showed that the initial soil structure is an important factor in predicting root-induced compaction alongside others as soil texture, drying cycles and plant species (Helliwell et al., 2019).
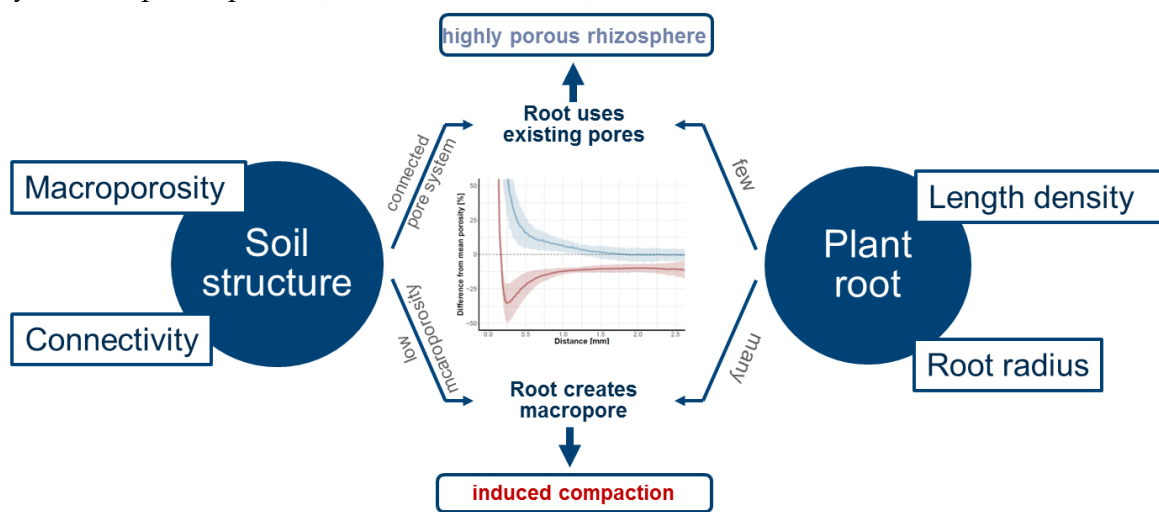
FIGURE 4.11: *Mechanisms of root induced compaction.*

Although we partly include sub-resolution pores through the analysis of grey values, it can be assumed that not all changes, e.g. induced by root hairs (Koebernick et al., 2017), are covered by our analyses. In all samples we found an increased porosity directly next to the exodermis (distance <100 μm). These findings are in line with various studies with high resolution (Helliwell et al., 2017; Helliwell et al., 2019; Koebernick et al., 2019). Helliwell et al. (2019) observed changes in porosity with distance to the root of three different plants in a loamy sand and a clay loam with bulk densities of 1.20 and 1.50 g cm^{-3}. They found a significant interaction of changes in porosity with bulk density, plant and texture. They mainly accounted cracks formed by shrinking and swelling processes and gap formation for the increase of porosity in the direct vicinity of the root exodermis. A visual assessment of our images revealed only a low number of this cracks typically formed radially around roots. This processes therefore only played a minor role in the increased porosity around roots. In addition, Koebernick et al. (2019) found no significant influence of moisture conditions (wet vs wet and dry) on pore structure around roots. The fitted model of Koebernick et al. (2019) resulted in a particle size of around 2 mm which is in line with our sieving procedure. Therefore we can assign the increased porosity directly next to the exodermis (distance <100 μm) to the surface/wall effect described in Koebernick et al. (2019).

However, samples of 1.30 g cm^{-3} showed a decreased porosity up to a distance of around 250 μm and the rate of compaction decreased with depth in samples from the intermediate bulk density (Fig. 4.6). There was also a tendency of less compacted rhizospheres in the

high-density samples up to a distance of 2 mm (Fig. 4.7). This effect was observed beyond the 'surface/wall effect' described above. These samples only differ by the ratio of root volume to visible porosity (Fig. 4.8), i.e. if there are enough macropores of the appropriate size available in relation to root length density and their diameter class distribution, roots do not necessarily need to create new pores. These findings are in line with research on root soil contact, i.e. root-soil contact decreases if a connected macropore system exists (Colombi et al., 2017; Kooistra et al., 1992; Schmidt et al., 2012).

Only for intermediate bulk density along with relative high root length densities compaction of the rhizosphere as described by Dexter (1987) was observed. The decreases of visible porosity (Fig. C.2) by more than 25% is in line with findings of Bruand et al. (1996), who observe a reduced porosity of $22 - 24\%$ around maize roots. If we transfer all these findings to the field, we can suggest following processes, which led to the differences in compaction around biopores in the field:

1. Directly after reclamation the roots of Lucerne found sufficient macropores and therefore the rhizosphere of the created biopores remained highly porous and no changes in pore size distribution in $40 - 60$ cm were observed. At later time points roots could not find sufficient empty connected macropores which led to an increase in root-induced compaction over time (Fig. C.4).

2. Due to tillage in the topsoil on the 6, 12 and 24 year old fields some biopores were destroyed, but visible porosity increased. Roots of the current crop therefore could use these new available macropores created by tillage, which facilitated a more porous rhizosphere compared to the bulk soil underneath the plough layer. However, Lucas et al. (2019) also found that on tilled fields a lower amount of connections occurred (Fig. 3.7). If roots therefore grow into existing dense clods, they needed to create new channels while compacting the surrounding soil. These two processes may have led to the high standard deviation in this depth (Fig. C.5).

The compaction was mainly visible around roots >250 μm in the lap experiment (Fig. 7), which is in line with the model of Dexter (1987). In addition, small roots (<250 μm) were more likely to find existing pores of the appropriate size, since sufficient pores larger than the root diameter were available (Fig. 4.8). This is in line with Bodner et al. (2014) who showed that especially plants with coarse root types have increase macropore volume while roots of fine rooting types only have an impact on micropores, since they can use existing macropores (Bodner et al., 2014).

However, the resulting densities around coarse and fine roots in the samples of the lowest bulk density showed a contradictory result. The only explanation for this is that fine roots in these samples predominantly grew into more dense areas. Potentially such a behavior could have been triggered by secondary factors such as water or nutrient availability. Large pores are drained first during drying, this can induce laterals to form resulting in so called 'hydropatterning' Orosa-Puente et al. (2018).

These differences in rhizosphere physics cause dramatic differences in hydraulic properties of the biopore walls (Aravena et al., 2011, 2014). A high density, such as in the rhizosphere of roots in 1.45 g cm^{-3} samples, leads to high mechanical resistance. The maximum density (grey values) in the rhizosphere of these samples is similar to that of the bulk soil in the 1.60 g cm^{-3} samples (Fig. 4.5). Since the density of 1.60 g cm^{-3} at the given water level already strongly limited root elongation it is likely that roots can also not elongate into the compacted rhizosphere of roots in 1.45 g cm^{-3} treatment. If we transfer this to the field, roots growing into biopores on the 12-year old soil, with similarly compacted walls, may be trapped. This would be in line with findings that growing roots can be trapped within biopores (Stirzaker et al., 1996), especially in more compacted soil layers (Kautz et

al., 2013). Lucas et al. (2019) calculated the Euclidean distances between the biopores and showed that with the high biopore length densities on the 12-year old field, the distance between biopores is typically around 2 – 3 mm (Fig. 3.10). If we consider a compacted area which reaches up to 1 mm into soil, this means one dense zone borders on the next. A new root can therefore only grow within the biopore or right in the middle of two biopores. The later would probably lead to destruction of the old biopores since the new root also align the particles radial up to 1 mm distance. This all could be the possible explanation of the maximum of biopore densities found by Lucas et al. (2019) that reached a plateau already half-way through the chronosequence (Fig. 3.9).

Chapter 5

Pore connectivity across scales and resolutions
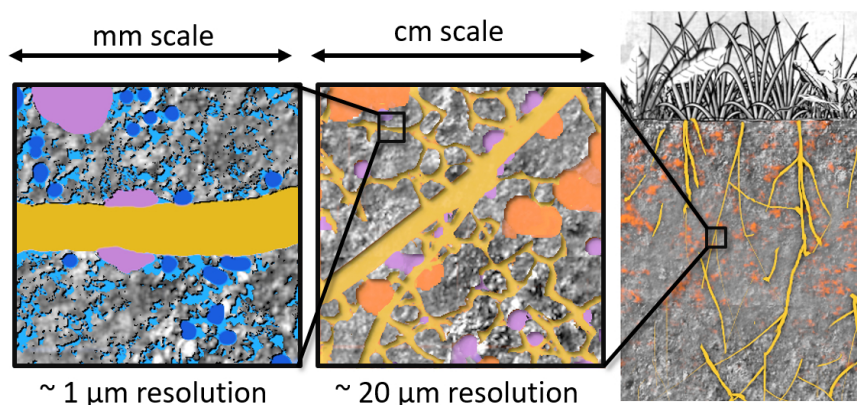
Connectivity is one of the most important parameters to quantify pore structure and link it to soil functions. One of the great challenges in quantifying connectivity with X-ray microtomography (X-ray μCT) is that high resolution as required for small pores can only be achieved in small samples in which the connectivity of larger pores can no longer be quantified in a meaningful way. The objective of this study was to investigate the changes in pore connectivity with changing samples size covering a range of analysed pore diameters of more than three orders of magnitude. With this we wanted to address whether pore types formed by different processes in an agricultural chronosequence leave characteristic traces in certain connectivity metrics. The Euler number, χ and the connection probability of two random points within the pore system, i.e. the Γ-indicator, were determined as a function of minimum pore diameter. The results show that characteristic signatures of certain pore types overlap with scale artefacts in the connectivity functions. The Γ-indicator, gives highly biased information in small samples. Therefore, we developed a new method for a joint-Γ-curve that merges information from three samples sizes. However, χ does not require such a scale fusion. It can be used to define characteristic size ranges for pore types and is very sensitive to the occurrence of bottle-necks. Our findings suggest a joint evaluation of both connectivity metrics to disentangle different pore types with χ and to identify the contribution of different pore types to the overall pore connectivity with Γ. This evaluation on the chronosequence showed that biopores mainly connect pores of diameters between 0.5 and 0.1 mm. This was not coupled with an increase in pore volume. In contrast, tillage lead to a shift of pores of diameter >0.05 mm towards pores of diameter >0.20 mm and thus increased connectivity of pores >0.20 mm. This work underlines the importance to account for the scale dependence of connectivity measures and provides a methodological approach for doing so.

5.1   Introduction

Important soil functions are defined or influenced by soil structure. Soil properties and processes such as hydraulic conductivity, gas exchange and water retention as well as erosion are controlled by the spatial structure of pores and solid (Bronick et al., 2005; Rabot et al., 2018). Besides porosity and pore size distribution one of the most important parameters for soil functions is pore connectivity (Rabot et al., 2018). It affects both air permeability (Paradelo et al., 2016) and saturated hydraulic conductivity (Luo et al., 2010; Sandin et al., 2017; Zhang et al., 2019). Moreover, the connectivity of different pore size classes is also essential for soil as habitat for a myriad of organisms and for the accessibility of SOC for these organisms and their aeration status (Kravchenko et al., 2015; Negassa et al., 2015; Rabbi et al., 2016).

Digital imaging techniques, such as X-ray microtomography (X-ray μCT), have developed rapidly in recent years and are used to visualise and quantify the 3D pore space. This provides an impressive insight into the complexity of soil structure. It shows how pore structure is shaped by soil management or biological activity (Helliwell et al., 2013; Lucas et al., 2019, Chapter 3), how different characteristic pores or pore types form the overall soil architecture (Pagliai et al., 2002) and suggests a hierarchy of pores of different size and origin (Elliott et al., 1998). Pores can be divided into textural pores, defined by the arrangement of soil primary particles and larger structural pores. The latter is mainly shaped by biological activity and soil cultivation. A challenge in analysing the resulting complex structure is that pores of various sizes, shapes and origin cannot be disentangled by simple metrics. Currently, there are two promising approaches to tackle this problem:

1. Identification and segmentation of structural pores by their characteristic shape. This differentiation enables to link pores to their processes of formation. One example are those structural pores created by plants, which form a dense network of cylindrically shaped pores (biopores) (Leue et al., 2019; Lucas et al., 2019; Zhang et al., 2018). Also different tillage system lead to characteristically formed pores (Pires et al., 2019; Pires et al., 2017).

2. Using a hierarchical sampling scheme and combining the information of images from different sample sizes and resolution to derive a complete description of multi-scale heterogeneity. (Bacq-Labreuil et al., 2018; Dal Ferro et al., 2014; Karsanina et al., 2018; Leuther et al., 2019; Schlüter et al., 2018b, 2011b; Vogel et al., 2010). By merging the pore size distribution (PSD) of several sample sizes (Vogel et al., 2010) a joint pore size distribution can be created while increasing the size range of visible porosity (Φ-vis).

These two approaches lead to the open question whether pore connectivity metrics are sensible enough to disentangle different pore types across different scales and whether a scale fusion of these metrics is possible and helpful as has been demonstrated for the PSD. We calculated connectivity for different pore sizes of an existing X-ray μCT data set of a lignite mining reclamation site (Garzweiler, Germany) from Lucas et al. (2019). The data set consists of around 500 samples of different diameters (10 cm, 3 cm and 0.7 cm) scanned at different resolutions (57 μm, 19 μm and 5 μm). The development of the pore network during the chronosequence was mainly affected by tillage and by the formation of biopores reflected by a steady increase of biopore density over time. For this study we pooled samples with vastly different macroporosities, partly due to inherent differences in bulk density directly after reclamation and partly due to different age and type of management. The rationale for this pooling is that the processes which shape characteristic pore types are universal, e.g. biopores look the same in all samples. The samples only differ vastly in the volume proportion of these characteristic pore types. The objective of this paper is to find generally

applicable features in connectivity measures that can be used to distinguish pore types despite this large variability. Thus the data set covering multiple scales and structures provides an excellent basis to investigate how measures of connectivity as a function of pore sizes can be used to disentangle different pore types and to characterise the entire pore system with regard to its formation.

5.1.1 Theoretical consideration

There are several mathematical approaches to characterise 3D connectivity in porous media (Renard et al., 2013). We here focus on two different connectivity metrics, which are often used in soil hydrology: (i) the Euler number χ, a topological measure from integral geometry and (ii) the Γ-indicator or connection probability based on pore cluster size distribution. The metric χ is the result of the total number of unconnected clusters (N) minus the total number of redundant loops (C) plus the total number of closed cavities (H) (Vogel, 1997). The latter are typically negligible in soil pore systems (Vogel, 2002):

$$\chi = N - C + H \tag{5.1}$$

When neglecting H, χ becomes negative if the number of redundant connections exceeds the number of unconnected clusters and positive if it is the other way round. The χ-number is a global metric that can be efficiently calculated from the frequency of local pixel configurations within 2x2x2 voxel neighbourhoods (Renard et al., 2013; Vogel, 2002). It is not sensitive to the size of connected clusters. Thus, a negative χ does not necessarily mean that there is a long-range connection through a connected pore cluster. In contrast, the dimensionless Γ-indicator is sensitive for long-range connectivity, i.e. it is higher if a large fraction of the porosity belongs to a large, connected cluster. It is obtained from calculating the second moment of cluster size distribution (Renard et al., 2013):

$$\Gamma_p = \frac{1}{N_p^2} \sum_{k=1}^{N_i} n_k^2 \tag{5.2}$$

where N_p is the number of all pore voxels p, N_i the number of all clusters and nk the number of pore voxels in cluster k. Γ reflects the probability of two randomly chosen pore voxels to belong to the same pore cluster and is highly affected by the largest pore cluster n_k (Jarvis et al., 2017). It can range from 0 (many unconnected clusters) to 1, when all pore voxels belong to a single connected cluster. The Γ-indicator typically increases with increasing porosity in an s-shaped curve without a clear percolation threshold (Renard et al., 2013). The slope of this curve reflects how connected pore clusters vary in size, i.e. it is a measure of the variability of the percolation among samples of the data set (Renard et al., 2013). We here use Φ-vis and the slope of this curve at the inflection point to characterise connectivity. In summary, Γ reflects the probability to find a continuous path through the pore system and χ reflects the number of internal connections without considering their lengths (Herring et al., 2015).

There is typically a fixed factor of 1000-2000 between CT image resolution and sample size (Rabot et al., 2018). This means that on the one hand high resolution can only be obtained within small samples, but on the other hand this small volumes cannot be regarded as representative elementary volume (REV) with respect to soil structure anymore (Page-Dumroese et al., 1999; Timm et al., 2005). The range of scales that is captured representatively for a given sample size is further reduced by the fact that (1) pore objects typically need to have a diameter larger than the actual voxel resolution and that (2) the sample volume must be much larger than the typically size of pore objects to detect connectivity

features. Consequently, the size range of objects which can be quantified based on a given sample size is very narrow (i.e. the factor between smallest and largest objects is about 10 at most). However, it can be extended substantially when combining pore structure information obtained from different sample sizes scanned at different resolutions (Vogel et al., 2010). We calculate the connection probability, Γ, and the Euler number, χ, as a function of pore sizes based on the maximum inscribed sphere method. This allows us to continuously add smaller pores starting from the largest unconnected pores and ending at pore diameters slightly larger than the voxel resolution. This can be done for samples of different size and resolution and allows to investigate how different pore sizes contribute to the connectivity of the pore space (Vogel, 2002).

Based on the definitions of Γ and χ, different scaling behavior of the two metrics can be expected when changing sample size and resolution. Subsampling of an intact soil core cuts off long-distance connections, which leads to an underestimation of Γ. In the following we will refer to this scaling artefact as the "REV artefact" since the sample size falls below a representative elementary volume in terms of pore connectivity. In addition, we assume that the connectivity metrics are very sensitive to the total volume of investigated pores. This decreases considerably when only the largest pores are considered for a given sample size by removing smaller pores with the maximum inscribed sphere method. In this case, the connectivity metrics are based on very limited information up to the point where only one isolated pore remains and Γ and χ approach one. In the following, we will refer to this scaling artifact as a "low-count artifact". Small scale features contribute to χ in the same way as large scale features, but small scale features are typically much more abundant and are captured more representatively. Reducing sample size while increasing resolution continuously adds smaller pores for which χ is highly sensitive. Accordingly, a continuous change of χ is expected. Thus, with regard to the open question, we hypothesise that scale fusion while analysing connectivity across different sample sizes is only necessary for Γ.

5.2   Materials and methods

A description of the reclamation procedure and field management together with a detailed site characterisation of the space-for-time chronosequence can be found in Pihlap et al. (2019, Chapter 2.2). In short, an 20-metre-thick layer of loess including about 2.2 m of developed Luvisol is excavated, thoroughly mixed and deposited as an at least 2 m thick layer of new topsoil. In this way, reclaimed soils developed from the same loess substrate characterized by a loess material with high $CaCO_3$ content and weakly alkaline pH. Crop rotation consists of three years alfalfa (*Medicago sativa*) in a pioneering phase without any mechanical disturbances. Afterwards the fields are ploughed and the crop rotation consists of *Triticum aestivum* L. (wheat) and *Hordeum vulgare* L. (barley), *Brassica napus* L. (rapeseed) and *Zea mays* L. (maize) in the years after the pioneering phase. Three intact soil cores were taken on three plots from fields with 0 (directly after first seeding), 1, 3, 6, 12 and 24 years in two different depth (0-20 cm and 40 – 60 cm) as described in Lucas et al. (2019, Chapter 3.2). The field 0 was not sampled in the second depth. The 99 soil cores (10 cm Ø, 20 cm height, 1500 cm^3 volume) were scanned at a resolution of 57 μm with an X-ray microtomograph (X-Tek XCT 225, Nikon Metrology). The obtained images are used to describe the pores larger than 200 μm assuming that pores smaller than four voxels in diameter cannot be properly captured and are very sensitive to the choices made during image processing (Fig. 5.1). Subsamples of 3 cm Ø, 3 cm height, 21 cm^3 volume (3 per core, 297 in total) and 0.7 cm Ø, 1 cm height, 0.6 cm^3 (1 per core, 99 in total) were taken to enhance the resolution to 19 μm and 5 μm respectively. Thus, the pore sizes of ∼50-200 μm could be described with the 3 cm samples and pore size from 10-50 μm were described using the 0.7 cm samples. Images

of all sample sizes were processed and segmented into binary images of visible pores and matrix voxels and pore size distribution was computed as described by Lucas et al. (2019, Chapter 3.2) using Fiji/ImageJ (Schindelin et al., 2012) and associated plugins (Legland et al., 2016; Ollion et al., 2013). Subsamples of 3 cm Ø were also used to separate all cylindrical pores (biopores) from all visible pores by an shape-based tubeness-algorithm in Fiji (Version 1.3.3) as described in Lucas et al. (2019, Chapter 3.2). Biopore length was not determined for the other sample sizes, because either the sample volume was too small or the voxel resolution too coarse to capture them representatively. A joint pore size distribution of the different sample sizes was created by considering the maximum frequency of all three pore size distribution at each pore diameter (Vogel et al., 2010) as shown in Figure 5.1B (inset). The scale transitions, i.e., the pore diameters at which the frequency distributions cross, varied between 0.04 mm and 0.07 mm (for Ø 0.7 cm and 3 cm) and 0.19 mm and 0.304 mm (for Ø 3 cm and 10 cm). A joint, cumulative pore size distribution (PSD, Fig. 5.1B) is constructed from this joint frequency distribution by integration, starting with the largest pore diameters (from right to left).

In anaology to Φ-vis (Fig. 5.1B), Γ and χ were calculated and for pores larger than a certain pore diameter g at all resolutions using the MorphoLibJ plugin (Legland et al., 2016) in Fiji, which is based on the maximum inscribed sphere method. In the following we will refer to this pore size threshold as the "minimum pore diameter". For each sample size only pores larger than 4 voxels in diameter were considered to minimise misclassification and noise, since χ is highly sensitive to such errors (Armstrong et al., 2019). To compare the results from different sample sizes we normalised the χ-numbers by the sample volume, which in the following is referred to as χ-density [cm^{-3}].

5.2.1 Measuring water retention

Additional undisturbed samples (10 cm ×10 cm height, 1 cylindrical soil cores per plot and depth) were taken to measure the water retention curve using the HYPROP evaporation method (Hydraulic Property Analyzer; METER former UGT, Germany). In this way the experimentally obtained PSD derived from the water retention curves can be used to validate the image derived PSD after scale fusion. The soil cores were saturated with water prior to evaporation. The gravimetrically measured air contents were analysed without parametric model adaptation to compare water retention data with image derived pore size distributions. The air-filled porosity was calculated by subtracting the water content at a given matrix potential from the water content at saturation. In the following, only the retention curves of the ploughed fields (3, 6 and 12 year after reclamation) are presented.

5.2.2 Statistics

To evaluate the interaction of ϕ-vis with χ a linear model was fitted using R (version 3.5.3). Due to S-shape of Γ-indicator as a function of ϕ-vis a logistic function was fitted with a non-linear least squares using a Gauss-Newton algorithm in R:

$$\Gamma(\phi) = \frac{a}{1 + e^{-k(\phi - \phi i)}} \tag{5.3}$$

Where a is the asymptote, k the growth factor, $\phi i'$ porosity ϕ at the inflexion / midpoint. Therefore the slope at the midpoint is:

$$\left. \frac{df}{d\phi} \right|_{\phi_i} = a\frac{k}{4} \tag{5.4}$$

The assumptions of the different models were visually assessed by evaluating plots of residuals (residuals vs residuals, QQ plot of standardised residuals). For the linear models also R^2 as a measures of goodness of fit is given.
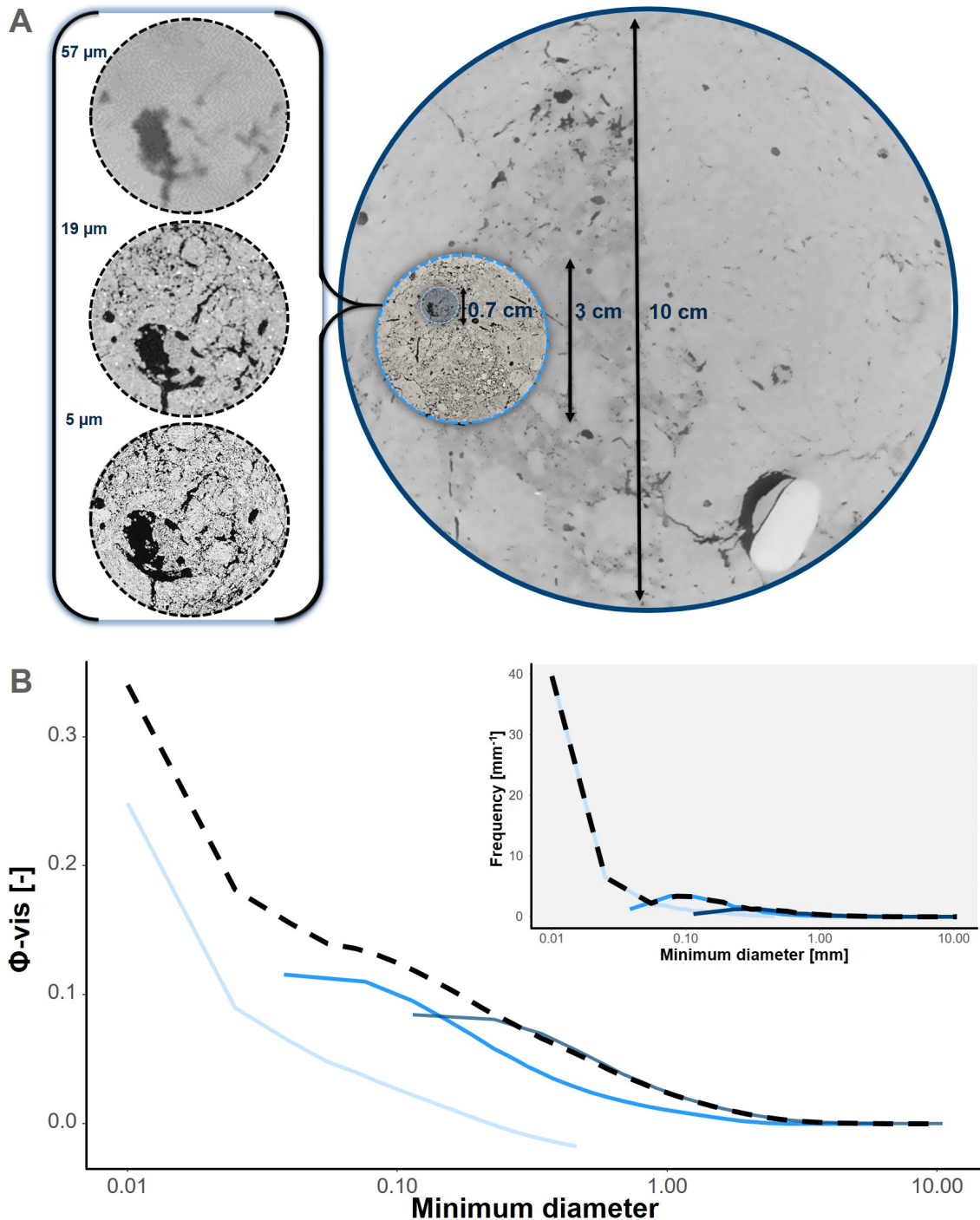
FIGURE 5.1: *X-ray µCT derived pore size distribution within different sample sizes. A: A cross section through one sample at three sample sizes to illustrate the relation in size (right) and the change in resolution (left). B: Cumulative pore size distribution of the 12 year old field in 0 − 20 cm depth (dashed line) and corresponding distribution of the different sample sizes (decreasing intensity of blue = decreasing sample size). Inset shows the frequency distribution of the corresponding curves. The intersection points reflected the transition between two sample sizes to calculate the joint, cumulative distribution.*

5.3   Results

5.3.1   3.1 General behaviour of Euler number and Γ-indicator

The χ-density across the minimum pore diameter reveals a huge standard deviation, which is related to a high variability of Φ-vis in the pooled data set (Fig. 5.2A). Moreover, three salient features emerge. (1) The χ-density always decreased linearly with increasing Φ-vis at any given minimum pore diameter. The slope of these linear trends are reported in Table D.1. (2) The addition of certain pore size classes, represented by the minimum pore diameters of 0.11 mm, 0.05 and 0.03 mm caused a vast increase towards positive χ-densities. Apparently, a new pore type must have emerged at this pore size that is still isolated at this diameter but likely to reconnect at the next smaller pore size class. (3). This gain in redundant connections was most dramatic when the smallest considered pore diameter of 0.02 mm was added, which dramatically improved pore network connectivity, as shown in Figure 5.2C. The observations (2) and (3) became even more salient when showing average values of Φ-vis and χ as discussed below. The scatterplot of Γ and Φ-vis exhibits two major patterns (Fig. 5.2B). (1) The logistic relationship between both metric seems to hold except for the largest pore size classes (<1 mm), which are affected by the low count artefact as discussed below. (2) The same level of clustering represented by Γ was reached at very different Φ-vis for different minimum pore diameters. The average Φ-vis and slope f'(Γ/Φ-vis) at the inflexion point are reported in Table D.1. Obviously the smallest pores were distributed very uniformly in space (Fig. 5.2B) and therefore it took a rather high Φ-vis to reach good long range connectivity through that disperse network (Φ-vis at the inflexion point: 12.2%). In contrast, Φ-vis was low (5.8% and 7.2%) at the inflexion point for minimum pore diameters of 0.11 mm and 0.23 mm, respectively, with a high slope at the inflection. Thus, these pores must be shaped in a way that facilitates long range connectivity with only little Φ-vis.
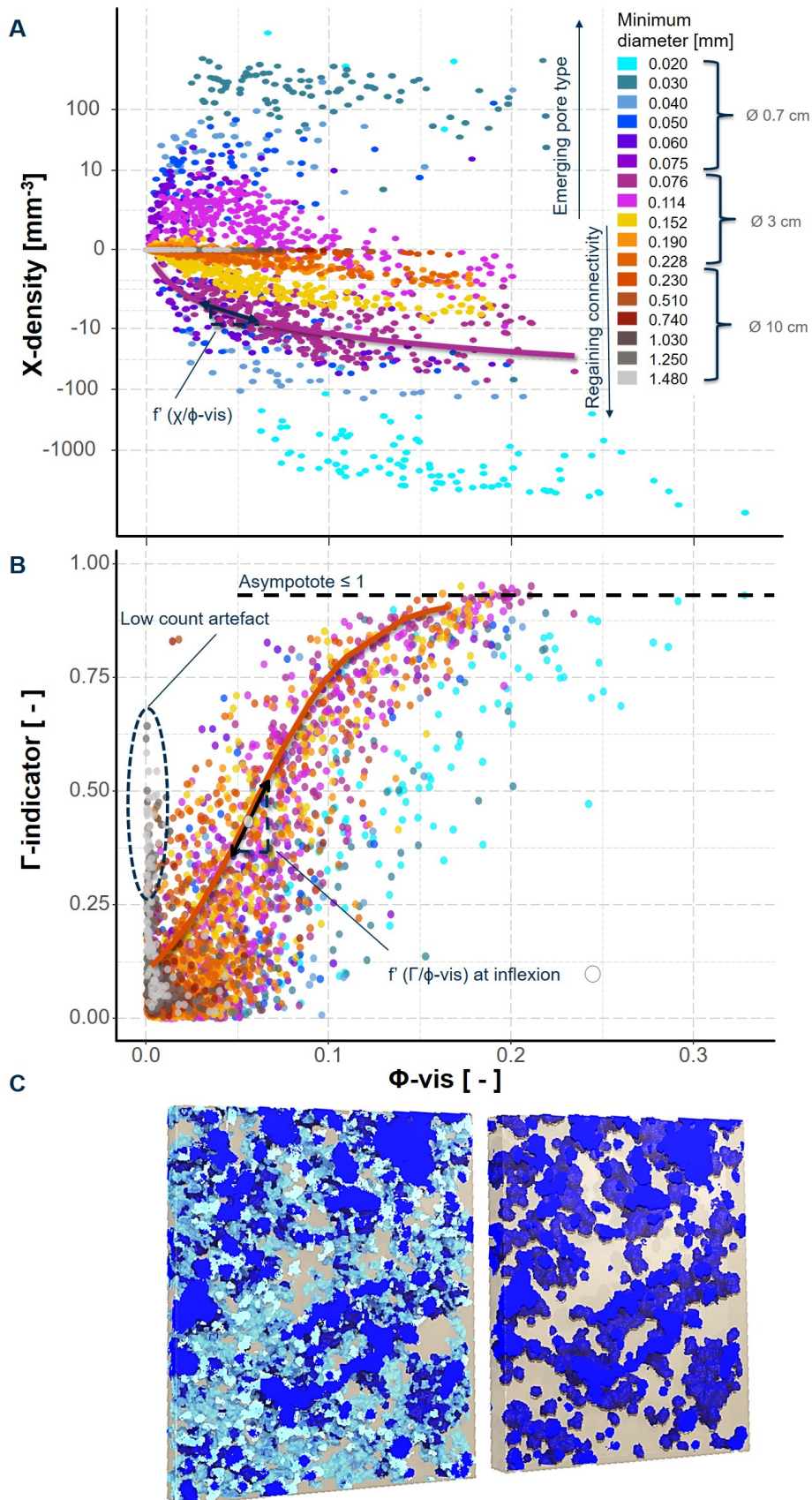
FIGURE 5.2: *Scatterplots for χ-density (A) and Γ-indicator (B) as a function of Φ-vis for all minimum pore diameters. Plotted curves are example for a linear model for χ-density (distorted by the non-linear axis) and a logistic model for the Γ-indicator. The image C shows a 125 μm thick section from a 7 mm sample (12 year old field, 40-60 cm depth). The two parts of the same image section reveal how pores of > 30 μm diameter (dark blue) get connected at various locations through pores <30 μm diameter (light blue), thus causing a shift towards more negative χ-densities.*

5.3.2 Secondary pores: Biopores

The pore shape effect on the Γ-indicator becomes obvious when only the extracted network of biopores is analysed. This is demonstrated for the two fields 3 and 12 years after reclamation in a depth of 40-60 cm, which had the same pore size distribution (Fig. D.3) but very different biopore volumes. The total biopore volume was more than doubled on the 12 year old field (Fig. 5.3A). The highest contribution to total biopore length density occurs in a pore diameter range of 0.1-0.5 mm.

The steady increase in biopore length density with decreasing pore diameter did not cause a steady increase in Γ. The mean values of Γ jumped towards lower Γ-indicators at the transition from one sample size to the next smaller sample size (Fig. 5.3B, Table D.1). This indicates, that large pore clusters were disrupted in the smaller sample size due to the "REV artefact". In order to get a continuous, smooth trajectory at the scale transition, corrected for the REV-artefact, we suggest a joint-Γ-curve: Large samples contain a well-connected pore network that is composed of long-reaching large pores and short-reaching smaller pores. When looking at the same pore size threshold in smaller samples at higher resolution the larger pores are not captured representatively due to the smaller volume. This inevitably leads to lower Γ-indicators and, thus, to a bias with respect to the entire pore system. In contrast, the change in Γ-indicators for changing pore size thresholds within a single sample size is assumed to be not biased. We therefore calculated the joint-Γ-curve by correcting for the offset: For the largest pores of a subsample, we took the corresponding Γ-value of the larger sample and then considered only the slope between Γ-indicators within each subsample. Interestingly, the joint-Γ-curve adds up to about one (Fig 5.3C).

The joint-Γ-curve reveals different trends between the 3 and 12-year-old fields in the typical biopore diameter range of 0.1-0.5 mm (Fig. 5.3C). The values of the 3-year field were almost constant at Γ = 0.2 in that range as the biopore volume is too low for the emergence of well connected biopore cluster. The values of the 12-year field increased towards Γ = 0.4 when adding the entire range of typical pore diameters (>0.1 mm) as the critical volume fraction for a well connected macropore cluster decreased to 7% (Table D.1). In other words, only approx. 1 Vol-% of the elongated shaped biopores lead to good long-range connectivity of the pore space at rather low volume fractions. The most significant contribution to long-range connectivity came from biopore diameters around 0.2 mm and decreases towards smaller biopore diameters (Fig. D.4)
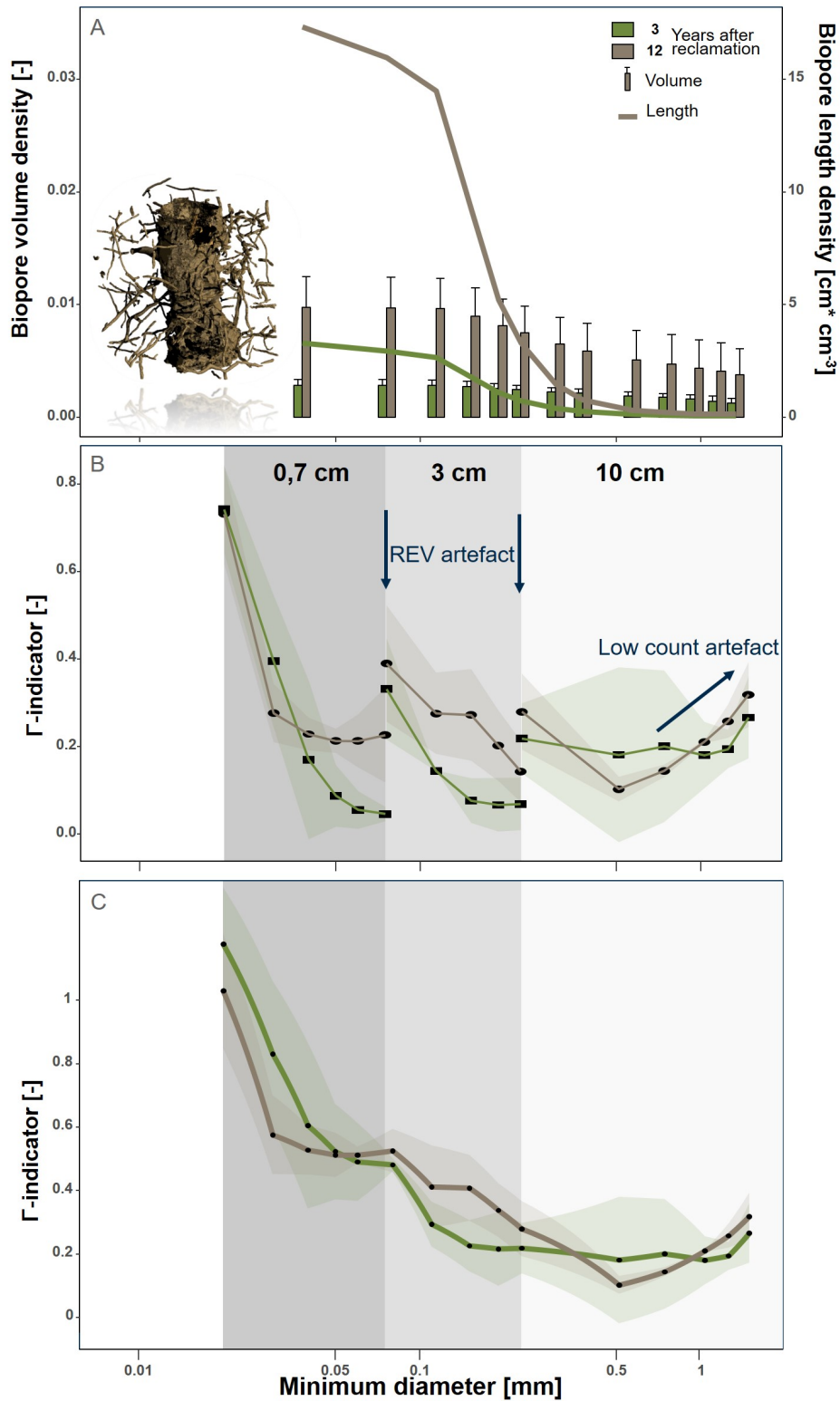
FIGURE 5.3: *Biopore volume and biopore length and Γ-indicator at different minimum pore diameter. A: Biopore volume and biopore length of the for the depth of 40-60 cm of the three and twelve year old field analysed in the 3 cm subsamples. B: Γ-indicator as a function of minimum pore diameter for the depth of 40-60 cm of the three and twelve year old field for the three sample sizes. C: Corresponding joint-Γ-distribution for the depth of 40-60 cm of the three and twelve year old field. Shadows and whiskers indicates standard deviation of the plots sampled.*

5.3.3 Secondary pores: Tillage induced

Fig. 5.4 shows both connectivity metrics as a function of minimum pore diameter as well as volume fractions derived from X-ray μCT and from the evaporation method for the ploughed topsoil (0-20 cm) and subsoil (40-60 cm) of the 6, 12 and 24 year old field.

The mean of the corrected Γ-indicator of the tilled fields, i.e. average of three plots in a depth of 0-20 cm, revealed a steady increase beginning at a pore diameter of 1 mm to Γ-indicators close to 1 at about 0.08 mm (Fig. 5.4B). Like the 12-year-old field, the Γ-indicators of the 6- and 24-year-old subsoils (40-60 cm) increased constantly, but only starting at 0.5 mm as larger pores are almost absent without ploughing and reaching values close to 1 at 0.02 mm. The increase was especially high between pore diameters of 0.03 mm and 0.02 mm, i.e. in the typical size range of biopores.

Similar to the mean values of all fields (Table D.1), the χ-density in the subsoil (40-60 cm) of the three fields (6, 12 and 24 years) decreased with decreasing minimum pore diameter towards highly negative values, but positive values occurred at 0.11 mm and 0.03 mm (Fig. 5.4A, note the non-linear y-axis), suggesting the emergence of a new pore type. With the exception of pore diameters of 0.076 mm and 0.02 mm, the χ-densities of the ploughed soil layers (0-20 cm) were lower at all pore sizes than in undisturbed subsoil (Fig. D.1, Fig. 5.4A), indicating an overall improvement in connectivity (both in terms of Γ and χ) due to the periodic soil loosening by ploughing. The χ-densities in the 0.7 cm $\varnothing$ samples were higher compared to those in 3 cm $\varnothing$ directly at the scale transition (minimum pore diameter of 0.08mm). At this pore size, which is located at the scale transitionof 0.7 cm $\varnothing$ and 3 cm $\varnothing$ samples (Fig. 5.1), especially the χ-densities of the subsoil showed a "low count artefact". The reason for this was the particularly small volume of pores of the subsoil at this minimum pore diameter (Fig. D.1). In the topsoil the volume fraction of largest pores in the smallest sample size was still high enough to be captured representatively so that it matched the more trustworthy χ-values for the same minimum pore diameter in the next larger sample size. In summary, the Euler number was continuous across scales unless the remaining pore volume at large minimum pore diameter reached a critically low value.

The macropore volume was higher within the topsoil in both kind of measurement techniques, evaporation method and X-ray μCT. The two layers mainly differed by the increase of Φ-vis for macropores >0.2 mm and a decrease between 0.05 mm and 0.2 mm in the tilled layers (Lucas et al., 2019, Fig. 3.5). These differences can be also seen in the visualised pore systems at a minimum diameter of 0.1, 0.2 and 0.3 mm for one selected, representative sample out of approx. 80 each (Fig. 5.5). The curves from the measurements of topsoil and subsoil slowly converge around a minimum pore diameter of 0.2 mm, due to the lower amount of pores between 0.05 and 0.2 mm in the topsoil (Fig. 5.4C). Yet the pore size distribution, measured by the evaporation method only showed a clear increase of pore volume in the subsoil for pores <0.03 mm (Fig. 5.4D). This is because the evaporation method in fact does not measure the size distribution of pores per se, but the size distribution of pore bottle-necks.
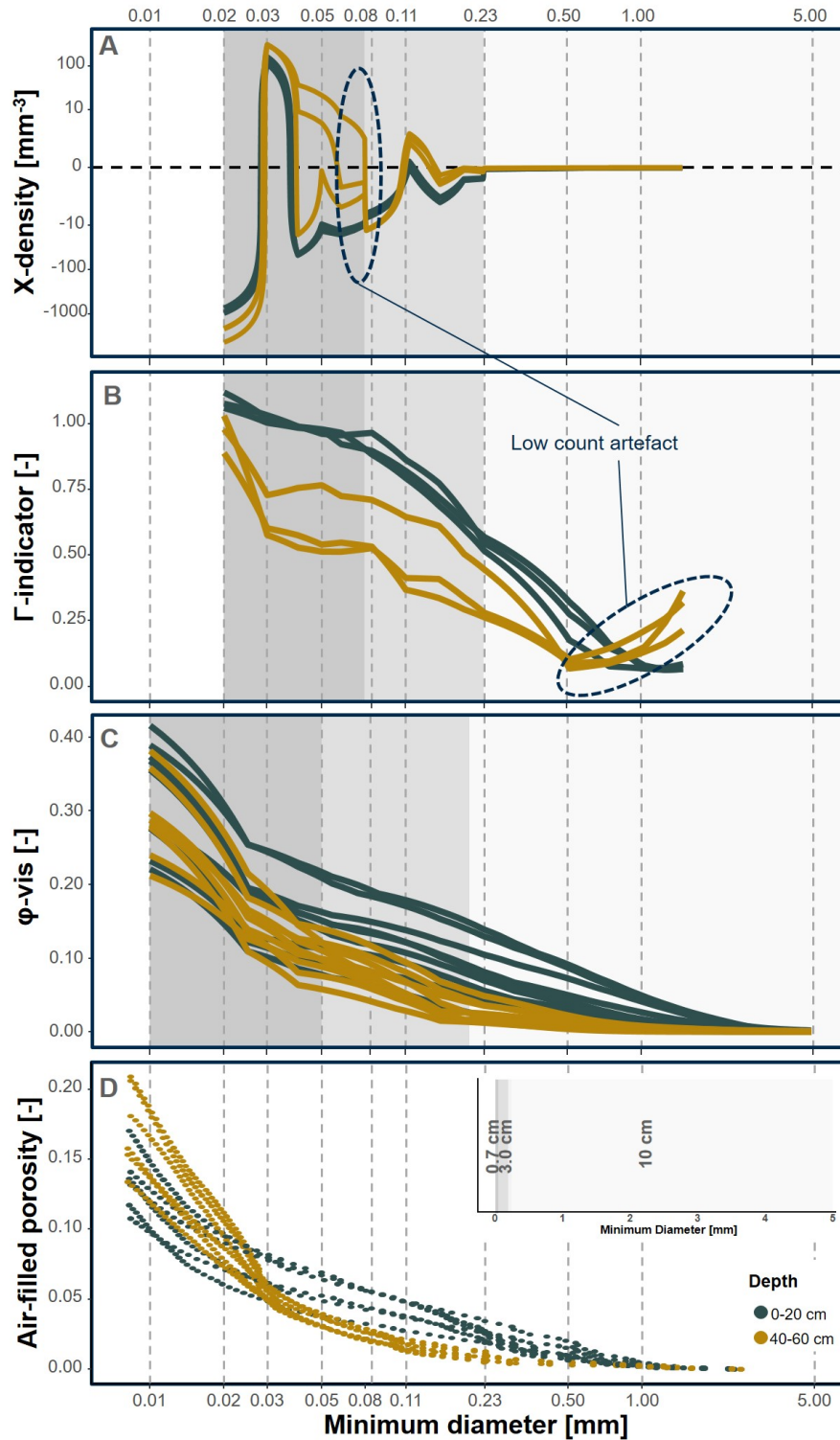
FIGURE 5.4: *Relation between pore size distribution and connectivity metrics for the ploughed topsoil's (0-20 cm) and subsoils (40-60 cm) of the 6, 12 and 24 year old fields. Shown are pore size distribution measured by an evaporation method (D) and by X-ray μCT (C) such as the connectivity metrics Γ-indicator (B) and χ-density (A). The different intensities of gray in the background reflect the range of sample sizes. Inset in D shows the range of the sample sizes without a logarithmic x-axis.*
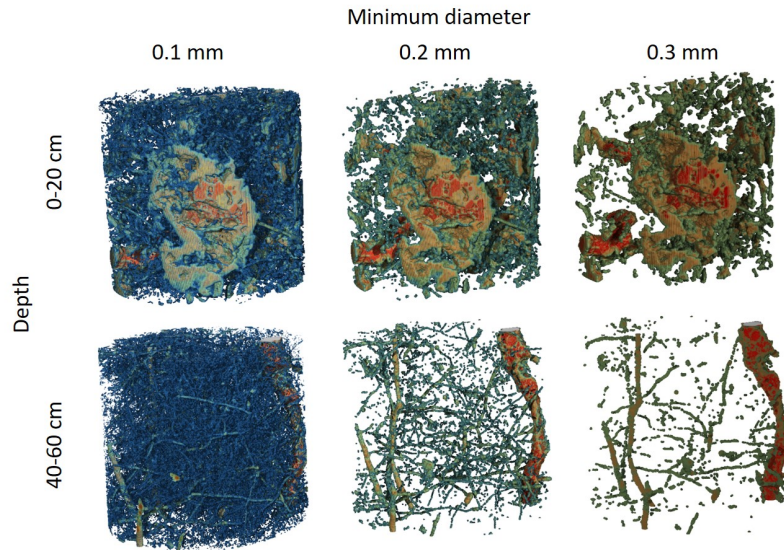
FIGURE 5.5: *3D visualisation of pores with a minimum diameter of 0.1, 0.2 and 0.3 mm of a 3 cm column from topsoil (top row), which is ploughed and a column from subsoil (bottom row) reveal the differences in structure and show the shift of narrow macropores (< 0.2 mm) towards macropores (> 0.2 mm) during ploughing as written in Lucas et al. (2019, Chapter 3).*

5.4 Discussion

The results of this study indicate that the χ-number and the Γ-indicator together are suitable to disentangle different pore types and to describe their effect on connectivity. The reason for this is that the two connectivity metrics reflect different pore characteristics. One of the issues that emerges from these findings is that scale artefacts have different impact on the two measures: Since Γ as a percolation-based characteristic is strongly related to the biggest pore clusters (Jarvis, 2007), it is highly underestimated in samples that are too small to capture these clusters (Fig. 5.3). We proposed a new method for a joint-Γ-curve, integrating information obtained from various sample sizes (i.e. scales). Therefore less biased information on how the connection probability changes as a function of minimum pore diameter and at which point the pore system connects into one percolating system can be achieved (Fig. 5.3). This curve increases drastically when Φ-vis approaches the inflexion point. Thus, we demonstrated how this distribution can be used to estimate the influence of management practices (i.e. tillage), and biological activity (i.e. biopores) on the connectivity of the pore space (Fig. 5.4).

The hypothesis raised by this study was that χ does not need such a scale fusion. We could show, that cutting of long range connections when reducing the sample size had indeed a minor effect on χ. In addition, the sensitivity to small scale features enabled us to link drastic changes in χ-density across the pore size distribution to a transition between different types of pores having different origin. However, both, χ-density and Γ-indicator, were affected by the "low count artefact" (Fig. 5.4). This underlines that both connectivity measures require a sufficient number of pores larger than a certain pore diameter in the sample to provide reasonable information on their connectivity.

Our findings about changes in volume fractions of specific pore types and connectivity metrics of the entire pore system (and biopores only) with changing minimum pore diameter revealed some common trends that are summarised in the conceptual scheme in Fig. 5.6.

Growing roots and other biota like earthworms form biopores of different sizes. Consistent with the literature, this study showed that these sizes vary extremely from several μm,
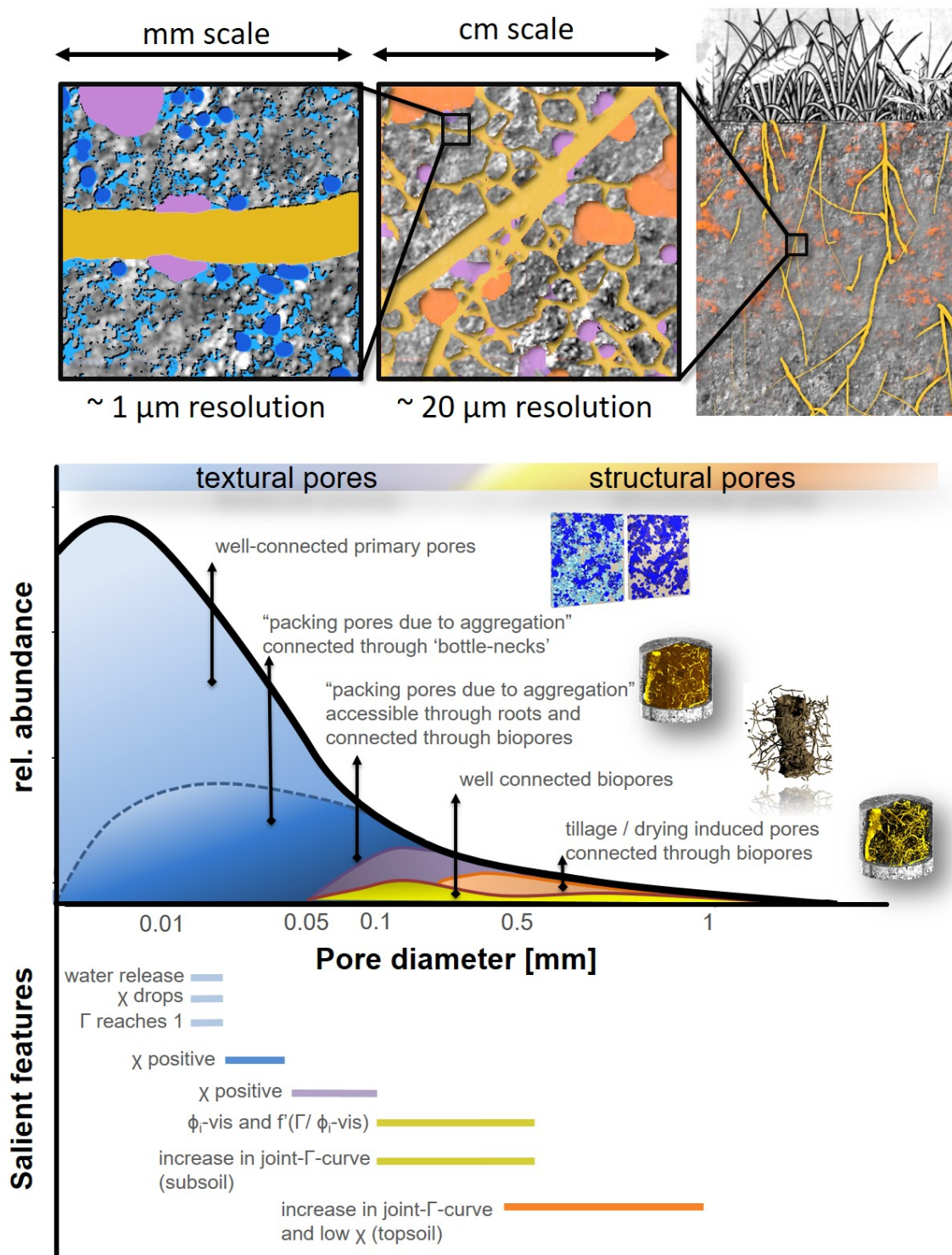
FIGURE 5.6: *Conceptual scheme of connectivity across scales. The upper part shows visible pores at different scales, which become connected through long-ranging biopores of different diameters (lower part). In the lower part also the salient features of the connectivity measures are shown, allowing to distinguish different pore types within the pore space.*

formed by fine roots to several mm in diameter formed by earthworms or tap roots (Yunusa

et al., 2003). Smaller biopores between 0.03-0.3 mm are formed by first and second order lateral roots of cereals (Yunusa et al., 2003) are adequately captured within 3 cm Ø samples and these contribute to the majority of biopores (Fig. 5.3). We could show, that due to the high biopore length between 0.1 and 0.5 mm long-ranging pores are able to connect the existing pore system at low Φ-vis (Fig.5.3, Fig. D.4). Similar to this, Tippkötter (1983) could link an interconnected network of biopores between 0.1 and 1 mm in a loes subsoil, with a maximum between 0.15 and 0.25 mm to the morphology of living root systems, The differences of the joint-Γ-distribution of the three year and twelve year old field, which share almost the same joint pore size distribution (Fig. 5.2) in combination with the decrease of the percolation threshold at pore diameters at 0.11 and 0.23 mm (Table D.1) shows that growing roots do not necessarily increase Φ-vis or change the PSD over time (Fig. D.3). Instead, in the examined reclaimed soil, they rearranged the existing macropore system and thus reduced the percolation threshold without changing Φ-vis (Table D.1).

On the other hand, tillage lead to an increase in Φ-vis for pores > 0.2 mm (Fig. 5.4C, Fig. 5.5). By this the increase in the joint-Γ-curve was shifted towards larger pore diameters. Thus, connection probabilities of the topsoil's already reached values close to 1 at pore diameters around 0.05 mm as compared to values of approx. 0.5 in the subsoil (Fig. 5.4B). Different X-ray μCT studies, which examined the influence of tillage on the connectivity of macropores, showed both, that tillage increases (Pihlap et al., 2019; Pires et al., 2019; Pires et al., 2017; Schlüter et al., 2018b) or decreases (Dal Ferro et al., 2014; Lucas et al., 2019; Zhao et al., 2017) the connectivity of the pore space. This inconsistency may be due to the differences in the resolution of the images analysed, which ranged from around 0.003 mm to 0.06 mm. Thus the connectivity metrics may have reflected different pore types.

Studies that examined χ in soil as a function of pore size often showed positive and increasing values for χ in macroporous range (>0.2 mm), but these then became negative at a certain threshold and continuously decreased to a minimum (Bacq-Labreuil et al., 2018; Schlüter et al., 2011a; Vogel et al., 2010). In contrast, however, in the investigated Loess substrate, the χ-density showed that even the pores >0.5 mm were well connected and had slightly negative values. At minimum diameters $\gg$0.5 mm the pore system mainly consisted of big biopores in untilled soils (Fig. 5.4), but also in the tilled topsoil a lot of fragmented biopores existed (Lucas et al., 2019, Fig. 3.9), which were able to connect more randomly distributed pores created by tillage (Fig. 5.6).

However, deriving Φ-vis with the evaporation method, showed the highest increase at equivalent diameters <0.03 mm in the subsoil (Fig. 5.4D). In contrast to the pore size distribution derived by X-ray μCT, the evaporation method is only capable to show the pore neck distribution. At pores >0.03 mm more isolated pores than new connections emerged, as χ-densities become positive (Fig. 5.4A). These pores with a diameter of approx. 0.03 mm apparently correspond to dispersedly distributed secondary pores (dark blue in Fig. 5.2C), which tend to be isolated from the network of larger macropores formed by biological activity and tillage (Fig. 5.6). At pore diameters between 0.03 mm and 0.05 mm several pore types overlap (Fig. 5.6), therefore the heterogeneity between samples is rather high (Table D.1, Fig. D.1). These samples are composed of different volumes of well-connected secondary and unconnected textural pores. The subsoil contains a relatively high amount of unconnected pores of approx. 0.05 mm (Fig. 5.4B). At the smallest pore diameter of 0.02 mm the χ-density decreases again massively towards the minimum of -2115.80 [mm^{-3}] as even smaller pore necks emerge (light blue in Fig. 5.2C). Through them the entire pore network becomes connected and Γ reaches values of around 1. As a result, at the corresponding tension also the water of the unconnected pores >0.3 mm is drained and causes the shift between PSD and bottle-neck distribution (Fig. 5.4).

5.5 Conclusion

This study examined the nature of the connectivity metrics Euler number (χ) and the connection probability (Γ) in terms of their sensitivity to different pore types across scales.

The most obvious findings to emerge from this study are: (1) Different scale artefacts overlap with actual pore features, which must be carefully considered during the interpretation of connectivity across scales. (2) Γ is highly sensitive for long-ranging pore clusters and thus prone to the "REV-artefact", which occures when subsampling of an intact soil core cuts off long-distance connections. Therefore a scale fusion between subsamples of different size is needed. We showed that this is possible by integrating information obtained from various samples to a joint-Γ-curve. The Euler number (χ) as a local metric does not need this scale fusion. It is dominated by small scale features (i.e. small pores) leading to a smooth transition between scales. (3) By combining the information of χ and Γ the contribution of different pore types to the overall pore connectivity can be described and disentangled across scales. The Euler number as a function of pore size can be used to detect transitions between more continuous pore types (e.g. biopores) to packing voids between particles characterised by pore necks. The joint-Γ-curve provides valuable information on the overall connectivity across scales and reveals how much different pore types contribute to this overall pore connectivity.

We showed that biopores mainly connect the pore system of diameters between 0.5 and 0.1 mm. For the specific soil investigated in this study this was not necessarily coupled with an increase in pore volume. In contrast tillage could be seen as a shift of pores of diameter >0.05 mm towards pores larger than 0.2 mm which went along with an increase in pore volume and thus also in connectivity.

Overall, the current data highlight the importance of choosing an appropriate sample volume to identify effects of soil management or the creation of biopores with X-ray μCT. To cover the relevant scales of structural pores we therefore suggest to combine at least two sample sizes.

Chapter 6

Combination of Imaging Infrared Spectroscopy and X-ray Computed Microtomography for the Investigation of Bio- and Physicochemical processes in Structured Soils

iron oxide rich aggregate

1 mm

biopore with root

organic matter-rich luvisol material

earth worm cast
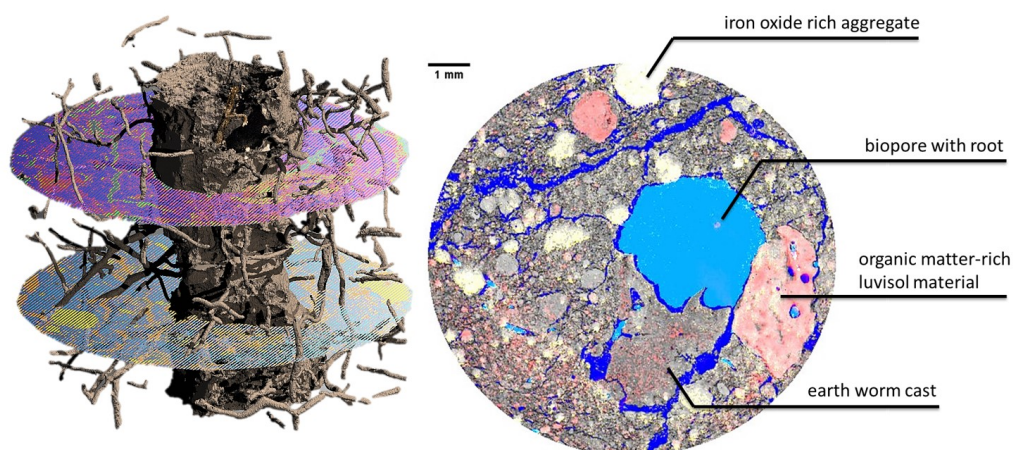
Soil is a heterogeneous mixture of various organic and inorganic parent materials. Major soil functions are driven by their quality, quantity and spatial arrangement, resulting in soil structure. Physical protection of organic matter (OM) in this soil structure is considered as a vital mechanism for stabilising organic carbon turnover, an important soil function in times of climate change. Herein, we present a technique for the correlative analysis of 2D imaging visible light near-infrared spectroscopy and 3D X-ray computed microtomography (μCT) to investigate the interplay of biogeochemical properties and soil structure in undisturbed soil samples. Samples from the same substrate but different soil management and depth (no-tilled topsoil, tilled topsoil and subsoil) were compared in order to evaluate this method in a diversely structured soil. Imaging spectroscopy is generally used to qualitatively and quantitatively identify OM with high spatial resolution, whereas 3D X-ray μCT provides high-resolution information on pore characteristics. The unique combination of these techniques revealed that, in undisturbed samples, OM can be found mainly at greater distances from macropores and close to biopores. However, alterations were observed because of disturbances by tillage. The correlative application of imaging infrared spectroscopic and X-ray μCT analysis provided new insights into the biochemical processes affected by soil structural changes.

6.1 Introduction

Soils are heterogeneous and complex mixtures of organic matter (OM), mineral particles and pore space. Their inherent functionality emerges from the spatial arrangement of these constituents on various spatial scales (Portell et al., 2018; Ritz et al., 2004; Wanzek et al., 2018). Important soil physical properties and processes such as conductivity, water retention, gas exchange and root penetration are defined by soil structure, i.e. the spatial arrangement of solids and voids (Bronick et al., 2005; Rabot et al., 2018). The interplay of soil chemical and biological properties through physical protection has been considered a key factor in stabilising soil carbon (Dungait et al., 2012; Mueller et al., 2012; Stockmann et al., 2013; Wiesmeier et al., 2019). This, in turn, is influenced by soil structure, which defines the microenvironmental conditions for microbial carbon turnover. OM is not evenly distributed in soils. For instance, the walls of biopores have been often reported as OM rich compared with bulk soil (Banfield et al., 2017; Hoang et al., 2017; Hobley et al., 2018). It is assumed that the heterogeneous location of OM in soil may be a significant factor controlling the extent of OM mineralisation (Dungait et al., 2012; Steffens et al., 2017). Therefore, to understand the relationship between soil structure, carbon dynamics and biogeochemical processes, it is crucial to characterise undisturbed soil samples. However, so far this relationship is often investigated by techniques based on soil disturbance, e.g. by extracting aggregate fractions (Young et al., 2008) from the bulk soil, which indeed provides insights into microscale processes, but the complete image of the soil architecture is lost (Baveye et al., 2018).

Visible light near-infrared spectroscopy (Vis-NIR) is an established method for the simultaneous analysis of various soil properties (Soriano-Disla et al., 2014; Stenberg et al., 2010). However, soil samples have to be ground and homogenised for optimum performance. Imaging Vis-NIR (imVNIR) is an emerging technique that allows the spatial analyses of intact soil samples (Buddenbaum et al., 2011; Steffens et al., 2013). Steffens et al. (2014) and Steffens et al. (2013) and Hobley et al. (2018) demonstrated the potential of imVNIR by improving our understanding in soil classification, chemical composition and carbon storage on the micrometre scale for whole pedons.

The combinatory application of 2D and 3D imaging of chemical composition and soil structure, respectively, may provide new insights for the physical properties and the spatial extent of soil structures along with their chemical information. X-ray computed microtomography (X-ray μCT) is nowadays considered as a commonly used technique for describing soil structure with physical parameters such as pore size distribution and connectivity (Rabot et al., 2018). As 2D imVNIR and 3D X-ray μCT give different but corroborating information on the same material, the combination of the two techniques can therefore be used to uncover and quantify biogeochemical processes in intact soil samples. The combination of different biogeochemical imaging methods, designated as correlative microscopy or correlative imaging, is increasingly used in life sciences (Caplan et al., 2011; Guyader et al., 2018; Handschuh et al., 2013). Few recent applications have demonstrated that there is a great potential for the application of correlative imaging in soil sciences (Hapca et al., 2011; Juyal et al., 2019; Kravchenko et al., 2019; Schlüter et al., 2019). Schlüter et al. (2019) highlighted that a combination of different 2D techniques for chemical and microbial imaging, such as scanning electron microscope-energy dispersive using X-ray (SEM-EDX) analysis and nanoscale secondary ion mass spectrometry (nanoSIMS) or fluorescence microscopy and X-ray μCT, can be used to reveal specific soil microenvironments and thus biogeochemical and physical processes in structured soil. Compared with these 2D techniques, the spatial resolution of Vis-NIR imaging spectroscopy is lower (several μm instead of nm) but allows the investigation of larger samples up to a complete pedon. Therefore, adding imVNIR to the toolbox of correlative analyses of 2D imaging techniques and 3D X-ray μCT for fast imaging of several samples may reveal patterns of soil biochemical processes at the pedon level of intact soils.

In this study, we developed a procedure for the correlative image analysis of 2D imVNIR and 3D X-ray CT on intact soil cores. Our approach consisted of X-ray μCT, followed by impregnation with resin, slicing and imVNIR and classification of the same undisturbed soil core sample. After image registration, the classified imVNIR images and the X-ray μCT images were analysed with correlative image analysis, e.g. by analysing the OM distribution as a function of distance to pores and biopores. We used cores sampled from a space-for-time reclaimed chronosequence. These displayed both structural and chemical differences within the same substrate (Lucas et al., 2019; Pihlap et al., 2019, Chapters 2, 3) and thus provided perfect conditions for validating the correlation analysis method on undisturbed field samples.

6.2   Materials and methods

6.2.1   Sampling and sample preparation

Intact soil cores were obtained from reclaimed soils in the Garzweiler open pit mine area, 40 km west of Cologne (Germany). A detailed site characterisation together with a description of the reclamation procedure and crop rotation of the space-for-time chronosequence is described in the study of (Pihlap et al., 2019, Chapter 2). Briefly, an approx. 20-metre-thick layer of loess, including approx. 2.2 m of developed Luvisol, was excavated during coal mining, mixed to afford a Luvisol/loess ratio of 1:10 and deposited. This mixture was used for reclamation with alfalfa (*Medicago sativa*) in a pioneering phase for 3 years. Between the 4th and 6th year, the reclamation was based on a crop rotation including *Triticum aestivum* L. (wheat) and *Hordeum vulgare* L. (barley). In the years after, a variation of *Triticum aestivum* L. (winter wheat and summer wheat), *Hordeum vulgare* L. (winter barley), *Brassica napus* L. (rapeseed) and *Zea mays* L. (maize) were grown. About 30 t/ha of organic fertiliser (compost or manure) were added in the 4th and 7th year of the reclamation procedure.

Three cores with different soil structures were selected on the basis of the study of Lucas et al. (2019, Chapter 3) for correlative analysis with imVNIR, representing different soil development levels (3, 6 and 12 years after reclamation) and management stages (no tillage/tillage) (Table 6.1). The selected undisturbed soil cores (height 20 cm and width 10 cm) were obtained from fields with different ages, in depths of 0–20 and 40-60 cm, using a custom-made drill for undisturbed sampling of cylindrical soil cores (UGT GmbH, Germany). To overcome the trade-off between resolution and sample size, three subsamples of 3 cm diameter and 3 cm height were collected per core.

The no-tilled topsoil is an initial soil with low OM content and dense soil structure that was not affected by soil tillage. After 6 years of reclamation, the tilled topsoil was characterised by high macroporosity due to ploughing and high OM content owing to the organic fertiliser amendment. The subsoil represents a sample with many macropores due to high biological activity, namely, high biopore density, which developed for 12 years under a tilled topsoil.

TABLE 6.1: *Basic soil parameters from selected samples. Macroporosity and biopore length density are shown for the exact same sample (Lucas et al., 2019), whereas bulk density, organic carbon (OC) concentration and pH values represent a mean value from the plot where the sample was taken (Pihlap et al., 2019).*

Sample name	Year after reclamation	Sampling Depth [cm]	Bulk Density [g cm^{-3}]	Macroporosity > 38 μm [Vol-%]	OC [mg g^{-1}]	pH	Biopore length density [cm/cm^3]
No-tilled top-soil	3	10–13	1.59	3.05	3.7	7.59	11.22
Tilled top-soil	6	3–6	1.48	13.3	5.89	7.44	17.8
Subsoil	12	55–58	1.45	19.3	3.26	7.52	17.6

6.2.2 X-ray μCT

The cylindrical subsamples with a diameter of 3 cm were scanned using an X-ray micro-tomograph (X-TEk XCT 225, Nikon 162 Metrology). Reconstruction was achieved with a spatial resolution of 19 μm, and the images were processed and segmented into solids and pores, as described in detail by Lucas et al. (2019, Chapter 3). Specifically, all biopores were segmented in the binary images using the Tubeness plugin in Fiji to separate all tubular objects. All biopores, including filled biopores with roots or earthworm cast, were separated from the remaining, irregularly shaped, pore network in the binary images. Biopores in the resulting images were therefore empty, and the rough pore wall was excluded. These bio-pores were dilated several times in all 3D directions, and then the image of the segmented pores was subtracted. This allowed us to include the walls of the biopores and solids, like earthworm cast within the biopores, to the resulting image.

6.2.3 imVNIR

After X-ray μCT analysis, the same intact soil cylinders were dehydrated gradually with acetone (series from 30% to 100% (v/v)), and subsequently, the soil cores were impregnated with polyester resin (PALATAL P 6-01, BÜFA, Germany). After 5 weeks of polymerisation, the cores were placed in an oven at 40 ° C for 48 h to cure the surface of the impregnated samples. All cores were cut in two slices of 1 cm thick, polished and scanned with a hyper-spectral camera (VNIR-1800, Norsk Elektro Optikk Ås, Norway). The camera lens distance from the sample surface was set to approx. 30 cm, and the sample was illuminated with two light sources in front of and behind the camera (angle about 45°). An image of 53×53 μm^2 /px (1800 px/line) and spectral range with 196 bands between 400 and 990 nm was thus obtained. A certified reflectance standard (reflectance 50%) was adopted and used to normalise the reflectance on the target image in order to adjust the differences in illumination:

$$\rho_{obj} = \frac{L_{obj}}{L_{ref} * \rho_{ref}} \tag{6.1}$$

where L$_{obj}$ is the radiance of the recorded sample, L$_{ref}$ the radiance of the certified reflectance standard and ρ_{ref} the reflectance of the certified reflectance standard (Peddle et al., 2001; Steffens et al., 2013).

Hyperspectral images were processed in ENVI Classic (Version 5.2, Exelis Visual Information Solutions, Boulder, Colorado, USA) following the workflow in Figure 6.1. In particular, we used a principal component analysis to concentrate the spectral information

in images and remove the correlation between neighbouring bands (Kavzoglu et al., 2018; Rodarmel et al., 2002). The first 10 principle components were used to separate polyester resin and pores filled with polyester from the soil matrix and to identify pure spectral endmembers for the subsequent image processing steps. The main criteria for the endmember collection were to select the most abundant features and to cover pixels from different spatial segments in the image. The selected endmembers were the loess parent material, OM particles, Fe oxide (FeOx) dominated pixels and iron-manganese concretions. For the tilled topsoil and subsoil, two additional endmembers were selected because of their specific features. The tilled topsoil was affected by ploughing, which created voids on top of the loess. This gave different reflectance than the voids created by roots and earthworms, thus forming additional endmembers for tillage voids. An additional endmember was also selected from the subsoil to describe fresh, OM-rich pixels, which displayed the most defined OM spectrum compared with that of other OM-dominated areas. The statistical significance of the selected endmembers was tested with the Jeffries–Matusita distance test (Dabboor et al., 2014). For detecting and mapping the abundance of each spectral endmember, linear spectral unmixing (LSU) was conducted using the manually selected endmembers (Fig. E.1). LSU generates abundance maps, where the contribution of the selected endmembers to each pixel is depicted (Ravel et al., 2018). The obtained abundance maps (Figures E.2-E.4) were subsequently used for a supervised classification using maximum likelihood classifier (Borra et al., 2019). For the supervised classification, new additional ROIs were selected along with the Jeffries–Matusita distance evaluation. The accuracy of the maximum likelihood supervised classification was tested with a confusion matrix, and the subsequent area coverage of the classes was calculated in the classified images.
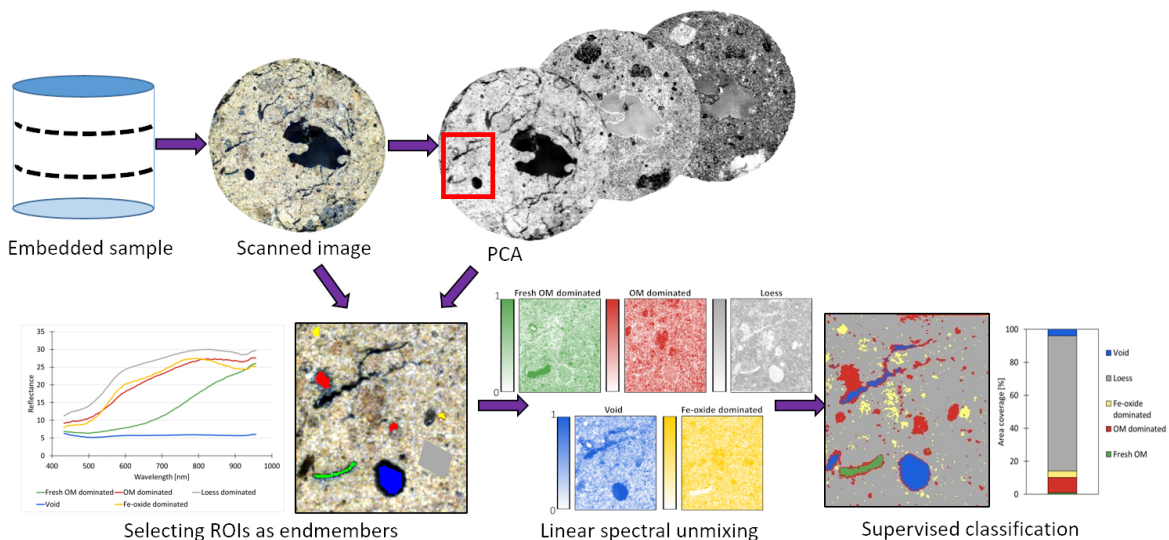
FIGURE 6.1: *Workflow of imVNIR image processing.*

6.2.4 Image registration

The images obtained from X-ray μCT and imVNIR had different resolution and orientation. To overcome these constraints, an image registration was needed prior to correlative analysis. The aim of the registration is to find a geometric transformation to map the pixels of the first (moving) image into the second (target) image. Therefore, 2D/3D image registration was performed using the elastix software (Klein et al., 2010; Shamonin, 2013) along with a protocol similar to that described by Schlüter et al. (2019). In the current study, the moving image was always the filtered X-ray μCT image and the imVNIR image was the target

image. We also used a combination of two metrics, the mean of the Euclidean distance between the corresponding landmark points and the mutual information criterion (Mattes et al., 2001), which defines the objective function that has to be optimised. Mutual information allows the entropy to be matched with the corresponding image pairs (Maes et al., 1997). For example, homogenous features, such as macropores in μCT images, should be matched with homogenous features visible in imVNIR (Fig. 6.2).
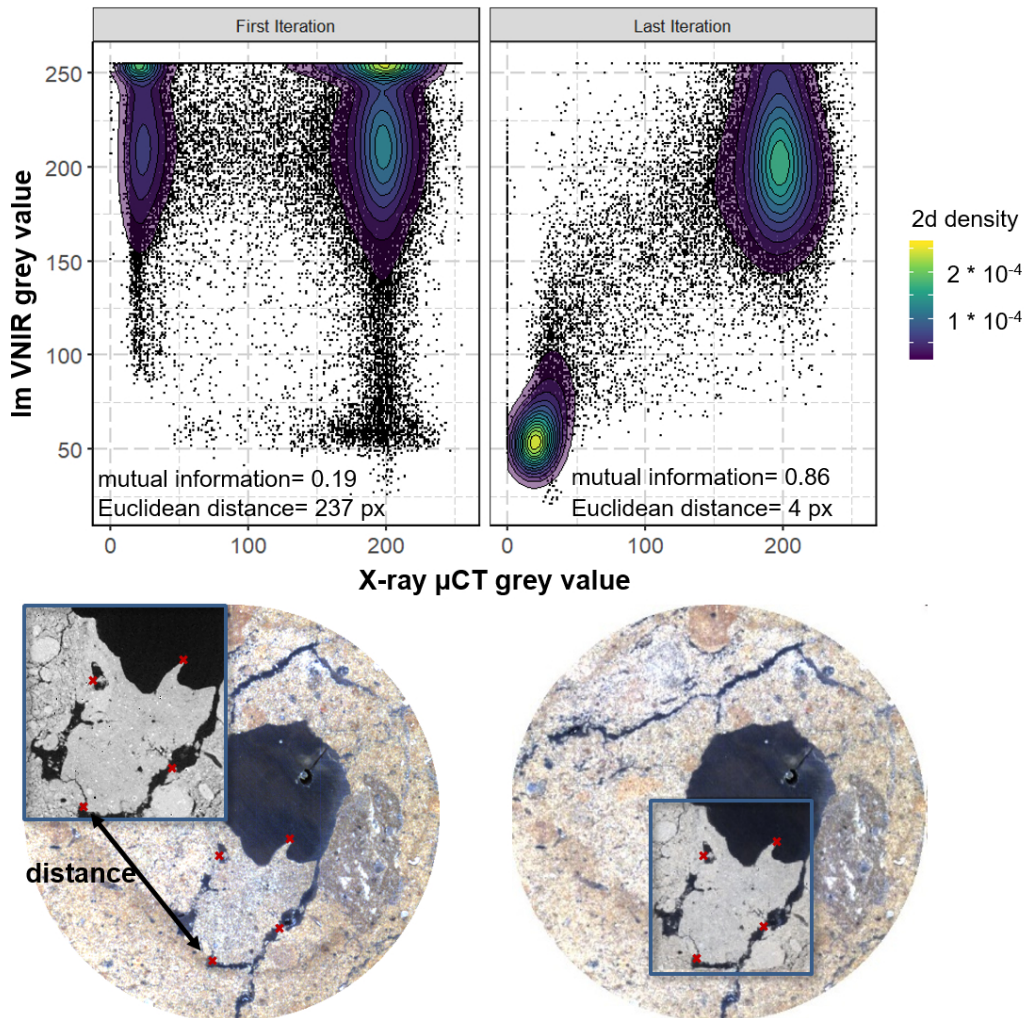
FIGURE 6.2: *Principle of metrics for the optimisation of a transformation matrix. A 2D cut from a μCT image and a 2D imVNIR slice were chosen as a registration example. The upper graphics represent scatter plots of grey values from imVNIR and μCT at the beginning of the registration and after the last iteration. Polygons show the 2D kernel density. The corresponding images below illustrate a 2D section of the 3D μCT image (grey) and its position on the imVNIR slices. Through different iterations, the μCT image was transformed so that both images match at each position. Therefore, two metrics were used to optimise the transformation matrix. The Euclidean distance metric aims to minimise the distance between the manually set points (red crosses). In this example, it is minimised from a mean of 237 to 4 px. The second metric represents the extent of mutual information between the registered μCT image and the imVNIR image. The scatter plot reveals several clusters, which are formed by the μCT image (pores and matrix) in the first iteration. After the final iteration, pore and matrix clusters were formed by both variables, thus increasing the mutual information.*

A second metric, which uses landmarks (at least three manually selected points), was also added. This ensured that the optimisation of the moving image did not result in local minima. A pyramid schedule was used to achieve a fast registration, starting with a coarse resolution and moving towards the next finer scale.

The best results were obtained by using a similarity transform, defined firstly by the objective function of the two metrics. Afterwards, the resulting parameters were used as the initial transform for affine transformations, for which only one metric was used to define the objective function. A first rough registration was thus performed and was mainly guided by the landmark points, and a second step, using only the mutual information metric, resulted in a more accurate result that did not rely on manually set points. Additionally, the similarity transformation involved rotation, translation and scaling and therefore had 7 degrees of freedom in 3D. Instead, the affine transformation added aspect ratio and shear to the allowed transformation, resulting in 12 degrees of freedom in 3D.

6.2.5   Correlative image analysis

X-ray μCT analysis allowed the characterisation and the localisation of pores >38 μm (2 px), whereas imVNIR enabled the determination of the soil's chemical composition. In this study, we calculated the Euclidean distances from μCT images and correlated them with OM and FeOx abundance maps obtained with LSU. The Euclidean distance transformation (EDT) in Fiji was computed to obtain the 3D images of pores. The EDT of the biopores, which are a subset of all pores, was calculated as well. These distance images were transformed with transformix, a subroutine of elastix, using the transformation parameters of the original μCT image to assure that the EDT images match the imVNIR image. Multichannel images of the Euclidean distances, pores and results of LSU were created in Fiji, where we could calculate the relative contribution of OM-rich pixels with distance to pores or biopores. Only distances with a certain number of pixels (100), equal to an area of about 0.3 cm^2, were taken into account, to avoid high standard deviation for smaller quantities.

6.3   Results

6.3.1   Soil composition characterisation using imVNIR

Fig. 6.3 displays the classification images for the three soil cores and the respective coverage of the five endmembers. The overall classification accuracy was 92.0% (k = 0.89) in the no-tilled topsoil, 91.6% (k = 0.90) in the tilled topsoil and 88.3% (k = 0.85) in the subsoil. Our technique enabled the clear separation of voids and soil matrix in all samples. The soil matrix was characterised by a patchy structure originating from the different components (loess, Luvisol material) that were mixed during the soil reclamation procedure. Images recorded at later reclamation stages (tilled topsoil and subsoil images) also showed the soil management effects on the soil chemical structural composition. Specifically, the no-tilled topsoil was characterised by a dense soil matrix with a higher area coverage of loess soil and spherical aggregates, as e.g. shown in the areas 5E-F, 1-2L and 3M in Fig. 6.3. In two tilled topsoil slices, we observed an increase in OM content and aggregate shape, due to the organic fertiliser amendment (Fig. 3, 11B-C and 12B, 11-12K, 10L-M and 11L-M). The area coverage of OM in the slices of the subsoil was comparable with that of the tilled topsoil, although the total organic carbon of the topsoil was rather low (Table 6.1). Although Fe/Mn concretions could only be found in the no-tilled topsoil, all samples contained FeOx-rich areas. The most distinguishable was slice 1 from the no-tilled topsoil sample, which had exceptionally high percentages of FeOx-dominated areas.
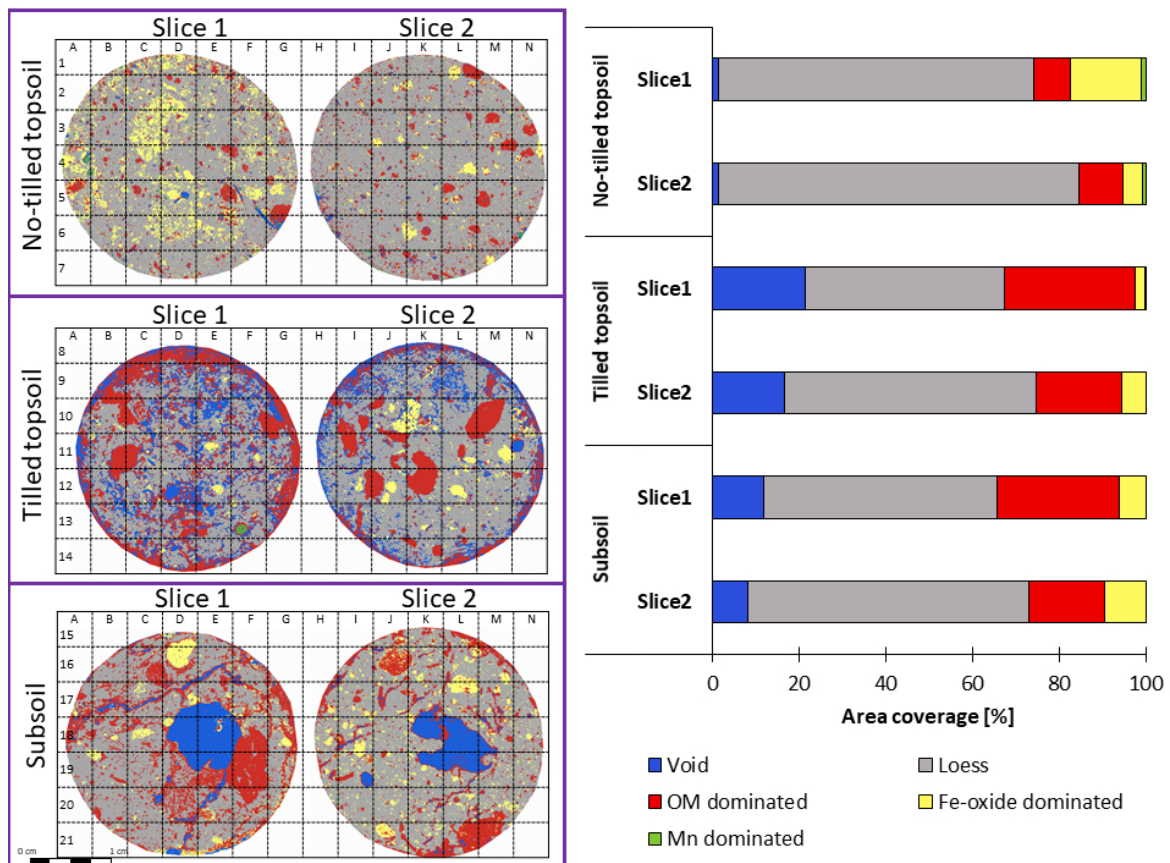
FIGURE 6.3: *Classification images and relative coverage of each class.*

6.3.2 Image registration

Only 4–5 common points were sufficient to align the μCT images with the imVNIR images by a similarity transformation. This initial registration was suitable to ensure a good result of the affine transformation, which relied only on mutual information. Fig. 6.4 depicts all 2D slice cuts corresponding to original μCT images, which were mapped according to the imVNIR images. The similarity could be distinguished especially in large pores, such as the central biopore in the subsoil sample or in large cracks. An example for a large crack can be found in A-E 14-15 and G-J 14-15, whereas a large biopore is visible in N-P 15-16 and S-U 15-16 (Fig. 6.4). These characteristics were less pronounced in other denser or more mixed samples. However, other features such as aggregates also indicated correct registrations. For example, in the tilled topsoil sample (e.g. Fig. 6.4, areas G10-11 and U9), the identified aggregates were rich in OM and therefore had lower reflectance in the imVNIR images. The corresponding regions in the μCT image were also darker because of the low electron density of the OM compared with that of the other solid substances. However, in some areas, slight differences could be observed because of the pre-treatment of the intact soil cores during resin impregnation. It should be noted that some pores in the imVNIR images are not black. In shallow pores, solid material from deeper layers was visible through the transparent resin (Fig. 6.4, areas I9, H10, I10, H12 and T9), hence the reflectance was affected by the signal from the material below.
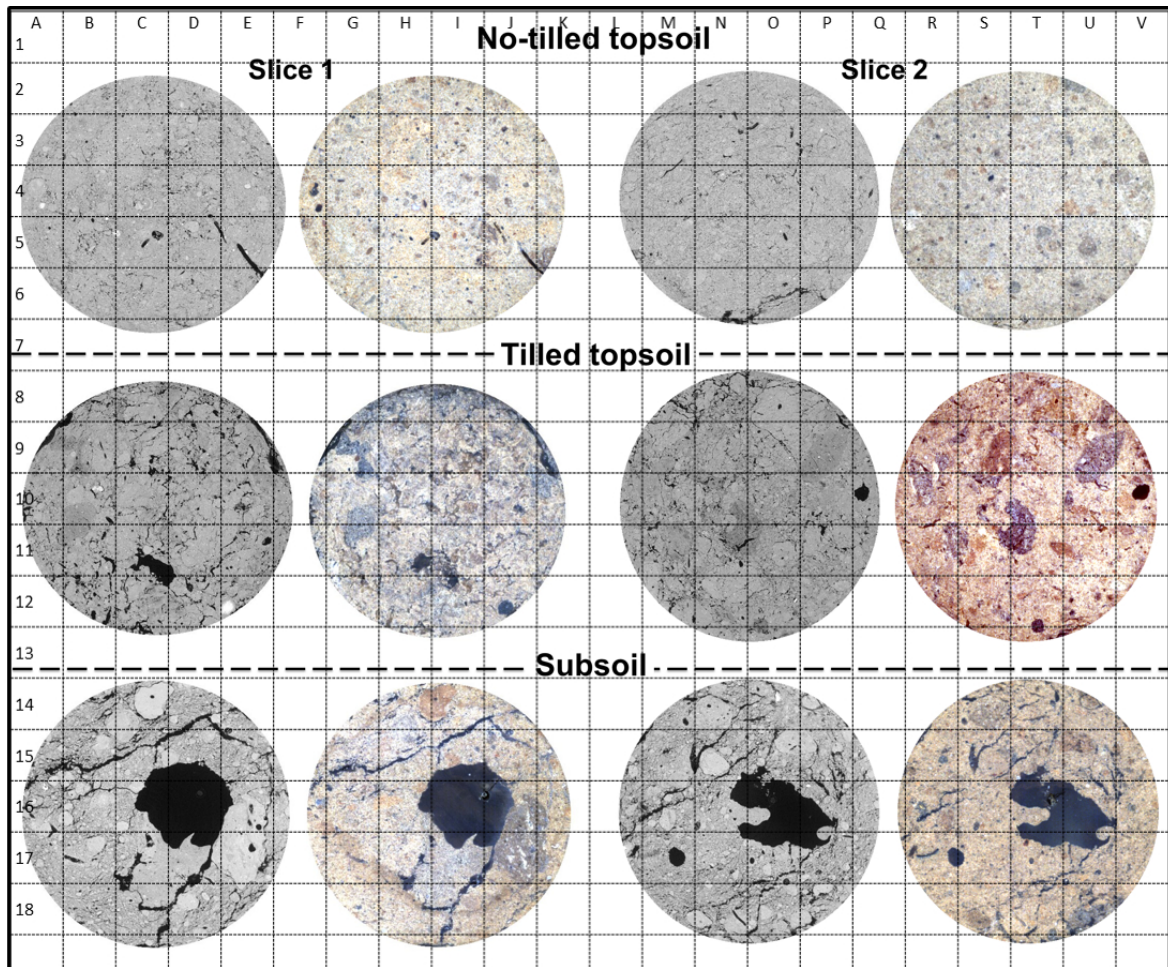
FIGURE 6.4: *Registered 2D slices of μCT and imVNIR images (visible spectra). Grey values of μCT represent dense areas (white) and pores (black). The pores in the imVNIR images can be black or light coloured, since the resin used is transparent.*

6.3.3   Correlative analysis of μCT and imVNIR detectable features

The EDT was computed individually for segmented pores and biopores, and the corresponding images show the Euclidean distance from any non-pore/non-biopore voxel to the next pore/biopore. Fig. 6.5 illustrates the results of the correlative analysis by observing the OM intensity distribution over the distance to the macropores and biopores. Correlative analysis with macropore distances in the no-tilled sample demonstrated a small increase in OM content with increasing distance. In contrast, the tilled topsoil sample revealed a decreasing trend of OM content with increasing distance to macropores. Furthermore, in the tilled topsoil sample, there were no soil matrix pixels more than 0.5 mm away from the next macropore. The subsoil sample (slice 1) had a relatively small abundance of OM-rich pixels near the pores, which then increased to about 100% at a distance of 0.75 mm. This relatively high distance was observed only in the subsoil sample. The density of biopores in samples was much lower compared with that of the total amount of macropores, leading to much longer distances (>4 mm). Compared with the distance to pores, the OM trends around the biopores were less pronounced (Fig. 6.5). In both slices of the tilled topsoil sample and in one slice of the subsoil, a small increase in OM was observed with increasing distance. Moreover, the biopores (0 mm distance) of the tilled soil samples exhibited low OM content. Fig. 6.6A illustrates the macroporosity distribution relative to the distance to biopores. In

all samples, macroporosity decreased with increasing distance (up to roughly 0.2 mm), but this gradient was predominant in the subsoil (Fig. 6.6A). The relative abundance of OM in the vicinity of the subsoil biopores increased after normalising the local OM contribution by the corresponding fraction of dense soil material, i.e. taking the shift in macroporosity into account (Fig. 6.6B). The contribution of FeOx (Fig. E.5) did not significantly change in any sample with the distance to pores and biopores. Interestingly, the FeOx abundance next to biopores increased in the no-tilled topsoil sample. The deviation of the FeOx distribution directly in the pores from zero can be attributed to the high amount of pores, which are smaller than the spatial resolution of the hyperspectral camera (53 μm). In this case, smaller pores are not detectable in the imVNIR images, but they are visible in μCT (19 μm resolution), resulting in a mixed spectrum of pores and FeOx-rich solid volume. This can explain the strong signal of FeOx in the LSU images at locations that are instead classified as pores in the μCT image.
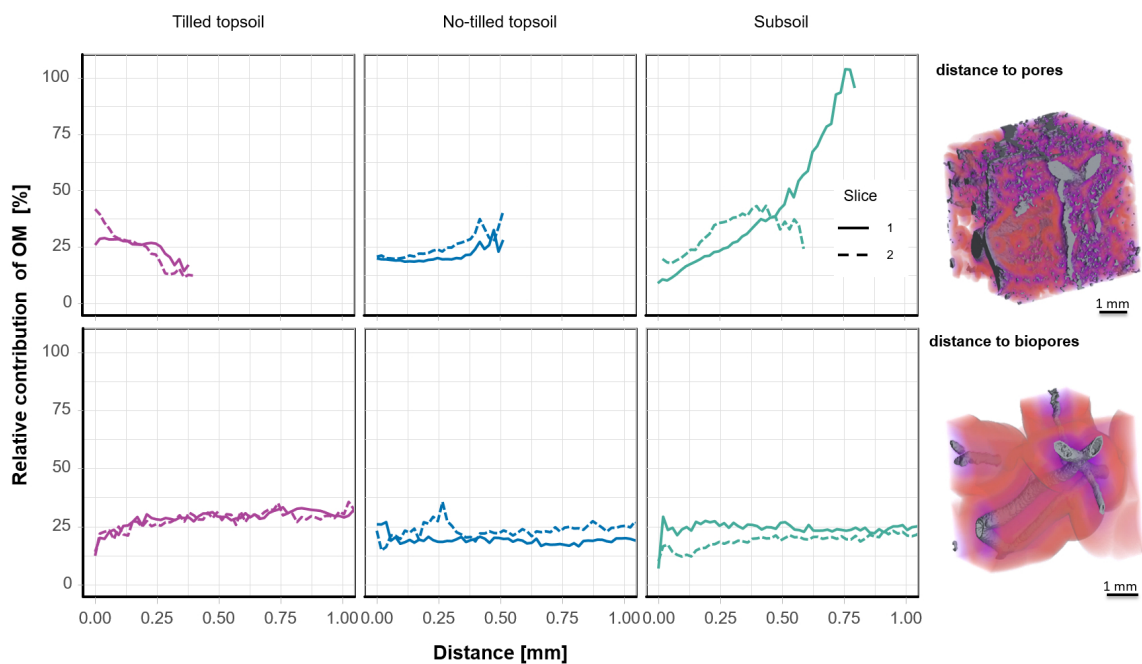
FIGURE 6.5: *Relative contribution of OM in LSU images with the 3D Euclidean distance to pores (upper graphs) and biopores (bottom graphs). The pictures on the right display the same cutout of macropores and biopores (grey) and the corresponding distances (small distance = purple, high distance = orange).*
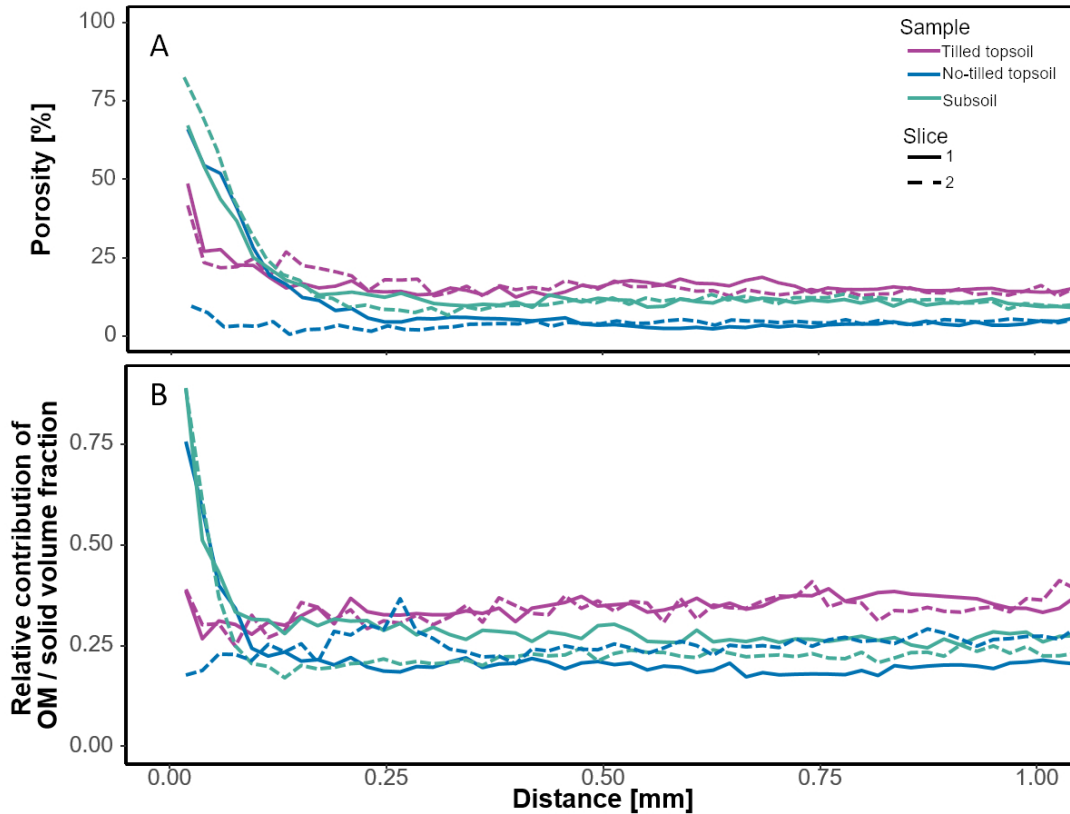
FIGURE 6.6: *(A) Porosity and (B) spectral intensity of OM normalised by the solid volume fraction, as a function of the 3D Euclidean distance to biopores.*

6.4 Discussion

ImVNIR is a non-destructive analysis to characterise physicochemical properties in soil. However, when slicing field moist samples, several artefacts such as smearing soil can be created, thus destroying the macropore system and creating surface topography that leads to shadows. In our study, we successfully applied, for the first time, resin impregnation with polyester followed by cutting in combination with subsequent imVNIR. The developed impregnation procedure allowed us to sustain the integrity of the soil microstructure and avoid the destruction of the macropore system (Gutiérrez Castorena et al., 2016; Jangorzo et al., 2014; Mueller et al., 2017; Rasa et al., 2012; Schlüter et al., 2019). In rare instances, we observed small changes occurring especially in looser areas, due to sample preparation artefacts. In the acetone dehydration pre-treatment, a large pore collapsed in the tilled topsoil (Fig. 6.4, areas C11 and H-I 11) during the impregnation, whereas some cracks that were visible in the no-tilled topsoil (Fig. 6.4, areas O6 and T6) diminished. Although there are different dehydration methods available (e.g. drying in the oven), they can create other specific artefacts, such as crack formation, that could complicate the registration and interpretation (Jongerius and Heintzberger, 1975). Despite the occurrence of small changes, the currently developed sample pre-treatment method allowed the horizontal cut of the soil in larger slices without smearing (Fig. 6.4), and thus, a good registration of μCT and imVNIR images was achieved (Fig. 6.4). The impregnated soil slices provided a perfect basis for the segmentation of different compositional and structural features, such as OM- and FeOx-dominated areas (Fig. 6.3), with imVNIR. The slopes in the spectrum (Fig. E.1) of selected endmembers were in line with data reported by Steffens et al. (Steffens et al., 2013), as their selected regions, such as Mn- and FeOx-dominated areas in a loess-derived stagnic Luvisol,

exhibited comparable spectra. As soil cores originated from the same substrate, imVNIR image processing revealed that the chemical and structural features were distributed differently within the samples due to the soil development after reclamation. In the no-tilled topsoil and subsoil, we observed features that were influenced by the reclamation process. Moreover, μCT revealed structural pores inside the OM-rich aggregates of these samples. These aggregates, known as 'rolled aggregates', are typically formed on the conveyor belt during transportation of the reclamation soil in the area and can be rich in OM due to the admixture of old topsoil (Luvisol) (Pihlap et al., 2019, Chapter 2). In contrast, the sample from the tilled topsoil was characterised by a tillage-induced structure and contained distinctively shaped, OM-rich aggregates (Fig. 6.3, areas B-C 11-12 and K11-12). Segmentation and analysis of the soil composition in undisturbed soil cores defined their 2D spatial distribution and their heterogeneity in 53 μm resolution from samples of 3 cm diameter.

Correlative imaging allowed the enhancement of the information obtained by imVNIR with data provided by μCT. Hence, we were able to correlate the compositional information of the solid phase with the soil structure, such as the OM distribution as a function of the 3D Euclidean distance to pores and biopores (Fig. 6.5). Nowadays, besides imVNIR, several techniques are available for chemical mapping of 2D slices, such as SEM-EDX, near edge X-ray absorption fine structure spectroscopy, nanoSIMS, or matrix-assisted laser desorption/ionisation (Baveye et al., 2018). These techniques could be also applied for correlative analyses to obtain additional chemical information on the 3D pore structure derived from the μCT, as reported in the study of (Schlüter et al., 2019) for SEM-EDX and nanoSIMS analysis. Most of these techniques can even have a resolution on the nm scale and thus exceed the resolution of both imVNIR and μCT. However, high-resolution results in small sample sizes, thus limiting these techniques to microaggregate analyses (Baveye et al., 2018). In contrast, the combination of imVNIR and μCT can be applied to scan soil cores up to 10 cm width and infinite length. Thus the linkage between soil structure and soil composition can be investigated in larger soil volumes up to a complete pedon.

The methods employed in the present correlative imaging had different spatial resolutions. The resolution of the 3 cm scanned samples in X-ray μCT images was higher (19 μm) than that of the Vis-NIR images (53 μm), thus making only the pores with diameter >53 μm detectable, whereas local differences within the micropores (diameter <19 μm) could not be addressed. Alternatively, we analysed sub-resolution features from greyscale μCT images (Baveye et al., 2018) and used the grey values around macropores to normalise the OM contribution (Fig. 6.6). This normalisation indicated a closer linkage between the soil composition and the soil structural features, visible in μCT. Potentially, an even broader spectrum of pore sizes could be investigated using subsamples for μCT images and combining the information of pore size distribution from different sample sizes (Vogel et al., 2010). In the current study, we demonstrated that registering higher-resolution μCT images and combining them with imVNIR images expands the information level on the sub-resolution features in larger samples.

Correlative imaging with imVNIR and μCT revealed patterns in FeOx and OM distribution through the distance to pores and biopores (Fig. 6.5). The different trends in OM, as a function of distance to macropores, demonstrated that OM accumulated with increasing distance to macropores, most probably due to physical protection, as the absence of macropores may lead to a deficient aeration but may also hinder microorganisms of reaching OM (Dungait et al., 2012). The comparison between the tilled topsoil and subsoil samples revealed how tillage affects the OM distribution, as shown by previously observed homogenised OM distribution (Kay et al., 2002; Yang et al., 1999). In contrast to our expectations, we did not identify higher OM quantities in biopore walls; in some samples even lower intensities were detected (Fig. 6.5), perhaps due to local differences in macroporosity that were higher close to biopores (Fig. 6.6). When the OM contribution was normalised according to the density

shift from μCT, the OM in the no-tilled topsoil and subsoil was higher next to the walls of biopores compared with that in bulk soil (Fig. 6.6). Consequently, based on the OM quantity per gram soil, the OM content would be higher close to pore walls. Considering that the impact of soil management on carbon stabilisation has been particularly investigated (Cárcer et al., 2019; Chivenge et al., 2007; Follett, 2001), correlative analysis with imVNIR and X-ray μCT may broaden our understanding of OM distribution, associated with physical protection due to its location in the porous soil.

6.5   Conclusion

In this study, we present an approach for the identification and correlation of soil chemical composition and pore structure in intact soil cores. To that end, we developed a novel combination of 2D imVNIR and 3D μCT through registration and correlative analysis. As a proof of principle, we analysed three intact soil samples, each with two slices that differed in soil structure and OM content (no-tilled topsoil, tilled topsoil and subsoil). Correlative analysis along with 3D soil structural information about pores can give new insights into the linkage between the biopore network and the soil chemical composition including OM distribution. The analysis indicated that, when the soil is not disturbed by tillage, OM accumulates and is more protected as the distance to macropores increases. μCT data gave valuable input not only by locating pores and biopores but also through local shifts in bulk density. As both techniques give complementary and partly corroborating information on the same material, the development of the applied method improves our understanding on the spatial distribution of soil components and their correlation to soil structure.

Chapter 7

Synthesis and Conclusion

7.1 The use of X-ray μCT to characterize the soil structure

The main objective of the present was to quantify the role of plants on soil structure formation over time. To do so, undisturbed samples from a chronosequence had to be analysed with X-ray μCT. Thus, numerous demands were made on this method to disentangle the effect of roots on pore structure from other processes like tillage. In addition to state-of-the-art imaging analysis techniques, this thesis presented several new or further developed protocols:

1. By extending the nested strategy from Schlüter et al. (2018b) to three different sample diameters, the disadvantage of the method, which results from the trade-off between sample size and resolution, could be minimised (Fig. 5.1). Hence, all scales at which changes on the pore structure over time occurred could be covered (Fig. 3.6).

2. A new protocol was developed to detect biopores by their tubular shape (Fig. 3.3). The development of biopores with different diameters down to 38 µm could therefore be described for the first time.

3. Root induced compaction could be analysed using a composition of different images containing different information such as euclidean distances to roots/biopores and porosity (Fig. 4.1). This enabled a fast analysis of gradients around roots/biopores of different sizes with the software Fiji.

4. Chapter 5 reveals how to account for the scale dependence of connectivity measures. It was shown, how a joint evaluation of two connectivity metrics could be used to disentangle different pore types with χ and to identify the contribution of different pore types to the overall pore connectivity with Γ. Since Γ gives highly biased information in small samples a joint-Γ-curve was created, which accounts for this problem.

5. In Chapter 6 a new method for the combination of imVNIR and X-ray µCT was introduced, which can provide new insights on how soil structure affects biogeochemical processes.

In combination with the vast number of samples, which is unique for X-ray µCT studies, the analysis of X-ray µCT images could be used to representatively describe changes in soil structure. Thus, this thesis is able to provide the first comprehensive analysis of soil structure formation through the action of plants by establishing a quantitative framework for detecting changes in three-dimensional pore structure over time.

7.2 Soil structure formation through the action of plants

When roots grow into soil, they interact with the structures surrounding them (Fig. 7.1). The most obvious finding to emerge from this study is that a complex system of biopores

was created on the chronosequence, which reached an equilibrium state already 6 years in the topsoil and 12 years after reclamation in the subsoil (Fig. 3.9). The biopore length distribution revealed that the majority of these biopores were between 0.04 and 0.25 mm in diameter. The distribution of these corresponded to the root diameters of the cultivated plants over time (Fig. F.1). This shows that the majority of biopores are the result of growing plant roots. Thus, plants were able to connect pores between 0.1 mm and 0.5 mm which resulted in a highly connected macropore system (Fig. 5.3). Consequently, this should increase infiltration and preferential flow phenomena (Jarvis, 2007; Koestel et al., 2014; Naveed et al., 2013; Rasse et al., 2000; Wuest, 2001). In addition, for this relatively dense soil (Table 4.1), plants should benefit from this connected system, as they can bypass dense areas and thus get access to nutrients and water from deeper soil layers (Gao et al., 2016).
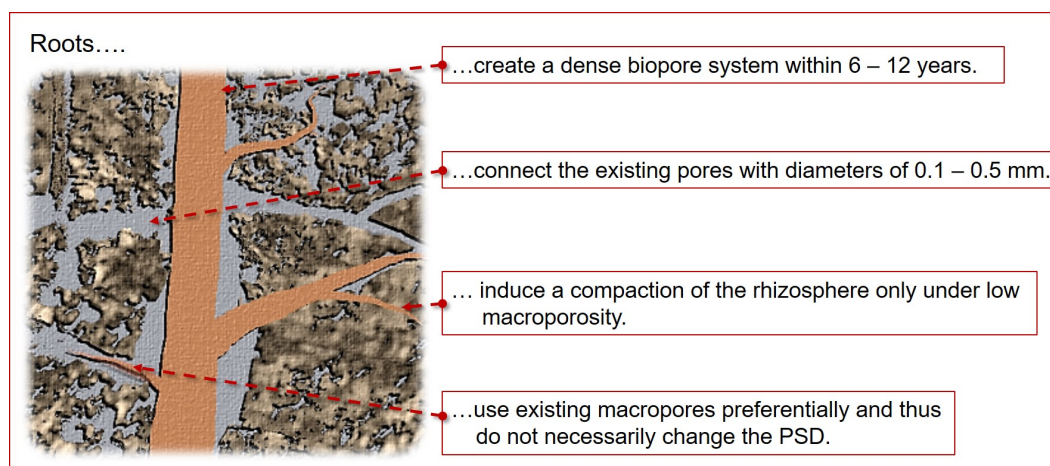
FIGURE 7.1: *Summary of the main changes on soil structure by roots.*

Besides changes of soil structure through plant roots, soil structure also influences plant growth. Therefore, one of the most important results of this work is the importance of considering this mutual interaction for soil structure formation through the plant. Or in other words, this means that the effect of plants on soil structure cannot be predicted without the context of their surrounding environment. This is particularly evident in two findings of this thesis:

1. Immediately after recultivation lucerne created large biopores and later the cereals used in the crop rotation led to the formation of a dense system of biopores (Fig. C.4). However, there were no significant changes of the pore size distribution over time due to plant growth (Fig. 3.4). This shows, that the existing system of macropores offered enough space for the plants to grow, and thus they only had to rearrange the existing pore-system without significantly increasing the macroporosity.

2. The rhizosphere of plants was only compacted when they grew into a soil with a small volume of unconnected macropores but not in soils providing a sufficient volume of macropores or in which mechanical impedance did not allow roots to penetrate into the soil (Fig. 4.11, 4.6). This finding could only be explained by merging (a) the mechanistic physical effect of root growing into the soil pushing particles to the side and inducing compaction during the creation of new pores, and (b) plant interaction with existing soil pore structure, i.e. root growing in existing macropores with larger diameters than the root itself (Fig. 4.11). Thus, this thesis reconciles contradictory results from previous studies where on the one hand root induced compaction was measured (Aravena et al., 2011; Bruand et al., 1996; Koebernick et al., 2019) or on the other hand

an increase in porosity was described (Feeney et al., 2006; Helliwell et al., 2017; Koebernick et al., 2017; Whalley et al., 2005).

However, the increase in biopore density in the subsoils of the chronosequence also led to an increase in compaction of the former rhizosphere (Fig. C.5). This reveals that with increasing biopore density the existing macropore system may not provided enough macropores (Fig. 4.9). Therefore, there was a need for a compaction of mesopores, which led to the compaction of biopore walls. At the same time, it is possible that new biopores may be created by the destruction of old biopores. This would be an explanation for the biopore densities reaching a plateau after 12 years in the subsoil. This assumption can be supported by the observation that the compaction of the biopore wall within these samples reached up to a distance of 1 mm into the bulk soil (Fig. 4.9) and at the same time the typical Euclidean distances between biopores decreased to 2-3 mm (Fig. 3.10). Under such conditions, a root could either expand into the space between two biopores and thus pushing aside the surrounding soil and destroying existing biopores or grow into existing biopores. The differences in rhizosphere porosity on the fields, certainly had an affect on transport of water and nutrients to the roots. For example an increase in water flow to the roots in non saturated conditions for a compacted rhizosphere could be expected (Aravena et al., 2011, 2014; van Veelen et al., 2019).

The SOC concentration of the topsoil increased during the 6 years after reclamation (Table 2.1), analogous to the increase in the biopore density. Yet, this increase was mainly caused by the change in management after 3 years, from an initial pioneering phase to an agricultural management phase, including tillage and increased use of organic fertiliser (Chapter 2.4.2). However, in parallel to the biopore density, the concentration of SOC and microbial abundance were the highest in the subsoil of the 12 year old field. This indicates that roots may be an important factor in transporting organic material into the subsoil and after decay leave behind biopores that can be hotspots for nutrient mobilisation for several years (Banfield et al., 2018).

In contrast to the formation of biopores, the change in soil management and thus the beginning of periodic loosening of the soil by tillage led to a shift in pores >0.05 mm in diameter towards pores >0.20 mm. Hence, the connectivity of pores >0.20 mm was increased in the tilled topsoils compared to the subsoil (Fig. 5.4). Surprisingly, however, there were also many fragmented biopores in the tilled topsoil. (Fig. C.4). These were able to connect more randomly distributed pores created by tillage in the topsoil (Fig. 5.6). The presence of these biopores suggests that they tolerated tillage in large aggregates (>6.3 mm) that were predominant in all samples of the chronosequence, including ploughed topsoils (Fig. 2.4), due to the stability induced by the high $CaCO_3$-concentrations (Table 2.1).

7.3 Outlook and recommendation

A chronosequence has the big advantage to observe soil structure formation on the field scale. Although the biopore length densities could be quantified over time, one of the limitations of this thesis is that a quantification of the re-use of existing biopores was not possible. Although visual expectation of the images often revealed, that roots grew into existing biopores, the turnover rate of the biopores, i.e. to which extend biopores are reused or destroyed and renewed, could not be observed. However, this thesis provides the methodological tools (e.g. segmentation of biopores and roots) to do so in future research.

Root system architecture plays a critical role in the two-way interaction of plant roots and soil structure (Bacq-Labreuil et al., 2019b; Pierret et al., 2011). Despite the large number of samples, the underlying data set offers only limited possibilities to distinguish the effect

of different plant species on soil structure as only 6 time-points out of 24 years were investigated. Thus, the development of biopores over time to an equilibrium biopore density, after 6 years in the topsoil and 12 years in the subsoil, may have taken place slightly earlier, since no information is available between the sampled years. In addition, use of other plants in the crop rotation, could probably have led to other degrees of root induced compaction on the fields (Helliwell et al., 2019).

As stated in the above section the effect of plants on soil structure cannot be predicted without the context of the surrounding environment. This shows that the effect of plant on soil structure over time could be quite different on other soils. For example, Bacq-Labreuil et al. (2019a) showed in pot experiments, that plants effect macroporosity and pore connectivity differently in two different soil textures (clay and sandy soil). In addition, the high clay content and the high $CaCO_3$-content lead to a high stability of soil macroaggregates (Table 2.1, Fig. 2.4). Thus, in a different substrate, e.g. sandy soils, biopores are less stable (Schneider et al., 2019), which would have led to a lower equilibrium biopore density.

Future research should focus on these different factors influencing root-soil interaction to fully characterise soil structure formation through the action of plants under different environmental conditions. Fig. 4.10 shows that repacking of soil columns produces a completely different soil structure as compared to the field. Therefore, it has to be considered that the porosity of the rhizosphere may be completely different on the field. Thus, to understand and quantify processes related to rhizosphere physics, one should focus more on experiments on fields or at least on undisturbed field samples. As Baveye et al. (2018) stated:

> "We are often forced by journals to use repacked soil columns in order to have actual replicates, and be able to calculate statistics, which some reviewers view as sacred and indispensable."

However, the experiment conducted in Chapter 4 shows that pot experiments under controlled conditions are still a helpful tool to disentangle these different factors.

An issue that was only marginally addressed in this study was how changes in structure are linked to soil functions. A major disadvantage of the HYPROP-method used here is that hydraulic properties in the macropore range can hardly be covered (Fig. 3.6). By using devices like tension infiltrometer, the influence of the biopores on the conductivity close to saturation could have been measured.

However, this unique data set of pore structure may also be the groundwork for future modelling applications, e.g. the influence of root induced compaction of water flow towards the root could have be modelled like shown in Aravena et al. (2014).

Notwithstanding the relatively limited sample number in Chapter 6, this thesis offers a valuable new method investigating the influences of soil structure on biogeochemical processes. Figures 6.5 and 6.6 show the potential of the correlative analysis of X-ray μCT and imVNIR. It was shown, that OM is mainly found far away from macropores due to physical protection and that the amount of organic material around biopores may also depend on local gradients in macroporosity. As this shows the potential of this method a natural progression of this work would be to analyse a larger amount of samples, e.g. to further investigate how to increase physical protection of organic material by improving soil structure.

Appendix A

Appendix for chapter 2

TABLE A.1: *Reaction composition, thermal profiles and primer references of qPCR reactions used in this study.*

Target genes	PowerSYBR Green (μl)	F and R primer (μl)	BSA (μl)	Initial denaturation time at 95 °C (min)	Touchdown Thermal profile	Touchdown No. of cycles	Thermal profile	No. of cycles	Primers and references	Standard plasmid sources
16S rRNA bacteria	12.5	0.5	0.5	10	-	-	95 °C (45s) 58 °C (45s) 72 °C (45s)	40	FP, RP (Bach et al., 2002)	*Pseudomonas putida*
16S rRNA archaea	12.5	0.5	0.5	10	95 °C (20s) 55 °C (60s)* 72 °C (60s)	5	95 °C (15s) 50 °C (30s) 72 °C (30s)	40	rSAf(i) (Nicol et al., 2005), 958r (Bano et al., 2004)	Methanobacterium sp.
ITS	12.5	1	-	10	-	-	94 °C (30s) 50 °C (30s) 72 °C (30s)	40	ITS1, ITS4 (White et al., 1990)	*Trichoderma reesei*

* -1 °C/cycle

TABLE A.2: *Mean values of macroporosity [Vol-%] and bulk density [g cm^{-3}]. Equivalent mass represents soil mass per volume that was used for SOC stock calculations according to equivalent mass approach (Ellert et al., 1995). Equivalent height represents soil depth correction according to the equivalent mass. Standard deviations are calculated from field replicates (n=3, except at 3 years where n=2).*

Reclamation age [years]	Depth [cm]	Macroporosity [Vol-%]	Bulk density [g cm^{-3}]	Equivalent mass [kg m^{-2} cm^{-1}]	Equivalent height [cm]
0		2.29 ± 0.15	1.47 ± 0.01	14.6 ± 0.1	10.0 ± 0.0
1		2.28 1.09	1.58 ± 0.01	-	9.2 ± 0.1
3		3.11 ± 2.12	1.60 ± 0.01	16.0 ± 0.1	9.1 ± 0.1
6	1-5	9.18 ± 2.27	1.46 ± 0.02	14.6 ± 0.2	11.0 ± 0.2
12		10.23 ± 3.42	1.46 ± 0.02	-	10.0 ± 0.1
24		9.31 ± 5.62	1.55 ± 0.04	15.5 ± 0.4	9.5 ± 0.3
Mature		-	1.28 ± 0.04	-	12.2 ± 0.7
0		2.18 ± 1.58	1.63 ± 0.01	16.3 ± 0.1	20.0 ± 0.0
1		1.45 ± 0.90	1.64 ± 0 03	-	19.9 ± 0.2
3		0.96 ± 0.58	1.62 ± 0.01	16.2 ± 0.1	20.2 ± 0.2
6	16-20	6.55 ± 0.98	1.45 ± 0.03	14.5 ± 0.3	22.5 ± 0.4
12		9.24 ± 3.58	1.53 ± 0.06	-	19.1 ± 1.0
24		7.26 ± 5.49	1.55 ± 0.04	15.5 ± 0.4	18.8 ± 0.2
Mature		-	1.43 ± 0.03	-	21.7 ± 0.7
0		-	1.58 ± 0.07	15.8 ± 0.7	20.0 ± 0.0
1		4.62 ± 0.56	1.66 ± 0.04	-	19.0 ± 1.0
3		2.89 ± 0.89	1.40 ± 0.03	14.0 ± 0.3	22.1 ± 0.6
6	41-45	4.04 ± 2.12	1.63 ± 0.06	16.3 ± 0.6	17.2 ± 0.7
12		2.24 ± 0.49	1.50 ± 0.08	-	21.7 ± 0.9
24		3.49 ± 1.04	1.52 ± 0.03	15.2 ± 0.3	21.5 ± 1.1
Mature		-	1.48 ± 0.07	-	20.6 ± 1.4

TABLE A.3: *F-values and R-squares from the general linear model with setting reclamation age and soil management as main influencing factors. Significance levels: $*p \leq 0.05$, $**p \leq 0.01$, $***p \leq 0.001$ and ns-no significance.*

1-5 cm

	Macro-porosity	Bulk density	SOC	TN	C/N	DOC	DON	Cmic	Nmic	Cmic/Nmic	DNA	Bacteria	Fungi	Archaea
Corrected model	4.567*	23.046***	42.716***	21.351***	29.686***	5.750**	19.804***	16.954***	21.325***	13.471***	2.342ns	2.214ns	9.116***	8.966***
Intercept	64.804***	80050.669***	1454.833***	1593.194***	3982.454***	123.781***	2401.478***	697.343***	262.278***	274.348***	204.142***	7206.56***	358.670***	269.472***
Reclamation age	4.567*	23.046***	42.716***	21.351***	29.686***	5.575**	19.804***	16.954***	21.325***	13.471***	2.342ns	2.214ns	9.116***	8.966***
R square	0.675	0.913	0.951	0.907	0.931	0.723	0.9	0.885	0.906	0.86	0.502	0.806	0.803	0.713
Adjusted R square	0.527	0.873	0.929	0.864	0.9	0.597	0.855	0.864	0.88	0.833	0.295	0.75	0.713	0.576
Corrected model	29.853***	2.988ns	38.579***	28.063***	22.292***	0.403ns	2.585ns	4.096ns	2.816ns	3.782ns	9.305**	0.183ns	24.745***	8.790*
Intercept	86.596***	11582.019***	340.087***	576.803***	950.129***	50.265***	41.068***	2039.811***	122.598***	46.553***	138.772***	5143.639***	57.938***	
Soil management	29.853***	2.988ns	38.579***	28.063***	22.929***	0.403ns	2.585ns	4.096ns	2.816ns	3.782ns	9.305**	0.183ns	24.745***	8.790*
R square	0.666	0.166	0.72	0.652	0.605	0.026	0.147	0.215	0.201	0.383	0.012	0.623	0.369	0.262
Adjusted R square	0.643	0.111	0.701	0.628	0.578	-0.039	0.09	0.162	0.148	0.342	-0.054	0.597	0.327	0.213

16-20 cm

	Macro-porosity	Bulk density	OC	TN	C/N	DOC	DON	Cmic	Nmic	Cmic/Nmic	DNA	Bacteria	Fungi	Archaea
Corrected model	3.957*	13.991***	34.424***	45.898***	7.996**	3.219*	18.592***	4.189*	9.547***	6.832**	6.306**	2.627ns	2.829ns	5.347**
Intercept	40.999***	36641.838***	654.576***	755.967***	1352.976***	148.261***	1710.68***	499.28***	186.854***	194.352***	62.718***	213.673***	19.928***	385.975***
Reclamation age	3.957*	13.991***	34.424***	45.898***	7.996**	3.219*	18.592***	4.189*	9.547***	6.832**	6.306**	2.627ns	2.829ns	5.347**
R square	0.643	0.864	0.94	0.954	0.784	0.594	0.894	0.656	0.813	0.756	0.741	0.544	0.563	0.709
Adjusted R square	0.48	0.802	0.913	0.933	0.686	0.41	0.846	0.499	0.728	0.646	0.624	0.337	0.364	0.576
Corrected model	21.738***	33.150***	106.136***	94.149***	23.552***	0.226ns	15.055**	22.725***	42.314***	17.724***	40.268***	2.969ns	10.116**	5.337**
Intercept	50.658***	22232.324***	446.019***	342.701***	1037.775***	2134.842***	489.722***	605.627***	3494.974***	139.054***	83.945***	168.786***	21.201***	207.748***
Soil management	21.738***	33.150***	106.136***	94.149***	23.552***	0.226ns	15.055**	22.725***	42.314***	17.724***	40.268***	2.969ns	10.116**	5.337**
R square	0.592	0.688	0.876	0.863	0.611	0.015	0.501	0.602	0.738	0.542	0.729	0.165	0.403	0.262
Adjusted R square	0.564	0.668	0.868	0.853	0.585	-0.051	0.468	0.576	0.721	0.511	0.71	0.11	0.363	0.213

TABLE A.4: *F-values, coefficients and R-squares of the linear regression model with setting SOC, bulk density and macroporosity as independent variables. Significance levels: *p≤ 0.05, **p≤ 0.01, ***p≤ 0.001 and ns-no significance.*

Depth	Var	Metric	Macro-porosity	Bulk density	SOC	TN	C/N	DOC	DON	Cmic	Nmic	Cmic/Nmic	DNA	Bacteria	Fungi	Archaea
1-5 cm	SOC	Regression F-value	12.122**			408.986***	80.490***	0.385ns	7.580*	4.498*	19.946***	20.323***	29.669***	1.698ns	1.685ns	9.871**
		Constant	-1.216ns			0.144***	5.076***	-4.514***	0.000ns	0.405***	0.003ns	134.841***	-0.002ns	528413.460***	230811.122***	7187.338ns
		Coefficient	1.661**			0.068***	0.991***	0.046ns	0.001**	0.012*	0.002***	-16.744***	0.005***	43643.135ns	-26780.984ns	2608.588**
		R square	0.447			0.965	0.843	0.025	0.336	0.231	0.571	0.575	0.664	0.102	0.101	0.397
		Adjusted R square	0.41			0.962	0.832	-0.04	0.291	0.179	0.542	0.547	0.642	0.042	0.041	0.357
	Bulk density	Regression F-value	3.455ns		0.218ns	0.001ns	0.071ns	0.004ns	0.113ns	0.404ns	2.033ns	3.148ns	1.040ns	4.102ns	5.956*	0.319ns
		Constant	53.847ns		0.737ns	0.470ns	6.239ns	-4.090ns	-0.002ns	0.642*	-0.023ns	9.057ns	-0.045ns	-208411.579ns	-2.132ns	-7545.975ns
		Coefficient	-31.492ns		1.586ns	-0.013ns	2.173ns	-0.142ns	0.005ns	-0.121ns	0.022ns	-3.379ns	0.042ns	1857703.574ns	8.723*	17490.334ns
		R square	0.187		0.014	0	0.005	0	0.007	0.026	0.119	0.173	0.065	0.215	0.284	0.021
		Adjusted R square	0.133		-0.051	-0.067	-0.062	-0.066	-0.059	-0.039	0.061	0.118	0.003	0.162	0.237	-0.044
	Macroporosity	Regression F-value		3.455ns	12.122**	9.360**	11.728***	0.019ns	1.495ns	5.873*	1.246ns	1.269ns	6.188*	0.389ns	10.035**	6.951*
		Constant		1.549***	2.809ns	0.342***	7.728***	-4.279***	0.004*	0.426***	0.008***	4.142***	0.011*	669681.840***	11.942***	13044.328***
		Coefficient		-0.006ns	0.000**	0.017**	0.288**	-0.004ns	0.000ns	0.005*	0.000ns	-0.031ns	0.001*	8752.793ns	-0.142**	937.743*
		R square		0.178	0.447	0.384	0.439	0.001	0.091	0.281	0.077	0.078	0.292	0.025	0.401	0.317
		Adjusted R square		0.133	0.41	0.343	0.401	-0.065	0.03	0.233	0.015	0.017	0.245	-0.04	0.361	0.271
16-20 cm	SOC	Regression F-value	12.527**			683.954***	22.738***	0.464ns	17.198***	11.518**	30.563***	15.582***	11.291**	4.236ns	5.739*	4.143ns
		Constant	0.611ns			0.092***	7.345***	-4.125***	-0.003ns	0.269***	-5.889***	94.459***	0.003ns	429563.666***	202584.260***	18754.638***
		Coefficient	0.873**			0.079***	0.465***	-0.020ns	0.003***	0.019**	0.174***	-7.017***	0.002**	28102.655ns	-20374.664*	1145.990ns
		R square	0.455			0.979	0.603	0.03	0.534	0.434	0.671	0.51	0.429	0.22	0.277	0.216
		Adjusted R square	0.419			0.977	0.576	-0.035	0.503	0.397	0.649	0.477	0.391	0.168	0.228	0.164
	Bulk density	Regression F-value	8.220*		63.518***	75.969***	11.364**	1.719ns	19.597***	11.223**	16.292***	9.003**	25.684***	7.178*	6.670*	3.191ns
		Constant	7.029**		63.737***	5.223***	35.378***	-6.673**	0.193***	1.615***	5.017ns	-333.741*	0.197***	2796642.180**	-1303235.895*	91867.086*
		Coefficient	-13.138*		-37.567***	-3.030***	-16.444***	1.562ns	-0.116***	-0.799**	-6.418***	251.463**	-0.117***	-1422952.628*	897532.641*	-43096.042ns
		R square	0.354		0.809	0.835	0.431	0.103	0.566	0.428	0.521	0.375	0.631	0.324	0.308	0.175
		Adjusted R square	0.311		0.796	0.824	0.939	0.043	0.538	0.39	0.489	0.333	0.607	0.279	0.262	0.12
	Macroporosity	Regression F-value		8.220*	12.527**	13.707**	12.078**	0.082ns	4.062ns	5.812*	17.702***	10.663**	7.049*	0.035ns	6.677*	1.819ns
		Constant		0.479***	2.310*	-1.319***	8.098***	-4.255***	-5.967***	0.305***	0.004**	84.222***	-5.361***	554387.321***	184399.945***	21263.837***
		Coefficient		-0.027*	0.521*	0.090**	0.310**	0.007ns	0.153ns	0.012*	0.001***	-4.897***	0.140*	2225.665ns	-16612.848*	626.095ns
		R square		0.354	0.455	0.477	0.446	0.005	0.213	0.279	0.541	0.416	0.32	0.002	0.308	0.108
		Adjusted R square		0.311	0.419	0.443	0.409	-0.061	0.161	0.231	0.511	0.377	0.274	-0.064	0.262	0.049

TABLE A.5: *Pearson's correlation between years 0-3. Only correlations that are statistically significant (*p≤ 0.05, **p≤ 0.01, ***p≤ 0.001 and ns-no significance) are presented in the table.*

1-5 cm

	Age	DOC	DON	Cmic	Nmic	DNA	Cmic/Nmic	Bacteria	Fungi	SOC	TN	C/N	Bulk density	Macroporosity
Age	X	-	0.920**	-	0.977**	0.992**	-0.879*	-	-	-	-	-	-	-
DOC		X	-	-	-	-	-	-	-	-	-	-	-	-
DON			X	-	0.931**	0.902**	-0.809*	-	-	0.915**	0.919**	0.857**	0.748*	-
Cmic				X	0.891**	-	-	-	-	-	-	-	-	-
Nmic					X	0.967**	-0.713*	-	-	0.942**	0.897**	0.816*	0.840**	-
DNA						X	-0.833*	0.824*	0.824*	0.914**	0.886**	0.852**	0.854**	-
Cmic/Nmic							X	-	-0.781*	-0.841*	-0.761*	-0.874*	-0.891*	-
Bacteria								X	-	-	-	0.859**	-	-
Fungi									X	-	-	-	-	-
SOC										X	0.976**	0.837**	0.887**	-
TN											X	0.751*	0.818*	-
C/N												X	0.908**	-
Bulk density													X	-
Macroporosity														X

16-20 cm

	Age	DOC	DON	Cmic	Nmic	DNA	Cmic/Nmic	Bacteria	Fungi	SOC	TN	C/N	Bulk density	Macroporosity
Age	X	-	-	-	-	-	-	-	-	-	-	-	-	-
DOC		X	-	-	-	-	-	-	-	-	-	-	-	-
DON			X	-	-	-	-	-	-	-	-	-	-	-
Cmic				X	-	-	-	-	-	-	-	-	-	-
Nmic					X	-	-	-	-	-	-	-	-	-
DNA						X	-	-	-	-	-	-	-	-
Cmic/Nmic							X	-	-	-	-	-	-	-
Bacteria								X	-	-	-	-	-	-
Fungi									X	-	-	-	-	-
SOC										X	-	-	-	-
TN											X	-	-	-
C/N												X	-	-
Bulk density													X	-
Macroporosity														X

TABLE A.6: *Pearson's correlation between years 3 and 6. Only correlations that are statistically significant (*p≤ 0.05, **p≤ 0.01, ***p≤ 0.001 and ns-no significance) are presented in the table.*

1-5 cm

	Age	DOC	DON	Cmic	Nmic	DNA	Cmic/Nmic	Bacteria	Fungi	SOC	TN	C/N	Bulk density	Macroporosity
Age	X	0.973**	-	-	-	-	-	-	-	-	-	-	-0.981**	-
DOC	-	X	0.939*	-	-	-	-	-	-0.927*	-	-	-	-0.944*	-
DON	0.904*	-	X	-	-	-	0.887*	-	-0.887*	-	-	-	-	-
Cmic	-	-	-	X	0.919*	-	-	-	-	-	-	-	-	-0.891*
Nmic	0.951*	-	0.936*	-	X	-	-0.989**	-	-	-	-	-	-	-0.979**
DNA	-	-	-	-	-	X	-	-	-	-	-	-	-	-
Cmic/Nmic	-0.884*	-	-	-	-	-	X	-	-	-	-	-	-	0.960**
Bacteria	0.938*	-	0.934*	-	-	0.920*	-0.912*	X	-	-	-	-	-	-
Fungi	-	-	-	-0.956*	-	-	-	-	X	-0.891*	-	-	-	-
SOC	0.909*	-	-	-	0.976**	-	-	-	-	X	0.966**	-	-	-
TN	0.931*	-	0.892*	-	0.987**	-	-	-	-	0.995**	X	-	-	-
C/N	-	-	-	-	-	-	-	-	-	-	-	X	-0.937*	-
Bulk density	-0.982**	-	-0.883*	-	-0.979**	-	-	-	-	-0.969**	-0.976**	-	X	-
Macroporosity	0.971**	-	-	-	0.942*	-	-0.914*	-	-	0.952*	0.959*	-	-0.987**	X

16-20 cm

TABLE A.7: *Pearson's correlation between years 6-24. Only correlations that are statistically significant (*p ≤ 0.05, **p ≤ 0.01, ***p ≤ 0.001 and ns-no significance) are presented in the table.*

1-5 cm

	Age	DOC	DON	Cmic	Nmic	DNA	Cmic/Nmic	Bacteria	Fungi	SOC	TN	C/N	Bulk density	Macroporosity
Age	X	-	-	-	-	-	-	-	-	-	-	-	0.772*	-
DOC	-0.689*	X	-	-	-	-	-	-	-	-	-	-	-	-
DON	-	0.789*	X	-	-	-	-	-	-	-	-	-	-	-
Cmic	-	-	-0.770*	X	-	-	-	0.747*	-	-	-	-	-	-
Nmic	-	-	-	-	X	-	-0.930**	-	0.717*	-	-	-0.703*	-	-
DNA	-	-	-	-	-	X	-0.807**	-	-	-	-	-	-	-
Cmic/Nmic	-	-	-	-	-0.930**	-0.807**	X	0.711*	-	-	-	-	-	-
Bacteria	0.703*	-	-	0.747*	-	-	0.711*	X	-	-	-	0.691*	-	-
Fungi	-	-	-	-	0.717*	-	-	-	X	-	-	-0.794*	-	-
SOC	-0.742*	-	-	-	-	-	-	-	-	X	0.810**	-0.675*	-0.675*	-
TN	-0.761*	-	0.713*	-	-	-	-	-	-	0.972**	X	-0.752*	-	-
C/N	-	-	-	-	-0.703*	-	-	0.691*	-0.794*	-0.675*	-0.752*	X	-	-
16-20 cm / **Bulk density**	0.730*	0.728*	-	-	-	-	-	-	-	-0.675*	-	-	X	-
Macroporosity	-	-	-	-	-	-	-	-	-	-	-	-	-	X

FIGURE A.1: *Research area in Garzweiler mining area.*
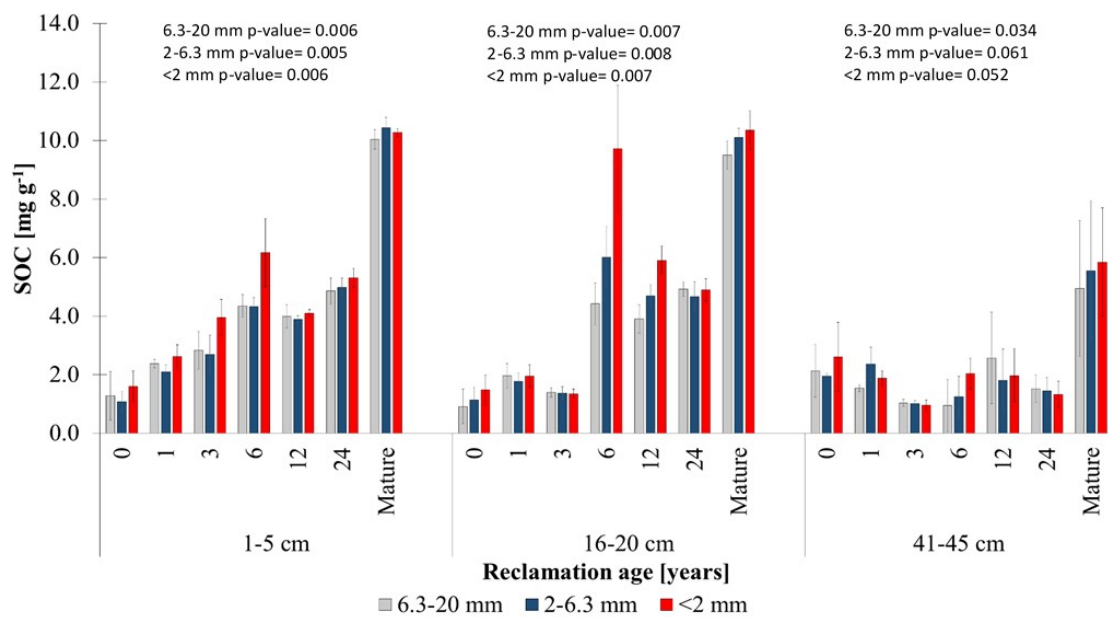
FIGURE A.2: *Mean SOC concentrations [mg g^{-1}] of the different aggregate size classes (<2 mm, 2-6.3 mm and 6.3-20 mm) at three sampling depths (1-5 cm, 16-20 cm and 41-45 cm) along the chronosequence and in the mature soil. Standard deviation is calculated through field replicates (n=3, except at 3 years n=2). P-value characterises significant difference within the sampling depth.*

Appendix B

Appendix for chapter 3

TABLE B.1: *Mean values and standard deviation of total visible porosity and different pore size classes. n = 3 plots, which in turn each are determined by the result of 15 CT scans (L3: n= 2). Asterisks shows significant differences at p<0.05 between the two layers of the 6, 12 and 24 year old fields. Different letters indicate significant differences in the two depths at p<0.05 between all fields.*

Depth	Field	Visible Porosity [%]		0.01 mm > ∅< 0.05mm [%]		0.05 mm > ∅< 0.2 mm [%]		∅>0.2 mm [%]	
0 – 20 cm	L0	23.7	± 2.2	17.1	± 3.1	4.1ab	± 0.8	2.5 ^{c}	± 0.9
	L1	24.1	± 3.0	18.5	± 3.4	3.1^{a}	± 0.1	2.5 ^{bc}	± 0.6
	L3	27	± 5.1	19.7	± 5.5	4.1^{ab}	± 0.4	3.2 ^{abc}	± 0.0
	B6	28.9	± 6.3	16.3	± 5.7	4.8^{ab}	± 0.3	7.9 ^{abc}	± 1.3
	W12	34.3	± 5.9	19.9	± 2.2	4.8^{ab}	± 1.3	9.6 ^{a}	± 4.9
	W24	33.6	± 9.9	19.5	± 4.0	4.6^{ab}	± 0.8	9.5 ^{ab}	± 5.5
40 – 60 cm	L1	28.9	± 8.6	15.3	± 4.2	7.1b	± 2.1	6.5 ^{abc}	± 2.6
	L3	35.6	± 2.8	25.0	± 0.7	5.8^{ab}	± 1.7	4.8 ^{abc}	± 1.7
	B6	25.5	± 3.6	15.4	± 2.7	5.7^{ab}	± 0.9	4.4 ^{abc}	± 0.7
	W12	32.9	± 5.1	23.4	± 3.6	6.1^{ab}	± 1.3	3.5 ^{abc}	± 0.6
	W24	31.6	± 4.0	21.1	± 2.6	5.6^{ab}	± 1.7	4.9 ^{abc}	± 2.3
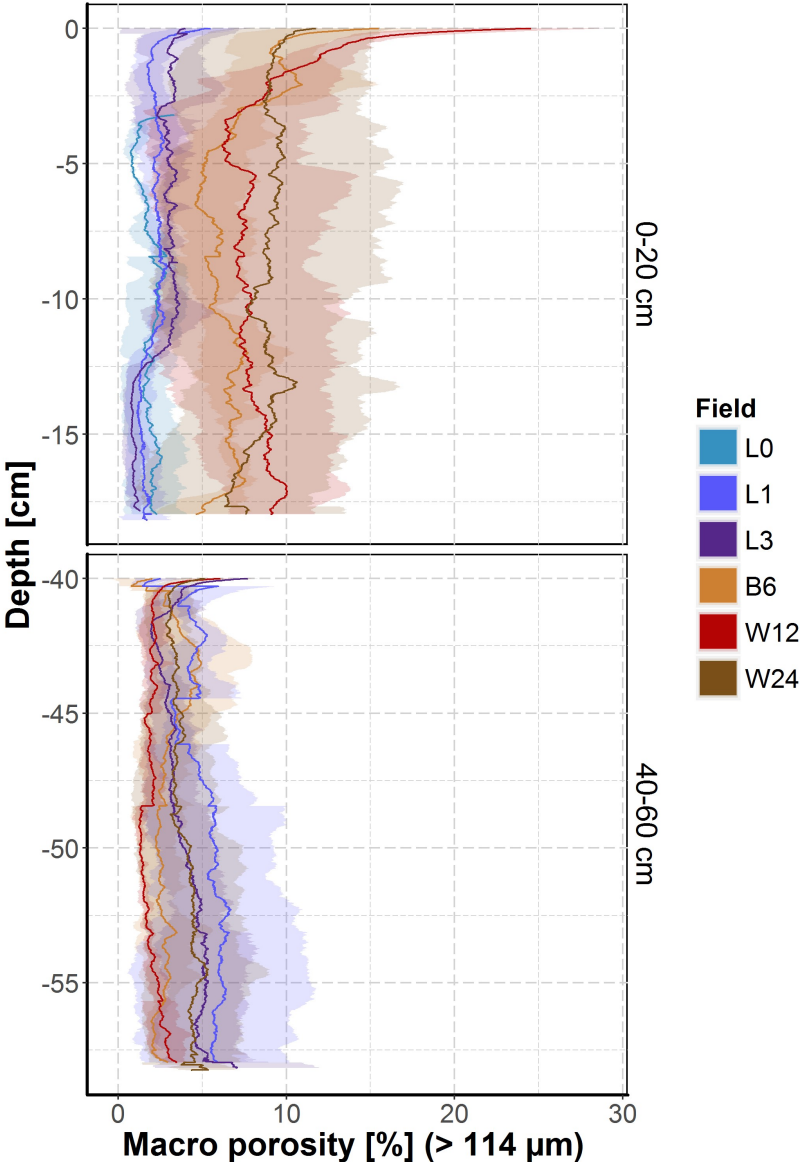
FIGURE B.1: *Mean values of macro porosity (coloured lines) and standard deviation (coloured shadows.*
n=9. L3: n=2) with soil depth.
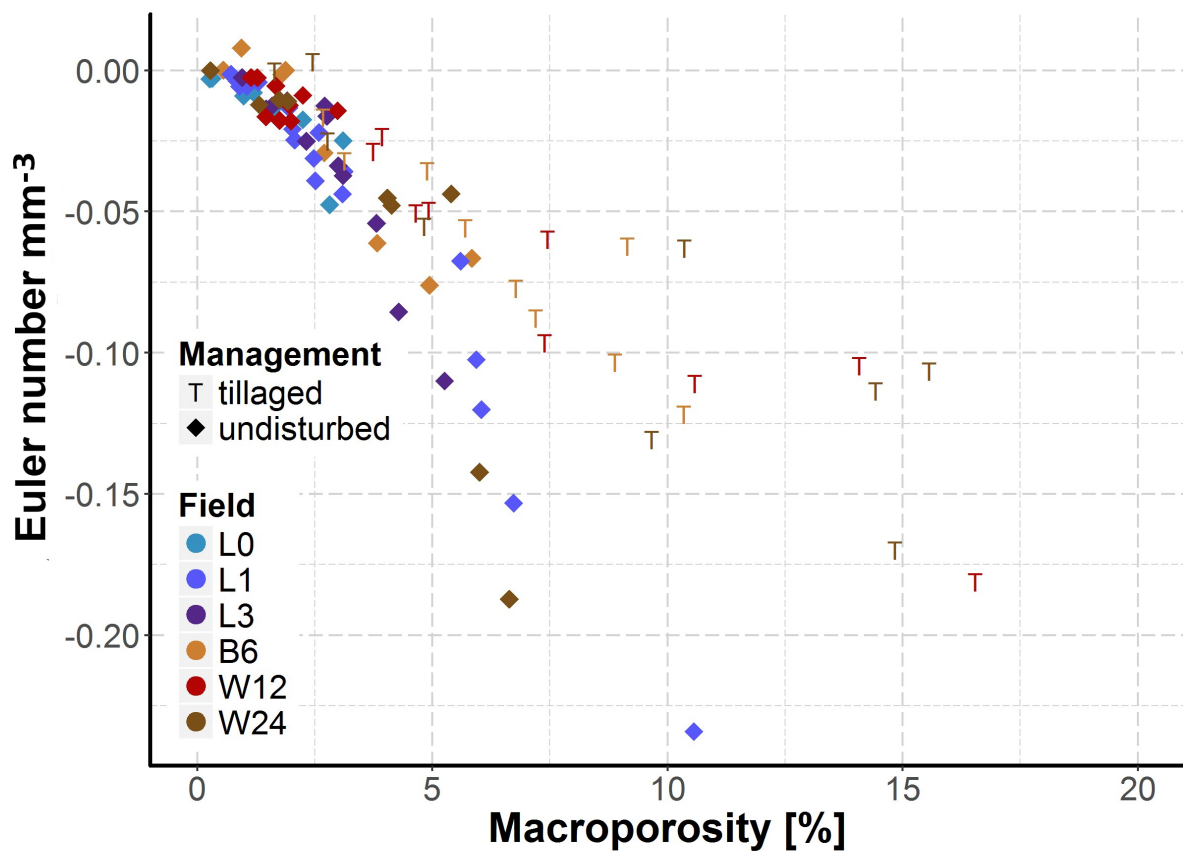
FIGURE B.2: *Comparison of the connectivity (Euler Number) plotted with the macroporosity in 10 cm soil columns. Low values of the Euler Number reveal a high amount of connections / redundant loops in a pore system.*
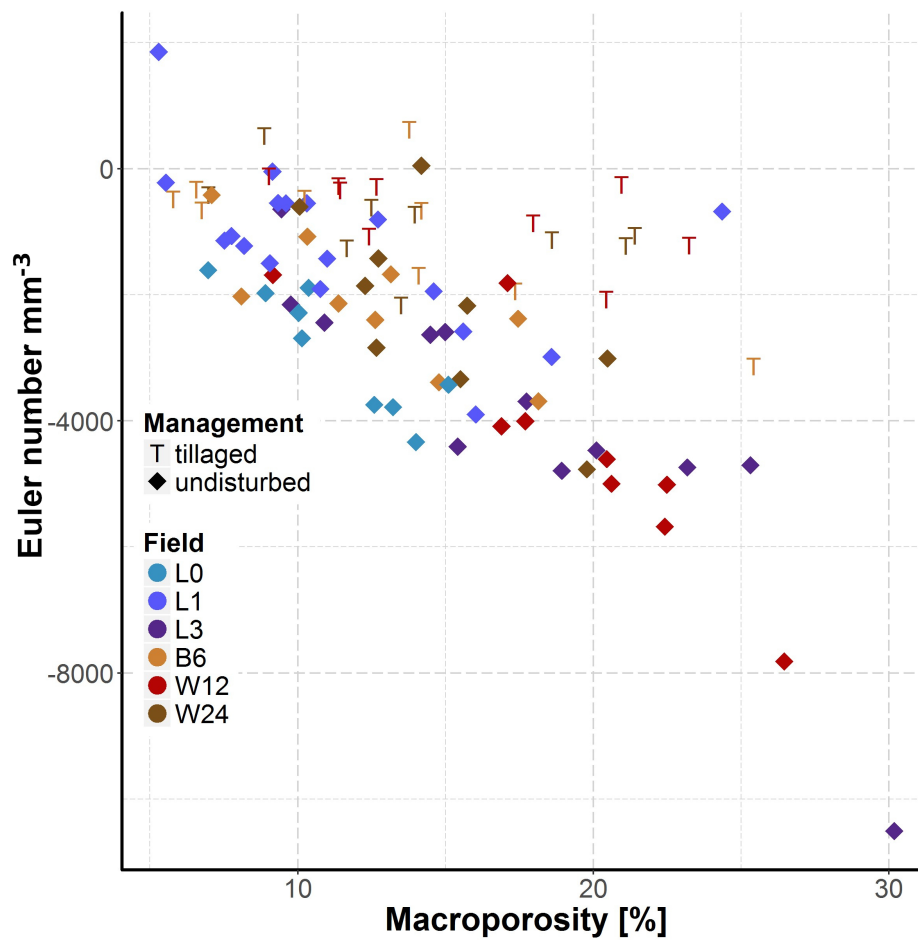
FIGURE B.3: *Comparison of the connectivity (Euler Number) plotted with the macroporosity in 7 mm subsamples. Low values of the Euler Number reveal a high amount of connections / redundant loops in a pore system.*
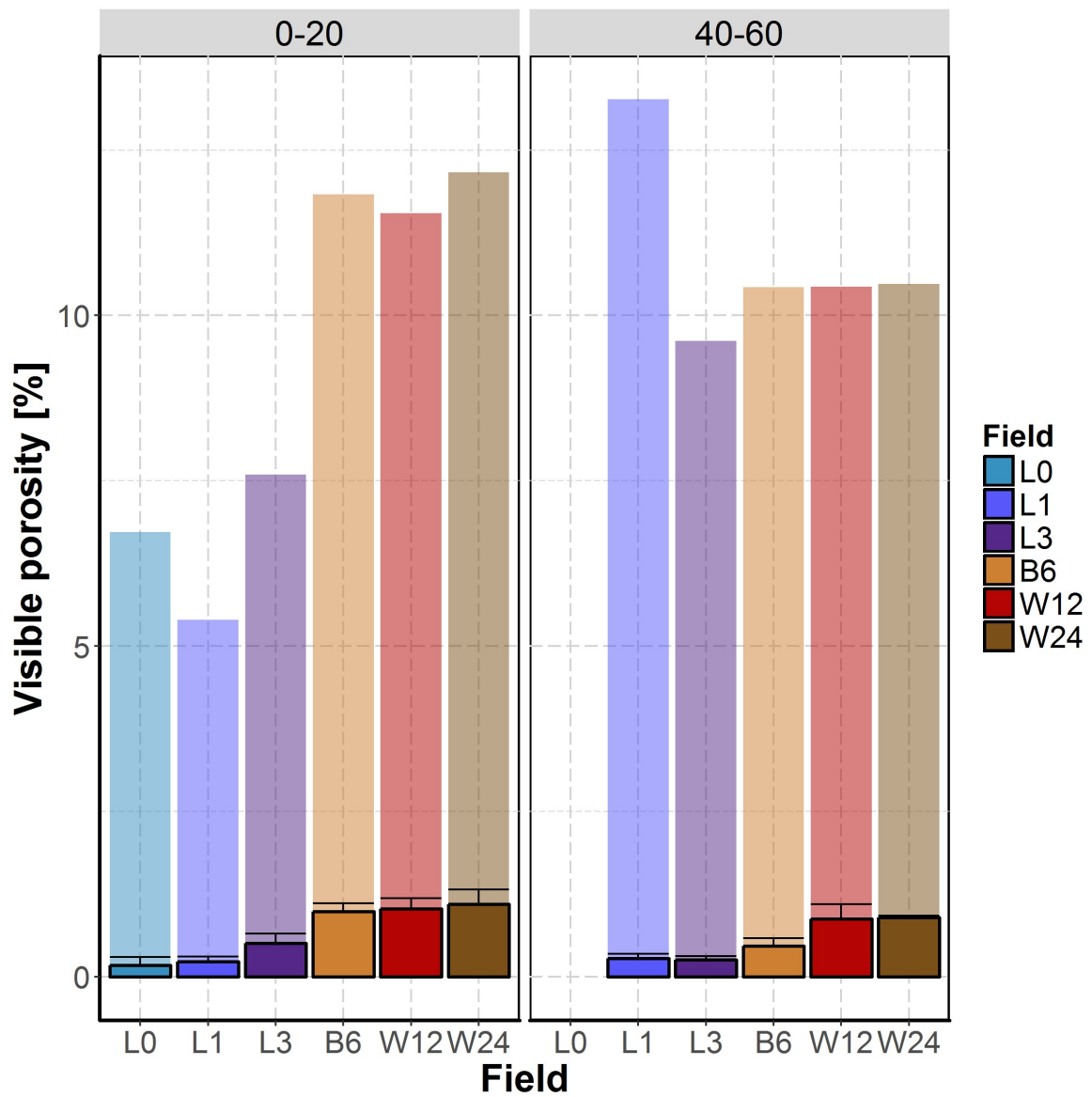
FIGURE B.4: *Mean Volume of biopores in 3x3 cm soil column of different ages and mean visible porosity (light bars). Error bars show standard deviation (n= 3 Plots. each represented by 9 soil columns. L3: n= 2).*

Appendix C

Appendix for chapter 4

TABLE C.1: *Mean values and standard error of plant dry weight and measured nutrients. Different letters indicate significant differences between treatments.*

	Treatment					
	1.30 [g cm^{-3}]		1.45 [g cm^{-3}]		1.60 [g cm^{-3}]	
Plant dry weight [g]	0.69a	$\pm$0.06	0.55^a	$\pm$0.06	0.24^b	$\pm$0.04
C [mg g^{-1}]	418.41^a	$\pm$1.02	418.45^a	$\pm$1.27	416.90^a	$\pm$2.39
N [mg g^{-1}]	28.60^a	$\pm$0.61	30.25^a	$\pm$0.59	30.15^a	$\pm$0.46
C/N-ratio [-]	14.66^a	$\pm$0.34	13.89^a	$\pm$0.34	13.83^a	$\pm$0.30
P [mg g^{-1}]	1.83^a	$\pm$0.04	1.74^{ab}	$\pm$0.05	1.59^b	$\pm$0.05
K [mg g^{-1}]	26.85^a	$\pm$0.61	28.46^a	$\pm$0.63	17.66^b	$\pm$0.55
Ca [mg g^{-1}]	15.51^{ab}	$\pm$0.77	14.45^b	$\pm$0.80	20.02^a	$\pm$0.63
Mg [mg g^{-1}]	5.13^a	$\pm$0.07	4.39^a	$\pm$0.23	4.90^a	$\pm$0.23
Mn [µg g^{-1}]	71.99^a	$\pm$2.68	68.05^a	$\pm$2.54	42.54^a	$\pm$2.10
Fe [µg g^{-1}]	93.38^{ab}	$\pm$3.94	105.29^a	$\pm$4.12	89.78^b	$\pm$5.05
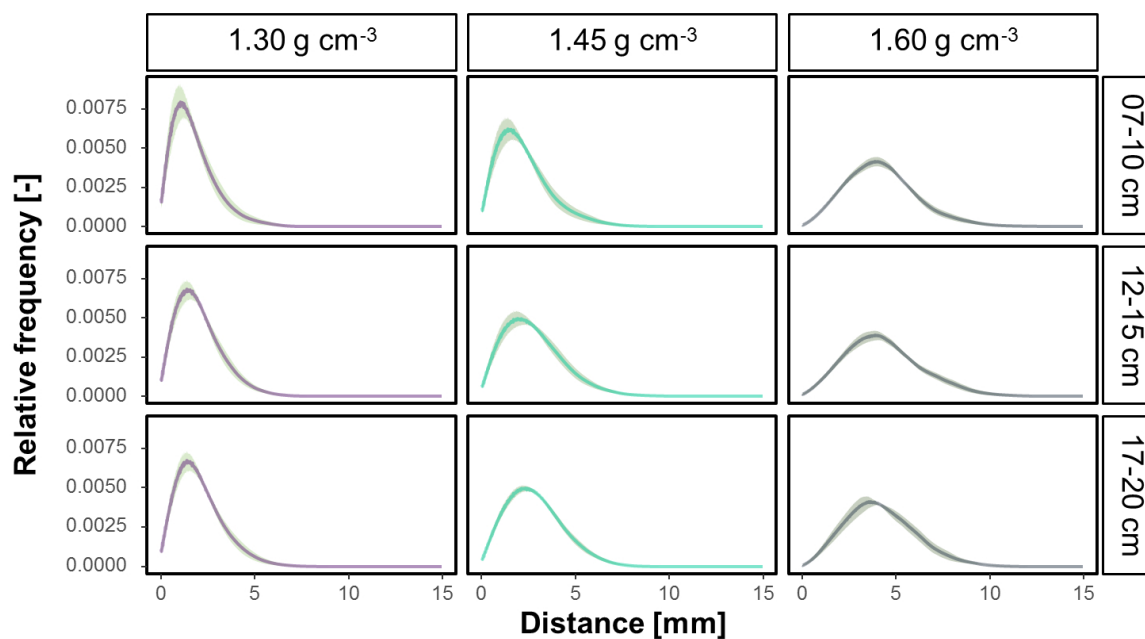
FIGURE C.1: *Frequency histograms of the Euclidean distance from soil voxels to the next root for each of the three different treatments (bulk density of 1.30, 1.45 and 1.60 g cm^{-3}) and depth within column (7 – 10 cm, 12-15 cm, 17-20 cm). Shadows indicate the standard error (n=5).*
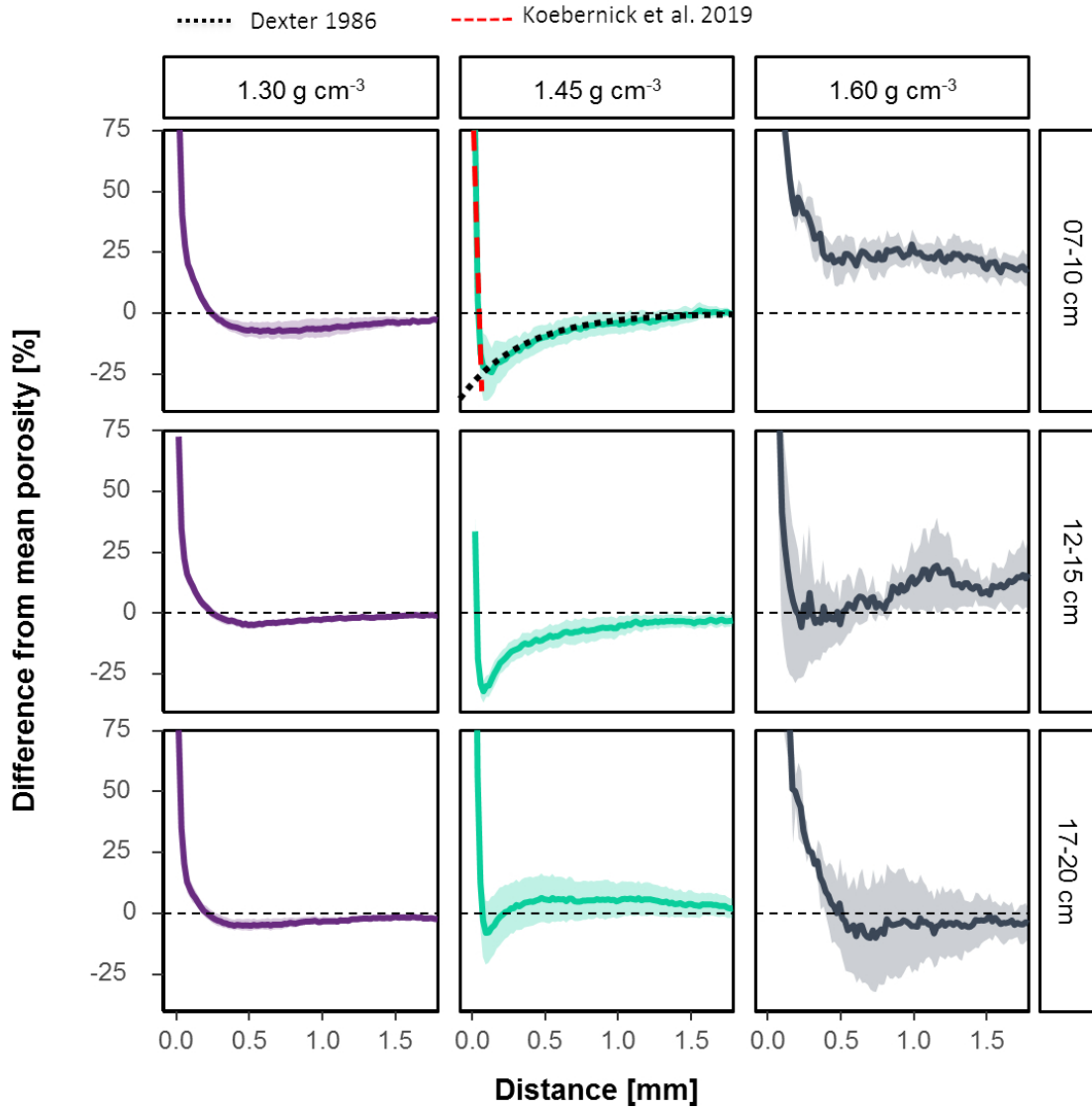
FIGURE C.2: *Mean change in visible porosity with the distance to the root surface relative to the mean visible porosity of a sample. Shadows indicate the standard errors (n=5). For the first depth of the treatment with a bulk density of 1.45 g cm^{-3} the model of Dexter (1987) was used to calculate the exponential decrease of porosity at the root surface toward the bulk porosity. The same value for k (0.68) was used like in Dexter (1987), the mean root diameter and the porosity at the distance of the highest compaction and mean porosity in 07 − 10 cm of the treatment were used. The model of Koebernick et al. (2019) was fitted accordingly for only the points starting at the direct vicinity of the epidermis up to the point of highest compaction with a NLS in R. For this model only two parameters were unknown, the constant δ and the particle diameter. This resulted in a particle diameter of 1.974 mm, which corresponds to the 2 mm sieving.*
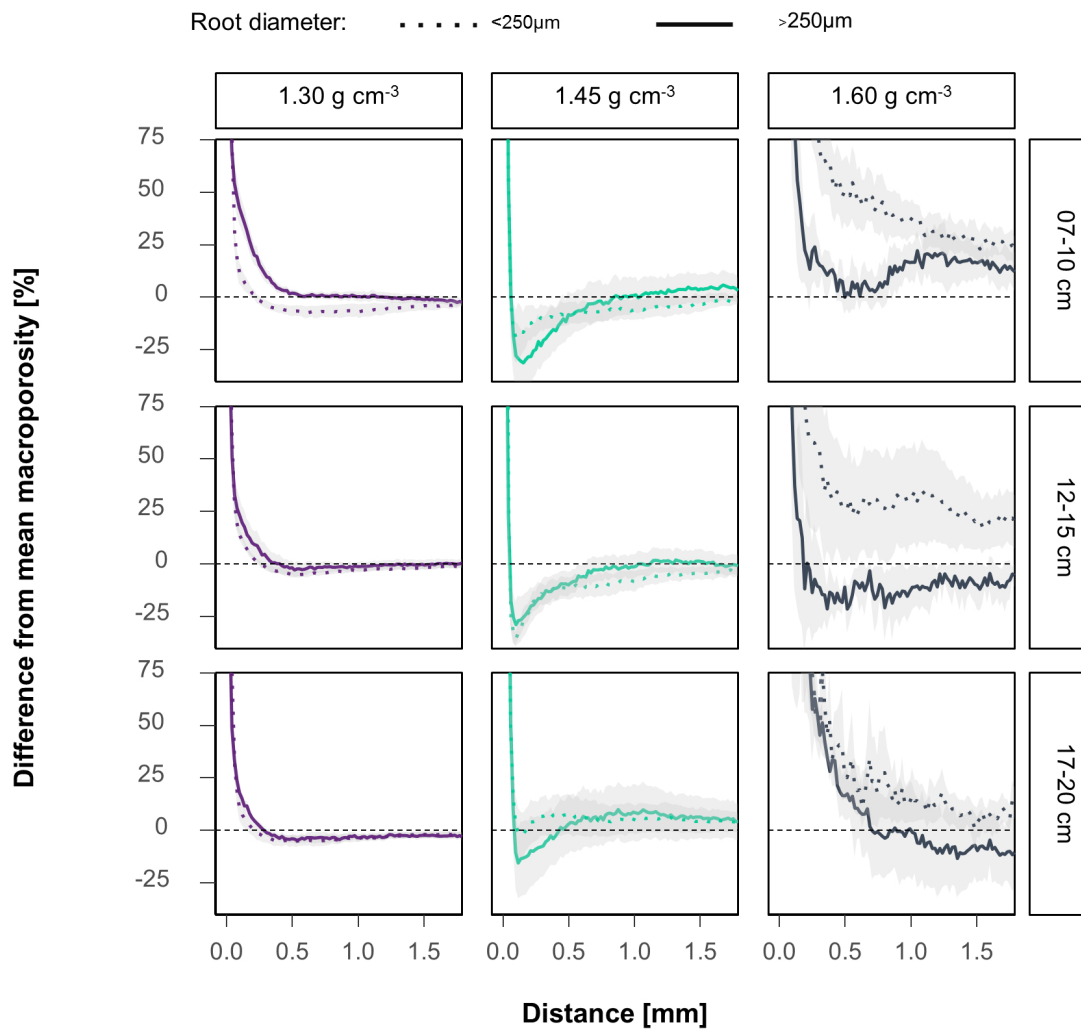
FIGURE C.3: *Mean change in macroporosity with the distance to the root surface of different root diameters relative to the mean macroporosity of a sample. Dotted lines represent the mean changes around roots smaller 250 μm and solid lines these for roots with diameters greater than 250 μm. Shadows indicate the standard errors (n=5).*
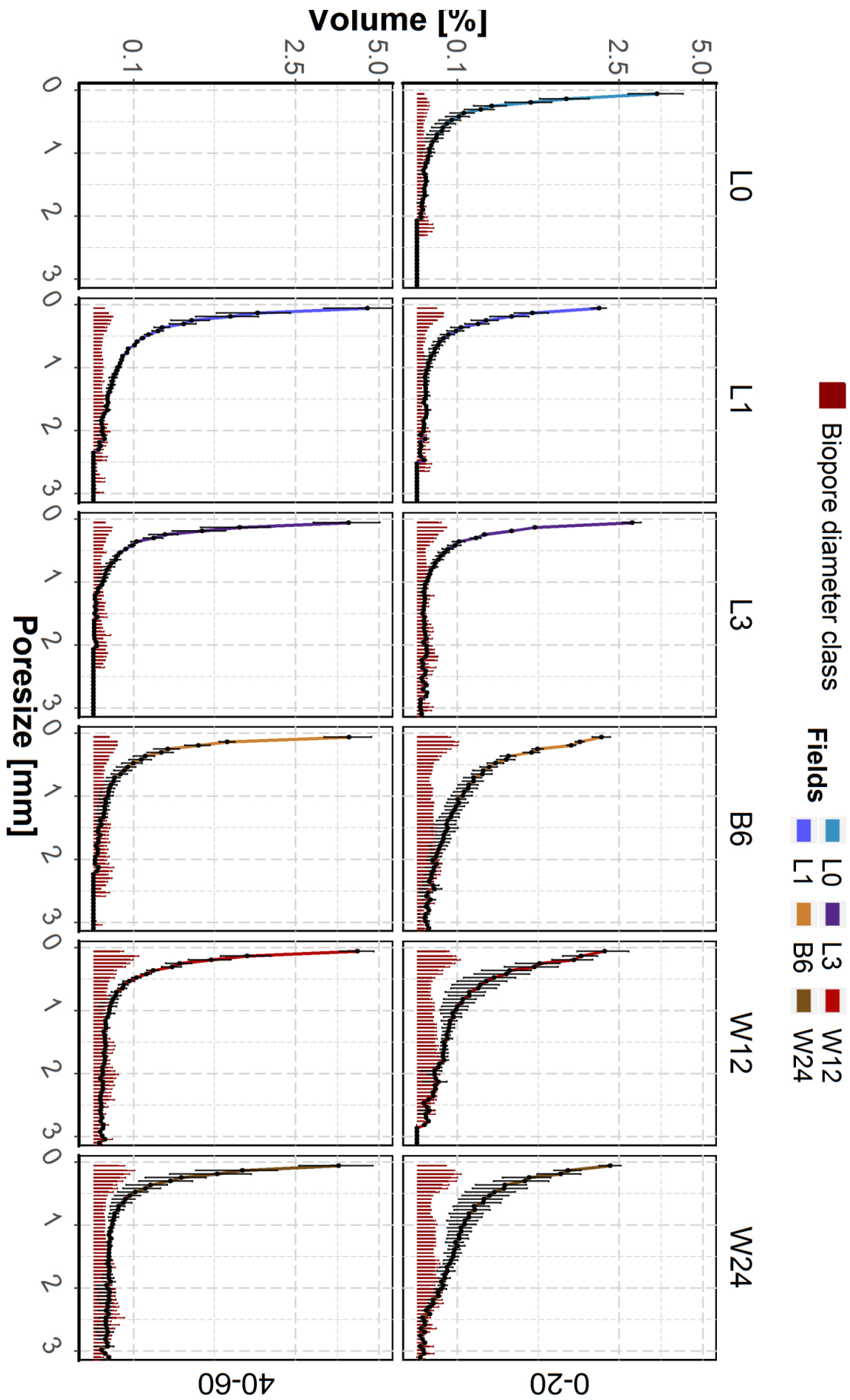
FIGURE C.4: *Mean volume of biopore and pore diameter classes of all field samples. L0, L1, L3 were lucerne sites (0, 1, 3 years after reclamation). B6 was a barley field (6 years after reclamation).*
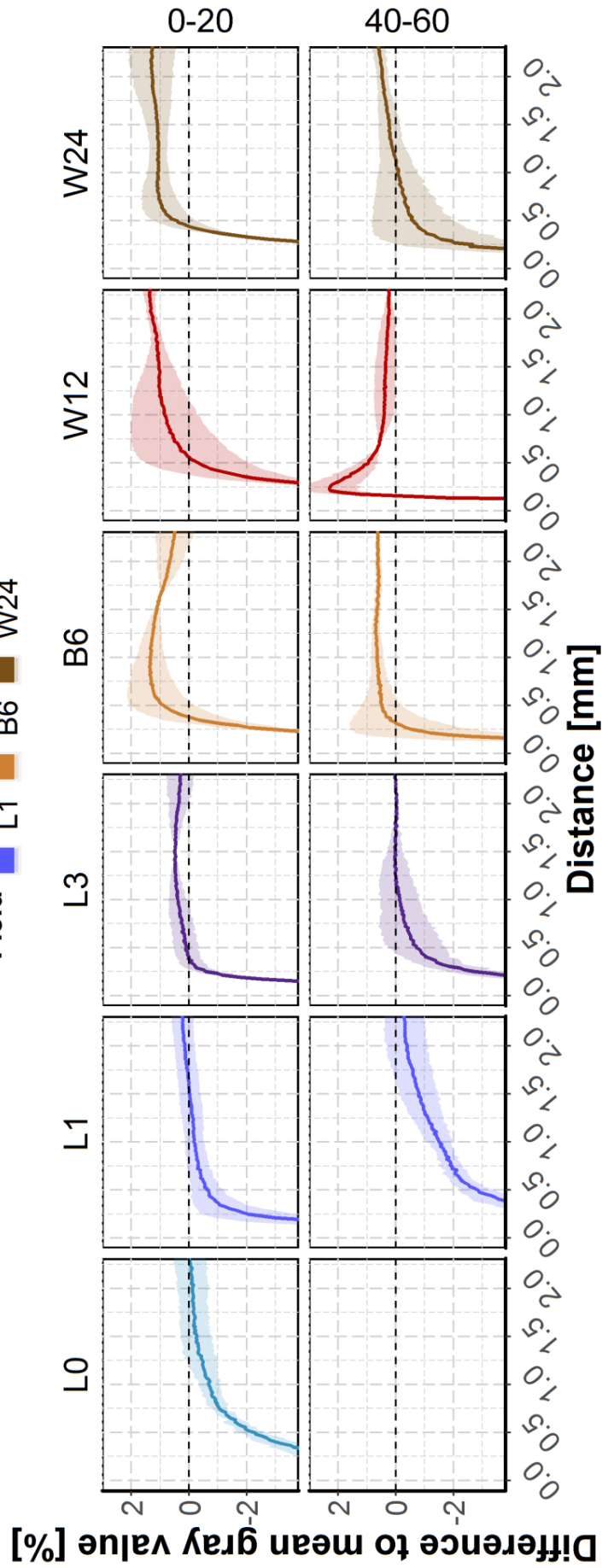
FIGURE C.5: *Mean change in gray value with the distance to the biopore surface relative to the mean gray value of a sample for all field samples. L0, L1, L3 were Lucerne sites (0, 1, 3 years after reclamation). B6 was a barley field (6 years after reclamation) and W12 and W24 wheat fields (12 and 24 years after reclamation). Shadows indicate the standard deviation (n = 3 plots, which in turn each are determined by the result of 9 µCT scans (L3: n= 2).*

Appendix D

Appendix for chapter 5

TABLE D.1: *Mean values and standard deviation of all samples for χ-density, Γ-indicator and φ-vis across all minimum pore diameters. Also shown are the slopes and R2 of the linear regression of χ-density as a function of φ-vis and Γ-indicator such as the slope and the porosity within the inflexion point of the logistic function of Γ-indicator as a function of φ-vis. Significant code: ***= p-value <0.001, p-value=**>0.001, ns=p-value>0.05.*

Minimum diameter	χ-density [mm-3]		Γ-indicator [-]		ϕ-vis [%]		$f'(\chi / \phi - vis)$	R^2	ϕ-vis at inflexion point [%]	$f'(\Gamma / \phi$-vis) at inflexion
0.02	-2115.8	±1878.17	0.52	±0.23	15.54	±5.96	-203.08	0.41***	12.2	0.045
0.03	240.04	±154.63	0.31	±0.27	9.3	±5.17	-9.67	0.10**	11.58	0.052
0.04	-8.73	±63.95	0.27	±0.27	6.73	±4.69	-4.2	0.09**	12.45	0.06
0.05	2.49	±23.66	0.25	±0.26	5.48	±4.40	-1.11	0.04*	10.54	0.063
0.06	-4.01	±14.27	0.23	±0.24	4.57	±4.14	-2.05	0.35***	9.67	0.06
0.075	-3.18	±8.49	0.22	±0.22	3.72	±3.81	-1.74	0.61***	8.75	0.055
0.076	-10.17	±10.33	0.47	±0.29	8.6	±4.66	-1.17	0.28***	7.94	0.084
0.114	1.20	±1.91	0.35	±0.30	6.42	±4.59	-0.25	0.37***	7.16	0.093
0.152	-1.34	±1.42	0.28	±0.27	5.05	±4.33	-0.3	0.82***	7.23	0.082
0.19	-0.25	±0.43	0.21	±0.25	4.17	±4.04	-0.1	0.84***	8.09	0.076
0.228	-0.25	±0.33	0.17	±0.21	3.47	±3.74	-0.08	0.87***	9.78	0.069
0.228	-0.05	±0.05	0.34	±0.26	4.22	±3.66	-0.01	0.71***	5.8	0.081
0.513	-0.01	±0.01	0.14	±0.17	2.37	±2.74	<|0.01|	0.97***	10.68	0.073
0.741	<|0.01|	±0.00	0.12	±0.12	1.58	±2.10	<|0.01|	0.88***	NA	NA
1.026	<|0.01|	±0.00	0.14	±0.11	1.09	±1.57	<|0.01|	0.89***	NA	NA
1.254	<|0.01|	±0.00	0.17	±0.14	0.82	±1.23	<|0.01|	0.90***	NA	NA
1.482	<|0.01|	±0.00	0.21	±0.15	0.63	±0.97	<|0.01|	0.92***	NA	NA
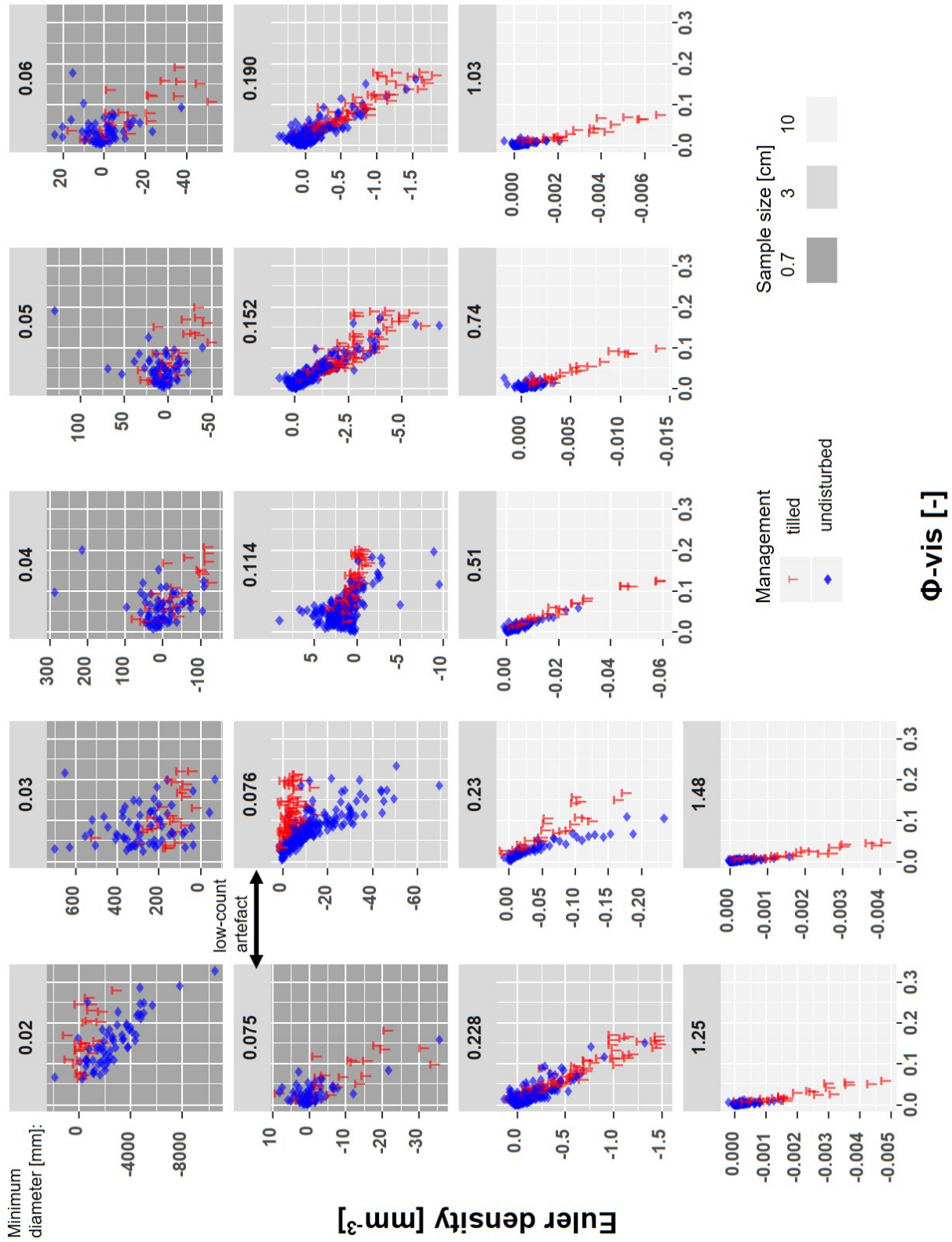
FIGURE D.1: *Scatter plots of χ-density and φ-vis for all PSO steps.*
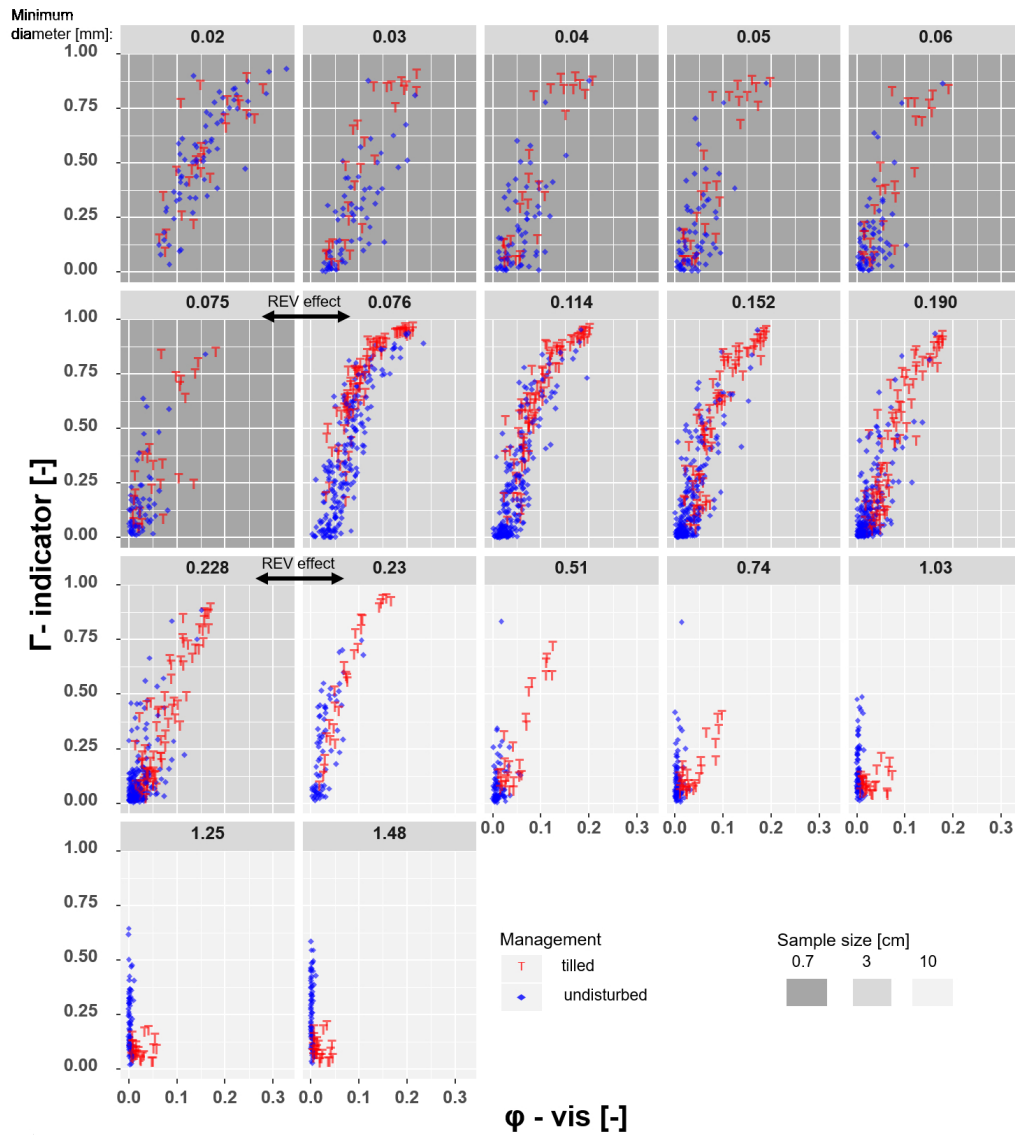
FIGURE D.2: *Scatter plots for Γ-indicator and φ-vis for all PSO-steps.*
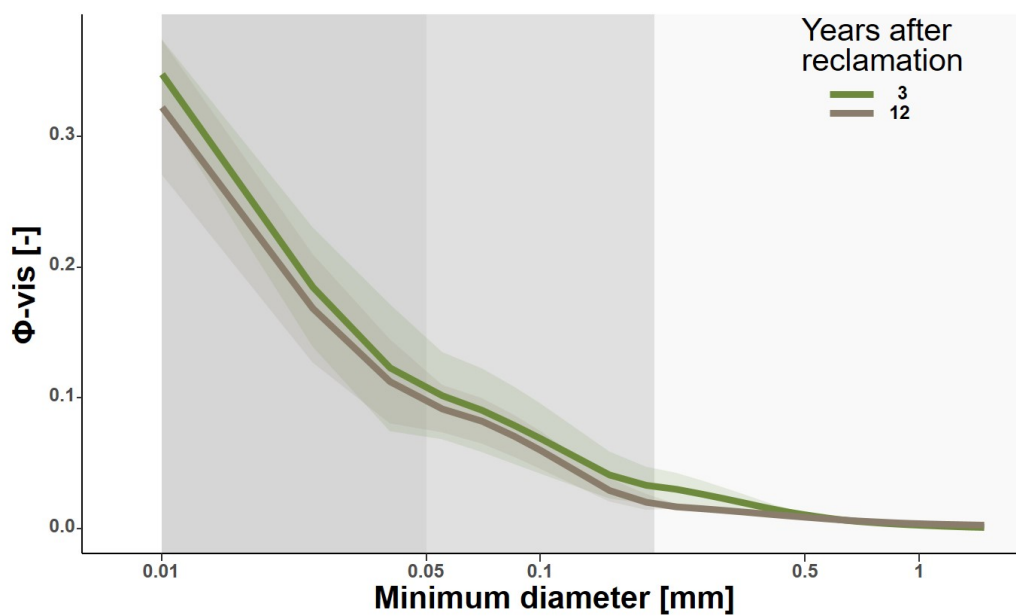
FIGURE D.3: *Joint pore size distribution for the 3 and 12 year old field. Shadows show standard deviation.*
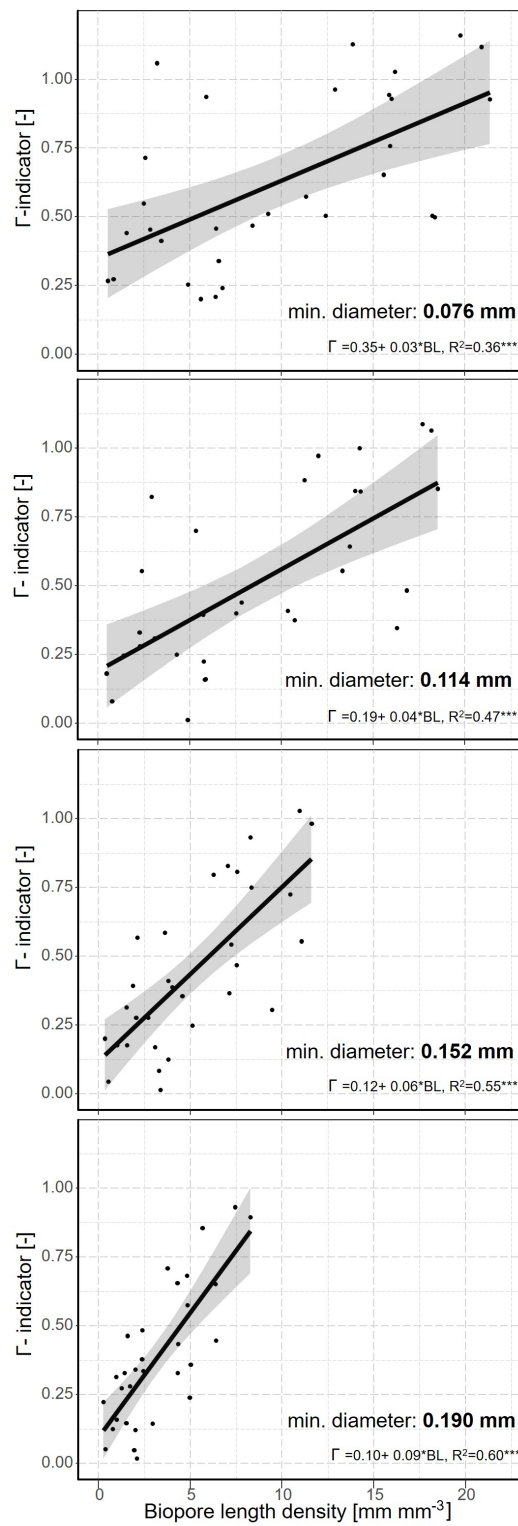
FIGURE D.4: *Scatterplots of mean biopore length density and the joint-Γ-distribution per plot for the different minimum pore diameter calculated within the 3 cm ⌀ samples.*

Appendix E

Appendix for chapter 6
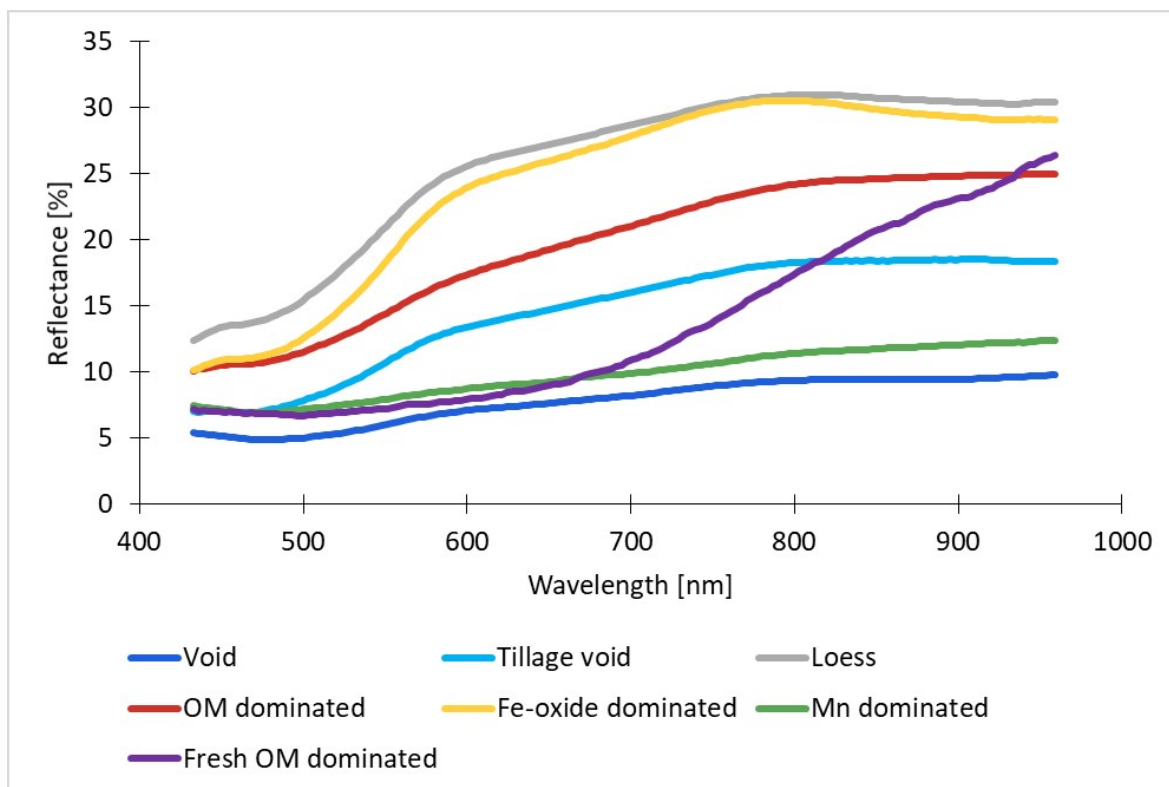
FIGURE E.1: *Mean spectra of regions of interest (ROIs) that were manually selected and used as a endmembers for the linear spectral unmixing.*

No-tilled topsoil
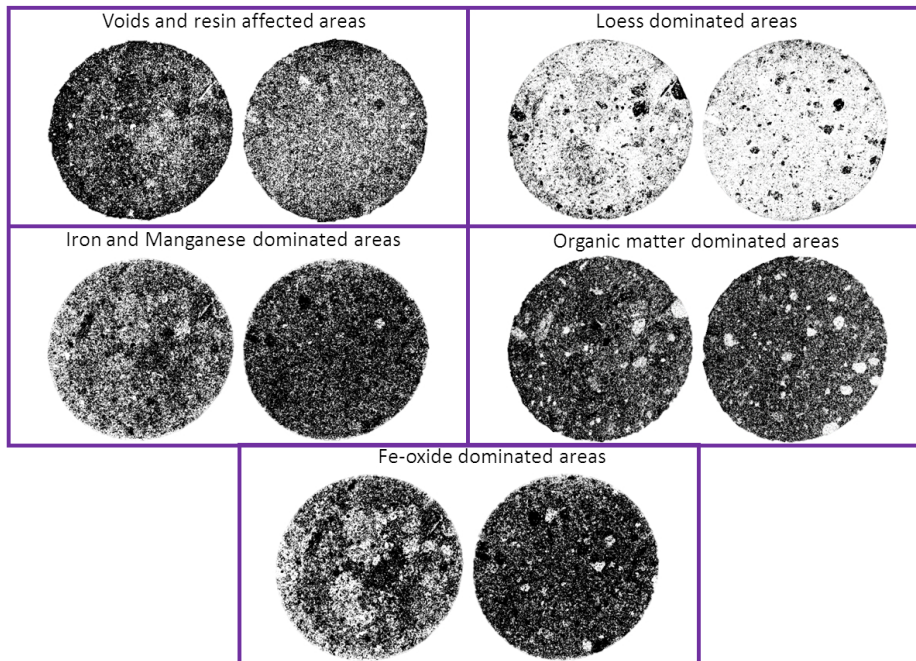
FIGURE E.2: *Abundance map from linear spectral unmixing in no-tilled topsoil.*
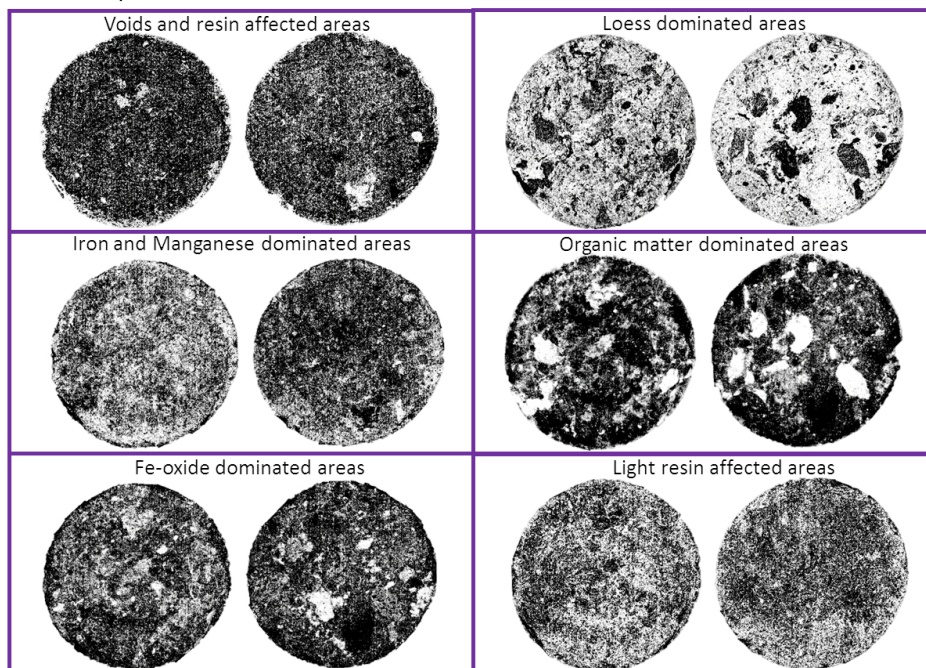
Tilled topsoil

FIGURE E.3: *Abundance map from linear spectral unmixing in tilled topsoil.*
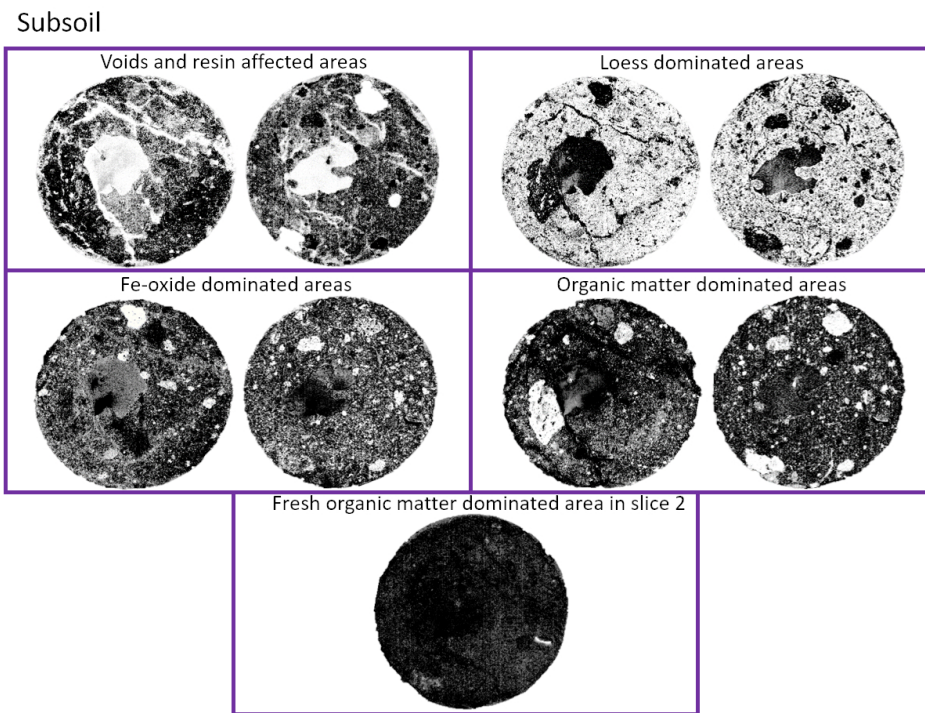
Subsoil

FIGURE E.4: *Abundance map from linear spectral unmixing in the suboil.*
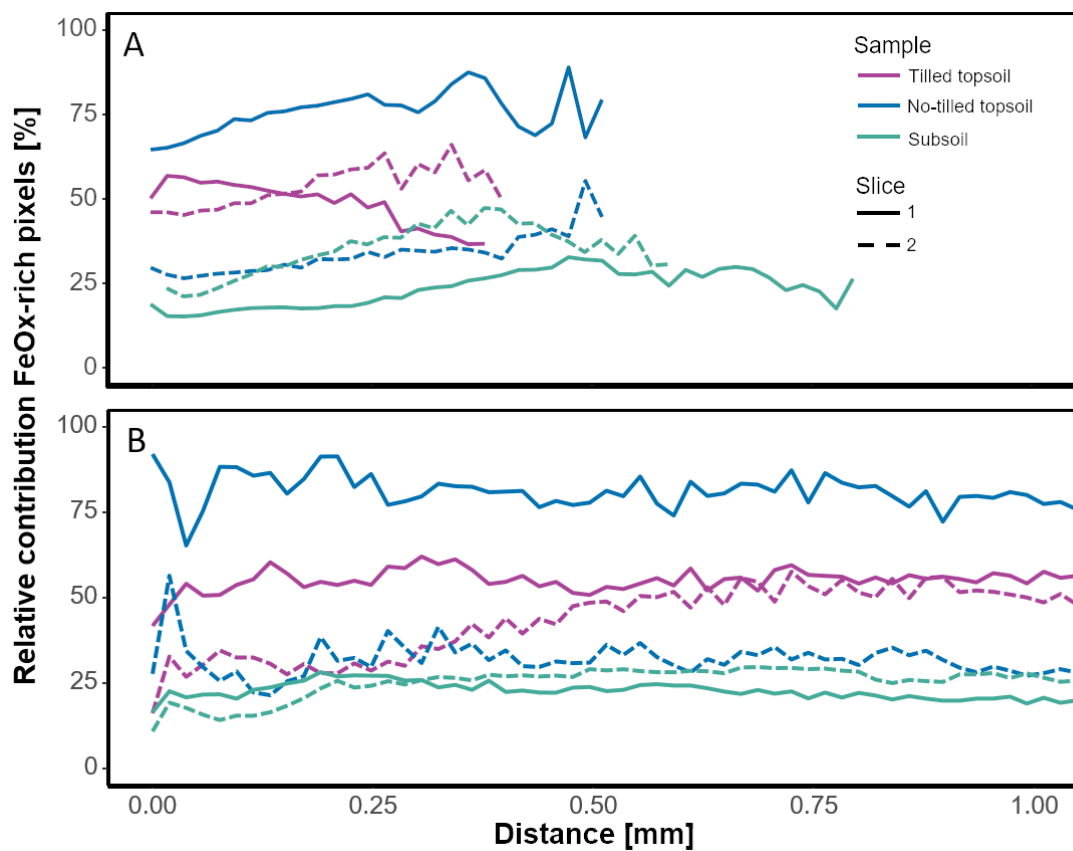
FIGURE E.5: *Rel. intensity of Fe-oxide in images of linear spectral unmixing with 3D euclidean distance to pores (A) and biopores (B).*

Appendix F

Appendix for chapter 7

Fig. F.1 shows the biopore and associated root diameter classes of all fields analysed on the chronosequence. It is immediately visible that in all fields the biopore diameter classes as well as the root diameter classes between 0.04 and 0.25 mm contribute most to the total lengths. As shown for the total biopore lengths in Chapter 3, the biopore classes increase over time. While in 0.20 cm a kind of steady-state condition is already reached after 6 years, the biopore length densities in 40-60 cm depth reach similar values after 12 years.
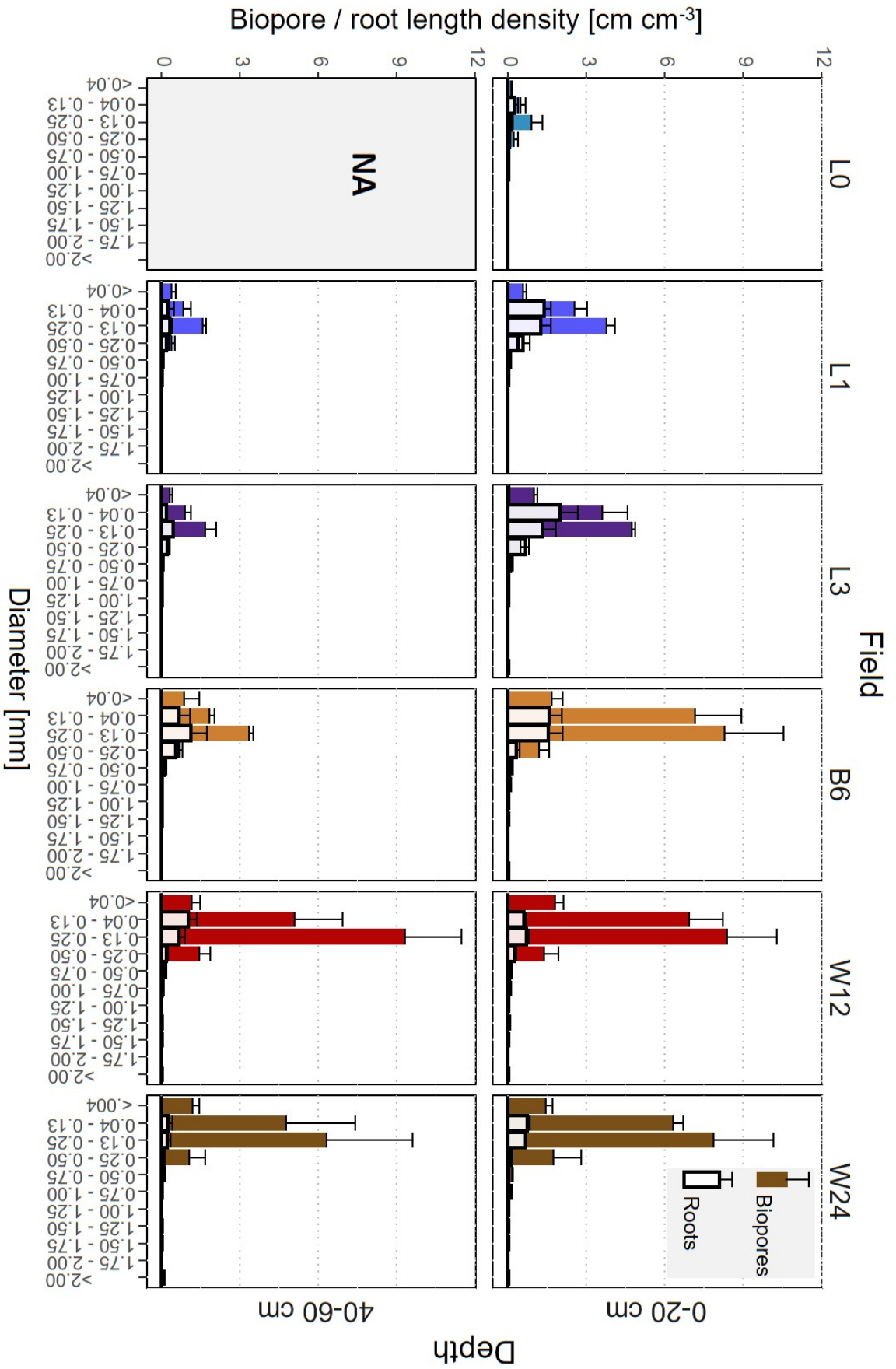
FIGURE F.1: *Biopore diameter classes and corresponding root diameter classes for all field samples. L0, L1, L3 were Lucerne sites (0, 1, 3 years after reclamation), B6 was a barley field (6 years after reclamation) and W12 and W24 wheat fields (12 and 24 years after reclamation). Whiskers indicate the standard deviation (n = 3 plots, which in turn each are determined by the result of 9 µCT scans and 9 WinRhizo analysis, respectively (L3: n= 2). For details on the analysis of biopore and root length density the reader is referred to Chapter 2*

Bibliography

Ambert-Sanchez, M., S. Mickelson, S. Ahmed, J. N. Gray, and D. Webber (2016). "Evaluating Soil Tillage Practices Using X-Ray Computed Tomography and Conventional Laboratory Methods". In: *Transactions of the ASABE* 59.2, pp. 455–463. DOI: 10.13031/trans.59.11308.

Aravena, J. E., M. Berli, T. A. Ghezzehei, and S. W. Tyler (2011). "Effects of root-induced compaction on rhizosphere hydraulic properties–X-ray microtomography imaging and numerical simulations". In: *Environmental science & technology* 45.2, pp. 425–431. DOI: 10.1021/es102566j.

Aravena, J. E., M. Berli, S. Ruiz, F. Suárez, T. A. Ghezzehei, and S. W. Tyler (2014). "Quantifying coupled deformation and water flow in the rhizosphere using X-ray microtomography and numerical simulations". In: *Plant and Soil* 376.1-2, pp. 95–110. DOI: 10.1007/s11104-013-1946-z.

Armstrong, R. T., J. E. McClure, V. Robins, Z. Liu, C. H. Arns, S. Schlüter, and S. Berg (2019). "Porous Media Characterization Using Minkowski Functionals: Theories, Applications and Future Directions". In: *Transport in Porous Media* 130.1, pp. 305–335. DOI: 10.1007/s11242-018-1201-4.

Athmann, M., T. Kautz, R. Pude, and U. Köpke (2013). "Root growth in biopores—evaluation with in situ endoscopy". In: *Plant and Soil* 371.1-2, pp. 179–190. DOI: 10.1007/s11104-013-1673-5.

Bach, H.-J., J. Tomanova, M. Schloter, and J. Munch (2002). "Enumeration of total bacteria and bacteria with genes for proteolytic activity in pure cultures and in environmental samples by quantitative PCR mediated amplification". In: *Journal of Microbiological Methods* 49.3, pp. 235–245. DOI: 10.1016/S0167-7012(01)00370-0.

Bacq-Labreuil, A., J. Crawford, S. J. Mooney, A. L. Neal, and K. Ritz (2019a). "Phacelia (Phacelia tanacetifolia Benth.) affects soil structure differently depending on soil texture". In: *Plant and Soil* 441.1-2, pp. 543–554. DOI: 10.1007/s11104-019-04144-4.

Bacq-Labreuil, A., J. Crawford, S. J. Mooney, A. L. Neal, E. Akkari, C. McAuliffe, X. Zhang, M. Redmile-Gordon, and K. Ritz (2018). "Effects of cropping systems upon the three-dimensional architecture of soil systems are modulated by texture". In: *Geoderma* 332, pp. 73–83. DOI: 10.1016/j.geoderma.2018.07.002.

Bacq-Labreuil, A., J. Crawford, S. J. Mooney, A. L. Neal, and K. Ritz (2019b). "Cover crop species have contrasting influence upon soil structural genesis and microbial community phenotype". In: *Scientific reports* 9.1, p. 7473. DOI: 10.1038/s41598-019-43937-6.

Banfield, C. C., M. A. Dippold, J. Pausch, D. T. T. Hoang, and Y. Kuzyakov (2017). "Biopore history determines the microbial community composition in subsoil hotspots". In: *Biology and Fertility of Soils* 53.5, pp. 573–588. DOI: 10.1007/s00374-017-1201-5.

Banfield, C. C., J. Pausch, Y. Kuzyakov, and M. A. Dippold (2018). "Microbial processing of plant residues in the subsoil – The role of biopores". In: *Soil Biology and Biochemistry* 125, pp. 309–318. DOI: 10.1016/j.soilbio.2018.08.004.

Bano, N., S. Ruffin, B. Ransom, and J. T. Hollibaugh (2004). "Phylogenetic composition of Arctic Ocean archaeal assemblages and comparison with Antarctic assemblages". In: *Applied and environmental microbiology* 70.2, pp. 781–789. DOI: 10.1128/aem.70.2.781-789.2004.

Bardgett, R., W. BOWMAN, R. KAUFMANN, and S. Schmidt (2005). "A temporal approach to linking aboveground and belowground ecology". In: *Trends in Ecology & Evolution* 20.11, pp. 634–641. DOI: 10.1016/j.tree.2005.08.005.

Bauke, S. L., C. von Sperber, N. Siebers, F. Tamburini, and W. Amelung (2017). "Biopore effects on phosphorus biogeochemistry in subsoils". In: *Soil Biology and Biochemistry* 111, pp. 157–165. DOI: 10.1016/j.soilbio.2017.04.012.

Baveye, P. C., W. Otten, A. Kravchenko, M. Balseiro-Romero, É. Beckers, M. Chalhoub, C. Darnault, T. Eickhorst, P. Garnier, S. Hapca, S. Kiranyaz, O. Monga, C. W. Mueller, N. Nunan, V. Pot, S. Schlüter, H. Schmidt, and H.-J. Vogel (2018). "Emergent Properties of Microbial Activity in Heterogeneous Soil Microenvironments: Different Research Approaches Are Slowly Converging, Yet Major Challenges Remain". In: *Frontiers in Microbiology* 9, p. 11054. DOI: 10.3389/fmicb.2018.01929.

Bengough, A. G., M. F. Bransby, J. Hans, S. J. McKenna, T. J. Roberts, and T. A. Valentine (2006). "Root responses to soil physical conditions; growth dynamics from field to cell". In: *Journal of experimental botany* 57.2, pp. 437–447. DOI: 10.1093/jxb/erj003.

Bengough, A. G., B. M. McKenzie, P. D. Hallett, and T. A. Valentine (2011). "Root elongation, water stress, and mechanical impedance: a review of limiting stresses and beneficial root tip traits". In: *Journal of experimental botany* 62.1, pp. 59–68. DOI: 10.1093/jxb/erq350.

Blaser, S. R. G. A., S. Schlüter, and D. Vetterlein (2018). "How much is too much?-Influence of X-ray dose on root growth of faba bean (Vicia faba) and barley (Hordeum vulgare)". In: *PloS one* 13.3, e0193669. DOI: 10.1371/journal.pone.0193669.

Boddington, C. L. and J. C. Dodd (2000). "The effect of agricultural practices on the development of indigenous arbuscular mycorrhizal fungi. II. Studies in experimental microcosms". In: *Plant and soil* 218.1-2, pp. 145–157.

Bodner, G., D. Leitner, and H.-P. Kaul (2014). "Coarse and fine root plants affect pore size distributions differently". In: *Plant and soil* 380.1-2, pp. 133–151. DOI: 10.1007/s11104-014-2079-8.

Böhme, L., U. Langer, and F. Böhme (2005). "Microbial biomass, enzyme activities and microbial community structure in two European long-term field experiments". In: *Agriculture, Ecosystems & Environment* 109.1-2, pp. 141–152. DOI: 10.1016/j.agee.2005.01.017.

Borra, S., R. Thanki, and N. Dey (2019). *Satellite Image Analysis: Clustering and Classification*. SpringerBriefs in Computational Intelligence. Singapore: Springer Singapore. DOI: 10.1007/978-981-13-6424-2.

Bradshaw, A. (1997). "Restoration of mined lands—using natural processes". In: *Ecological Engineering* 8.4, pp. 255–269. DOI: 10.1016/S0925-8574(97)00022-0.

Brankatschk, R., S. Töwe, K. Kleineidam, M. Schloter, and J. Zeyer (2011). "Abundances and potential activities of nitrogen cycling microbial communities along a chronosequence of a glacier forefield". In: *The ISME Journal* 5.6, pp. 1025–1037. DOI: 10.1038/ismej.2010.184.

Bronick, C. J. and R. Lal (2005). "Soil structure and management: a review". In: *Geoderma* 124.1-2, pp. 3–22. DOI: 10.1016/j.geoderma.2004.03.005.

Brookes, P. C., A. Landman, G. Pruden, and D. S. Jenkinson (1985). "Chloroform fumigation and the release of soil nitrogen: A rapid direct extraction method to measure microbial biomass nitrogen in soil". In: *Soil Biology and Biochemistry* 17.6, pp. 837–842. DOI: 10.1016/0038-0717(85)90144-0.

Bruand, A., I. Cousin, B. Niccoullaud, O. Duval, and J. C. Begon (1996). "Backscattered Electron Scanning Images of Soil Porosity for Analyzing Soil Compaction around Roots". In: *Soil Science Society of America Journal* 60, pp. 895–901. DOI: 10.2136/sssaj1996.03615995006000030031x.

Buades, A., B. Coll, and J.-M. Morel (2011). "Non-Local Means Denoising". In: *Image Processing On Line* 1. DOI: 10.5201/ipol.2011.bcm{\textunderscore}nlm.

Buddenbaum, H. and M. Steffens (2011). "Short communication: Laboratory imaging spectroscopy of soil profiles". In: *Journal of Spectral Imaging*. DOI: `10.1255/jsi.2011.a2`.

Caplan, J., M. Niethammer, R. M. Taylor, and K. J. Czymmek (2011). "The power of correlative microscopy: multi-modal, multi-scale, multi-dimensional". In: *Current opinion in structural biology* 21.5, pp. 686–693. DOI: `10.1016/j.sbi.2011.06.010`.

Cárcer, P. S. de, S. Sinaj, M. Santonja, D. Fossati, and B. Jeangros (2019). "Long-term effects of crop succession, soil tillage and climate on wheat yield and soil properties". In: *Soil and Tillage Research* 190, pp. 209–219. DOI: `10.1016/j.still.2019.01.012`.

Carminati, A. and D. Vetterlein (2013). "Plasticity of rhizosphere hydraulic properties as a key for efficient utilization of scarce resources". In: *Annals of botany* 112.2, pp. 277–290. DOI: `10.1093/aob/mcs262`.

Chenu, C. (1995). "Extracellular polysaccharides: an interface between microorganisms and soil constituents". In: *Environmental impact of soil component interactions* 1, pp. 217–233.

Chivenge, P., H. Murwira, K. Giller, P. Mapfumo, and J. Six (2007). "Long-term impact of reduced tillage and residue management on soil carbon stabilization: Implications for conservation agriculture on contrasting soils". In: *Soil and Tillage Research* 94.2, pp. 328–337. DOI: `10.1016/j.still.2006.08.006`.

Clayton, H. G., A. F. Wick, and W. L. Daniels (2009). "Microbial biomass in reclaimed soils following coal mining in virginia". In: *Journal American Society of Mining and Reclamation* 2009.1, pp. 227–236. DOI: `10.21000/JASMR09010227`.

Colica, G., H. Li, F. Rossi, D. Li, Y. Liu, and R. de Philippis (2014). "Microbial secreted exopolysaccharides affect the hydrological behavior of induced biological soil crusts in desert sandy soils". In: *Soil Biology and Biochemistry* 68, pp. 62–70. DOI: `10.1016/j.soilbio.2013.09.017`.

Colombi, T., S. Braun, T. Keller, and A. Walter (2017). "Artificial macropores attract crop roots and enhance plant productivity on compacted soils". In: *The Science of the total environment* 574, pp. 1283–1293. DOI: `10.1016/j.scitotenv.2016.07.194`.

Colombi, T. and T. Keller (2019). "Developing strategies to recover crop productivity after soil compaction—A plant eco-physiological perspective". In: *Soil and Tillage Research* 191, pp. 156–161. DOI: `10.1016/j.still.2019.04.008`.

Czyż, E. A. (2004). "Effects of traffic on soil aeration, bulk density and growth of spring barley". In: *Soil and Tillage Research* 79.2, pp. 153–166. DOI: `10.1016/j.still.2004.07.004`.

Dabboor, M., S. Howell, M. Shokr, and J. Yackel (2014). "The Jeffries–Matusita distance for the case of complex Wishart distribution as a separability criterion for fully polarimetric SAR data". In: *International Journal of Remote Sensing* 35.19, pp. 6859–6873. DOI: `10.1080/01431161.2014.960614`.

Dal Ferro, N., L. Sartori, G. Simonetti, A. Berti, and F. Morari (2014). "Soil macro- and microstructure as affected by different tillage systems and their effects on maize root growth". In: *Soil and Tillage Research* 140, pp. 55–65. DOI: `10.1016/j.still.2014.02.003`.

Darbon, J., A. Cunha, T. F. Chan, S. Osher, and G. J. Jensen (2008). "Fast nonlocal filtering applied to electron cryomicroscopy". In: *2008 5th IEEE International Symposium on Biomedical Imaging: From Nano to Macro*. IEEE, pp. 1331–1334. DOI: `10.1109/ISBI.2008.4541250`.

Delschen, T. (1999). "Impacts of long-term application of organic fertilizers on soil quality parameters in reclaimed loess soils of the Rhineland lignite mining area". In: *Plant and soil* 213.1/2, pp. 43–54. DOI: `10.1023/A:1004373102966`.

Dexter, A. R. (1987). "Compression of soil around roots". In: *Plant and soil* 97, pp. 401–406.

Diaz-Zorita, M. (2002). "Disruptive methods for assessing soil structure". In: *Soil and Tillage Research* 64.1-2, pp. 3–22. DOI: `10.1016/S0167-1987(01)00254-9`.

Dumbeck, G. (1992). *Bodenkundliche Aspekte bei der landwirtschaftlichen Rekultivierung im Rheinischen Braunkohlenrevier*.

Dumbeck, G. (2014). "Rekultivierung unterschiedlicher Böden und Substrate". In: *Handbuch der Bodenkunde*. Ed. by H.-P. Blume, K. Stahr, W. Fischer, G. Guggenberger, R. Horn, H.-G. Frede, and P. Felix-Henningsen. Vol. 3. Weinheim, Germany: Wiley-VCH Verlag GmbH & Co. KGaA, pp. 1–40. DOI: 10.1002/9783527678495.hbbk1995026.

Dungait, J. A. J., D. W. Hopkins, A. S. Gregory, and A. P. Whitmore (2012). "Soil organic matter turnover is governed by accessibility not recalcitrance". In: *Global Change Biology* 18.6, pp. 1781–1796. DOI: 10.1111/j.1365-2486.2012.02665.x.

Dunn, O. J. (1964). "Multiple Comparisons Using Rank Sums". In: *Technometrics* 6.3, pp. 241–252. DOI: 10.1080/00401706.1964.10490181.

Eavis, B. W. (1972). "Soil physical conditions affecting seedling root growth". In: *Plant and Soil* 37.1, pp. 151–158. DOI: 10.1007/BF01578487.

Ellert, B. H. and J. R. Bettany (1995). "Calculation of organic matter and nutrients stored in soils under contrasting management regimes". In: *Canadian Journal of Soil Science* 75.4, pp. 529–538. DOI: 10.4141/cjss95-075.

Elliott, E. T. and D. C. Coleman (1998). "Let the Soil Work for Us". In: *Ecological Bulletins* 39.5, pp. 23–32.

Emerson, W. W. (1971). "Determination of the contents of clay-sized particles in soils". In: *Journal of Soil Science* 22.1, pp. 50–59. DOI: 10.1111/j.1365-2389.1971.tb01592.x.

Feeney, D. S., J. W. Crawford, T. Daniell, P. D. Hallett, N. Nunan, K. Ritz, M. Rivers, and I. M. Young (2006). "Three-dimensional microorganization of the soil-root-microbe system". In: *Microbial ecology* 52.1, pp. 151–158. DOI: 10.1007/s00248-006-9062-8.

Follett, R. (2001). "Soil management concepts and carbon sequestration in cropland soils". In: *Soil and Tillage Research* 61.1-2, pp. 77–92. DOI: 10.1016/S0167-1987(01)00180-5.

Frangi, A. F., W. J. Niessen, K. L. Vincken, and M. A. Viergever (1998). "Multiscale vessel enhancement filtering". In: *International conference on medical image computing and computer-assisted intervention*, pp. 130–137.

Gao, W., L. Hodgkinson, K. Jin, C. W. Watts, R. W. Ashton, J. Shen, T. Ren, I. C. Dodd, A. Binley, A. L. Phillips, P. Hedden, M. J. Hawkesford, and W. R. Whalley (2016). "Deep roots and soil structure". In: *Plant, cell & environment* 39.8, pp. 1662–1668. DOI: 10.1111/pce.12684.

Gao, W., S. Schlüter, S. R. G. A. Blaser, J. Shen, and D. Vetterlein (2019). "A shape-based method for automatic and rapid segmentation of roots in soil from X-ray computed tomography images: Rootine". In: *Plant and Soil* 441.1-2, pp. 643–655. DOI: 10.1007/s11104-019-04053-6.

Görres, J. H., M. C. Savin, and J. A. Amador (2001). "Soil micropore structure and carbon mineralization in burrows and casts of an anecic earthworm (Lumbricus terrestris)". In: *Soil Biology and Biochemistry* 33.14, pp. 1881–1887. DOI: 10.1016/S0038-0717(01)00068-2.

Grayston, S., C. Campbell, R. Bardgett, J. Mawdsley, C. Clegg, K. Ritz, B. Griffiths, J. Rodwell, S. Edwards, W. Davies, D. Elston, and P. Millard (2004). "Assessing shifts in microbial community structure across a range of grasslands of differing management intensity using CLPP, PLFA and community DNA techniques". In: *Applied Soil Ecology* 25.1, pp. 63–84. DOI: 10.1016/S0929-1393(03)00098-2.

Greenland, D. J. (1977). *Soil damage by intensive arable cultivation: Temporary or permanent?* DOI: 10.1098/rstb.1977.0133.

Gutiérrez Castorena, E. V., M. d. C. Gutiérrez-Castorena, T. González Vargas, L. Cajuste Bontemps, J. Delgadillo Martínez, E. Suástegui Méndez, and C. A. Ortiz Solorio (2016). "Micromapping of microbial hotspots and biofilms from different crops using digital image mosaics of soil thin sections". In: *Geoderma* 279, pp. 11–21. DOI: 10.1016/j.geoderma.2016.05.017.

Guyader, J.-M., W. Huizinga, D. H. J. Poot, M. van Kranenburg, A. Uitterdijk, W. J. Niessen, and S. Klein (2018). "Groupwise image registration based on a total correlation dissimilarity measure for quantitative MRI and dynamic imaging data". In: *Scientific Reports* 8.1, p. 137. DOI: 10.1038/s41598-018-31474-7.

Han, E., T. Kautz, N. Huang, and U. Köpke (2017). "Dynamics of plant nutrient uptake as affected by biopore-associated root growth in arable subsoil". In: *Plant and Soil* 415.1-2, pp. 145–160. DOI: 10.1007/s11104-016-3150-4.

Han, E., T. Kautz, U. Perkons, D. Uteau, S. Peth, N. Huang, R. Horn, and U. Köpke (2015). "Root growth dynamics inside and outside of soil biopores as affected by crop sequence determined with the profile wall method". In: *Biology and Fertility of Soils* 51.7, pp. 847–856. DOI: 10.1007/s00374-015-1032-1.

Handschuh, S., N. Baeumler, T. Schwaha, and B. Ruthensteiner (2013). "A correlative approach for combining microCT, light and transmission electron microscopy in a single 3D scenario". In: *Frontiers in zoology* 10.1, p. 44. DOI: 10.1186/1742-9994-10-44.

Hapca, S. M., Z. X. Wang, W. Otten, C. Wilson, and P. C. Baveye (2011). "Automated statistical method to align 2D chemical maps with 3D X-ray computed micro-tomographic images of soils". In: *Geoderma* 164.3-4, pp. 146–154. DOI: 10.1016/j.geoderma.2011.05.018.

Harris, J. A., P. Birch, and K. C. Short (1989). "Changes in the microbial community and physico-chemical characteristics of topsoils stockpiled during opencast mining". In: *Soil Use and Management* 5.4, pp. 161–168. DOI: 10.1111/j.1475-2743.1989.tb00778.x.

Helingerová, M., J. Frouz, and H. Šantrůčková (2010). "Microbial activity in reclaimed and unreclaimed post-mining sites near Sokolov (Czech Republic)". In: *Ecological Engineering* 36.6, pp. 768–776. DOI: 10.1016/j.ecoleng.2010.01.007.

Helliwell, J. R., C. J. Sturrock, K. M. Grayling, S. R. Tracy, R. J. Flavel, I. M. Young, W. R. Whalley, and S. J. Mooney (2013). "Applications of X-ray computed tomography for examining biophysical interactions and structural development in soil systems: a review". In: *European Journal of Soil Science* 64.3, pp. 279–297. DOI: 10.1111/ejss.12028.

Helliwell, J. R., C. J. Sturrock, S. Mairhofer, J. Craigon, R. W. Ashton, A. J. Miller, W. R. Whalley, and S. J. Mooney (2017). "The emergent rhizosphere: imaging the development of the porous architecture at the root-soil interface". In: *Scientific reports* 7.1, p. 14875. DOI: 10.1038/s41598-017-14904-w.

Helliwell, J. R., C. J. Sturrock, A. J. Miller, W. R. Whalley, and S. J. Mooney (2019). "The role of plant species and soil condition in the structural development of the rhizosphere". In: *Plant, cell & environment* 42.6, pp. 1974–1986. DOI: 10.1111/pce.13529.

Herring, A. L., L. Andersson, S. Schlüter, A. Sheppard, and D. Wildenschild (2015). "Efficiently engineering pore-scale processes: The role of force dominance and topology during nonwetting phase trapping in porous media". In: *Advances in Water Resources* 79, pp. 91–102. DOI: 10.1016/j.advwatres.2015.02.005.

Hinsinger, P., A. G. Bengough, D. Vetterlein, and I. M. Young (2009). "Rhizosphere: biophysics, biogeochemistry and ecological relevance". In: *Plant and Soil* 321.1-2, pp. 117–152. DOI: 10.1007/s11104-008-9885-9.

Hoang, D. T., S. L. Bauke, Y. Kuzyakov, and J. Pausch (2017). "Rolling in the deep: Priming effects in earthworm biopores in topsoil and subsoil". In: *Soil Biology and Biochemistry* 114, pp. 59–71. DOI: 10.1016/j.soilbio.2017.06.021.

Hobley, E., M. Steffens, S. L. Bauke, and I. Kögel-Knabner (2018). "Hotspots of soil organic carbon storage revealed by laboratory hyperspectral imaging". In: *Scientific Reports* 8.1, p. 151. DOI: 10.1038/s41598-018-31776-w.

Insam, H. and K. H. Domsch (1988). "Relationship between soil organic carbon and microbial biomass on chronosequences of reclamation sites". In: *Microbial Ecology* 15.2, pp. 177–188. DOI: 10.1007/BF02011711.

IUSS Working Group WRB (2015). *World reference base for soil resources 2014. Update 2015: International soil classification system for naming soils and creating legends for soil maps*. Vol. 106. World soil resources reports. Rome: FAO.

Jackson, R. B., H. A. Mooney, and E. D. Schulze (1997). "A global budget for fine root biomass, surface area, and nutrient contents". In: *Proceedings of the National Academy of Sciences of the United States of America* 94.14, pp. 7362–7366. DOI: 10.1073/pnas.94.14.7362.

Jangorzo, N. S., C. Schwartz, and F. Watteau (2014). "Image analysis of soil thin sections for a non-destructive quantification of aggregation in the early stages of pedogenesis". In: *European Journal of Soil Science* 65.4, pp. 485–498. DOI: 10.1111/ejss.12110.

Jansa, J., M. A., A. T., R. R., S. I., and F. E. (2002). "Diversity and structure of AMF communities as affected by tillage in a temperate soil". In: *Mycorrhiza* 12.5, pp. 225–234. DOI: 10.1007/s00572-002-0163-z.

Jarvis, N. J. (2007). "A review of non-equilibrium water flow and solute transport in soil macropores: principles, controlling factors and consequences for water quality". In: *European Journal of Soil Science* 58.3, pp. 523–546. DOI: 10.1111/j.1365-2389.2007.00915.x.

Jarvis, N., M. Larsbo, and J. Koestel (2017). "Connectivity and percolation of structural pore networks in a cultivated silt loam soil quantified by X-ray tomography". In: *Geoderma* 287, pp. 71–79. DOI: 10.1016/j.geoderma.2016.06.026.

Jin, K., J. Shen, R. W. Ashton, I. C. Dodd, M. A. J. Parry, and W. R. Whalley (2013). "How do roots elongate in a structured soil?" In: *Journal of experimental botany* 64.15, pp. 4761–4777. DOI: 10.1093/jxb/ert286.

Joergensen, R. G. (1996). "The fumigation-extraction method to estimate soil microbial biomass: Calibration of the kEC value". In: *Soil Biology and Biochemistry* 28.1, pp. 25–31. DOI: 10.1016/0038-0717(95)00102-6.

Juyal, A., W. Otten, R. Falconer, S. Hapca, H. Schmidt, P. C. Baveye, and T. Eickhorst (2019). "Combination of techniques to quantify the distribution of bacteria in their soil microhabitats at different spatial scales". In: *Geoderma* 334, pp. 165–174. DOI: 10.1016/j.geoderma.2018.07.031.

Karsanina, M. V., K. M. Gerke, E. B. Skvortsova, A. L. Ivanov, and D. Mallants (2018). "Enhancing image resolution of soils by stochastic multiscale image fusion". In: *Geoderma* 314, pp. 138–145. DOI: 10.1016/j.geoderma.2017.10.055.

Kaufmann, M., S. Tobias, and R. Schulin (2009). "Development of the mechanical stability of a restored soil during the first 3 years of re-cultivation". In: *Soil and Tillage Research* 103.1, pp. 127–136. DOI: 10.1016/j.still.2008.10.002.

Kautz, T. (2015). "Research on subsoil biopores and their functions in organically managed soils: A review". In: *Renewable Agriculture and Food Systems* 30.4, pp. 318–327. DOI: 10.1017/S1742170513000549.

Kautz, T., U. Perkons, M. Athmann, R. Pude, and U. Köpke (2013). "Barley roots are not constrained to large-sized biopores in the subsoil of a deep Haplic Luvisol". In: *Biology and Fertility of Soils* 49.7, pp. 959–963. DOI: 10.1007/s00374-013-0783-9.

Kavzoglu, T., H. Tonbul, M. Yildiz Erdemir, and I. Colkesen (2018). "Dimensionality Reduction and Classification of Hyperspectral Images Using Object-Based Image Analysis". In: *Journal of the Indian Society of Remote Sensing* 46.8, pp. 1297–1306. DOI: 10.1007/s12524-018-0803-1.

Kay, B. D. and A. J. VandenBygaart (2002). "Conservation tillage and depth stratification of porosity and soil organic matter". In: *Soil and Tillage Research* 66, pp. 107–118. DOI: 10.1016/s0167-1987(02)00019-3.

Kels, H. and W. Schirmer (2010). "Relation of loess units and prehistoric find density in the Garzweiler open-cast mine, Lower Rhine". In: 59, pp. 59–65. DOI: 10.3285/eg.59.1-2.05.

King, J. A. (1988). "Some physical features of soil after opencast mining". In: *Soil Use and Management* 4.1, pp. 23–30. DOI: 10.1111/j.1475-2743.1988.tb00732.x.

Klein, S., M. Staring, K. Murphy, M. A. Viergever, and J. Pluim (2010). "elastix: A Toolbox for Intensity-Based Medical Image Registration". In: *IEEE Transactions on Medical Imaging* 29.1, pp. 196–205. DOI: 10.1109/TMI.2009.2035616.

Koebernick, N., K. R. Daly, S. D. Keyes, A. G. Bengough, L. K. Brown, L. J. Cooper, T. S. George, P. D. Hallett, M. Naveed, A. Raffan, and T. Roose (2019). "Imaging microstructure of the barley rhizosphere: particle packing and root hair influences". In: *The New phytologist* 221.4, pp. 1878–1889. DOI: 10.1111/nph.15516.

Koebernick, N., K. R. Daly, S. D. Keyes, T. S. George, L. K. Brown, A. Raffan, L. J. Cooper, M. Naveed, A. G. Bengough, I. Sinclair, P. D. Hallett, and T. Roose (2017). "High-resolution synchrotron imaging shows that root hairs influence rhizosphere soil structure formation". In: *The New phytologist* 216.1, pp. 124–135. DOI: 10.1111/nph.14705.

Koestel, J., A. Dathe, T. H. Skaggs, O. Klakegg, M. A. Ahmad, M. Babko, D. Giménez, C. Farkas, A. Nemes, and N. Jarvis (2018). "Estimating the Permeability of Naturally Structured Soil From Percolation Theory and Pore Space Characteristics Imaged by X–Ray". In: *Water Resources Research* 54.11, pp. 9255–9263. DOI: 10.1029/2018WR023609.

Koestel, J. and M. Larsbo (2014). "Imaging and quantification of preferential solute transport in soil macropores". In: *Water Resources Research* 50.5, pp. 4357–4378. DOI: 10.1002/2014WR015351.

Kołodziej, B., M. Bryk, A. Słowiłska-Jurkiewicz, K. Otremba, and M. Gilewska (2016). "Soil physical properties of agriculturally reclaimed area after lignite mine: A case study from central Poland". In: *Soil and Tillage Research* 163, pp. 54–63. DOI: 10.1016/j.still.2016.05.001.

Kooistra, M. J., D. Schoonderbeek, F. R. Boone, B. W. Veen, and M. van Noordwijk (1992). "Root-soil contact of maize, as measured by a thin-section technique". In: *Plant and Soil* 139.1, pp. 119–129. DOI: 10.1007/BF00012849.

Kravchenko, A. N., A. K. Guber, B. S. Razavi, J. Koestel, M. Y. Quigley, G. P. Robertson, and Y. Kuzyakov (2019). "Microbial spatial footprint as a driver of soil carbon stabilization". In: *Nature communications* 10.1, p. 3121. DOI: 10.1038/s41467-019-11057-4.

Kravchenko, A. N., A. N. W. Wang, A. J. M. Smucker, and M. L. Rivers (2011). "Long-term Differences in Tillage and Land Use Affect Intra-aggregate Pore Heterogeneity". In: *Soil Science Society of America Journal* 75.5, p. 1658. DOI: 10.2136/sssaj2011.0096.

Kravchenko, A. N. and A. K. Guber (2017). "Soil pores and their contributions to soil carbon processes". In: *Geoderma* 287, pp. 31–39. DOI: 10.1016/j.geoderma.2016.06.027.

Kravchenko, A. N., W. C. Negassa, A. K. Guber, and M. L. Rivers (2015). "Protection of soil carbon within macro-aggregates depends on intra-aggregate pore characteristics". In: *Scientific reports* 5, p. 16261. DOI: 10.1038/srep16261.

Krümmelbein, J. and T. Raab (2012). "Development of soil physical parameters in agricultural reclamation after brown coal mining within the first four years". In: *Soil and Tillage Research* 125, pp. 109–115. DOI: 10.1016/j.still.2012.06.013.

Kruskal, W. H. and W. A. Wallis (1952). "Use of Ranks in One-Criterion Variance Analysis". In: *Journal of the American Statistical Association* 47.260, pp. 583–621. DOI: 10.1080/01621459.1952.10483441.

Kuka, K., B. Illerhaus, C. A. Fox, and M. Joschko (2013). "X-ray Computed Microtomography for the Study of the Soil–Root Relationship in Grassland Soils". In: *Vadose Zone Journal* 12.4, p. 0. DOI: 10.2136/vzj2013.01.0014.

Laszlo, G., B. Janos, and R. Magda (1995). "Determination of total carbonate content in some representative loess-paleosol profiles". In: *GeoJournal* 36.2-3, pp. 187–188. DOI: 10.1007/BF00813165.

Legland, D., I. Arganda-Carreras, and P. Andrey (2016). "MorphoLibJ: integrated library and plugins for mathematical morphology with ImageJ". In: *Bioinformatics (Oxford, England)* 32.22, pp. 3532–3534. DOI: 10.1093/bioinformatics/btw413.

Lehmann, J. and M. Kleber (2015). "The contentious nature of soil organic matter". In: *Nature* 528.7580, pp. 60–68. DOI: 10.1038/nature16069.

Lehmkuhl, F., J. Zens, L. Krauß, P. Schulte, and H. Kels (2016). "Loess-paleosol sequences at the northern European loess belt in Germany: Distribution, geomorphology and stratigraphy". In: *Quaternary Science Reviews* 153, pp. 11–30. DOI: 10.1016/j.quascirev.2016.10.008.

Leue, M., D. Uteau-Puschmann, S. Peth, J. Nellesen, R. Kodešová, and H. H. Gerke (2019). "Separation of Soil Macropore Types in Three-Dimensional X-Ray Computed Tomography Images Based on Pore Geometry Characteristics". In: *Vadose Zone Journal* 18.1, p. 0. DOI: 10.2136/vzj2018.09.0170.

Leuther, F., S. Schlüter, R. Wallach, and H.-J. Vogel (2019). "Structure and hydraulic properties in soils under long-term irrigation with treated wastewater". In: *Geoderma* 333, pp. 90–98. DOI: 10.1016/j.geoderma.2018.07.015.

Li, Y. (2018). "A review of shear and tensile strengths of the Malan Loess in China". In: *Engineering Geology* 236, pp. 4–10. DOI: 10.1016/j.enggeo.2017.02.023.

Lin, H. (2010). "Earth's Critical Zone and hydropedology: concepts, characteristics, and advances". In: *Hydrology and Earth System Sciences* 14.1, pp. 25–45. DOI: 10.5194/hess-14-25-2010.

Lipiec, J. and R. Hatano (2003). "Quantification of compaction effects on soil physical properties and crop growth". In: *Geoderma* 116.1-2, pp. 107–136. DOI: 10.1016/S0016-7061(03)00097-1.

Liu, X., Z. Bai, W. Zhou, Y. Cao, and G. Zhang (2017). "Changes in soil properties in the soil profile after mining and reclamation in an opencast coal mine on the Loess Plateau, China". In: *Ecological Engineering* 98, pp. 228–239. DOI: 10.1016/j.ecoleng.2016.10.078.

Lucas, M., S. Schlüter, H.-J. Vogel, and D. Vetterlein (2019). "Soil structure formation along an agricultural chronosequence". In: *Geoderma* 350, pp. 61–72. DOI: 10.1016/j.geoderma.2019.04.041.

Luo, L., H. Lin, and J. Schmidt (2010). "Quantitative Relationships between Soil Macropore Characteristics and Preferential Flow and Transport". In: *Soil Science Society of America Journal* 74.6, p. 1929. DOI: 10.2136/sssaj2010.0062.

Maes, F., A. Collignon, D. Vandermeulen, G. Marchal, and P. Suetens (1997). "Multimodality image registration by maximization of mutual information". In: *IEEE Transactions on Medical Imaging* 16.2, pp. 187–198. DOI: 10.1109/42.563664.

Mattes, D., D. R. Haynor, H. Vesselle, T. K. Lewellyn, and W. Eubank (2001). "Nonrigid multimodality image registration". In: *Medical Imaging 2001: Image Processing*. Ed. by M. Sonka and K. M. Hanson. SPIE Proceedings. SPIE, pp. 1609–1620. DOI: 10.1117/12.431046.

Mendiburu, F. d. (2017). *Package 'agricolae'*.

Menge, D. N. L., L. O. Hedin, and S. W. Pacala (2012). "Nitrogen and Phosphorus Limitation over Long-Term Ecosystem Development in Terrestrial Ecosystems". In: *PloS one* 7.8, e42045. DOI: 10.1371/journal.pone.0042045.

Milbert, G. and M. Frielinghaus (2019). "Boden des Jahres 2019 – Kippenboden (Kipp-Regosol, Kipp-Pararendzina): Fünfzehnter Boden des Jahres in Deutschland". In: *Bodenschutz* 24, pp. 4–15.

Moreno-de las Heras, M. (2009). "Development of soil physical structure and biological functionality in mining spoils affected by soil erosion in a Mediterranean-Continental environment". In: *Geoderma* 149.3-4, pp. 249–256. DOI: 10.1016/j.geoderma.2008.12.003.

Mueller, C. W., C. Hoeschen, M. Steffens, H. Buddenbaum, K. Hinkel, J. G. Bockheim, and J. Kao-Kniffin (2017). "Microscale soil structures foster organic matter stabilization in permafrost soils". In: *Geoderma* 293, pp. 44–53. DOI: 10.1016/j.geoderma.2017.01.028.

Mueller, C. W., S. Schlund, J. Prietzel, I. Kögel-Knabner, and M. Gutsch (2012). "Soil Aggregate Destruction by Ultrasonication Increases Soil Organic Matter Mineralization and Mobility". In: *Soil Science Society of America Journal* 76.5, p. 1634. DOI: 10.2136/sssaj2011.0186.

Mukhopadhyay, S., R. E. Masto, A. Yadav, J. George, L. C. Ram, and S. P. Shukla (2016). "Soil quality index for evaluation of reclaimed coal mine spoil". In: *Science of The Total Environment* 542, pp. 540–550. DOI: 10.1016/j.scitotenv.2015.10.035.

Naveed, M., P. Moldrup, E. Arthur, D. Wildenschild, M. Eden, M. Lamandé, H.-J. Vogel, and L. W. de Jonge (2013). "Revealing Soil Structure and Functional Macroporosity along a Clay Gradient Using X-ray Computed Tomography". In: *Soil Science Society of America Journal* 77.2, p. 403. DOI: 10.2136/sssaj2012.0134.

Negassa, W. C., A. K. Guber, A. N. Kravchenko, T. L. Marsh, B. Hildebrandt, and M. L. Rivers (2015). "Properties of soil pore space regulate pathways of plant residue decomposition and community structure of associated bacteria". In: *PloS one* 10.4, e0123999. DOI: 10.1371/journal.pone.0123999.

Nicol, G. W., D. Tscherko, T. M. Embley, and J. I. Prosser (2005). "Primary succession of soil Crenarchaeota across a receding glacier foreland". In: *Environmental microbiology* 7.3, pp. 337–347. DOI: 10.1111/j.1462-2920.2005.00698.x.

Nosalewicz, A. and J. Lipiec (2014). "The effect of compacted soil layers on vertical root distribution and water uptake by wheat". In: *Plant and Soil* 375.1-2, pp. 229–240. DOI: 10.1007/s11104-013-1961-0.

Ollion, J., J. Cochennec, F. Loll, C. Escudé, and T. Boudier (2013). "TANGO: a generic tool for high-throughput 3D image analysis for studying nuclear organization". In: *Bioinformatics (Oxford, England)* 29.14, pp. 1840–1841. DOI: 10.1093/bioinformatics/btt276.

Orosa-Puente, B., N. Leftley, D. von Wangenheim, J. Banda, A. K. Srivastava, K. Hill, J. Truskina, R. Bhosale, E. Morris, M. Srivastava, B. Kümpers, T. Goh, H. Fukaki, J. E. M. Vermeer, T. Vernoux, J. R. Dinneny, A. P. French, A. Bishopp, A. Sadanandom, and M. J. Bennett (2018). "Root branching toward water involves posttranslational modification of transcription factor ARF7". In: *Science (New York, N.Y.)* 362.6421, pp. 1407–1410. DOI: 10.1126/science.aau3956.

Page-Dumroese, D. S., R. E. Brown, M. F. Jurgensen, and G. D. Mroz (1999). "Comparison of Methods for Determining Bulk Densities of Rocky Forest Soils". In: *Soil Science Society of America Journal* 63.2, p. 379. DOI: 10.2136/sssaj1999.03615995006300020016x.

Pagliai, M., N. Vignozzi, and S. Pellegrini (2004). "Soil structure and the effect of management practices". In: *Soil and Tillage Research* 79.2, pp. 131–143. DOI: 10.1016/j.still.2004.07.002.

Pagliai, M. and N. Vignozzi (2002). "Soil pore system as an indicator of soil quality". In: *Advances in GeoEcology* 35, pp. 71–82.

Paradelo, M., S. Katuwal, P. Moldrup, T. Norgaard, L. Herath, and L. W. de Jonge (2016). "X-ray CT-Derived Soil Characteristics Explain Varying Air, Water, and Solute Transport Properties across a Loamy Field". In: *Vadose Zone Journal* 15.4, p. 0. DOI: 10.2136/vzj2015.07.0104.

Passioura, J. B. (1991). "Soil structure and plant growth". In: *Soil Research* 29.6, p. 717. DOI: 10.1071/SR9910717.

Paterson, E., T. Gebbing, C. Abel, A. Sim, and G. Telfer (2007). "Rhizodeposition shapes rhizosphere microbial community structure in organic soil". In: *New Phytologist* 173.3, pp. 600–610. DOI: 10.1111/j.1469-8137.2006.01931.x.

Pécsi, M. (1990). "Loess is not just the accumulation of dust". In: *Quaternary International* 7-8, pp. 1–21. DOI: 10.1016/1040-6182(90)90034-2.

Peddle, D. R., H. Peter White, R. J. Soffer, J. R. Miller, and E. F. LeDrew (2001). "Reflectance processing of remote sensing spectroradiometer data". In: *Computers & Geosciences* 27.2, pp. 203–213. DOI: 10.1016/S0098-3004(00)00096-0.

Peng, X., R. Horn, and P. Hallett (2015). "Soil structure and its functions in ecosystems: Phase matter & scale matter". In: *Soil and Tillage Research* 146, pp. 1–3. DOI: 10.1016/j.still.2014.10.017.

Peth, S., R. Horn, F. Beckmann, T. Donath, J. Fischer, and A. J. M. Smucker (2008). "Three-Dimensional Quantification of Intra-Aggregate Pore-Space Features using Synchrotron-Radiation-Based Microtomography". In: *Soil Science Society of America Journal* 72.4, p. 897. DOI: 10.2136/sssaj2007.0130.

Pierret, A., C. Hartmann, J.-L. Maeght, and L. Pagès (2011). "Biotic Regulation: Plants". In: *The architecture and biology of soils*. Ed. by K. Ritz and I. Young. Wallingford Oxfordshire and Cambridge MA: CABI.

Pihlap, E., M. Vuko, M. Lucas, M. Steffens, M. Schloter, D. Vetterlein, M. Endenich, and I. Kögel-Knabner (2019). "Initial soil formation in an agriculturally reclaimed open-cast mining area - the role of management and loess parent material". In: *Soil and Tillage Research* 191, pp. 224–237. DOI: 10.1016/j.still.2019.03.023.

Pires, L. F., W. L. Roque, J. A. Rosa, and S. J. Mooney (2019). "3D analysis of the soil porous architecture under long term contrasting management systems by X-ray computed tomography". In: *Soil and Tillage Research* 191, pp. 197–206. DOI: 10.1016/j.still.2019.02.018.

Pires, L. F., J. A. Borges, J. A. Rosa, M. Cooper, R. J. Heck, S. Passoni, and W. L. Roque (2017). "Soil structure changes induced by tillage systems". In: *Soil and Tillage Research* 165, pp. 66–79. DOI: 10.1016/j.still.2016.07.010.

Poeplau, C., C. Vos, and A. Don (2017). "Soil organic carbon stocks are systematically overestimated by misuse of the parameters bulk density and rock fragment content". In: *SOIL* 3.1, pp. 61–66. DOI: 10.5194/soil-3-61-2017.

Portell, X., V. Pot, P. Garnier, W. Otten, and P. C. Baveye (2018). "Microscale Heterogeneity of the Spatial Distribution of Organic Matter Can Promote Bacterial Biodiversity in Soils: Insights From Computer Simulations". In: *Frontiers in microbiology* 9, p. 1583. DOI: 10.3389/fmicb.2018.01583.

Qiang, M. A., Y. U. Wan-Tai, Z. Shao-hua, and Z. Lu (2007). "Relationship Between Water-Stable Aggregates and Nutrients in Black Soils After Reclamation". In: *Pedosphere* 17.4, pp. 538–544. DOI: 10.1016/S1002-0160(07)60064-2.

Rabbi, S. M. F., H. Daniel, P. V. Lockwood, C. Macdonald, L. Pereg, M. Tighe, B. R. Wilson, and I. M. Young (2016). "Physical soil architectural traits are functionally linked to carbon decomposition and bacterial diversity". In: *Scientific reports* 6, p. 33012. DOI: 10.1038/srep33012.

Rabot, E., M. Wiesmeier, S. Schlüter, and H.-J. Vogel (2018). "Soil structure as an indicator of soil functions: A review". In: *Geoderma* 314, pp. 122–137. DOI: 10.1016/j.geoderma.2017.11.009.

Ramirez, K. S., J. W. Leff, A. Barberán, S. T. Bates, J. Betley, T. W. Crowther, E. F. Kelly, E. E. Oldfield, E. A. Shaw, C. Steenbock, M. A. Bradford, D. H. Wall, and N. Fierer (2014). "Biogeographic patterns in below-ground diversity in New York City's Central Park are similar to those observed globally". In: *Proceedings. Biological sciences* 281.1795. DOI: 10.1098/rspb.2014.1988.

Rasa, K., T. Eickhorst, R. Tippkötter, and M. Yli-Halla (2012). "Structure and pore system in differently managed clayey surface soil as described by micromorphology and image analysis". In: *Geoderma* 173-174, pp. 10–18. DOI: 10.1016/j.geoderma.2011.12.017.

Rasmussen, K. J. (1999). "Impact of ploughless soil tillage on yield and soil quality: A Scandinavian review". In: *Soil and Tillage Research* 53.1, pp. 3–14. DOI: `10.1016/S0167-1987(99)00072-0`.

Rasse, D. P., A. J. M. Smucker, and D. Santos (2000). "Alfalfa Root and Shoot Mulching Effects on Soil Hydraulic Properties and Aggregation". In: *Soil Science Society of America Journal* 64, pp. 725–731. DOI: `10.2136/sssaj2000.642725x`.

Ravel, S., C. Fossati, and S. Bourennane (2018). "Spectral Unmixing of Hyperspectral Images in the Presence of Small Targets". In: *Remote Sensing* 7.1. DOI: `10.18282/rs.v7i1.460`.

Renard, P. and D. Allard (2013). "Connectivity metrics for subsurface flow and transport". In: *Advances in Water Resources* 51, pp. 168–196. DOI: `10.1016/j.advwatres.2011.12.001`.

Rethemeyer, J., R.-H. Fülöp, S. Höfle, L. Wacker, S. Heinze, I. Hajdas, U. Patt, S. König, B. Stapper, and A. Dewald (2013). "Status report on sample preparation facilities for 14C analysis at the new CologneAMS center". In: *Nuclear Instruments and Methods in Physics Research Section B: Beam Interactions with Materials and Atoms* 294, pp. 168–172. DOI: `10.1016/j.nimb.2012.02.012`.

Ritz, K., J. W. McNicol, N. Nunan, S. Grayston, P. Millard, D. Atkinson, A. Gollotte, D. Habeshaw, B. Boag, C. D. Clegg, B. S. Griffiths, R. E. Wheatley, L. A. Glover, A. E. McCaig, and J. I. Prosser (2004). "Spatial structure in soil chemical and microbiological properties in an upland grassland". In: *FEMS microbiology ecology* 49.2, pp. 191–205. DOI: `10.1016/j.femsec.2004.03.005`.

Rochette, P. and E. G. Gregorich (1998). "Dynamics of soil microbial biomass C, soluble organic C and CO 2 evolution after three years of manure application". In: *Canadian Journal of Soil Science* 78.2, pp. 283–290. DOI: `10.4141/S97-066`.

Rodarmel, C. and J. Shan (2002). "Principal Component Analysis for Hyperspectral Image Classification". In: *Surveying and Land Information Systems*, pp. 115–123.

Roy, J., R. Reichel, N. Brüggemann, S. Hempel, and M. C. Rillig (2017). "Succession of arbuscular mycorrhizal fungi along a 52-year agricultural recultivation chronosequence". In: *FEMS microbiology ecology* 93.9. DOI: `10.1093/femsec/fix102`.

Ruamps, L. S., N. Nunan, V. Pouteau, J. Leloup, X. Raynaud, V. Roy, and C. Chenu (2013). "Regulation of soil organic C mineralisation at the pore scale". In: *FEMS Microbiology Ecology* 86.1, pp. 26–35. DOI: `10.1111/1574-6941.12078`.

Rumpel, C. and I. Kögel-Knabner (2004). "Microbial use of lignite compared to recent plant litter as substrates in reclaimed coal mine soils". In: *Soil Biology and Biochemistry* 36.1, pp. 67–75. DOI: `10.1016/j.soilbio.2003.08.020`.

Rumpel, C., J. O. Skjemstad, H. Knicker, I. Kögel-Knabner, and R. F. Hüttl (2000). "Techniques for the differentiation of carbon types present in lignite-rich mine soils". In: *Organic Geochemistry* 31.6, pp. 543–551. DOI: `10.1016/S0146-6380(00)00026-7`.

Sandin, M., J. Koestel, N. Jarvis, and M. Larsbo (2017). "Post-tillage evolution of structural pore space and saturated and near-saturated hydraulic conductivity in a clay loam soil". In: *Soil and Tillage Research* 165, pp. 161–168. DOI: `10.1016/j.still.2016.08.004`.

Schindelin, J., I. Arganda-Carreras, E. Frise, V. Kaynig, M. Longair, T. Pietzsch, S. Preibisch, C. Rueden, S. Saalfeld, B. Schmid, J.-Y. Tinevez, D. J. White, V. Hartenstein, K. Eliceiri, P. Tomancak, and A. Cardona (2012). "Fiji: an open-source platform for biological-image analysis". In: *Nature Methods* 9.7, pp. 676–682. DOI: `10.1038/nmeth.2019`.

Schirmer, W. (2016). "Late Pleistocene loess of the Lower Rhine". In: *Quaternary International* 411, pp. 44–61. DOI: `10.1016/j.quaint.2016.01.034`.

Schlüter, S., F. Leuther, S. Vogler, and H.-J. Vogel (2016a). "X-ray microtomography analysis of soil structure deformation caused by centrifugation". In: *Solid Earth* 7.1, pp. 129–140. DOI: `10.5194/se-7-129-2016`.

Schlüter, S., S. R. G. A. Blaser, M. Weber, V. Schmidt, and D. Vetterlein (2018a). "Quantification of Root Growth Patterns From the Soil Perspective via Root Distance Models". In: *Frontiers in plant science* 9, p. 1084. DOI: 10.3389/fpls.2018.01084.

Schlüter, S., T. Eickhorst, and C. W. Mueller (2019). "Correlative Imaging Reveals Holistic View of Soil Microenvironments". In: *Environmental science & technology* 53.2, pp. 829–837. DOI: 10.1021/acs.est.8b05245.

Schlüter, S., C. Großmann, J. Diel, G.-M. Wu, S. Tischer, A. Deubel, and J. Rücknagel (2018b). "Long-term effects of conventional and reduced tillage on soil structure, soil ecological and soil hydraulic properties". In: *Geoderma* 332, pp. 10–19. DOI: 10.1016/j.geoderma.2018.07.001.

Schlüter, S., A. Sheppard, K. Brown, and D. Wildenschild (2014). "Image processing of multiphase images obtained via X-ray microtomography: A review". In: *Water Resources Research* 50.4, pp. 3615–3639. DOI: 10.1002/2014WR015256.

Schlüter, S. and H.-J. Vogel (2011a). "On the reconstruction of structural and functional properties in random heterogeneous media". In: *Advances in Water Resources* 34.2, pp. 314–325. DOI: 10.1016/j.advwatres.2010.12.004.

Schlüter, S. and H.-J. Vogel (2016b). "Analysis of Soil Structure Turnover with Garnet Particles and X-Ray Microtomography". In: *PloS one* 11.7, e0159948. DOI: 10.1371/journal.pone.0159948.

Schlüter, S., U. Weller, and H.-J. Vogel (2011b). "Soil-structure development including seasonal dynamics in a long-term fertilization experiment". In: *Journal of Plant Nutrition and Soil Science* 174.3, pp. 395–403. DOI: 10.1002/jpln.201000103.

Schmidt, M. W. I., C. Rumpel, and I. Kögel–Knabner (1999). "Evaluation of an ultrasonic dispersion procedure to isolate primary organomineral complexes from soils". In: *European Journal of Soil Science* 50.1, pp. 87–94. DOI: 10.1046/j.1365-2389.1999.00211.x.

Schmidt, S., A. G. Bengough, P. J. Gregory, D. V. Grinev, and W. Otten (2012). "Estimating root-soil contact from 3D X-ray microtomographs". In: *European Journal of Soil Science* 63.6, pp. 776–786. DOI: 10.1111/j.1365-2389.2012.01487.x.

Schneider, F. and A. Don (2019). "Root-restricting layers in German agricultural soils. Part II: Adaptation and melioration strategies". In: *Plant and Soil* 442.1-2, pp. 419–432. DOI: 10.1007/s11104-019-04186-8.

Shamonin, D. (2013). "Fast parallel image registration on CPU and GPU for diagnostic classification of Alzheimer's disease". In: *Frontiers in Neuroinformatics* 7. DOI: 10.3389/fninf.2013.00050.

Sheoran, V., A. S. Sheoran, and P. Poonia (2010). "Soil Reclamation of Abandoned Mine Land by Revegetation: A Review". In: *International Journal of Soil, Sediment and Water* 3.2.

Shipitalo, M., W. Dick, and W. Edwards (2000). "Conservation tillage and macropore factors that affect water movement and the fate of chemicals". In: *Soil and Tillage Research* 53.3-4, pp. 167–183. DOI: 10.1016/S0167-1987(99)00104-X.

Shrestha, R. K. and R. Lal (2011). "Changes in physical and chemical properties of soil after surface mining and reclamation". In: *Geoderma* 161.3-4, pp. 168–176. DOI: 10.1016/j.geoderma.2010.12.015.

Six, J., H. Bossuyt, S. Degryze, and K. Denef (2004). "A history of research on the link between (micro)aggregates, soil biota, and soil organic matter dynamics". In: *Soil and Tillage Research* 79.1, pp. 7–31. DOI: 10.1016/j.still.2004.03.008.

Smalley, I., S. B. Marković, and Z. Svirčev (2011). "Loess is [almost totally formed by] the accumulation of dust". In: *Quaternary International* 240.1-2, pp. 4–11. DOI: 10.1016/j.quaint.2010.07.011.

Soriano-Disla, J. M., L. J. Janik, R. A. Viscarra Rossel, L. M. Macdonald, and M. J. McLaughlin (2014). "The Performance of Visible, Near-, and Mid-Infrared Reflectance Spectroscopy

for Prediction of Soil Physical, Chemical, and Biological Properties". In: *Applied Spectroscopy Reviews* 49.2, pp. 139–186. DOI: 10.1080/05704928.2013.811081.

Steffens, M., M. Kohlpaintner, and H. Buddenbaum (2014). "Fine spatial resolution mapping of soil organic matter quality in a Histosol profile". In: *European Journal of Soil Science* 65.6, pp. 827–839. DOI: 10.1111/ejss.12182.

Steffens, M. and H. Buddenbaum (2013). "Laboratory imaging spectroscopy of a stagnic Luvisol profile — High resolution soil characterisation, classification and mapping of elemental concentrations". In: *Geoderma* 195-196, pp. 122–132. DOI: 10.1016/j.geoderma.2012.11.011.

Steffens, M., D. M. Rogge, C. W. Mueller, C. Höschen, J. Lugmeier, A. Kölbl, and I. Kögel-Knabner (2017). "Identification of Distinct Functional Microstructural Domains Controlling C Storage in Soil". In: *Environmental science & technology* 51.21, pp. 12182–12189. DOI: 10.1021/acs.est.7b03715.

Stenberg, B., R. A. Viscarra Rossel, A. M. Mouazen, and J. Wetterlind (2010). "Visible and Near Infrared Spectroscopy in Soil Science". In: vol. 107. Advances in Agronomy. Elsevier, pp. 163–215. DOI: 10.1016/S0065-2113(10)07005-7.

Stirzaker, R. J., J. B. Passioura, and Y. Wilms (1996). "Soil structure and plant growth: Impact of bulk density and biopores". In: *Plant and Soil* 185.1, pp. 151–162. DOI: 10.1007/BF02257571.

Stockmann, U., M. A. Adams, J. W. Crawford, D. J. Field, N. Henakaarchchi, M. Jenkins, B. Minasny, A. B. McBratney, V. d. R. d. Courcelles, K. Singh, I. Wheeler, L. Abbott, D. A. Angers, J. Baldock, M. Bird, P. C. Brookes, C. Chenu, J. D. Jastrow, R. Lal, J. Lehmann, A. G. O'Donnell, W. J. Parton, D. Whitehead, and M. Zimmermann (2013). "The knowns, known unknowns and unknowns of sequestration of soil organic carbon". In: *Agriculture, Ecosystems & Environment* 164, pp. 80–99. DOI: 10.1016/j.agee.2012.10.001.

Suzuki, M., T. Shinmura, K. Iimura, and M. Hirota (2008). "Study of the Wall Effect on Particle Packing Structure Using X-ray Micro Computed Tomography". In: *Advanced Powder Technology* 19.2, pp. 183–195. DOI: 10.1163/156855208X293817.

Timm, L. C., L. F. Pires, K. Reichardt, R. Roveratti, J. C. M. Oliveira, and O. O. S. Bacchi (2005). "Soil bulk density evaluation by conventional and nuclear methods". In: *Soil Research* 43.1, p. 97. DOI: 10.1071/SR04054.

Tippkötter, R. (1983). "Morphology, spatial arrangement and origin of macropores in some hapludalfs, West Germany". In: *Geoderma* 29.4, pp. 355–371. DOI: 10.1016/0016-7061(83)90021-6.

Totsche, K. U., W. Amelung, M. H. Gerzabek, G. Guggenberger, E. Klumpp, C. Knief, E. Lehndorff, R. Mikutta, S. Peth, A. Prechtel, N. Ray, and I. Kögel-Knabner (2018). "Microaggregates in soils". In: *Journal of Plant Nutrition and Soil Science* 181.1, pp. 104–136. DOI: 10.1002/jpln.201600451.

Tracy, S. R., C. R. Black, J. A. Roberts, and S. J. Mooney (2011). "Soil compaction: a review of past and present techniques for investigating effects on root growth". In: *Journal of the science of food and agriculture* 91.9, pp. 1528–1537. DOI: 10.1002/jsfa.4424.

Tristán-Vega, A., V. García-Pérez, S. Aja-Fernández, and C.-F. Westin (2012). "Efficient and robust nonlocal means denoising of MR data based on salient features matching". In: *Computer methods and programs in biomedicine* 105.2, pp. 131–144. DOI: 10.1016/j.cmpb.2011.07.014.

Valentine, T. A., P. D. Hallett, K. Binnie, M. W. Young, G. R. Squire, C. Hawes, and A. G. Bengough (2012). "Soil strength and macropore volume limit root elongation rates in many UK agricultural soils". In: *Annals of botany* 110.2, pp. 259–270. DOI: 10.1093/aob/mcs118.

van Veelen, A., N. Koebernick, C. S. Scotson, D. McKay-Fletcher, T. Huthwelker, C. N. Borca, J. F. W. Mosselmans, and T. Roose (2019). "Root-induced soil deformation influences Fe,

S and P: rhizosphere chemistry investigated using synchrotron XRF and XANES". In: *The New phytologist*. DOI: 10.1111/nph.16242.

Vance, E. D., P. C. Brookes, and D. S. Jenkinson (1987). "An extraction method for measuring soil microbial biomass C". In: *Soil Biology and Biochemistry* 19.6, pp. 703–707. DOI: 10.1016/0038-0717(87)90052-6.

Vogel, H.-J. (1997). "Morphological determination of pore connectivity as a function of pore size using serial sections". In: *European Journal of Soil Science* 48.3, pp. 365–377. DOI: 10.1111/j.1365-2389.1997.tb00203.x.

Vogel, H.-J., U. Weller, and S. Schlüter (2010). "Quantification of soil structure based on Minkowski functions". In: *Computers & Geosciences* 36.10, pp. 1236–1245. DOI: 10.1016/j.cageo.2010.03.007.

Vogel, H.-J. (2002). "Topological Characterization of Porous Media". In: *Morphology of Condensed Matter*. Ed. by K. Mecke and D. Stoyan. Vol. 600. Lecture Notes in Physics. Berlin and Heidelberg: Springer, pp. 75–92. DOI: 10.1007/3-540-45782-8{\textunderscore}3.

Vogel, H.-J., E. Eberhardt, U. Franko, B. Lang, M. Ließ, U. Weller, M. Wiesmeier, and U. Wollschläger (2019). "Quantitative Evaluation of Soil Functions: Potential and State". In: *Frontiers in Environmental Science* 7, p. 236. DOI: 10.3389/fenvs.2019.00164.

Vollsnes, A. V., C. M. Futsaether, and A. G. Bengough (2010). "Quantifying rhizosphere particle movement around mutant maize roots using time-lapse imaging and particle image velocimetry". In: *European Journal of Soil Science* 61.6, pp. 926–939. DOI: 10.1111/j.1365-2389.2010.01297.x.

Wanzek, T., M. Keiluweit, T. Varga, A. Lindsley, P. S. Nico, S. Fendorf, and M. Kleber (2018). "The Ability of Soil Pore Network Metrics to Predict Redox Dynamics is Scale Dependent". In: *Soil Systems* 2.4, p. 66. DOI: 10.3390/soilsystems2040066.

Watteau, F., G. Villemin, G. Burtin, and L. Jocteur-Monrozier (2006). "Root impact on the stability and types of micro- aggregates in silty soil under maize". In: *European Journal of Soil Science* 57.2, pp. 247–257. DOI: 10.1111/j.1365-2389.2005.00734.x.

Weisskopf, P., R. Reiser, J. Rek, and H.-R. Oberholzer (2010). "Effect of different compaction impacts and varying subsequent management practices on soil structure, air regime and microbiological parameters". In: *Soil and Tillage Research* 111.1, pp. 65–74. DOI: 10.1016/j.still.2010.08.007.

Wendt, J. W. and S. Hauser (2013). "An equivalent soil mass procedure for monitoring soil organic carbon in multiple soil layers". In: *European Journal of Soil Science* 64.1, pp. 58–65. DOI: 10.1111/ejss.12002.

Whalley, W. R., B. Riseley, P. B. Leeds-Harrison, N. R. A. Bird, P. K. Leech, and W. P. Adderley (2005). "Structural differences between bulk and rhizosphere soil". In: *European Journal of Soil Science* 56.3, pp. 353–360. DOI: 10.1111/j.1365-2389.2004.00670.x.

White, R. G. and J. A. Kirkegaard (2010). "The distribution and abundance of wheat roots in a dense, structured subsoil–implications for water uptake". In: *Plant, cell & environment* 33.2, pp. 133–148. DOI: 10.1111/j.1365-3040.2009.02059.x.

White, T. J., T. Bruns, S. Lee, and J. Taylor (1990). "AMPLIFICATION AND DIRECT SEQUENCING OF FUNGAL RIBOSOMAL RNA GENES FOR PHYLOGENETICS". In: *PCR Protocols*. Elsevier, pp. 315–322. DOI: 10.1016/B978-0-12-372180-8.50042-1.

Wiesmeier, M., L. Urbanski, E. Hobley, B. Lang, M. von Lützow, E. Marin-Spiotta, B. van Wesemael, E. Rabot, M. Ließ, N. Garcia-Franco, U. Wollschläger, H.-J. Vogel, and I. Kögel-Knabner (2019). "Soil organic carbon storage as a key function of soils - A review of drivers and indicators at various scales". In: *Geoderma* 333, pp. 149–162. DOI: 10.1016/j.geoderma.2018.07.026.

Wuest, S. B. (2001). "Soil biopore estimation: effects of tillage, nitrogen, and photographic resolution". In: *Soil and Tillage Research* 62, pp. 111–116.

Yang, X.-M. and M. M. Wander (1999). "Tillage effects on soil organic carbon distribution and storage in a silt loam soil in Illinois". In: *Soil and Tillage Research* 52.1-2, pp. 1–9. DOI: 10.1016/S0167-1987(99)00051-3.

Yates, K., C. H. Fenton, and D. H. Bell (2018). "A review of the geotechnical characteristics of loess and loess-derived soils from Canterbury, South Island, New Zealand". In: *Engineering Geology* 236, pp. 11–21. DOI: 10.1016/j.enggeo.2017.08.001.

Young, I. M., J. W. Crawford, N. Nunan, W. Otten, and A. Spiers (2008). "Chapter 4 Microbial Distribution in Soils". In: vol. 100. Advances in Agronomy. Elsevier, pp. 81–121. DOI: 10.1016/S0065-2113(08)00604-4.

Young, I. M., J. Crawford, and C. Rappoldt (2001). "New methods and models for characterising structural heterogeneity of soil". In: *Soil and Tillage Research* 61.1-2, pp. 33–45. DOI: 10.1016/S0167-1987(01)00188-X.

Yunusa, I. A. M. and P. J. Newton (2003). "Plants for amelioration of subsoil constraints and hydrological control: the primer-plant concept". In: *Plant and soil* 257.2, pp. 261–281. DOI: 10.1023/A:1027381329549.

Zhang, Z., C. Wei, D. Xie, M. Gao, and X. Zeng (2008). "Effects of land use patterns on soil aggregate stability in Sichuan Basin, China". In: *Particuology* 6.3, pp. 157–166. DOI: 10.1016/j.partic.2008.03.001.

Zhang, Z., L. Lin, Y. Wang, and X. Peng (2016). "Temporal change in soil macropores measured using tension infiltrometer under different land uses and slope positions in subtropical China". In: *Journal of Soils and Sediments* 16.3, pp. 854–863. DOI: 10.1007/s11368-015-1295-z.

Zhang, Z., K. Liu, H. Zhou, H. Lin, D. Li, and X. Peng (2018). "Three dimensional characteristics of biopores and non-biopores in the subsoil respond differently to land use and fertilization". In: *Plant and Soil* 428.1-2, pp. 453–467. DOI: 10.1007/s11104-018-3689-3.

Zhang, Z., K. Liu, H. Zhou, H. Lin, D. Li, and X. Peng (2019). "Linking saturated hydraulic conductivity and air permeability to the characteristics of biopores derived from X-ray computed tomography". In: *Journal of Hydrology* 571, pp. 1–10. DOI: 10.1016/j.jhydrol.2019.01.041.

Zhao, D., M. Xu, G. Liu, X. Yao, D. Tuo, R. Zhang, T. Xiao, and G. Peng (2017). "Quantification of soil aggregate microstructure on abandoned cropland during vegetative succession using synchrotron radiation-based micro-computed tomography". In: *Soil and Tillage Research* 165, pp. 239–246. DOI: 10.1016/j.still.2016.08.007.

Zhao, Z., I. Shahrour, Z. Bai, W. Fan, L. Feng, and H. Li (2013). "Soils development in opencast coal mine spoils reclaimed for 1–13 years in the West-Northern Loess Plateau of China". In: *European Journal of Soil Biology* 55, pp. 40–46. DOI: 10.1016/j.ejsobi.2012.08.006.

Zhou, W., K. Yang, Z. Bai, H. Cheng, and F. Liu (2017). "The development of topsoil properties under different reclaimed land uses in the Pingshuo opencast coalmine of Loess Plateau of China". In: *Ecological Engineering* 100, pp. 237–245. DOI: 10.1016/j.ecoleng.2016.12.028.

List of Publications

- Lucas, M., A. Balbín-Suárez, K. Smalla, and D. Vetterlein, (2018). Root growth, function and rhizosphere microbiome analyses show local rather than systemic effects in apple plant response to replant disease soil. In: PloS one, 13, e0204922. DOI: 10.1371/journal.pone.0204922.

- Lucas, M., E. Pihlap, M. Steffens, D. Vetterlein, and I. Kögel-Knabner (submitted). "Combination of Imaging Infrared Spectroscopy and X-ray Computed Microtomography for the Investigation of Bio- and Physicochemical processes in Structured Soils".

- Lucas, M., S. Schlüter, H.-J. Vogel and D. Vetterlein (2019). "Roots compact the surrounding soil depending on the structures they encounter". In: Scientific reports, 9, 16236. DOI: 10.1038/s41598-019-52665-w.

- Lucas, M., S. Schlüter, H.-J. Vogel, and D. Vetterlein (2019). "Soil structure formation along an agricultural chronosequence". In: Geoderma 350, pp. 61–72. DOI: 10.1016/j.geoderma.2019.04.041.

- Lucas, M., D. Vetterlein, H.-J. Vogel and S. Schlüter (submitted). "Pore connectivity across scales and resolutions".

- Pihlap, E., M. Vuko, M. Lucas, M. Steffens, M. Schloter, D. Vetterlein, M. Endenich, and I. Kögel-Knabner (2019). "Initial soil formation in an agriculturally reclaimed open-cast mining area - the role of management and loess parent material". In: Soil and Tillage Research 191, pp. 224–237. DOI: 10.1016/j.still.2019.03.023.

Curriculum vitae

Maik LUCAS

Persönliche Daten

GEBURTSORT UND DATUM: Lingen (EMS) | 22 05 1992
EMAIL: maik.lucas@ufz.de

Beruflicher Werdegang

Current NOVEMBER 2016	Doktorand und wissenschaftlicher Mitarbeiter am *Helmholtz-Zentrum für Umweltforschung - UFZ* Arbeitsgruppe Boden-Pflanze-Interaktion des Departments Bodensystemforschung

Ausbildung

2014-2016	Masterstudium Management natürlicher Ressourcen an der **Martin Luther Universität Halle-Wittenberg**	Abschluss: M.Sc (1,6)
2011-2014	Bachelorstudium der Geoökologie an der **TU Bergakademie Freiberg**	Abschluss: B.Sc. (2,2)
2004-2011	**Gymnasium Leoninum-Handrup**	Abschluss: Abitur (2,3)

_____   _____
Datum / Date   Unterschrift /Signature

Eidesstattliche Erklärung / Declaration under oath

Ich erkläre an Eides statt, dass ich die Arbeit selbstständig und ohne fremde Hilfe verfasst, keine anderen als die von mir angegebenen Quellen und Hilfsmittel benutzt und die den benutzten Werken wörtlich oder inhaltlich entnommenen Stellen als solche kenntlich gemacht habe.
I declare under penalty of perjury that this thesis is my own work entirely and has been written without any help from other people. I used only the sources mentioned and included all the citations correctly both in word or content.

_____   _____
Datum / Date   Unterschrift /Signature

Danksagung / Acknowledgement